City Research Online

City St George's, University of London

Citation: Hassan, U. (1979). Effects of turbulence scale on the correlation of pressures on rectangular section prisms. (Unpublished Doctoral thesis, The City University)

EFFECTS OF TURBULENCE SCALE ON THE CORRELATION OF PRESSURES ON RECTANGULAR SECTION PRISMS

by

Unsal Hassan B.Sc.

A thesis presented for the Degree of Doctor of Philosophy
in the Department of Aeronautical Engineering of
The City University.

May 1979

Dedicated to [redacted], without their patience and understanding this work would never have been completed.

CONTENTS

CONTENTS (Concluded)

ACKNOWLEDGEMENTS

The research reported in this thesis was carried out in the Department of Aeronautics of The City University between October 1972 and September 1975, during which period the author was supported by a SRC Research Studentship.

The author wishes to acknowledge the help afforded to him by many of the academic, technical and secretarial staff of the University. It is not possible to mention each individually, however the author wishes to thank particularly:

Mr D M Sykes, under whose supervision the work was carried, for his advice and encouragement and for introducing the author to the field of industrial aerodynamics. Also for reading the manuscript and his valuable criticisms.

[redacted] and the entire technical staff of the Department of Aeronautics for invaluable assistance in all stages of the experimental work.

[redacted] and other staff of the Computer Unit for assistance in overcoming many computing problems, in particular for providing the data link between the laboratory and hybrid computer and for extending the capabilities of the hybrid computer system.

DECLARATION

I hereby grant powers of discretion to the university librarian to allow this thesis to be copied in whole or in part without further reference to me. This permission covers only single copies made for study purposes, subject to normal conditions of acknowledgement.

[redacted]

ABSTRACT

With recent construction practice, modern tall structures tend to be lightweight with low structural damping which can give rise to the structure being sensitive to dynamic excitation by the wind, with potential problems with local or overall structural fatigue failure or discomfort to occupants.

At present the UK Code of Practice for wind loading of structures provides no method for determining dynamic wind loads for building design. Codes of Practice in other countries which do present methods for determining these dynamic loads tacitly assume that the fluctuating pressures on the windward and leeward face of the building are perfectly correlated. Further, it is suggested that the spatial correlation of fluctuating pressures on the building faces are identical to the spatial correlation of atmospheric turbulence. It is also often assumed that the effects of turbulence scale on the flow around bluff bodies such as buildings is of secondary importance. There is very little experimental evidence to substantiate such assumptions and the principal objective of the study was to examine their validity and also provide data with which to validate design calculations and refine current procedures.

The experimental programme to investigate in considerable detail and provide quantitative data on the effects of turbulence scale on the cross-correlations of fluctuating pressures on and between the windward and leeward faces of rectangular section prisms was conducted in the 3 m × 1.5 m industrial aerodynamics wind tunnel. To isolate the effects of turbulence scale the velocity profile of the atmospheric boundary layer was not modelled. Turbulence was generated using bi-planar grids and longitudinal integral scales, L_x, of 58, 100 and 198 mm were achieved with an intensity of 10%. Cross-spectral analyses of fluctuating pressures on models with breadth/depth ratios B/D of 1, 2 and 4 and an aspect ratio of 6 show that the coherence between the windward and leeward face pressures has a constant value of about 0.3 for wavelengths 1-100 times model breadth. On the windward and leeward faces the coherence data is not accurately represented by the simple exponential function

$$\gamma(n) = \exp\,[-c \cdot nr/\bar{U}]$$

but found to be a function of both $nr/\bar{U}$ and r/L_x, where c is a decay constant and r is the spatial separation. For the windward face values for the decay constant which give the best fit to the data have been determined and found to be a function of separation r. For lateral separations c ranged in value from about 2 to 6 corresponding to r/B=0.2 to 0.8. These are smaller than the generally accepted values of about 6-8 which are based on measurements of spatial correlations of atmospheric turbulence. The variations of these measurements with turbulence scale are found to be significant and application of the results to design concepts is briefly discussed along with areas for future research.

NOTATION

Symbol	Definition
B	Model breadth
b	Grid bar width
C_α	Empirical constant in coherence relationship, where α represents x, y or z, respectively
C(n)	Co-spectral density function
C_m	Virtual mass coefficient
C_D	Drag coefficient
C_{p_α}	Pressure coefficient, where α represents ω or ℓ (windward or leeward) respectively
C'_{p_α}	Fluctuating pressure coefficient (= $\hat{p}/\frac{1}{2}\rho\bar{U}^2$), where α represents ω or ℓ (windward or leeward) respectively
D	Model depth
D(t)	Drag force
G	Gust factor
g	Gravitational acceleration
H	Model height
H(n)	Frequency response function
h(t)	Impulse response function
I_u	Intensity of turbulence
K	Kurtosis of probability density function
k	von Karman's constant (≃0.4)
L	Monin-Obukhov stability length scale
L_α	Integral turbulence length scale, where α represents x, y or z, respectively
L	Empirical length scale in spectral density function for turbulence
M	Grid mesh width
m_r	r^{th} moment of probability density function
N	Number of data values
N(n)	Along-wind cross-correlation function
n	Frequency
$\tilde{n}$	Reduced frequency $\left(= nL_\alpha/\bar{U}(10)\right)$
n_s	Sampling rate
n_f	Nyquist or folding frequency

NOTATION (Contd.)

Symbol	Definition
δn	Bandwidth
$\bar{P}$	Mean pressure
$p(t)$	Fluctuating pressure
$P(x)$	Probability distribution function of the variable x
$p(x)$	Probability density function of the variable x
$Q(n)$	Quad-spectral density function
$R(x)$	Space correlation function
$R(\tau)$	Auto-correlation function
$R_{12}(\tau)$	Cross-correlation function
Ri	Richardson's number
r	Spatial separation in correlations
S	Skew of probability distribution function
$S_D(n)$	Spectral density function for drag fluctuations
$S_p(n)$	Spectral density function for pressure fluctuations
$S_u(n)$	Spectral density function for turbulence
$S_{12}(n)$	Cross-spectral density function
T	Ambient temperature or averaging period
T_x	Integral time scale
$-\partial T/\partial z$	Atmospheric lapse rate
t	Time
δt	Sampling interval
$\bar{U}$	Mean wind speed
$u(t)$	Longitudinal velocity fluctuations
u_*	Friction velocity
W	Probability density bandwidth
$X^2(n)$	Along-wind cross-correlation function $\left(= \left[C_{P_\omega}^2 + 2\, C_{P_\omega}\, C_{P_\ell}\, N(n) + C_{P_\ell}^2\right] / \left[C_{P_\omega} + C_{P_\ell}\right]^2\right)$
x	Downstream distance from grid
x,y,z	Cartesian co-ordinate axis system
z_o	Surface roughness length
α	Wind speed power law exponent
γ	Adiabatic lapse rate

NOTATION (Concluded)

Symbol	Definition
$\gamma^2(n)$	Coherence function
$\Theta(n)$	Argument of cross-spectral density function
ρ	Air density
$\rho_{12}(\tau)$	Cross-correlation coefficient
σ	Standard deviation
ε	Normalised standard error
κ	Surface drag coefficient $(=\{0.4/\ell n(10/Z_o)\}^2)$
τ	Time lag
$\chi_a^2(n)$	Aerodynamic admittance function

Over Symbols

$(\bar{\;})$	Mean value
$(\hat{\;})$	Root mean square deviation about mean value

CHAPTER 1

INTRODUCTION

1.1 General Background

An understanding of wind loading on structures is important for their economic design; increasingly so as high-rise construction activities increase and as design improvements using refined structural analysis of steel frames together with lightweight flooring and cladding materials lead to lighter, more flexible structures with less damping than earlier structures of more conventional design and construction. Equally, or more important is the safety and protection of human life from injury arising from local or overall structural failure which is a potential problem with some modern tall structures since they may be sensitive to dynamic excitation by the wind. Finally, structures such as buildings should be serviceable; therefore dynamic excitation of the structure by the wind should not cause discomfort to occupants due to excessive movements.

Reminders of the seriousness of the problem of wind damage are constantly with us. One example is the large scale destruction and damage to over 100,000 houses in Sheffield by wind, during gales in November 1962[1]. Other, less conventional structures which suffer wind damage such as the collapse of cooling towers at the Ferrybridge B Power Station in November 1969[2] tend to overshadow the more common occurrences of wind damage to conventional structures. In a survey of wind damage to buildings in the UK covering the period 1962 to 1969[3] it was found that more than 100,000 buildings were damaged on average each year, costing £7 million in repairs and replacements. A similar survey, of a gale in 1976[4], showed that it alone damaged more than 1.5 million properties, with the damage costing about £30 million. Besides gales, there are other sources of wind damage, such as from tornadoes. It is not generally realised how frequently tornadoes occur in the UK; there is evidence of 78 in the period 1963 to 1966[5], and they are now being reported more frequently[6,7]. The problem is that because a tornado is a very localised phenomena, typically of the order of 50 m in diameter, it very rarely passes close to a meteorological station and information has to be from public reports. For this reason there are probably a number of tornadoes each year which are not identified.

Wind damage of structures is a far from new problem. There have been many catastrophic failures, notably the destruction of a chain pier at Brighton in 1836, the collapse of Telford's original suspension bridge over the Menai Straits in 1839 and the Tay rail bridge which was overturned by wind during a gale in 1879. The inquiry into the Tay rail bridge disaster initiated the first large scale discussion on the subject of wind forces and resulted in an allowance being made for static wind loading in the design of later structures. Despite many previous examples, the problem of wind loading was not given serious attention until the dramatic collapse of the Tacoma Narrows bridge in 1940, which failed structurally from fatigue loading due to torsional oscillations caused by a steady wind.

To minimise the problem of wind damage to structures, standard Codes of Practice were introduced which enabled structural designers to make adequate allowances for wind loading. In order to keep these codes up to date it is necessary to revise them constantly, incorporating new knowledge of atmospheric wind and the interaction of the wind with the structure. At present there is no method in the British Code of Practice[8] for determining the unsteady loads on buildings for wind loading design; it deals mainly with extreme load analysis. In the case of modern tall structures, however, large resonant motions induced by the wind may occur and this contingency must be predicted and adequately accounted for in the design.

There are Codes of Practice and Standards such as the American[9], Australian[10] and Canadian[11] which do include procedures for calculating the along-wind response of flexible structures to the buffeting effects of wind turbulence. They are all mainly based on statistical models proposed by Davenport[12] and Vickery[13], and generally result in a gust factor which can be used to estimate peak loads, stresses, deflections or for that matter any other similar quantity. The gust factor, G, is defined as:

$$G = 1 + \frac{x_{\text{max}}}{\bar{x}} \qquad \ldots (1)$$

where x_{max} and $\bar{x}$ are respectively the maximum and mean values of the quantity $x(t)$.

Although it is not implicit, Simiu[14] has shown that in the derivation of gust factors it is generally assumed the fluctuating pressures on the windward face of a tall building are perfectly correlated to those acting on the leeward face. This groundless assumption results in over-estimates of gust factors for the dynamic loading or response and as a consequence the building design could be uneconomic. However, another invalid assumption generally made is that the vertically and laterally separated cross-correlations of fluctuating pressures on the building faces are identical to the spatial cross-correlations of longitudinal velocity fluctuations measured in strong winds. Reports of measurements made on full scale buildings by for example Newberry[15,16] and Mackey[17] demonstrate this is not the case, with fluctuating pressures on the building having higher correlations. The net result of these two incorrect assumptions is that the value for the gust factor is approximately correct.

Velozzi and Cohen[18] recognised that the fluctuating pressures on the windward and leeward faces of a tall building could not be perfectly correlated, and proposed a method to account for this, which is incorporated in the American Codes of Practice. However, as explained by Vickery[19] and Simiu[20] the procedure is incorrect since it applies the alongwind cross-correlation function, N(n), not just to the windward-leeward face cross-spectra of pressure but also to the pressures acting on each face. The result is that the dynamic response, in particular the resonant amplification, is under-estimated. Simiu[14] also recognised the shortcoming of the usual gust factor approach to adequately account for the imperfect correlation and from first principles shows that the alongwind cross-correlation function $X^2(n)$ is given by:

$$X^2(n) = \frac{C_{p_\omega}^2 + 2\, C_{p_\omega}\, C_{p\ell}\, N(n) + C_{p\ell}^2}{\left(C_{p_\omega} + C_{p\ell}\right)^2} \qquad \ldots (2)$$

in which C_{p_ω} and $C_{p\ell}$ are pressure coefficients, assumed to be constant for the windward and leeward faces, respectively; and N(n) is the alongwind cross-correlation function.

Davenport[12], Vickery[21] and others assume that N(n) = 1, therefore $X^2(n) = 1$; however, based on limited data N(n) is found to probably lie in the range ±0.2 and therefore $X^2(n) < 1$. From Equation 2 it is evident that $X^2(n)$, and therefore the gust factor, is also a function of C_{p_ω} and $C_{p\ell}$, the values of which can differ from one code to another.

It is apparent that present Codes of Practice for wind loading are of limited use in designing for alongwind oscillations of modern tall structures. Hence, the object of this research programme is to try to bridge this gap in knowledge by commencing with a study of the effects of turbulence characteristics on the correlation of pressures across rectangular prisms in a wind tunnel.

1.2 The Nature of Atmospheric Winds

To be able to understand and predict the behaviour of structures in wind it is essential to have some knowledge of the behaviour and structure of natural winds.

The winds, in the macro-meteorological sense, are movements of air masses in the atmosphere, mainly caused by solar radiation. Because the energy per unit area received from the sun depends on geographical latitude, temperature differences arise and hence pressure gradients which with forces like the Coriolis and centripetal induce movement of air masses known as the gradient wind. In the lower atmosphere[22], termed the planetary boundary layer in which most civil engineering structures lie, the movement of the air is retarded by frictional forces and large obstructions at the earth's surface, as well as the Reynolds stresses produced by vertical exchange of momentum due to turbulence. The turbulence which may be mechanical and/ or thermal in origin also causes rapid fluctuations in the wind velocity over a wide range of frequencies and amplitudes, commonly termed gusts.

Most structural wind loading problems are concerned with high wind conditions during which surface friction causes so much mechanical mixing of the atmosphere that the thermal gradients giving rise to convection processes are destroyed. The Richardson number, Ri, has long been used as an index of atmospheric stability and is defined as:

$$\mathrm{Ri} = \frac{g\left(\frac{\partial T}{\partial z} + \gamma\right)}{T\left(\frac{\partial \bar{U}}{\partial z}\right)^2} \qquad \ldots (3)$$

where $-\partial T/\partial z$ and γ are the atmospheric and adiabatic lapse rates, respectively; $\partial \bar{U}/\partial z$ is the mean wind velocity gradient of the boundary layer; T is ambient temperature and g is gravitational acceleration. In high winds it is found that the Richardson number is near zero, which implies the lapse rate is approximately adiabatic and the atmosphere is neutrally stable.

A brief study of a typical anemograph record of wind speed in Fig.1 indicates that the natural wind can be considered to consist of a broad band of high frequency gusts superimposed upon a more slowly varying wind speed. It is obvious that the fluctuations are random in character and cannot be analysed using deterministic methods. At present, turbulence is best defined using statistical techniques to describe its characteristics.

The spectrum of horizontal wind velocity near the ground shown in Fig.2, was pieced together by Van der Hoven[23] from measurements at Brookhaven, New York, and gives an indication of the long-term distribution of turbulent energy. Long-term spectra measured at other locations demonstrate similar characteristics although there are differences in detail. The low frequency side of the spectrum forms the macro-meteorological range and the variations are due to large scale movements of air masses. These usually occur as depressions and anti-cyclones with periods of about four days. On the high frequency side the variations are due to atmospheric turbulence and form the micro-meteorological range. These are a consequence of the mechanical mixing of the lower layers of the atmosphere by the surface roughness, and have their energy centred around periods of one minute. In between these two regions there is a meso-meteorological section due to the diurnal variations in wind velocity caused by the sun rising and setting. It has been found that although the spectrum is only applicable to the location where it was recorded, the general shape and positions of the peaks remain very much the same for any other location. An important feature of all long-term spectra is the gap between periods of about 10 minutes and 2 hours where the spectrum contains very little energy. The significance of the spectral gap is that it enables the fluctuations in the macro-meteorological range to be analysed as quasi-static to obtain mean wind speeds, and the wind then defined as consisting of turbulent fluctuations superimposed on the quasi-static mean values.

Defining wind speeds without reference to the period over which the mean was taken is meaningless. Davenport[24] suggests that a good averaging period T for defining mean wind speeds is approximately 5-30 minutes. The mean wind speed may be defined as:

$$\bar{U} = \frac{1}{T} \int_{t-T/2}^{t+T/2} U(t)dt \qquad \ldots (4)$$

where $U(t)$ is the wind speed component along the average wind direction at time t; and $\bar{U}$ is the mean wind speed averaged over the time interval T.

Reasons for choosing a value in the 5-30 minutes range for the averaging period are[24]:

- it lies near the centre of the spectral gap ensuring that, in general, trends will not be strong;
- it is short enough to reflect sharp, sudden storms, such as thunder storms which usually last 5-10 minutes;
- it is normally quite adequate for steady state oscillations to develop since the natural frequency of

structures ranges from approximately 0.1 Hz and higher;

- although different averaging periods are used throughout the world, it can be assumed that provided they within the spectral gap, stable averages will be obtained.

Although the general shape of long-term spectra have been found to be very similar, the positions of the peaks do differ, including the spectral gap. For this reason the author considers that without precise knowledge of the spectrum for the location being considered averaging periods less than about 15 minutes are too short.

1.2.1 Mean wind velocity gradient

As noted earlier the wind in the planetary boundary layer is retarded by surface roughness. The lower layers of air then retard those above them, resulting in a change of mean wind speed with height, until the shear forces are reduced to zero. At that height, called the gradient height, changes in wind speed are unaffected by ground effects and are dependent only upon the pressure field and its latitude position. The rate of change of wind speed with height is called the wind shear. The planetary boundary layer can be considered to consist of a number of layers each governed by a different set of flow parameters; however, of these it is the surface layer and the Ekman layer which are of direct interest to structural designers.

The surface layer which extends from the ground to a height of approximately 30 m, is the region where the variation of shear stress can be neglected. The vertical variation of mean wind speed in the surface layer can be accurately represented by the Prandtl logarithmic law or its extensions[25,32] such as:

$$\bar{U}(z) = \frac{u_*}{k}\left[\ell n\,\frac{z}{z_o} + \frac{5z}{L}\right] \qquad \dots (5)$$

where $\bar{U}(z)$ is the mean wind speed at height z above ground level;

u_* is the friction velocity; k is von Karman's constant ≈0.4; z_o is a roughness length characterising the terrain and L is the Monin-Obukhov length scale. Typical values of z_o for various types of surfaces are given in Table 1.

The logarithmic profile agrees well with measurements made over surfaces of roughness ranging from smooth mud flats to tall grass. The profiles of particular importance in the design of tall buildings however are those for built-up areas such as city centres. Unfortunately, it is for these conditions for which there is the least information available; the reason is that the majority of meteorological research has been carried out in well exposed, level terrain. Typical values for the roughness length z_o appropriate to suburban, and urban areas have been included in Table 1. However, caution must be exercised when using these values since the flow in urban areas, defined as an interfacial layer by Pasquill[26], is determined by local obstructions and consists of wake flows and large variations of static pressure.

Using Nikuradses criterion for fully rough flow, Sutton[27] concluded that natural surfaces are aerodynamically rough. This together with the large Reynolds numbers involved in atmospheric flows means that turbulent flow conditions exist throughout the depth of the atmospheric boundary layer.

Above the surface layer and extending to the top of the atmospheric boundary layer is the Ekman layer. In this region the Coriolis force increases and the shear stress decreases with increasing height. The shear stress is zero at the gradient height, which is approximately 500 m to 1000 m, and the change in frictional force not only affects the wind speed but also its direction. This change in wind direction is known as the Ekman spiral and wind direction rotates from being nearly parallel to the isobars at the top of the layer to 15^o-30^o towards the lower pressure region near the bottom. The logarithmic law of Equation 4 can be modified to be approximately applicable up to heights of a few hundred metres. However, the underlying assumptions are no longer valid and values to be used for the parameters in the equation are difficult to determine. For these reasons, and because of its simplicity, engineers have favoured using the empirical power law:

$$\frac{\bar{U}(z)}{\bar{U}(z_1)} = \left(\frac{z}{z_1}\right)^{\alpha} \qquad \text{... (6)}$$

in which $\bar{U}(z_1)$ is a reference velocity at height z_1 and the power exponent α is a constant dependent on surface roughness. Typical values of α for various types of terrain are included in Table 1. The reference velocity is usually standardised to either the gradient height Z_G or a height of 10 m. Since it is generally difficult to know what the gradient height is, current practice is to assume that the gradient height is only a function of the terrain, the reference height of 10 m has become the norm. In urban areas with a fairly constant roof level, Equation 6 is generally modified, by introducing a false origin, to give an improved description of the velocity profile.

It has been found that the power law relationship is also suitable for describing the variation of gust speeds with height, which is of particular interest in extreme load analysis, providing the appropriate exponents are used.

1.2.2 Atmospheric turbulence

The natural wind was defined earlier as consisting of turbulent fluctuations superimposed on a quasi-static mean. In order to understand the natural wind the turbulent fluctuations need to be defined in some manner as well as the mean wind speed. From the anemograph record of wind speed in Fig.1 it is obvious the variations are irregular and cannot be described in a deterministic manner. At present turbulence is best characterised using its statistical properties. Statistical techniques have been developed for analysis of randomly fluctuating signals and these methods can and are used in the analysis of turbulence.

From the definition of the natural wind, turbulence has been classified as including all fluctuations with frequencies higher than the quasi-static mean wind speed variation. Turbulence is therefore the deviations of the instantaneous wind speed U(t) from the quasi-static mean wind speed $\bar{U}$:

$$u(t) = U(t)-\bar{U} \qquad \ldots (7)$$

The variability of the wind speed is best described in terms of the variance σ_u^2, where:

$$\sigma_u^2 = \bar{u}^2 = \frac{1}{T} \int_{t-T/2}^{t+T/2} (U(t)-\bar{U})^2 \, dt \qquad \ldots (8)$$

A measure of the gustiness of the wind is the turbulence intensity I_u, defined as:

$$I_u = \frac{\sigma_u}{\bar{U}} \qquad \ldots (9)$$

Within the atmospheric boundary layer at a fixed height the variance generally increases with increasing wind. However, since the variance varies less rapidly with height above the ground than the quasi-static mean wind speed, the turbulence intensity usually decreases with increasing height.

To describe the turbulent fluctuations in more detail than simply its intensity, it is necessary to specify how eddies of different sizes contribute to the total turbulent flow.

The probability density function p(u) can be utilised to analyse the amplitude variability of the turbulent fluctuations. Experimental observations of the natural wind indicate that the probability density function of wind fluctuations agrees well with the Gaussian function[28], given by:

$$p(u) = \frac{1}{\sigma_u^2\sqrt{2\pi}} \cdot \exp\left(\frac{-u^2}{2\sigma_u^2}\right) \qquad \ldots (10)$$

This result is a consequence of the Central Limit Theorem which states that the probability distribution of the sum of a large number of uncorrelated random processes is nearly Gaussian. In reality, turbulence is not quite Gaussian because the eddies are not totally independent[29]. This is especially true very near ground level. It is considered that there would be some degree of non-Gaussian behaviour both at the origin and in the tails of the density function, but the deviations should be small. For calculations of wind loads and response of buildings in high winds, a Gaussian distribution is therefore considered to be satisfactory.

To provide information about the structure of turbulence in the time rather than the amplitude domain, one possible way is through the auto-correlation function R(τ):

$$R(\tau) = \frac{1}{T} \int_{t+T/2}^{t+T/2} \frac{u(t) \cdot u(t+\tau)}{\sigma_u^2} \cdot dt \qquad \ldots (11)$$

The auto-correlation function can provide a quantitative measure of how much information a measurement of the turbulence at one instant of time gives about a value which is measured τ seconds later.

The maximum possible value of R is evidently unity when τ = 0, and because the eddies interact and develop with time in the turbulent flow the value of R(τ) decreases as the time lag τ increases. The shape of the auto-correlation function curve is obviously a function of the structure of the turbulence; the auto-correlation function R(τ) will decrease more rapidly with time lag τ for a flow with only small eddies, than if the flow contained only large eddies. The area under the auto-correlation curve is a measure of the period associated with the average eddy in the turbulence, and provides a convenient measure of the 'scale' of the turbulence. That is:

$$T_x = \int_0^\infty R(\tau)\, d\tau \qquad \ldots (12)$$

Figure 3 shows a typical example of a measured auto-correlation for u(t).

Although the auto-correlation function contains information about the structure of turbulence, the relationship between the correlation of fluctuations in the wind are averaged over all eddy sizes. It is not easy to deduce from it immediately how much different eddy sizes contribute to the total variance of the turbulence. This information is provided by the spectral density function $S_u(n)$ which represents the distribution of turbulent energy over a frequency range.

The spectral density function is defined so that $S_u(n) \cdot dn$ is the contribution to the variance σ_u^2 from frequency components in the range n to n+dn. Summed over the whole possible range of frequencies, the total variance σ_u^2 must be:

$$\sigma_u^2 = \int_o^\infty S_u(n)\ dn \qquad \dots (13)$$

Measurements of spectra at different locations and for different mean wind speeds have shown that a feature of atmospheric turbulence is that its spectrum has a characteristic shape. This has led to attempts, notably by Davenport[30], to establish a standard or reduced spectrum which contained as parameters the mean wind speed and terrain roughness. Davenport based his empirical spectrum on the mean of reduced spectra shown in Fig.4 and suggested the following expression to represent the longitudinal wind velocity spectra:

$$n \,.\, S_u(n) = \frac{4\kappa\ \bar{U}(10)\ \tilde{n}_1^2}{(1+\tilde{n}_1^2)^{4/3}} \qquad \dots (14)$$

where $\tilde{n}_1 = nL_1/\bar{U}(10)$, L_1 is an arbitrary length scale equal to 1200 m; $\bar{U}(10)$ is the mean wind speed at a height 10 m above the ground; and κ is the surface drag coefficient $= \left(0.4/\ell n\,(10/z_o)\right)^2$.

The total variance σ_u^2 of the velocity fluctuations is determined using Equation 13, viz.

$$\sigma_u^2 = \int_o^\infty S_u(n)\ dn = 6\ \kappa\ \bar{U}^2(10) \qquad \dots (15)$$

which shows σ_u^2 to be invariant with height.

Harris[31] proposed an improvement to this spectrum to give better representation at lower frequencies and improve the fit to the experimental data using:

$$n \cdot S_u(n) = \frac{4\ \kappa\ \bar{U}^2(10)\ \tilde{n}_2}{(2 + \tilde{n}_2^2)^{5/6}} \qquad \ldots (16)$$

where $\tilde{n}_2 = nL/\bar{U}(10)$, L is equal to 1800 m. This expression turns out to be identical in form to a spectrum previously proposed by von Karman and quoted by Schlichting[32].

$$\frac{n \cdot S_u(n)}{\sigma_u^2} = \frac{4\tilde{n}}{(1 + 70.8\ \tilde{n}^2)^{5/6}} \qquad \ldots (17)$$

where $\tilde{n} = nL_x/\bar{U}(Z)$, L_x is the longitudinal integral scale of turbulence (see Equation 21). Equation 17 is generally accepted as the best analytical representation of turbulence in the atmospheric boundary layer.

It would appear, at first sight, the agreement of the reduced spectra for different locations given in Fig.4 was good. However, on further inspection certain points emerge which may put in doubt the value of using such expressions for evaluating wind loading on structures. Assuming the natural frequency of the structure was at the high frequency end of the spectrum (since structures such as tall buildings have natural frequencies in the range approximately 0.5-1.0 Hz this is a valid assumption) the mean quasi-static response due to the turbulence will be directly proportional to the total area of the spectrum, although the high frequency eddies will generally be ineffective due to a decay in spatial correlation and will contribute very little to the response. If, instead of the measured spectrum the empirical curve is used, this could result in an over or under estimation of approximately 20% in the quasi-static response to turbulence. Although this level of error is not unusual in engineering, it is necessary to be aware of its existence and likely magnitude. More serious is the consequence of utilising a reduced spectrum to evaluate the resonant response of a structure. Since the resonant response will be proportional to the energy at the wavelength of turbulence exciting structural resonance, using the reduced spectrum could result in under or over estimates by factors of about two, particularly for lightly damped structures. The net result is that the structure is either over designed or under designed.

A measure of the gustiness of the turbulence was expressed in Equation 9 as the ratio of the rms of the velocity fluctuations to the quasi-steady mean wind speed. Using Equations 5 and 15 it is possible to show that the intensity of turbulence I_u can be approximated by:

$$I_u = 1/\ln(z/z_o) \qquad \dots (18)$$

This is based on the assumption that the rms, σ_u, of the velocity fluctuations is proportional to the friction velocity $u*$ and the constant of proportionality, commonly assumed to be invariant with height, is approximately equal to $\sqrt{6}$. In practice the shear stress is not invariant with height and from empirical correlation of world-wide sources ESDU[33] have determined that the constant of proportionality is a function of the surface roughness length z_o.

The concept of using the period, T_x, associated with the average eddy in the turbulence, as a measurement to characterise turbulence was presented earlier (see Equation 12). Another, more conventional measurement utilised to characterise turbulence is a measure of the average eddy size, commonly referred to as the energy containing eddies, in the turbulence. Defined as:

$$L_x = \int_0^\infty R(r) \cdot dr \qquad \dots (19)$$

where R(r) is the cross-correlation function defined as:

$$R(r) = \frac{1}{T} \int_{t-T/2}^{t+T/2} \frac{u(x,t) \cdot u(x+r,t)}{\sigma_u^2} \cdot dt \qquad \dots (20)$$

where $u(x,t)$ and $u(x+r,t)$ are the velocity fluctuations at x and $x+r$ at time t, respectively; r is the spatial separation in the direction of the mean wind.

For the special case of isotropic turbulence, Taylor's frozen turbulence hypothesis states that the temporal length scale ($=U \cdot T_x$) and the spatial length scale L_x are equivalent, provided the level of turbulence is low. That is:

$$L_x = \bar{U} \cdot T_x \qquad \ldots (21)$$

Taylor's hypothesis has been tested in natural wind with high levels of turbulence, intensities of turbulence in the approximate range 16-30%, and found to be still approximately valid[34].

For the special case of isotropic turbulence Harris[35] has shown that the scale of turbulence for the atmospheric boundary layer increases with height at the same rate as the mean wind speed and is given by the relationship:

$$L_x(z) = 151\ (z/10)^{\alpha} \qquad \ldots (22)$$

The assumption of isotropic turbulence, which is a reasonable assumption at high altitudes ($z > 300$ m), is not valid in the region of the atmospheric boundary layer of particular relevance to a structural designer. In this region the scale of turbulence is influenced by surface roughness and ESDU[33] recommend the relationship:

$$L_x(z) = 25\ z^{0.35} / z_o^{0.063} \qquad \ldots (23)$$

based on data that was considered to be the most reliable. However, Equation 23 still only represents the data to within about ±30%. There is considerable variation in reported values of the integral scale and this is indicative of the difficulty associated with the usual method of determining the integral scale, viz.

$$L_x = \frac{1}{4} \cdot \frac{\bar{U}}{\sigma_u^2} \cdot S_u(n \rightarrow o) \qquad \ldots (24)$$

The difficulty occurs in defining the value of the spectrum as the frequency n tends towards zero; spectra of atmospheric turbulence at long wavelengths, in contrast to the gusts in high frequency range, do not conform to a set behaviour.

When evaluating wind loads on structures, in particular on large bluff structures such as tall buildings, it is necessary to include the spatial correlation of the fluctuating forces acting on the structure. Since the natural frequency of most tall buildings will lie in the high frequency region of the turbulence spectrum, the dynamic excitation of the building, in particular the narrow-band, is mainly due to high frequency gusts which are coincident with the natural frequency of the building. These high frequency gusts, however, have wavelengths much less than the dimensions of the building, with the result that fluctuating pressures on the faces of the building are poorly correlated and consequently the effective forces acting on the building are reduced. It is apparent that consideration of the spatial correlation of fluctuating wind loads in the design of a building will result in a more realistic loading situation in the structural analysis and consequently in a more economic design.

This implies that information for turbulence at one point in space is inadequate for design of tall buildings; information on the spatial structure of atmospheric turbulence is also required. In Appendix B it is shown that the function which accounts for the spatial correlation of gusts in wind loading is the real part of the cross-spectral density function $S_{xy}(n)$, the co-spectral density function C(n) (see Equation 52). It appears that there is however more information currently available for the cross-spectral density function expressed in the form:

$$\gamma_{12}^2(n) = \frac{|S_{12}(n)|^2}{S_1(n) \cdot S_2(n)} \qquad \dots (25)$$

where $\gamma_{12}^2(n)$ is the coherence function; $S_1(n)$ and $S_2(n)$ are spectra at points 1 and 2 in space, respectively; and $S_{12}(n)$ is the cross-spectral density function between points 1 and 2, and is a complex quantity (see Equation 52).

Evaluation of experimental data for the cross-spectral density function has shown that the imaginary part, the quad-spectral density function Q(n), is generally small relative to C(n) and can be ignored so that no significant errors are introduced into the calculations by using $\gamma^2(n)$ instead of normalised C(n) (see Appendix B). In fact since $\gamma^2(n)$ if not equal to will always be greater than normalised C(n), its use will therefore also result in slight but consistently conservative estimates for the wind loading.

Experimental data from atmospheric measurements have shown that the loss in coherence for both vertical and lateral separations can be approximated by the analytical expression:

$$\gamma_r(n) = \exp\ (-c \cdot nr/\bar{U}) \qquad \ldots (26)$$

where r is the distance between the two points in space. The value of the decay constant C is about 6-8 and appears to decrease with increasing height and decreasing gust size, but to increase with increasing mean wind speed. Shiotani et al[36] suggest that these variations are small and recommends using constant values corresponding to the reference velocity at 10 m height above the ground. A recent study by Ropelewski et al[37] on the subject of the decay constant C indicated that there are significant variations in values for C when the Richardson number Ri is greater than zero, and the values of 6-8 for C are current state-of-the-art values.

1.3 Design of Tall Structures for Wind Loads

For a structure to be safe there should be no local or overall structural failure due to buckling or fatigue. Should local failure occur, the structure should retain structural integrity. Further, buildings should not cause discomfort to occupants due to excessive movements.

The action of wind on structures can be categorised under the headings: static effects and dynamic effects. The former refers to the time averaged mean forces and is of importance in the analysis of overturning stability of buildings and structures, or more particularly the wind forces on the cladding of buildings. The second refers to the dynamic excitation of structures and is of particular importance when the structural damping is low; a condition under which large amplitudes of vibration are normally encountered.

The present UK Codes of Practice for wind load on buildings and structures is based on an ultimate load philosophy; using a discrete gust which is determined on the basis of what will be the largest gust speed that the structure is likely to experience in its lifetime and an acceptable level of risk. Provided the structure is of a conventional design and is not liable to dynamic excitation the UK Codes of Practice provide realistic information for the ultimate load analysis and although it will not be considered further here it is a subject of continued research. The following discussion will concentrate on the dynamic response of structures to both steady and turbulent flow.

1.3.1 Dynamic response of structures

Generally, the forces capable of causing a dynamic response are small compared to the mean drag forces, but potentially very dangerous. This is because a lightly damped flexible structure can extract energy from the wind to initiate and maintain dynamic excitation. There are several mechanisms of aerodynamic excitation which can cause structural instability; however, for most civil engineering structures these are:

- vortex excitation
- galloping instability
- buffeting by turbulence

VORTEX EXCITATION

Aerodynamic excitation by vortex shedding is probably the best documented of all the wind induced vibrations of structures. Alternate shedding of vortices from the sides of the structure leads to strong oscillatory pressure distribution in the crosswind direction. The oscillatory forces are typical of most bluff body shapes and it is when the frequency of the aerodynamic forces coincide with the natural frequency of the structure that large dynamic amplitudes can arise. Structures which have been most susceptible to vortex excitation have been chimneys. With the introduction of taller, new lightweight materials and construction techniques, the reported number of chimneys which oscillated with large amplitudes of vibration markedly increased. The solution to the problem was to destroy or reduce the coherence of the shed vortices by spoilers. For chimneys the most effective, and consequently also the most common, method (spoiler) has been the helical strake.

Experiments have shown that bluff bodies with sharp edges, such as a rectangle, in comparison with a cylindrical section tend to induce stronger vortex shedding which results in larger oscillatory crosswind forces. This is because there is an increase in the correlation length of the vortices brought about by the fixed separation points. The relevance of this result is that it is a reminder that other tall slender structures besides chimneys are also susceptible to vortex excitation. There are also instances when the excitation will be in the direction of flow, such as with marine piles. As tall structures tend to be flexible and vibrate in the wind, account must be taken of the interaction between the flow produced forces and the structure. One of the most important effects that structural movement has on vortex shedding is to induce it to 'lock-on' to the natural frequency of the structure and remain constant for a wide range of wind speeds. During the 'lock-on' region large amplitudes of oscillation can result.

Vortex excitation of structures has been extensively reported and the reader is referred to literature on the subject, such as Parkinson et al[38] and Wootton & Scruton[39], for detailed information.

GALLOPING

Galloping is an instability caused by the structure being aerodynamically unstable due to its sectional shape. Oscillations occur in the cross-wind direction at the natural frequency of the structure.

An explanation of galloping as given by Parkinson[40] is that it is due to the separated shear layers moving close to re-attaching to the side of the structure, thereby inducing an exciting force which is in the opposite direction to the motion of the structure, effectively acting as a negative damping force. The maximum galloping exciting force for the square prism corresponds to the shear layer re-attaching to the side.

The motion can be analysed using a quasi-steady theory developed by Parkinson[41]. However, the problem is complicated by three dimensionality, sheared flow, free stream turbulence and structural damping[42,43,44].

Galloping is rarely a problem for structures such as buildings because galloping oscillations cannot start from rest and the initial displacement required for the onset of oscillations must be relatively large; in galloping the instability forces are a function of the relative angle of attack of the wind to the structure which depends directly on the across-wind velocity of the structure. On buildings the displacements are usually so small that the instability forces are insignificant. Nevertheless, structural designers should be aware of the existence of this instability.

BUFFETING BY TURBULENCE

Oscillations of a structure may be caused by the buffeting action of the turbulent wake of an upstream obstruction or by the turbulence of the wind, which in many instances produce large along-wind (drag) oscillations.

Davenport[12] extended the work of Liepmann[45] and developed a technique, using a statistical approach, which enabled an estimate of the fluctuating drag response of bluff bodies in a turbulent wind to be made. The method is based on the assumption that a linear quasi-steady pressure-velocity relationship is valid. The fluctuating drag force is obtained by integration of the pressures over the structure, with suitable allowance for the decay in spatial correlation of the forces. The relationship between the force spectrum and the velocity spectrum can be expressed as:

$$S_D(n) = 4 \frac{C_D^2}{\bar{U}^2} \chi_a^2(n)\ S_u(n) \qquad \ldots (27)$$

where $S_D(n)$ and $S_u(n)$ are the force and velocity spectra, respectively; C_D is the drag coefficient for the structure; and $\chi_a^2(n)$ is the aerodynamic admittance function and accounts for the fact that in reality there is a loss in coherence associated with the high frequency eddies (§5.3).

The greatest physical inadequacy of the method is that it gives a force-velocity relationship which is almost independent of the flow distribution around the structure. On the other hand, methods which take this into consideration are more complicated and give many analytical and numerical problems[46,47,48]. In spite of present deficiencies the statistical approach does offer a means of describing the force-velocity relationship for structures in turbulent wind. The method is discussed in more detail in Appendix B.

1.4 Formulation of the Problem

In recent years, there has been a growing interest in the full-scale studies of wind forces and vibrations of tall buildings, the main objective being to correlate results with those from wind tunnel investigations. Full scale testing is also important in providing design information for wind loading of future structures.

The cost and time involved in carrying out full-scale investigations appear to be the limiting factors. In 1975 Stansby & Wootton[49] estimated that a full-scale investigation could cost up to £200,000 and take up to eight years from initiation to final report, compared with £20,000 and six months for a full-wind tunnel test.

Although results from full-scale measurements provide useful data, the only method currently available to a structural designer which enables him to evaluate the performance of a prototype design is by model testing in the wind tunnel. The general problem of wind tunnel model testing is that although the scaling criteria required to achieve dynamic similarity between model and prototype are known, they are extremely difficult to satisfy. Since it is not possible to achieve complete similarity the problem reduces to scaling those parameters known to have significant influence on the performance of the prototype.

1.4.1 Scope of the present research

The discussions in this chapter have outlined the scope and complexity of the general field of wind forces and effects on tall buildings and structures. A literature survey by the author indicated there is a need for data relating to gust loading of buildings by the turbulence of the wind, and in particular for information about the correlations between the fluctuating pressures on the windward and leeward faces of tall buildings. This data would as proposed by Simiu[14] (and discussed in Section 1.1) allow current procedures for estimating the fluctuating drag response of tall buildings in turbulent wind, such as that of Davenport[50], to be refined to account realistically for the imperfect correlation which must exist between the fluctuating pressures on the windward and leeward face of buildings.

The literature survey also revealed that whilst the effect of turbulence intensity on the flow field around and the pressures on bluff bodies has been the subject of considerable research effort there have been comparatively very few studies to investigate the effects of turbulence scale. McLaren et al[51] reported that their measurements of the drag force for two-dimensional square models showed a distinct maximum when the value of the turbulence scale was approximately equal to the width of the model. These observations have recently been substantiated by Lee[52]. The only other reported work on this subject, known to the author, is that by Cook[53] who investigated the general effects of turbulence scale on both the steady and fluctuating pressures and flow field around three-dimensional square section models. Unfortunately, as far as the effects of turbulence scale on correlation of fluctuating pressures was concerned, the study was inconclusive.

The present programme of work was therefore instituted to investigate the cross-correlations of fluctuating pressures on and between the windward and leeward faces of tall building models. The relevance of turbulence scale in significantly modifying the flow and hence the correlations, based on the results of mean drag forces from the 2-dimensional tests, was considered to be potentially important and to warrant inclusion in the programme. This would be achieved by testing building models in turbulent flow with turbulence scale equal to, less than and greater than the breadth of the models. Although a building in natural wind is subjected to a non-uniformly distributed load due to the atmospheric boundary layer velocity profile, in order to isolate the effects of turbulence scale it was considered that for the investigation no attempt to model the atmospheric boundary layer was necessary.

There is considerable variation in building-design particularly in geometric shape, and for the results from the study to be of general applicability to tall buildings of rectangular cross-section the depth of the models was included as a variable in the test programme.

CHAPTER 2

DATA ACQUISITION AND ITS ANALYSIS

2.1 Introduction

The nature of the proposed investigation would require the acquisition of information from processes which are random in character. In order to be able to handle the vast quantity of data which would be necessary to minimise statistical errors a data gathering and reduction system was developed during the early stages of the project. The aim was to have a fully operational system which enabled data to be analysed and monitored as an ongoing process; this would have made it possible to introduce changes in the experimental programme as the work proceeded. The industrial aerodynamics wind tunnel, under construction during this stage, was due to be completed at approximately the same time as the data handling and processing system. Unfortunately, the construction schedule was affected by national power restrictions and the wind tunnel was completed approximately six months behind time. There was, as a result, insufficient time available to carry out the original intention of data monitoring and consequently the proposed programme of work was adhered to and remained unaltered throughout the wind tunnel measurements.

To obtain joint relationships such as coherence functions, for the fluctuating pressures on the faces of the models and also the correlation between the free stream turbulence and the fluctuating pressures it was necessary for the data processing system to be capable of performing simultaneous analysis of two signals. At the commencement of the project there was a lack of general purpose analysis equipment available, especially any which was capable of joint statistical analysis between records. Therefore, both analogue and digital analysis were carefully considered to determine which system would be the most suitable to develop. The cost of analogue equipment necessary was found to be prohibitive, but apart from cost there were other considerations. The first was that it was considered desirable for the system to be inherently flexible and of use in other and future projects. It was felt at the time that this was not practical with the analogue equipment available. There are also technical difficulties associated with accurate analysis of random processes using analogue equipment. These are:

- insufficient range, making it difficult to obtain characteristics of the low frequency components of a signal
- narrow band analysis is generally not available and fine detail can be lost
- achieving accurate matching of filter characteristics over a wide frequency range

The analysis can also be very time consuming since long averaging periods are necessary when low frequency components are involved.

The alternative to analogue techniques is to analyse the data using digital methods. However, these also have limitations and problems. Analogue signals from the transducers have to be digitised using an analogue to digital converter (ADC) and if more than one signal is to be digitised then the system must include a multiplexor. If the phase relationship between signals has to be preserved then the ADC system has to simultaneously digitise the signals. Which all adds up to an expensive data logging system. The real problem, however, with a digital system concerns the means of storing large volumes of data in a digital form. The only practical way is on magnetic tape, cartridge disc or floppy disc, which adds to the overall cost of the system. A digital system has the advantage over analogue techniques in that it is very versatile which allows data to be readily and relatively quickly analysed using any desired mathematical computation. For this reason and, as will be described later, because there was a readily accessible ADC available and a suitable medium to store the data the digital system was chosen to analyse the experimental data.

The following is a description of the data gathering and analysis process used during the project. Because the results obtained and what is inferred from the results may very well depend on the manner by which the results were arrived at, each section will discuss in detail the different facets of the data gathering and analysis process.

2.2 Data Acquisition

2.2.1 Velocity measurements

Two methods of measuring wind velocity in the wind tunnel were used in the experiments:

- pitôt-static tube
- hot wire anemometer

The pitôt-static tube, connected to a Furness MDC Micromanometer, was used to monitor the mean velocity of the flow in the working section of the wind tunnel. The electronic manometer was calibrated against a Casella manometer, and a built-in meter in the Micromanometer gave direct readings in mm head of water. Because the pitôt-static tube was fixed in a permanent position and the flow behind the turbulence generating grids (§3.2) took a finite distance to establish the final mean velocity, a correction to the velocity measurements had to be applied to obtain the wind speed at the model position. During measurements of the flow behind the grids (§4.1) readings from the fixed pitôt-static tube were constantly compared against the readings from the hot-wire anemometer, used for the grid flow measurements, and found to be consistently repeatable.

Measurements of the fluctuating velocities of the free stream turbulence and of the flow around the models were made using hot-wire anemometers. A DISA type 55D01 universal hot-wire anemometer unit operating in the constant temperature mode with DISA miniature wire probes was used. The probes were calibrated in a low intensity of turbulence DISA calibration rig and in the range of mean velocities used in the experiments.

In the wind tunnel circuit frictional losses are dissipated, finally, as heat but because of the timber construction there is very little heat loss through the surfaces. Consequently, the ambient temperature of the air in the working section increases with running time, the rate of increase of temperature being a function of the mean wind velocity. The variation of the temperature of the air in the working section with duration of run has been measured by Sykes[54] and his results are shown reproduced in Fig.5 for three values of wind speed. During an hour of steady running at maximum wind speed it is seen that there can occur a temperature increase of approximately 20°C. Changes in ambient temperature alter the calibration of hot-wire anemometers, when operating at constant temperature, consequently there are errors associated with the measured mean and rms velocity values. This problem was overcome by measuring the ambient temperature of the flow with a thermocouple and applying a correction procedure suggested by Bearman[55] to give true mean and rms velocity values.

2.2.2 Pressure measurements

Distribution of time averaged static pressure around the building models (§3.3) was measured using a 36 tube inclined alcohol manometer. Plastic tubing, 1.6 mm bore, was used to connect the pressure taps on the model to the multitube manometer. Deliberately long lengths of plastic tubing were used so that pressure fluctuations acting on the model were damped out and not registered by the manometer.

Fluctuating pressures were measured using two DISA type 51F32 low pressure transducers. The sensing elements of these transducers are Brüel & Kjaer type 4135 ¼ inch condenser microphones. The transducers were connected to two 51E32 oscillators and the capacitance of the microphone forms part of the total capacitance in the tuned circuit of the oscillator. The carrier frequency of the circuit is modulated by the pressure difference across the microphone diaphram. The signal is demodulated by a DISA type 51E01 reactance converter to give an analogue voltage proportional to the pressure. The transducers are supplied calibrated over a pressure range of ±700 mm head of water, but are better operated over ±70 mm head of water, and have a frequency response which is flat from zero frequency to 5 kHz.

The transducers were mounted in Scanivalve Corporation model 48 D3, 48 port ½ inch pressure scanning switches. Adaptors were made in order for the transducers to be physically compatible with the scanning switches. A control unit with single step advance and reset capability was constructed with which to operate the scanning switches. The general layout of the complete system is shown in Figs.6 and 7.

Flexible plastic tubing with an inner diameter of 1.6 mm was used to connect the pressure taps on the model to the scanning valves. The plastic tubing and scanning valve modified the frequency characteristics of the pressure fluctuations sensed by the pressure transducer; viscous flow in the plastic tube and the Helmholtz resonance of the tube together with the many changes in cross-section in the system (which act as acoustic impedance) are the principal causes. The pressure tube-Scanivalve transducer system was dynamically calibrated and the frequency response transfer function for the system determined. Details of the calibration equipment and the results obtained are given in Appendix A.

2.3 Data Recording

Analogue signals from the anemometer and pressure transducers were recorded on magnetic tape using a Sangamo model 3562A portable magnetic tape recorder. Tape drive speeds available for recording were 1⅞ inch s^{-1} doubling sequentially to 60 inch s^{-1} and for reproducing at 3¾ and 30 inch s^{-1} in either forward or reverse directions. Although the tape recorder had a 14 channel capability only nine record-reproduce boards were available at the time, but since the maximum number of signals recorded simultaneously was three, this was quite adequate. The Sangamo is a frequency modulating (FM) carrier system tape recorder which is capable of recording signals over the frequency range dc to an upper frequency n_u, given by:

$$n_u \sim \frac{n_c}{5} \cdot Rr \qquad \ldots (28)$$

where n_c is the carrier frequency (= 1800 Hz/inch s^{-1}) and Rr is the recording speed of the tape in inch s^{-1}.

Memorex tapes, 1 inch wide and about 2500 m in length, were used.

To achieve optimum signal/noise ratio within the ±1.4 V range for the tape recorder, signals had their dc component backed-off and the fluctuating component amplified before being recorded, using DISA type 55D26 signal conditioners. The true mean and rms values of the signals were monitored and measured, before being modified by the signal conditioners, using DISA type 55D30 and 55D35 digital dc voltmeter and true rms meters respectively.

There are many advantages to storing data on analogue magnetic tape. It is a permanent record of the signal in its original raw state which can be replayed and analysed whenever required. This is most useful when a different method of analysis on the same data is required at a later date, eliminating the expensive and time consuming process of repeating experiments. Also the reproduce tape speed can be increased or decreased, relative to the recorded speed, effectively increasing the frequency range of processing equipment; a useful facility when analysing low frequency components of signals with an analogue spectrum analyser. With analogue equipment, speeding up signals reduces the analysis time and also increases the relative averaging times, with the result that values for the low frequency fluctuations are smoothed and therefore stable and repeatable.

2.4 Data Preparation and Storage

Recorded analogue data obtained from the wind tunnel measurements was digitised using the analogue to digital conversion (ADC) units in the City University EAI 690 hybrid computer. The ADC system was developed by the University Computing Unit, and used previously by Perera[56], becoming a standard facility for the department.

The use of sample-hold circuits in the ADC equipment allows channels to be sampled simultaneously and then to be held until a multiplexing switch passes the various signals. With this arrangement it is possible to avoid inter-channel time base errors, which occur when each channel is sampled and digitised individually, and for this study it was essential that the phase relationships between signals were preserved. Details of the complete system are given by Hassan & Perera[57].

Because the hybrid computer was physically some distance from the Laboratory there was, besides the real possibility of damaging the tape recorder, the inconvenience and the accelerated wear and tear resulting from frequent transportation. A land-line connecting the two facilities was therefore laid which allowed two analogue signals to be transmitted in parallel. With long transmission lines there is always the possibility of external signals being picked-up and causing interference. In addition there is an upper frequency limit imposed by the frequency response characteristics of the line; beyond this frequency the phase and amplitude of the signal is altered. These problems were avoided or the effects minimised by modulating the signals prior to their being transmitted down twisted pair cables. At the receiving end the signals were demodulated back into their original form ready for the processing stage. No interference signals were detected and the transmitted signal was identical to the original signal up to and above the maximum frequency sampling capabilities of the ADC system.

Initially two people, one to control the ADC system at the hybrid computer console, and the other to operate the tape recorder in the wind tunnel laboratory, were necessary; contact between the two was maintained via a communications link. The data transmission system was improved at a later date when a control unit for the tape recorder was manufactured making it possible for the operator at the hybrid computer console to have remote control of the tape recorder; the control unit reproduced all the control facilities on the tape recorder except the tape drive speed selector. The two man system is still available but would now be used for on-line processing of signals from wind tunnel experiments in progress. The transmission system and equipment are shown in Figs.8 & 9.

2.4.1 ADC process

The process of digitisation consists of converting continuous analogue data into discrete data. There are two separate and distinct operations involved:

- sampling
- quantisation

Sampling is the process of observing the values of a signal at defined time intervals over a period of time, and quantisation is the conversion of the data values at the sampling points into a numerical form.

2.4.1.1 Sampling

It is important to have a sufficient number of samples in a given period of time in order to describe properties of the signal at its high frequencies. Also when deciding on the sampling rate, care should be taken that the rate relative to the maximum frequencies of interest is fast enough to avoid aliasing errors. On the other hand, sampling at points which are too close together will yield correlated and highly redundant data which will increase both the time and cost of the computations. The sampling rate should be selected with these points in mind.

In aliasing, if the sampling rate is n_s samples s^{-1} then the frequency $n_f (= n_s/2)$ is known as the Nyquist or folding frequency. For any frequency n, in the range $o<n<n_f$ the higher frequencies which are aliased with n are given by:

$$(2n_f \pm n),\ (4n_f \pm n),\ (6n_f \pm n),\ \text{etc.} \qquad \text{... (29)}$$

Data with frequencies above n_f will be folded back into the frequency range 0 to n_f, and will be confused with the data in this lower range. An example of aliasing is illustrated in Fig.10.

There are two methods for overcoming the aliasing problem, either:

- choose the sampling rate such that it is physically unreasonable for data to exist above the Nyquist frequency, or
- pre-filter the data with an analogue low-pass filter to remove any information above the Nyquist frequency

The second method saves computing time and cost, but it is not physically possible to filter out all the data above the maximum required frequency n_f; even the best analogue filters have finite cut-off rates. The procedure adopted was to sample at a rate which gave three sample points per cycle for the highest frequency of interest, n_{max}, having pre-filtered the data using the low-pass filter on the signal conditioners set at 1.5 n_{max} and a roll-off characteristic of 18 dB/octave. It is estimated that with this method only about 1.5% of the energy of white noise above n_{max} will alias into n_{max}.

2.4.1.2 Quantisation

ADC systems convert analogue signals into series of discrete points by looking at them through finite width windows or levels. The signal is approximated to a value as it falls within a certain window. The accuracy of the approximations depends on how wide the windows are, but no matter how fine the quantisation levels are, a choice between two consecutive values is always present and this constitutes a possible source of error[58].

If it is assumed that the quantisation errors follow a uniform probability distribution over each level, then these errors will have a mean value of zero and a standard deviation (which can be considered as noise superimposed on the desired signal) of about 0.29 scale units. The mean value of the signal can therefore be determined very accurately using a coarse digitisation, whereas to ensure the signal to noise ratio is high a fine digitisation is necessary. The ADC unit in the EAI 690 hybrid computer operates over 13 binary bits which is equal to 8192 (i.e. 2^{13}) levels. The peak signal to noise ratio is then approximately 4700 : 1 (or ≈73 dB), assuming the signal is a normally distributed variable. The quantisation error is therefore relatively unimportant if the full quantisation range is used. To achieve good resolution the reproduced signals from the tape recorder were not only filtered to overcome aliasing they were also amplified by the signal conditioners so that they covered the full range of the ADC units.

2.4.2 Digital data storage

Analogue data once converted to digital form could be transferred to any of the peripherals associated with the ICL 1905E digital computer via a British Standard Interface[59]. For subsequent analysis on the ICL 1905E the data could be stored on cartridge disc, listed on a line printer, or punched on cards or paper tape. For this study the volume of data involved was very large and therefore cartridge disc was considered to be the only sensible method of data storage. This was, however, not the permanent storage medium, cartridge disc was used during the ADC process because data transfer from the EAI 690 to the ICL 1905E disc unit could be effected quickly and efficiently. When necessary, either because the storage capacity of the disc had been reached or the data was to be analysed, the data would be transferred to digital magnetic tape for permanent storage.

Since with magnetic tapes access to data is sequential, and therefore slow and inefficient, for all data analysis (either on the ICL 1905E or CDC 7600 (§2.5) the data was first copied to disc; with discs random access of data is possible which is fast and an efficient means of performing data retrieval and similar operations.

2.5 Digital Data Analysis

The majority of the computer software routines used for processing the digital data were written by the author. The exceptions were fast Fourier transform (FFT) subroutines written by Villasenor[60] and Anderson & Nettleton[61] which were, with some minor modifications, incorporated in the programme.

All the software routines were developed using the City University ICL 1905E digital computer and subsequently implemented on the

University of London Computer Centres CDC 7600 digital computer. The rationale behind this approach was that programme development could be carried out on the ICL 1905E, being an in-house machine, with expedience whereas for the analysis it was found that the CDC 7600, being a faster and more powerful machine, was more suitable. This arrangement also avoided the problem of the quality of service being provided to other users of the ICL 1905E becoming inferior due to slower processing and turnround.

Details of the structure of the data processing programme, titled PPT1, together with some of the main subroutines are described in Appendix D. In the next section the functions calculated by the software routine PPT1 and which are particularly applicable to this study are stated.

2.5.1 Basic statistical properties

To have a complete description of a random signal it may be necessary for the statistical analysis to be carried out in the amplitude, time and frequency domains. Although it is not necessary to use all of them at one time each can highlight particular characteristics of the signal. The software routine PPT1, is capable of analysing digital data to provide functions in all three domains.

In the following, the data is assumed to be stationary and ergodic. These assumptions allow the data to be analysed at any arbitary point in time knowing that the property measured is representative of the signal as a whole. Also, because the data is assumed to be ergodic then the statistical properties of the signal evaluated using ensemble averages are identical to those evaluated using time averages. Note that only stationary random processes can be ergodic.

Ergodic random processes are clearly an important class of random processes since all their properties can be determined by performing time averages over a single sample function. It is for this reason that the properties of stationary random phenomena can be measured properly with a digital computer. Since all digital computers have finite capacity they can handle only a limited volume of data at any given time. However, because of the above assumptions this problem is overcome in the following manner. The original data is segmented into sizes suitable for the computer to analyse each segment separately and then to ensemble average the results of the segments to arrive at the required function.

2.5.1.1 Amplitude characteristics

The mean value, $\bar{x}$, for discrete time series digital data x_i for i = 1,2.., N is:

$$\bar{x} = \frac{1}{N} \sum_{i=1}^{N} x_i \qquad \ldots (30)$$

Similarly, the mean square value $\overline{x^2}$, or variance σ_x^2, of the data is given by:

$$\overline{x^2} = \frac{1}{N} \sum_{i=1}^{N} (x_i - \bar{x})^2 \qquad \ldots (31)$$

and is used as an indication of the intensity of the random data (§1.2.2 discussion on intensity of turbulence is a good example).

The probability density function $p(x)$ and the probability distribution function $P(x)$ are related by:

$$p(x) = \frac{dP(x)}{dx} \quad \text{and} \quad P(x) = \int_{-\infty}^{x} p(x)\, dx \qquad \ldots (32)$$

A digital estimate for the probability density function $p(x)$ is obtained by dividing the range for x_i into an appropriate number of intervals and then tabulating the number of observations and the fraction of data in each interval. That is:

$$p_\ell = \frac{1}{W} \cdot \left[\frac{N_\ell}{N}\right] \qquad \ldots (33)$$

where p_ℓ is the value of the probability density function of data centred about a value x_ℓ and having a bandwidth of W. N_ℓ is the number of data points falling within the band.

The moments of probability density functions measure the degree to which the data cluster about their mean value or spread from it and are used to provide detailed information about the amplitude characteristics of signals. The r^{th} moment of a distribution about $\bar{x}=0$ is defined by:

$$m_r = \int_{-\infty}^{\infty} x^r \cdot p(x)\ dx \qquad \ldots (34)$$

$$r = 0,1,2,\ldots$$

The two most commonly used moments, besides m_1 and m_2 which equal the mean $\bar{x}$ and mean square $\overline{x^2}$ values respectively, are the third and fourth moments and are used to describe the deviation of the distribution from a norm. Their significance is in fact greater than this, they are a measure of the distribution of peaks about the mean $\bar{x}$ and also provide information about the characteristics of the peaks.

For a Gaussian distribution m_3, which is expressed as the skewness factor S, is zero. If m_3 does not equal zero then S is used as a measure of the lack of symmetry of the curve about its mean value, or of more relevance, it is a measure of the asymmetric distribution of the fluctuations occurring about the mean value of the signal. The fourth moment m_4 usually expressed as the Kurtosis factor K has a value of 3 for a Gaussian distribution, and deviations from this value describe the degree to which the distribution is flattened at its centre. It also provides information about the shape of the fluctuations in the signal, that is whether they are rounded or peaky. The skewness S and Kurtosis K of the digital data were estimated using:

$$S = \frac{1}{(\overline{x^2})^{3/2}} \left[\sum_{\ell=1}^{k} p_\ell \cdot W \cdot x_\ell^3 \right] \qquad \ldots (35)$$

$$\text{and } K = \frac{1}{(\overline{x^2})^2} \left[\sum_{\ell=1}^{k} p_\ell \cdot W \cdot x_\ell^4 \right] \qquad \ldots (36)$$

where k is the number of intervals for the data range.

2.5.1.2 Time characteristics

Time dependent characteristics of the data can be expressed by the auto-correlation function, which for continuous signals is defined as:

$$R_x(\tau) = \frac{1}{T} \int_{t-T/2}^{t+T/2} x(t) \cdot x(t+\tau) \, dt \qquad \ldots (37)$$

and for finite discrete data the equivalent auto-correlation function can be written as:

$$R_x(r) = \frac{1}{N-r} \sum_{i=1}^{N-r} x_i \, x_{i+r} \qquad \ldots (38)$$

$$r = 0,1,2\ldots, m$$

where τ and r are the time lag and lag number, respectively, and $\tau = r \cdot \delta t$; δt is the sampling period; and m is the maximum lag number.

For the special case of zero time delay $\tau=0$ (or $r=0$) Equations 37 & 38 reduce to:

$$R_x(\tau=0) = \frac{1}{T} \int_{t-T/2}^{t+T/2} x^2(t) \, dt \equiv \frac{1}{N} \sum_{i=1}^{N} x_i^2 = \overline{x^2} \qquad \ldots (39)$$

In a similar manner, the cross-correlation function for two continuous variables $x(t)$ and $y(t)$ is defined as:

$$R_{xy}(\tau) = \frac{1}{T} \int_{t-T/2}^{t+T/2} x(t) \cdot y(t+\tau) \, dt \qquad \ldots (40)$$

The auto- and cross-correlation values are usually normalised using $R_x(\tau=0)$ and $R_y(\tau=0)$ to give the auto- and cross-correlation coefficients, i.e.

$$\rho_x(\tau) = \frac{R_x(\tau)}{R_x(\tau=0)} \qquad \text{... (40a)}$$

$$\text{and } \rho_{xy}(\tau) = \frac{R_{xy}(\tau)}{(R_x(\tau=0) \cdot R_y(\tau=0))^{\frac{1}{2}}} \qquad \text{... (40b)}$$

Equation 38 is the direct method of estimating the auto-correlation function. The direct evaluation of Equation 38 on a digital computer, however, demands excessively large amounts of computing time and it has become normal practice to use an indirect method of estimating the auto-correlation function.

The alternative indirect method makes use of the Wiener-Khintchine theorem[58] which states that the power spectral density $S_x(n)$ and auto-correlation functions $R_x(\tau)$ are Fourier transforms of one another. The transform pair expressed in continuous form for real valued and even functions is:

$$S_x(n) = 4 \int_0^\infty R_x(\tau) \cos 2\pi n\tau \, d\tau \qquad \text{... (41a)}$$

$$\text{and } R_x(\tau) = \int_0^\infty S_x(n) \cos 2\pi n\tau \, dn \qquad \text{... (41b)}$$

In the following section the power spectral density function and its evaluation will be discussed with particular emphasis on using the fast Fourier transform (FFT) algorithm for the computations.

The indirect method of calculating auto-correlation function estimates is first to computate by the fast Fourier transform the power spectral density function and then to compute the inverse Fourier transforms of the result using the FFT. In practice the FFT algorithm is so fast it is quicker and more efficient to obtain both the spectral density and the auto-correlation functions using the FFT rather than to evaluate the auto-correlation function directly.

Calculation of the auto-correlation function from the inverse of the power spectral density function gives a representation which is biased and appears as if the net result was achieved using:

$$R_x(r) = \frac{1}{N} \sum_{i=1}^{N-r} x_i \; x_{i+r} \qquad \dots (42)$$

$$r = 0,1,2,\dots,\ m$$

The bias error increases linearly with lag number and comparing Equations 38 & 42 it is apparent that to obtain a true estimate the correlation values obtained from the indirect method must be corrected by the scale factor Wr given by:

$$Wr = \frac{N}{N-r} \qquad \dots (43)$$

2.5.1.3 Frequency characteristics

The power spectral density (PSD) function $S_x(n)$ may be used to express the frequency composition of random data and is defined for finite discrete data as:

$$S_x(n) = \frac{2}{\delta n} \left| X_k \right|^2 \qquad \dots (44)$$

where:

$$X_k = \frac{1}{N} \sum_{i=1}^{N} x_i \cdot \exp \left| \frac{-j2\pi ki}{N} \right| \qquad \dots (45)$$

at the discrete frequency values $Nk = K/T = K/(N \cdot \delta t)$ for $k=0,1,2,\dots,$ N-1. X_k is a complex value representing the Fourier coefficient of x_i at N data points.

For the special case of bandwidth limited white noise, which can be used as a guide to the best results that could be attained, it can be shown[58] that the normalized standard error for a highly resolved spectrum is:

$$\varepsilon = \frac{1}{\sqrt{\delta n \cdot T}} \qquad \dots (46)$$

Since δn is identical to T^{-1} the normalized standard error of the results from the raw spectral estimates of Equation 44 is unity.

Therefore, although $S_x(n)$ is an estimate of the power spectral density function, it is unreliable. There are two methods which can be used to obtain statistically improved and reliable estimates of the PSD function. They are frequency smoothing and ensemble averaging.

In the first method, adjacent raw spectral estimates are averaged over the frequency interval from $S_x(n-k)$ to $S_x(n+k)$, i.e.

$$\bar{S}_x(n) = \frac{1}{k+1} \sum_{L=-k/2}^{k/2} S_x(n-L) \qquad \text{... (47)}$$

This increases the bandwidth to $\delta n(k+1)$ and is in effect a simple moving averaging procedure; others are given in Reference 63. The normalised standard error of the estimate is now determined as:

$$\varepsilon = \frac{1}{\sqrt{k}} \qquad \text{... (48)}$$

The penalty for increasing the bandwidth is that fine resolution especially in the low frequency end of the spectrum is lost.

With ensemble averaging the original data is first divided into M record blocks and the data in each record block Fourier transformed to produce a raw spectral estimate of the PSD function. The M raw spectral estimates are then averaged to achieve a PSD function with 2M degrees of freedom and a normalised standard error of:

$$\varepsilon = \frac{1}{\sqrt{M}} \qquad \text{... (49)}$$

Examples of ensemble averaging are presented in Fig.11 which demonstrate the significance of Equation 49.

A combined averaging procedure using both the frequency smoothing and ensemble averaging has been shown[58] gives a normalised standard error of:

$$\varepsilon = \frac{1}{\sqrt{k \cdot M}} \qquad \text{... (50)}$$

Because the PSD function is calculated from a finite rather than an infinite data length, the energy at a given frequency is spread over a broad frequency range and into side lobes and is termed leakage[63]. The leakage into the side lobes can be reduced by using 'data windows', and of the many available[64] one of the most simple and effective is the Hanning filter which is easily implemented on a digital computer as the smoothing operation in the frequency domain:

$$\bar{S}_x(n) = 0.25\ S_x(n-1) + 0.5\ S_x(n) + 0.25\ S_x(n+1) \qquad \ldots (51)$$

on the raw spectral estimates. It is clear that the Hanning filter smooths the power spectral density function and it has been estimated that the effect is equivalent to doubling the data samples used in the computation.

The PSD function given by Equation 44 can be extended to cover the joint characteristics of two variables, $x(t)$ and $y(t)$, with the cross-spectral density (CSD) function $S_{xy}(n)$. The CSD function is generally complex such that:

$$S_{xy}(n) = C_{xy} - jQ_{xy}(n) \qquad \ldots (52)$$

where the real part, $C_{xy}(n)$, is the co-spectral density function while the imaginary part $Q_{xy}(n)$ is the quad-spectral density function.

An alternative form of Equation 52 is:

$$S_{xy}(n) = |S_{xy}(n)| \cdot \exp(-j\Theta_{xy}(n)) \qquad \ldots (53)$$

expressing the CSD function in modulus and argument form, where:

$$|S_{xy}(n)| = |C^2_{xy}(n) + Q^2_{xy}(n)|^{\frac{1}{2}} \qquad \ldots (54a)$$

$$\text{and } \Theta_{xy}(n) = \tan^{-1}\left|\frac{Q_{xy}(n)}{C_{xy}(n)}\right| \qquad \ldots (54b)$$

The joint characteristics can be compared to the individual frequency characteristics of the two variables by the real valued coherence function $\gamma^2_{xy}(n)$, defined by:

$$\gamma^2_{xy}(n) = \frac{\left|S_{xy}(n)\right|^2}{S_x(n) \cdot S_y(n)} \qquad \text{... (55)}$$

The coherence is the square of the correlation of two signals expressed in narrow frequency bands and has a value between 0 and 1, which indicates whether the two signals are completely unrelated or completely correlated.

The most important single development in digital techniques has been the rediscovery of the fast Fourier transform[64] (FFT). The usual method of obtaining the PSD function, known as the Blackman and Tukey method[62], was to first calculate the correlation function from the raw data and then to Fourier transform the result into the frequency domain. However the FFT, a computer algorithm by Cooley and Tukey, computes the discrete Fourier transform direct from the raw data and is much faster than all other known methods. In practice the algorithm is so fast that it is even quicker to obtain the auto-correlation via the spectrum using the FFT routine rather than to evaluate the auto-correlation using the lagged product method of Equation 38.

The principle behind the FFT is that a Fourier analysis of a series of numbers can be done faster by making one analysis of the odd indexed numbers and another for the even indexed numbers, then merging the two results to obtain a single analysis covering all the numbers. That is:

Odd: $x_1 \; x_3 \; x_5 \; \cdots\cdot \; x_{2N-3} \; x_{2N-1}$

Even: $x_2 \; x_4 \; x_6 \; \cdots\cdot \; x_{2N-4} \; x_{2N-2} \; x_{2N}$

The inverse Fourier transform of Equation 45 assuming it consists of 2N not N data points is:

$$x_i = \sum_{k=1}^{2N} X_k \cdot \exp\left[j\frac{2\pi ki}{2N}\right] \qquad \text{... (56)}$$

where i=1,2,...,2N.

Let the odd indexed points of the above series of numbers be $x(2\ell-1)$ where $\ell=1,2,\ldots,N$ and as with Equation 56 the series can be represented as:

$$x(2\ell-1) = \sum_{m=1}^{N} C_m \cdot \exp\left[j\frac{2\pi m\ell}{N}\right] \qquad \ldots (57a)$$

and similarly for the even indexed points $x(2\ell)$, $\ell=1,2,\ldots,N$

$$x(2\ell) = \sum_{m=1}^{N} CC_m \cdot \exp\left[j\frac{2\pi m\ell}{N}\right] \qquad \ldots (57b)$$

For the 2N points analysis the odd indexed points of Equation 56, with $i=2\ell-1$, $\ell=1,2,\ldots,N$ are:

$$x(2\ell-1) = \sum_{k=1}^{2N} X_k \exp\left[j\frac{2\pi k\ell}{N}\right] \exp\left[-j\frac{2\pi k}{2N}\right] \qquad \ldots (58a)$$

and the even indexed points with $i=2\ell$, $\ell=1,2,\ldots,N$ are:

$$x(2\ell) = \sum_{k=1}^{2N} X_k \exp\left[j\frac{2\pi k\ell}{N}\right] \qquad \ldots (58b)$$

Replacing the index k by $k'=n-N$ in the second halves of the Equation 58, then re-arranging gives:

$$x(2\ell-1) = \sum_{k=1}^{N} (X_k-X_{k+N}) \cdot \exp\left[j\frac{2\pi k\ell}{N}\right] \cdot \exp\left[-j\frac{2\pi k}{2N}\right] \qquad \ldots 59a)$$

$$\text{and } x(2\ell) = \sum_{k=1}^{N} (X_k + X_{k+N}) \cdot \exp\left[j\frac{2\pi k\ell}{N}\right] \qquad \ldots (59b)$$

Comparing Equations 59 with 57 yields:

$$C_m = (X_k-X_{k+N}) \cdot \exp\left[-j\frac{2\pi k}{2N}\right] \qquad \ldots (60a)$$

$$\text{and } CC_m = (X_k + X_{k+N}) \qquad \ldots (60b)$$

which can be re-arranged to give:

$$X_k = \frac{1}{2}\left(CC_m + C_m \cdot \exp\left[j\frac{2\pi k}{2N}\right]\right) \qquad \ldots (61a)$$

$$\text{and } X_{k+N} = \frac{1}{2}\left(CC_m - C_m \cdot \exp\left[-j\frac{2\pi k}{2N}\right]\right) \qquad \ldots (61b)$$

Equations 61 show that N complex multiplications are required to go from the two N points analysis to the 2N point analysis. For each of the sub-sets of data there are N^2 complex multiplications, resulting in a total of $2N^2+N$ complex multiplications. This compares with $(2N)^2$ by the 2N point analysis of Equation 56. The ratio of computing times is:

$$\frac{2N^2+N}{4N^2} = \frac{1}{2} + \frac{1}{4N}$$

and as N becomes large, using the doubling routine is twice as fast as transforming the 2N points as a whole.

The time can further be decreased since each N point analysis can be processed using two N/2 point analysis and so on. For a series of N numbers the number of operations becomes about $N \log_2 N$ instead of the conventional N^2 demonstrating why the FFT is in fact fast.

The fast Fourier transform algorithm used is based on Villasenors[60] programmes which had been adapted to the City University ICL 1905E digital computer by Anderson and Nettleton[61]. The routines during programme development and testing however were found to have a few mistakes which produced inexact results. The errors were isolated and the routine corrected.

The computer programs used for the data processing are presented in Appendix D.

CHAPTER 3

APPARATUS, DESIGN AND CONSTRUCTION

3.1 Wind Tunnel

All the experiments were made in the Industrial Aerodynamics low speed wind tunnel. Shown in Fig.12, the tunnel is a closed return circuit tunnel with a contraction designed to be axisymmetric about the roof of the working section. The working section is of rectangular cross-section, 3 m wide by 1.5 m high and 8.1 m in length. The tunnel is constructed mainly from timber and all the internal surfaces are of plywood.

The two side by side contra-rotating fans are powered by a 57 kW variable speed ac electric motor through a 3 : 1 reduction gearbox. The electric motor and reduction gearbox are mounted on a steel tower, external to the wind tunnel. With the tunnel circuit empty and devoid of gauze screens, the wind speed could be varied continuously from about 4 ms^{-1} to 26 ms^{-1}. A detailed description of the design and construction of the wind tunnel is given by Glover & Sykes[65].

A delay in the delivery of the gauze screens was found to be holding up the experimental work; to avoid any further delays the decision was made that the flow in the empty tunnel without the gauze screens would be used to represent 'smooth' flow conditions. The intensity of longitudinal turbulence without gauze screens was about 3% with an integral scale of about 0.13 m.

3.2 Turbulence Generation

Turbulence in natural wind under neutrally stable atmospheric conditions was described earlier in Section 1.2 as being produced through the breakdown of the unstable sheared flow resulting from obstacles at ground level retarding the flow. Correct reproduction of the atmospheric boundary layer in a wind tunnel therefore generally requires the obstacles to be modelled with some degree of accuracy. However, the objective of this study is to isolate and determine the significance of turbulence scale in steady and fluctuating wind loads on buildings. To disassociate these effects from those attributable to a velocity gradient, the turbulent flow conditions in the wind tunnel were generated using bi-planer grids. With grids, areas of sheared flow are produced throughout the cross-section of the stream which eventually results in uniformly distributed and decaying turbulence.

A systematic series of measurements of both scale and intensity of turbulence behind grids made by Baines & Peterson[66] showed that the maximum intensity of turbulence occurs two to three mesh lengths from the grid and thereafter decays, following the relationship:

$$\frac{\hat{u}}{\bar{U}} = 1.12 \left(\frac{x}{b}\right)^{-5/7} \qquad \ldots (62)$$

where $\hat{u}$ and $\bar{U}$ are the rms and mean wind speed at position x, respectively; x is the distance downstream from the grid; and b is the bar width of the grid. Baines & Peterson's results are reproduced in Figs.13 & 14.

Unlike the intensity, there is considerable scatter in the experimental data for the variation of lateral scale of turbulence with downstream distance which would seem to imply that the scales of turbulence are not simply a function of downstream distance and bar width, as is the intensity, but are likely to be a function of other characteristics of the grid, such as mesh size. The scatter however may simply be indicative of the difficulty associated with measuring the scales of turbulence. Nevertheless, an empirical expression based on these results is still a useful indication of the scales likely to be achieved. Whitbread[67] suggested the following relationship for the longitudinal scale of turbulence L_x based on these and other experimental data:

$$\frac{L_x}{b} = 0.0706 \left(\frac{x}{b}\right)^{0.775} \qquad \ldots (63)$$

Since it is the longitudinal scale which is commonly used in investigating wind loading of structures, it was necessary for Whitbread to assume that the turbulent flow of Baines and Peterson was isotropic and the scales of turbulence theoretically related by:

$$L_x = 2L_y = 2L_z \qquad \ldots (64)$$

where L_y and L_z are the lateral and vertical scales of turbulence, respectively. This assumption should result in a reasonable approximation since grid generated turbulence has been found to be nearly isotropic[68].

There are two limitations on the maximum turbulence intensity and scale which can be achieved with grids. The first is that a distance of ten mesh lengths downstream of the grid is usually necessary before the flow can be assumed to have become uniform in turbulence intensity and mean wind speed. The ten mesh lengths recommendation is a useful guide to the minimum distance that should be used with Figs.13 & 14 and Equations 62 & 63. With a number of grids however, uniformity of flow is achieved much sooner than the distance of ten mesh lengths, but these positions can only be determined from a survey of the flow. The second restriction with grids applies to their area blockage ratio, the permissible maximum of 50% should not be exceeded otherwise the grid is considered to be unstable in that it tends to produce non-uniformities in the flow which persist well beyond the ten mesh distance downstream.

Three turbulence grids were used in the present investigations, their design was based on Equations 62 & 63 and was to create flow conditions at the test positions consisting of integral scales of about 5, 10 and 20 cm with a turbulence intensity of about 10%. They were constructed as bi-planer grids with square mesh using wooden slats. Their dimensions are given in Table 2, and Fig.15 shows a grid positioned in the working section of the tunnel. In their design, the structural strength of the grids to withstand the maximum aerodynamic loading situation during their operation was calculated using wind loads estimated from values of pressure drop across grids given by Baines & Peterson.

3.3 Models

Three rectangular models were used to obtain experimental data on the cross-correlation of fluctuating pressures on the windward and leeward faces of typical tall buildings with the emphasis on determining what influence the depth of a building has on the values of the correlations.

In their design, the size of the models was determined by the largest scale of turbulence which could be generated in the wind tunnel for a flow with a turbulence intensity of 10%, and by the requirement that the ratio of turbulence scale to model breadth L_x/B, covered the categories of the turbulence scale L_x being equal to, less than and greater than the model breadth B. To meet these specifications, L_x/B ratios equal to 0.5, 1.0 and 2.0 were chosen as being broadly representative of the three categories and with design data for the grids from the previous section, required the models to be 10 cm wide. The models were 60 cm in height which gave proportions of breadth : depth : height of 1 : 0.25, 0.5, 1 : 6 for the three models. The depths of the models were chosen to provide the widest range for the section ratio; the lower limit of 25 mm was considered to be the smallest dimension which could be sensibily achieved whilst ensuring:

- it was physically possible to incorporate the necessary number of pressure tubes inside the model
- model displacements were small
- natural frequency of the model was high

The proportions of the models were not chosen to be representative of typical buildings, although the 1 : 1 : 6 proportion could be considered as representing a very tall building.

The ratios $L_x/B = 0.5$, 1.0 and 2.0 were chosen to cover conditions which ranged from the spatial correlation of the turbulence being low and any effects principally a function of the total energy of the spectrum, to the situation where the forces acting on the model are strongly correlated with the free stream turbulence and analysis on a quasi-steady basis is broadly valid.

The models were designed to be rigid to keep their displacements small enough so as not to significantly affect the flow field around the models. In this respect it was also necessary to ensure that the natural frequency of the models was beyond the highest frequency of interest. Two of the models were constructed from perspex sheet 4.8 mm thick; however, to comply with the requirements for small displacements and high natural frequency the third model was constructed from mild steel plate. Details of the construction for all three models are given in Fig.16, and Fig.19 is a photograph of the models.

Prior to assembling the models, pressure tappings around the models were made by drilling a hole 0.80 mm in diameter through the face of the model. This hole was then enlarged to just below 1.6 mm in diameter to a depth of 3.2 mm from the inside face of the model. 12.5 mm lengths of brass tube 1.6 mm in diameter were cut and their ends filed square, and a piece was then press fitted into each hole from the inside face of the model. To achieve maximum accuracy in positioning the pressure tapping points, opposite faces of each model were machined and drilled in pairs using a vertical milling machine. Locations of the pressure tapping points are shown in Figs.17 & 18 together with details of a pressure tapping.

The pressure taps were designated numbers for ease of reference. A three number system was employed with the first number ascribed to the levels and the other two to positions around the circumference of the model. Details of the numbering system are shown in Figs.17 and 18.

Flexible plastic tube, 90 cm long and 1.6 mm in bore was used to connect the pressure taps to the pressure transducer. Such a pressure sensing system (plastic tubing and scanning valve with pressure transducer) modifies the true pressure fluctuations sensed by the pressure transducer. To determine in what manner the two pressure signals differed, various lengths of plastic tubing were tested using the method outlined in Appendix A. The results from these tests showed the resonant frequency of the system to be approximately inversely proportional to the square root of the plastic tube length. A length of 90 cm was chosen as providing an acceptable limit to the upper frequency for the data whilst still being long enough for the physical connections to the scanning valve to be made in a manageable fashion. The transfer function of the pressure sensing system used throughout the study is shown in Fig.20 and was determined using the calibration system outlined in Appendix A. An equation describing a single degree of freedom linear system with damping was fitted to the transfer function by the method of least squares and is shown as the solid line in Fig.20. This equation, incorporated in the data processing computer programme, was used in the manner suggested in Appendix A to apply corrections to the computed results, to account for the distortion of the original signals.

CHAPTER 4

GENERATED TURBULENT FLOW

4.1 General

The turbulence generating grids were made from wooden slats screwed together to form bi-planer square mesh grids. Figure 15 shows Grid 2 in position at the beginning of the working section of the wind tunnel. Details of dimensions for the three grids are given in Table 2.

A cartesian co-ordinate system is used to define the components of the generated turbulence, with the x-direction taken in the direction of the mean flow $\bar{U}$ and the y- and z-directions in the plane normal to $\bar{U}$ as shown in Fig.21.

4.2 Measurements and Results

The intensity of turbulence for each grid was measured on the tunnel centre-line at the distance ten mesh lengths downstream over a wide range of wind speed and the results in all instances were found to be higher than the values predicted by Equation 62. These point measurements not substantiating Equation 63 posed a number of questions, the most serious being, were the grids which had been designed based on data outlined in Section 3.2 generating turbulent conditions with the characteristics described in Section 1.2.2? Secondly, it was necessary to re-determine the positions at which the models should be located and to survey the flow at these positions since it had been estimated that they would be situated less than the customary ten mesh lengths downstream.

Decay of turbulence behind each grid was measured and the results are shown in Fig.22 together with the empirical equations suggested by Baines & Peterson and Whitbread. For Grid 2 the decay of turbulence was also measured for a number of different wind speeds and these results are shown in Fig.23. The above measurements were all made using a non-linearised hot-wire positioned at the working section centre-line and 30 cm from the tunnel floor; this position coincides with the midheight of the models. The time spent carrying out the above survey was significantly reduced with the aid of a motor driven traversing trolley which was used to position the hot-wire. This trolley was similar to that used by Cook[53] to measure the flow behind models of buildings. Positions for the models were selected relative to each grid from Fig.22 so that the intensity of turbulence in each instance was 10%.

In addition to the decay of turbulence the probability density and the spectrum of longitudinal turbulence were computed for four positions downstream of each grid, which included the selected model locations. The probability density functions, shown plotted in a non-dimensional form in Fig.24, exhibit the typical form of a random process normally distributed and for comparison the Gaussian distribution is shown superimposed on the results.

The probability density and spectral density functions were computed using the digital routines described in Section 2.5. For comparison the spectra were in a few instances also obtained by analysing the same recordings, using analogue equipment. The spectra from digital and 1/3 octave analogue analysis are presented in Fig.25. With the digital analysis the frequency range shown was covered in two stages. The analogue data was first digitised and analysed to cover the frequency band 0.65 to 52 Hz and then the same analogue signal was re-digitised at a sampling rate ten times faster than before to cover the lower frequency range of 6.5 to 520 Hz.

Since the model positions were to be less than the customary ten mesh lengths from the grid, it was necessary to ensure the flows at these positions had achieved uniform distribution and did not contain any undesirable characteristics. In addition, therefore, to the amplitude and frequency characteristics, which have been mentioned above, the degree of uniformity of the flows across the working section of the tunnel at the model positions were investigated. Of the measurements made a typical result is presented in Fig.26, which was for Grid 2. Finally, the velocity profiles at the model positions were also measured along a vertical traverse from the floor to the centre of the working section and these appear in Fig.27.

4.3 Discussion of Results

The decay of turbulence measured downstream of the grids were all except one, under-estimated by the expressions given by Baines & Peterson and Whitbread. The exception was with Grid 3, where the measured values accurately conformed to the empirical decay proposed by Whitbread. During these experiments on evaluating the performance of the grids, and also during subsequent model tests, there were no fine gauze screens fitted in the tunnel circuit as is customary in low speed wind tunnels, and this was considered to be the cause of the discrepancies between the predicted and the achieved decays of turbulence. It was argued at the time that one of the consequences of not having gauze screens upstream of the grids was that the flows approaching the grids were already turbulent, due to the residue of the turbulence generated by the grids and the general background turbulence of the tunnel circuit, which could increase the net turbulent energy in the flow downstream of the grid. Although with most studies in grid generated flow the turbulence upstream of the grid is deliberately kept to a negligible level, it was considered that such a method could be used to achieve intensities of turbulence not normally possible with grids. Since measurements showed that acceptable flow conditions had been achieved at the positions of the models, no measurements upstream of the grids were made and the matter was not pursued any further.

The above reasoning has since been vindicated by results from an investigation by Khader & Elangas[69] into the turbulence generated with grids situated in initially turbulent flow. They found that increasing the upstream turbulence resulted in an increase in the intensity of turbulence downstream and that the turbulence decayed at a rate which did not comply with any simple power law.

From the survey of the flow for the three grids the intensity of turbulence showed no systematic variation with wind speed for either the longitudinal traverse downstream or the point measurements taken at the positions of the models. This combined with the fact that the speed control for the wind tunnel could be used to achieve consistent results meant that identical flow conditions were being reproduced for each run. Lateral traverses across the working section at the model positions showed the flow to be uniform and independent of the grids. Spectra of the longitudinal turbulence at the positions of the models did not reveal any sharp peaks and exhibited the form typical of grid generated turbulence.

The longitudinal integral scales of turbulence were determined using the Fourier relationship between the auto-correlation and the spectral density function of Equation 41 and from Equation 21, viz.

$$L_x = \frac{\bar{U}}{4} \cdot \lim_{n \to 0} S_u(n) \qquad \ldots (65)$$

The length scales obtained are given in Table 3, where it is seen that they increase in value with distance downstream from the grids. This happens through the gradual disappearance of the smaller eddies. As the length scale is representative of the average eddy size, the gradual dissipation into heat of the smaller eddies results in an increase of the average eddy size. The problem associated with estimating length scales from Equation 65 is the scatter of the spectral data values at the low frequencies. Consequently, the problem reduces to one of curve fitting and interpretation. But according to Armitt[70] "Fitting curves to spectra in order to deduce length scales imposes the experimenter's ideas on the data. Even if the curves are correct in functional form there is still a requirement that the data analysis should be significantly accurate to allow a good curve fit. Even here, the requirements are not easily satisfied." Although there is an obvious difficulty in interpreting the scales, they can still give a qualitative feel to the structure of the turbulence. Values for the length scale L_x obtained for the model positions were 57 100 and 198 mm for Grids 1, 2 and 3 respectively.

Using these length scales, the spectra were replotted using the parameters:

$$\frac{\bar{U} \cdot S_u(n)}{2\pi L_x \cdot \sigma_u^2} \quad \text{and} \quad \frac{2\pi n L_x}{\bar{U}} \qquad \ldots (66)$$

and compared with the von Karman spectrum[32], viz.

$$\frac{S_u(n)}{\sigma_u^2} = \frac{4L_x}{\bar{U}} \left(1+1.8 \left(\frac{2\pi n L_x}{\bar{u}} \right)^2 \right)^{-5/6} \qquad \ldots (67)$$

The results are shown in Fig.28 where it is seen that the measured spectra show good collapse and that the von Karman spectrum closely follows the collapsed spectra. For reduced frequencies above $\tilde{n}=2$. Equation 67 begins to under-estimate the measured results. At even higher frequencies, however, in the dissipation range the experimental results fall off at a faster rate than -5/3 and Equation 67 over-estimates the measured values.

Comparing the results obtained for the spectra using both the analogue and digital techniques confirmed that the digital method not only produced results which were much the same as the analogue measurements but the results were also more detailed and would not smooth out peaks to the extent that the analogue measurements would. Considering that the analogue measurements were also very time consuming, and analogue equipment very limited at the time, the choice made for the data analysis system proved to be correct.

The probability density functions shown in Fig.24 exhibit the form of the Gaussian distribution and generally have a skewness value near zero and a Kurtosis value in the range 2.7 to 2.9. The deviations from the Gaussian distribution, which has a Kurtosis of 3.0, are only slight and then mainly at the tails of the distribution. This is because the return periods associated with these extreme values are approaching the sample period, therefore the number of samples used in the averaging is small and the assumption of stationarity is violated. Although results from this study will be applicable to extreme value analysis of wind loads on buildings through the use of gust factors, the study is principally concerned with the time averaged properties of turbulent wind loading of tall buildings and, therefore, the small deviations from a Gaussian distribution are considered to be unimportant.

CHAPTER 5

SURFACE PRESSURE MEASUREMENTS

5.1 General

Measurements of surface pressures on each model were made in smooth and turbulent flow conditions at a wind speed of about 13 ms^{-1}. This velocity represents a Reynolds number Re of about 8.6×10^4 for the models, based on the front face dimension of 100 mm.

Delaney and Sorenson[72] have shown that rounding the corners of bluff structures can have a significant influence on the drag forces acting on the structure, therefore, to ensure the models were insensitive to any Reynolds number effects, special attention had been paid to preserving the sharpness of the edges. Artificially high Reynolds number effects in particular for rounded structures such as chimneys and cooling towers can be produced with increased surface roughness. However, these effects were not investigated as they were outside the scope of this study and special attention was paid to ensure that the faces of the models were smooth.

A wind speed of 13 ms^{-1} was used for all the wind tunnel tests and was selected on the basis of:

- achieving a maximum reduced frequency ($nB/\bar{U}$) an order higher than the Strouhal frequency, which is normally 0.1 for the type of structure under investigation; whilst

- still achieving a dynamic head sufficient to produce sensible and accurate results

These pre-requisite conditions together with the limitations on the maximum acceptable frequency imposed by the pressure tube/Scanivalve system determined the maximum wind speed permissible.

A degree of adjustment was built into the model fixing arrangement so that the models could be rotated and locked into position. The models were positioned with the front face normal to the flow, and this was achieved by monitoring the mean pressure distribution around the model at its mid-height using the inclined multi-tube manometer. The models would be slowly rotated until a symmetrical pressure distribution was achieved.

Wind speed in all instances was determined from the free stream total and static pressures which were measured using a pitôt-static tube.

5.2 Measurements and Results

All measurements of mean pressure were made using the inclined multi-tube manometer. It was used in preference to the Scanivalve system because it was very effective in damping out the pressure fluctuations; it also gave a visual display of the distribution. The results, non-dimensionalised with reference to the dynamic pressure, are shown as pressure coefficients in Figs.29 & 30.

To measure the fluctuating component of pressure the pressure tappings were connected to a Scanivalve by 0.9 m lengths of 1.6 mm bore plastic tubing. The pressure tube/Scanivalve system had been calibrated using the method described in Appendix A and the transfer function for the system is shown in Fig.20. The Scanivalve with the pressure transducer were located beneath the wind tunnel floor. The results, again non-dimensionalised with reference to the dynamic pressure, are shown in Figs.31 & 32. Since the primary interest was in wind forces due to turbulent flow, no measurements were made of fluctuating surface pressures for the smooth flow condition. Although the transfer function for the pressure tube/Scanivalve system had been determined, no corrections have been applied to the data in Figs.31 & 32, which were measured using an rms meter, the signal having initially been filtered through a low-pass analogue filter set to 120 Hz.

The spectral density functions $S_p(n)$, which describe the frequency distribution of the surface pressure fluctuations, were determined for positions at the mid-height and top levels of the models. All spectra were corrected to account for the effects of the pressure tubing/Scanivalve system as suggested in Appendix A using the transfer function in Fig.20. The corrected results are shown scaled to the value of the variance in Fig.33 for levels 3, and Fig.34 for levels 9. The pressure signals from the transducer were recorded on magnetic tape at a recording speed of $3\frac{3}{4}$ inch s^{-1}. Before recording, the signals had most of their dc component backed off, were amplified and then filtered through a low-pass analogue filter set at 200 Hz with a roll-off rate of 18 dB/octave. For subsequent analysis analogue to digital conversions of the signals were made with the magnetic tape recorder reproducing at a tape speed of $3\frac{3}{4}$ inch s^{-1} and the analogue signals pre-filtered through a low-pass filter set at 200 Hz with a roll-off rate of 18 dB/octave. The signals were digitised at a sampling rate of 400 samples s^{-1}. For the analysis 25,600 digitised data samples were used to compute each spectral density function from 100 raw spectral estimates giving a band-width of about 1.5 Hz and a normalized standard error of 0.1 for the spectra. All recordings of pressure fluctuations and their subsequent analysis were made in pairs for the purpose of determining joint relationships; the results of which are the subject of Chapter 6.

For the same 25,600 samples, used to compute the spectrum, the probability density function for each signal was also determined and the distributions are shown in Fig.35 for the pressures at levels 3 and in Fig.36 for the pressures at levels 9. Associated skewness and kurtosis values are shown in Tables 4 and 5

5.3 Discussion of Results

The tunnel area blockage ratio with the models was about 1.4% and was deliberately kept low to avoid the problem of blockage effects. This was an important consideration because although corrections have been derived for the mean characteristics of the flow around bluff bodies by Maskell[73] and for the parameters Strouhal number and fluctuating lift coefficient by Vickery[74], and a number of investigations into the subject of blockage effects are in progress, the author knows of no suitable blockage corrections which are applicable to the statistical functions measured in this study. The surface pressure measurements were therefore considered to be independent of blockage effects.

The mean pressure distributions with height, on the centre lines of the windward and leeward faces of the models, in smooth flow conditions shown in Fig.29 are very similar to results reported by Baines[75] for a square section model with an aspect ratio of 8. In this study, in contrast with Baines, there were insufficient pressure taps distributed on the models to be able to draw isobars but, nevertheless, from the measurements made it was still possible to draw useful comparisons.

With the introduction of turbulence into the flow the effect is a gradual downward movement in the position of the stagnation point with decreasing turbulence scale. This effect was also noted by Cook[53] in his investigations. Mean pressure distribution on the leeward face of the models exhibited a gradual decrease in pressure with height for all three models and turbulence scale. The magnitude of these base pressures as demonstrated in Fig.29 are found to be a function of both turbulence scale and the depth of the model, a clear indication that the scale of turbulence does have a significant influence on the forces acting on tall buildings. Also, since these forces develop as a result of local velocities then the general flow field around the models must have been modified by the turbulence scale of the incident flow.

The significance of model proportions on the drag forces for two-dimensional rectangular models was investigated in detail by Bearman and Trueman[76]. They found that the base pressure decreased as the depth of the section increased, reaching a minimum at a depth/breadth ratio of 0.62 and thereafter increased. These results were from experiments limited to smooth flow conditions. In the present study the results of the base pressure measurements exhibit the same trend, but the effect is not as prominent with the smooth flow condition as it was with the turbulent conditions. Bearman and Trueman report that the influence of section ratio on base pressure is associated with the formation and shedding of vortices from the leading edges and argued that as the section ratio was increased the vortices formed closer to the rear face which lead to a decrease in base pressure, until the critical section ratio of about 0.6 was reached. Any further increase of the section ratio resulted in the vortex formation being affected by the section afterbody and the vortices were forced to form further downstream of the rear face.

The effect of introducing turbulence into the incident flow is to increase the rate of entrainment into the shear layers which in turn thicken more rapidly and also to reduce their radius of curvature. Both the rapid spreading and reduced radius of curvature of the shear layers will significantly alter the formation of vortices and the wake width which in turn will significantly alter the base pressure. In the present tests the results in Fig.30 show that for $L_x/B = 1.0$ and 1.98 the base pressure with model 2 ($B/D = 2$) was lower than with the two other models. Although the differences were much smaller, the same trends were apparent with the models in the smooth flow condition. With $L_x/B = 0.57$ the base pressure was found to decrease with decreasing section ratio.

The significance of turbulence scale on the mean drag forces on bluff bodies has received relatively very little attention in the past and in the few cases where the subject has been investigated, two-dimensional models have generally been used. The exception has been the work by Cook[53] who used three-dimensional square section models with an aspect ratio of 3. The results however were not conclusive and there still remained many questions unanswered. McLaren et al[51] and Lee[52] found that for two-dimensional square section models there is a definite variation of mean drag force with turbulence scale with a maximum occurring at a turbulence scale/model size ratio of about unity. The general trend can be seen in Fig.37 where the results of Lee[52] have been reproduced. Results from the three-dimensional models used in the present study exhibit the same characteristics as the two-dimensional investigations along the top 1/3 of the model height and surprisingly not at model mid-height, where it was found that increasing turbulence scale gave decreasing base pressure. This observation needs to be confirmed by more measurements and particularly in more detail around the $L_x = B$ region. Confirmation is also required to show that the trends reported for two-dimensional models[51,52] are valid.

The mean pressure distributions around the models were measured at levels 3, 7, 8 and 9; however, only some results from level 3 (model mid-height) are presented and are shown in Fig.30. The results for the three other levels were similar in character except that the pressures on the leeward face at levels 8 and 9 (top 10% of the models) displayed typical local effects due to the free end by producing a uniform pressure distribution across the face. In general, the distributions show the expected pressure lobe on the windward face of the models and negative pressure coefficients on the other three faces. No results have been presented for the pressures on the side faces of the models because only a limited number of pressure tappings were possible on these faces, and the numbers were considered to be insufficient to provide information on which to base any sensible conclusions; the restricted space inside the models limited the number of pressure tubes which could be accommodated by each model.

The exception was with Model 3 which had five pressure taps on each side at levels 3, 7, 8 and 9, and where it was observed that increasing the turbulence scale resulted in a decrease in the pressures, and in contrast to the smooth flow condition, the pressure increased slightly towards the rear corner in turbulent flow, suggesting that the radius of curvature of the shear layers is reduced. At model mid-height the pressure distributions on the side faces were fairly flat, with Grid 2 producing the lowest pressures with pressure coefficients of about -0.92 towards the leading edge and -0.88 towards the trailing edge and peaking to -0.98 at the centre. With Grids 3 and 1 pressure coefficients of about -0.91 and -0.74 respectively were measured at the centre of the side. At the top levels of the model the only effect on the side face pressures relative to the mid-height level was to cause the downstream variation of pressure distribution to increase from -1.09 at the leading edge to -0.89 at the trailing edge for Grid 2, with similar variations for Grids 3 and 1. On the whole the pressure distribution around the models at mid-height and below was effectively uniform with height.

Sectional drag forces acting on the models were calculated from the pressure distributions and the results are shown in Fig.38 as non-dimensionalised force coefficients. From these results it is evident that the effect of turbulence scale on the flow field around the models is such that not only are the magnitudes of the loading altered but also the vertical distributions, which demonstrates that although comparisons with two-dimensional situations may be useful it must be remembered that the flow field are vastly different. With the experimental data reduced to sectional force coefficients in Fig.38 the effects discussed above, of section ratio and turbulence scale, are seen to apply at all positions on the models.

The rms value of the pressure fluctuations on the models, in Fig.32, showed little variation across the windward face. On the leeward face, however, where pressures are dependent on the characteristics of the wake, large amplitude pressure fluctuations were measured at the edges which progressively reduced in amplitude for inner positions, reaching a minimum at the centre of the face. This occurs because of the formation and shedding of vortices from the models into the wake. The extent to which vortex shedding influences the pressure fluctuations at different positions around the models can be seen from the spectra in Fig.33. In all instances the two outer pressure taps (13 and 14) experienced the strongest influence with more energy being centred at the vortex shedding frequency than was found at the two inner pressure taps (15 and 16). With $L_x \approx B/2$ the spectra exhibit wide-band frequency characteristics; however, as turbulence scale is increased through $L_x = B$ to $L_x \approx 2B$ vortex shedding becomes evident and more coherent. It has been shown, for example by Laneville et al[43], Cook[53] and Lee[52] that increased free stream turbulence results in increased mixing and entrainment in the shear layers which tend to thicken and have reduced radius of curvature. Cook found that the rapid spreading of the shear layers caused them to dissipate energy by generating turbulence soon after separation and the result was that weaker vortices were formed. An explanation of why changes in turbulence scale appear to produce effects similar to those caused by changes in turbulence intensity is found by considering results by Gartshore[85] and Hunt[78].

Gartshore[85] has shown that small scale free stream turbulence approaching a bluff body along its front stagnation line effectively produces the major effects of incident turbulence on the flow around a body. A theoretical analysis by Hunt[78] of turbulent flow around two-dimensional bluff bodies, subsequently supported by the measurements of Petty[84] and Bearman[77] whose results are reproduced in Fig.39, has indicated that the change in turbulence upwind of a bluff body depends on the scale of turbulence relative to the size of the body. Based on these findings for high values of L_x/B the turbulence will be attenuated on the stagnation line which will result in a decrease in the base pressure, whereas for low values of L_x/B the turbulence on the stagnation line will be amplified and the result is an increase in the base pressure.

Base pressure measurements at model mid-height in Fig.29 substantiate these findings. However, the theory does not support the findings of McLaren et al[51] and Lee[52] that the maximum mean drag force on a two-dimensional square model is achieved for L_x/B equal to unity. In the present investigation the trends observed at the upper levels of the models could be considered to result from the three-dimensionality of the flow due to the free-end, and since Hunt's theory is for two-dimensional bluff bodies, deviations from the predicted behaviour are not surprising.

Referring to the pressure spectra in Fig.33 it is seen that model section ratio also has a significant influence on the vortex shedding, with Model 2 producing a sharp peak at the shedding frequency and a secondary peak at twice the shedding frequency. The secondary peak is only just evident with the other two models. The section ratio of Model 2 is approximately equal to the critical section ratio of 0.62 found by Bearman[76] and others, and it is considered that vortex formation was taking place very close to the rear face and consequently alternately shed vortices affected the whole of the rear face due to their close proximity.

The effects of turbulence scale and section ratio, as discussed using measurements of the power spectral density, are all reflected in the forces on the models as demonstrated by the magnitude and distribution of the forces in Figs.31 & 32.

Fluctuating pressures on the windward face, and at mid-height of the model, are uniformly distributed with the rms magnitudue of the fluctuations found to be influenced by the scale of turbulence. In all cases the highest rms pressures were produced with the smallest scale of turbulence and the lowest were with L_x/B equal to unity. This result, however, is considered to be incorrect, from examination of the variation of turbulence with height, along the centreline of the models in Fig.31, the reason is apparent. It is seen that although the rms values are generally uniformly distributed, this is not the case with Grid 1 ($L_x/B=0.57$) generated flow conditions. In this instance it is found that the fluctuating pressures, shown non-dimensionalised with reference to the dynamic pressure as fluctuating pressure coefficients, varied from about 0.2 at the bottom to about 0.1 at the top of the models. It would appear that Grid 1 had a very marked effect on the flow field and consequently the forces distributed on the models. A similar observation, in relation to the mean forces was made earlier for Grid 1 generated flow. If the average values from the upper half of the models were used for Grid 1 ($L_x/B=0.57$), on average $C'_{p_\omega}=0.13$, then the results would be consistent with those by Cook[53] and Bearman[77].

At present the most common approach to predicting the fluctuating drag forces on a structure due to turbulent flow is to assume that a quasi-steady linear relationship exists between the u-component of the incident turbulence and the fluctuating pressures. The basic assumptions for a quasi-steady theory are set out in Appendix B where it is shown that from such a theory the fluctuating pressure coefficient C'_p is:

$$C'_p = 2|C_p| \cdot \frac{\hat{u}}{\bar{U}} \qquad \dots (68)$$

where $\hat{u}/\bar{U}$ is the intensity of turbulence and C_p is the mean pressure coefficient. This relationship must be applicable, if anywhere, at the stagnation line where the flow is brought to rest; however, this is generally found not to be the case. Why Equation 68 is not strictly correct is that in its derivation it has been assumed that the turbulence scale relative to the size of the structure is large whereas in reality turbulence is composed of eddies of a wide range of sizes and therefore the smallest eddies will be affected by the distortion of turbulence by the structure. Bearman[77] found that the fluctuating pressures at the stagnation point of a two-dimensional flat plate, with the wake filled in, were consistently over-estimated by Equation 68 and was found to be due to attenuation of the pressures at high frequencies. The measurements of the power spectral density for fluctuating pressures and turbulence in Figs. 33 & 25 (for comparison typical examples are reproduced in Fig. 40) show that the rate of dissipation of energy for the pressure fluctuations is greater than that for the incident turbulence. As a comparison the line with the slope of $-5/3$ has been included. In all instances it is found that the highest drop-off rate occurs for the pressure fluctuations on the stagnation line and the lowest with the pressures measured at the edges of the front face. From the pressure spectra in Fig. 33 the high wave number pressure fluctuations appear to be independent of turbulence scale which is consistent with Hunt's[78] theory of rapid distortion of turbulence in the flow past bluff bodies where he has shown that when the reduced frequency $nB/\bar{U} \geqslant 0.15$ then the admittance function $\chi_a^2(n)$ for the pressure fluctuations at the stagnation line:

$$\chi_a^2(n) = \frac{S_p(n)}{\rho^2 \bar{U}^2 S_u(n)} \qquad \ldots \quad (69)$$

is a function of reduced frequency $nB/\bar{U}$ and not of turbulence scale/body size ratio, L_x/B.

In the derivation of Equation 68 (see Appendix B) it was assumed the surface pressures were related to the upstream flow by Bernoulli's equation, viz.

$$\bar{P} + p(t) = \tfrac{1}{2}\rho\left(\bar{U} + u(t)\right)^2 C_p \qquad \ldots \quad (70)$$

Separating into mean and fluctuating components.

$$\bar{P} = \tfrac{1}{2}\rho\bar{U}^2 C_p \left(1 + \frac{\overline{u^2}}{\bar{U}^2}\right) \qquad \ldots \quad (71a)$$

$$\text{and} \quad p(t) \approx \rho \bar{U} u(t)\, C_p \qquad \ldots (71b)$$

the term $\overline{u^2}/\bar{U}^2$ is usually only about 0.04 and can be neglected. At low frequencies it is found that Equation 71b is valid and is confirmed by the admittance function in Equation 69 which tends to the value unity at low wave numbers.

The pressure fluctuations on the leeward face are found to be less attenuated than those on the windward face, with the level of the pressure spectra reducing at a rate just faster than the -5/3 found for the velocity spectra. However, towards the higher wave numbers investigated the levels of the pressure spectra on the leeward face started to drop-off increasingly quickly, and it is considered that the pressure spectra at high wave numbers on the windward and leeward faces would probably follow a universal decay law.

On the windward face at the top level of the models it is observed that with L_x<B the pressure spectra in Fig.34 in comparison with the pressure spectra at model mid-height in Fig.33 have relatively more energy at the high wave numbers, but with increased turbulence scale the energy distribution at both levels are progressively changed so that there is relatively more energy at the lower wave numbers and the differences between levels 3 and 9 reduced. This is to be expected since with increasing L_x/B ratio the quasi-steady situation is being approached. The rms fluctuating pressure distribution and levels on the windward face at the top level are not affected by model geometry. On the leeward face there appears to be no appreciable effect due to turbulence scale. However as the model geometry B/D ratio is reduced there is a transfer of energy to the higher frequencies. There is no evidence of vortex shedding from any of the signals analysed with the exception of the outer pressure taps (numbers 13 and 19) for Model 2 (B/D=2) and then the energy at the shedding frequency is too small to be of significance. Differences between levels 3 and 9 arise because of the three dimensionality of the flow around the top of the models. Because of the large region of separated flow behind the models, which is at a low pressure relative to the ambient pressure, air at the front flows over the top and bleeds into the near wake region, interfering with the formation of the vortices.

In general, the spectra at level 9 have drop-off rates of about -5/3; however, those from the windward face only start to decay at this rate at reduced frequencies of about 0.4. These spectra tend to be fairly flat even up to reduced frequencies of about 0.1.

In wind loading on bluff bodies it has been customary to relate the drag forces to the flow, using a modified version of Morison's[79] equation by:

$$D(t) = \tfrac{1}{2}\rho\, U^2(t)\, B^2\, C_D + \rho B^3\, C_m \frac{dU(t)}{dt} \qquad \ldots (72)$$

where $U(t) = \bar{U} + u(t)$; B is a typical body dimension; and C_D and C_m are the drag and virtual mass coefficients respectively.

In terms of pressure at the stagnation point an analogous equation has been derived for the fluctuating pressures[77], viz.

$$p(t) = \rho\left(\bar{U} \cdot u(t) + \frac{B}{2}\frac{dU(t)}{dt}\right) \qquad \ldots (73)$$

which is also comparable with Equation 71b for C_p=1.

Equation 73 can be expressed in terms of power spectral density of the pressure fluctuations and upstream turbulence, and used to predict the pressure spectra. The result, however, is that the pressure spectra, particularly at the high wave numbers, are overestimated by a considerable amount. In fact the predicted pressure spectra drop off at a rate slower than the turbulence spectra, due to the contributions from the acceleration term, whereas the measured spectra as in Fig.33 are seen to drop off at a faster rate than the turbulence spectra in Fig.25 (see also Fig.40). Bearman concluded that the assumptions made in deriving Equation 73 fail before any acceleration effects are felt and Hunt has shown that the spatial variation of incident turbulence is more important than the temporal one.

Similarly, it is dubious whether Equation 72 is valid for wind loading of structures since Morison's equation was primarily for harmonically oscillating flows with zero mean flow and there is no evidence that the modification to include a mean flow is valid. Instances where Equation 72 has proved to be useful are where wave forces on marine structures need to be evaluated. Here the mass of the fluid relative to the mass of the structure is not insignificant, which is not the case with wind loading. In fact because the contribution of the virtual mass effect to the dynamic drag force is negligible for wind loading it is usually not retained in the analysis.

The distortion of turbulence near the stagnation line and its correlation with the fluctuating pressures is analysed further in the following chapter using cross-spectral analysis techniques.

The probability density function of the pressure fluctuations in Figs.35 & 36 for levels 3 and 9 respectively, exhibit typically Gaussian distribution. There are however deviations from the Gaussian distribution which are evident from the Kurtosis and skewness values in Tables 4 and 5 which may be of significance when dealing with localized loading problems such as with glass windows.

In nearly all instances the distributions are not truly symmetrical and as indicated by the Kurtosis values greater than 3.0 there are a large number of fluctuations frequently occurring at levels greater than the three standard deviations. Fluctuating pressures on the windward face have a positive skew and those on the leeward face have negative skew with the exception of Model 1 (B/D=4) for turbulence scale ratio L_x/B equal to 1.0 and 2.0 which on level 3 produced virtually symmetric distribution and the skew varied about zero. In general, Kurtosis values are higher on the leeward face than on the windward. This is particularly evident for the fluctuations on level 3 where in some instances Kurtosis values of nearly 5.0 were found for the leeward face.

At the top levels of the models, the effect of the free end appears to cause the pressure fluctuations to approach a normal distribution with Kurtosis values on the leeward face, generally only just higher than those on the windward face. Differences between the distributions from the mid-height and top of the models arise because at the top levels the pressure fluctuations are distributed over a wide frequency band as shown by the pressure spectra in Fig.34, whereas on level 3 there is also considerable energy in a narrow band associated with vortex shedding as shown in Fig.33.

In general there are no apparent effects due to turbulence scale or model geometry on the windward face probability distributions. The effects on the leeward face distributions are all considered to be a consequence of vortex shedding.

To summarise the probability distribution results, the measurements showed that for the leeward face not only are the pressure coefficients negative more often than would be predicted by the Gaussian distribution but there is also a higher probability for the occurrence of extreme values. However, although the localised pressure fluctuations may deviate from the normal distribution, and these deviations are of importance in estimating wind loads on building cladding and glass, for the overall drag forces and response of buildings there is plenty of evidence showing that a Gaussian distribution is approximately valid. This is because of the limited correlation that exists between the local pressures, which will be shown in the following chapter, and the Central Limit Theorem.

CHAPTER 6

SPATIAL CORRELATIONS

6.1 General

In order to determine the overall wind loading of structures from point measurements of surface pressure fluctuations, it is necessary to take into account that there is a loss in spatial correlation of these pressures over the surface of the structure. In the same way as the spectral density function was calculated for single pressure points so the cross-spectral density function was calculated for pairs of pressure points.

In the analysis of wind loads on structures it is commonly assumed that a quasi-steady linear relationship between the incident turbulence and the fluctuating pressures is valid. But as discussed in Chapters 1 & 5, and Appendix B, and confirmed with experimental data in Chapter 5, such an assumption is only valid for turbulence scale ratios $L_x/B>>1$ and then only for large wavelengths. An aerodynamic admittance function is usually employed to account for the losses in coherence of the eddies with high frequencies. Theories based on the quasi-steady assumption, such as Vickery's[80] lattice theory applied to bluff structures, tend to under-estimate consistently the drag spectra for turbulence scale ratios $L_x/B<1$ at the large wavelengths. This is because the structure distorts the turbulence such that the turbulence tends to increase in intensity as it approaches the structure. To investigate this situation in more detail than is possible with single point measurements, which was made in Chapter 5, the correlation between the incident turbulence and the fluctuating pressures was measured.

6.2 Measurements and Results

Two Scanivalves of the same type were used in the measurements of the fluctuating pressures and the plastic tubing used in all the models were of equal length, cut from the same consignment of plastic tube. This was to ensure that the pressure tube Scanivalve system was identical, within the frequency range of interest, for all the pressure taps thereby simplifying the correction procedure applied to the measured spectra. Calibration of the two Scanivalve systems confirmed that within the frequency range of interest the transfer function in Fig.20 was applicable to both. The correction procedure is described in detail in Appendix A.

The analogue electrical signals from the two pressure transducers, and when necessary from the hot-wire anemometer, were recorded simultaneously to retain the phase characteristics of the data.

The same recording and reproducing speeds and also the same analogue-to-digital conversion rates were used for the joint analysis as were used for the single point analysis in Chapter 5.

For the data processing 25,600 digitised data values for each signal were used. From these the co- and quad-spectral density and cross-correlation functions were computed. The cross-spectral density function as given by Equation 52 is complex and is normally reduced to form the coherence function (as expressed by Equation 55), which gives a measure of the spatial scale associated with fluctuating quantity for various frequencies.

The coherence may be thought of as a correlation between two signals in the frequency domain. More precisely it is a measure of the square of the correlation between the Fourier components of the two signals. The usual practice is to express the results as the square root of the coherence which gives a measure of the correlation between the two signals.

Signals from pairs of pressure tappings on the models for front face, rear face and front-rear face combinations were analysed, and the combinations were from both the mid-height and top level of the models. These two levels were chosen as producing representative results of the two different regions; the mid-height level for nominally two-dimensional flow and the top level for the three-dimensionality effect of the free end.

Lack of space prohibits including all the results and since for any model-grid configuration many are very similar in character, only a representative few will be presented for each case. The results for levels 3 and 9 are shown in Figs.41 & 42 for the front face combinations, Figs.43 & 44 for the rear face combinations and Figs.45 & 46 for the front-rear face combinations. Although both vertical and horizontal separations were investigated, only results from the horizontal separations are included. However, where applicable the vertical separation results will be used during the discussions.

Hot-wire measurements of the characteristics of incident turbulence at a few positions upstream of the stagnation line, at levels 3 & 9, were made to investigate the distortion of the turbulence in the proximity of the models. In order to achieve the experimental programme of work within the time scale, only a short time could be spent on this aspect of the problem and the experimental investigation was therefore limited to Grid 2 generated flow. Properties of the flow measured are shown in Figs.47 to 49, which include the mean velocity, intensity of turbulence, probability density function and the spectral density function of the longitudinal turbulence. In addition to these, measurements of the correlation between the turbulence and fluctuating pressures on the stagnation line were made and are shown in Figs.50 & 51 as cross-correlations and coherence functions.

6.3 Discussion of Results

In reviewing the results and their significance the following discussion has been divided into three parts so that the cross-correlation of pressures on the windward, leeward and between windward and leeward faces are covered separately. Other results including those from the velocity and velocity-pressure measurements will be included in the discussions where appropriate.

6.3.1 Windward face

The coherence measurements for the pressure fluctuations at levels 3 and 9 are shown in Figs.41 & 42 respectively, as a function of frequency n reduced by $r/\bar{U}$ where r is the spatial separation of the two points at which the pressures were measured. The peak coefficients of the cross-correlation function are listed in Table 6.

It has become almost standard practice in numerical analyses of unsteady pressure fields to approximate the coherence function by an exponential function of the form:

$$\gamma(n) = \exp\left[-C_y \cdot nr/\bar{U}\right] \qquad \ldots (74)$$

Equation 74 is popular, probably because of its simplicity. The value of its simplicity is however offset by the fact that it overestimates the coherence at low frequencies. Equation 74 tends to unity as the frequency tends to zero, whereas measured values in Figs.41 & 42 do not. In fact the measured values are seen to be a function of both $nr/\bar{U}$ and r/L_x, but there is no means of accounting for turbulence scale L_x in Equation 74.

Nevertheless, because Equation 74 is simple and widely used, an attempt to approximate it with the experimental data was made. Values for the decay constant C_y were determined for a number of model and grid combinations, the results are shown in Fig.52 plotted versus the separation distance r. The decay constant C_y was not determined for all model and grid combinations because visual inspection showed that the differences in experimental data for each separation distance r were small in comparison to the goodness of fit being achieved, particularly for small values of r. There are two points which are of significance arising from the results in Fig.52. The first is that the decay constant C_y is seen to be a function of the separation r and not a true constant as is often suggested by many workers. The value C_y is a measure of the effective gust width, but since the reduced frequency takes account of the spatial separation, as indicated in Equation 74, then there should be no significant variation in the results for any separation. The general assumption that the decay constant is invariant with spatial separation is however based on measurements of spatial correlations of velocity fluctuations in the atmosphere with separations generally much less than the turbulence scale[25,36], the results of which have been found to be adequately approximated by Equation 74.

The second point arising from Fig.52 concerns the general magnitude of the decay constants. It was found to increase in value from about 2 to 6 corresponding to r/B=0.2 to 0.8, and to be smaller than the generally accepted values of about 6-8 from wind structure data. In other words, the cross-correlation of the fluctuating pressures on the windward face are greater than that of the velocity fluctuations which generate them. It has generally been considered that they were identical, or very nearly, and assumed that observations from wind measurements could be adopted directly into analyses of wind loading of buildings. Although simple and convenient, such an assumption however makes no allowance for the fact that the mean and turbulent components of the wind will be distorted by a bluff body or a building, as demonstrated by the values in Fig.52. Hunt[78] in his theoretical treatment of the problem demonstrates that the coherence of the high frequency pressure fluctuations should be greater than the coherence of the high frequency components of the incident turbulence. He argues that the small eddies will be 'piled up' against the bluff body giving rise to fluctuating pressures with small magnitudes and higher coherence. The experimental results of this study, particularly the spectra in Fig.33 and coherence in Figs.41 & 42, are consistent with Hunt's predictions.

The problem of what is the value of the decay constant for the pressure correlations, is further complicated by the different values reported in the literature for both full-scale and wind tunnel measurements. Newberry et al[15], from full-scale measurements on Royex House found $C_y = 4.3 \pm 1.1$. This is lower than the value of $C_y = 7.7 \pm 2.6$ found by Dalgleish et al[81] from their full-scale measurements and in contrast to results from wind tunnel tests reported by Kao[82], and Vickery & Kao[83] which indicate that a similar value for the decay constant can be assumed for the pressure fluctuations as for the incident turbulence. The exponential decay value C_y of wind measurements has been found to be sensitive to atmospheric stability[37] which may account for discrepancies in C_y values for pressure correlation from full-scale measurements but not for the wind tunnel tests. Discrepancies in C_y values from full-scale measurements may also be attributed to the size and shape of the buildings. The buildings in Refs.15 & 81 are both situated in a city environment, and from Ref.33 it is estimated that they will both have L_x/B of approximately 2 to 4; this should therefore not account for the difference in C_y. Both buildings are rectangular in cross-section; however, Royex House[15] has a height/breadth ratio of only 1.5 in comparison to 5.7 for the other building[81], which will result in two different flow fields and possibly different C_y values.

Alternatives to the empirical relationship of Equation 74 for the coherence function, and based on physical arguments, are the expressions derived by Vickery[80] and Harris[35] for the special case of homogeneous isotropic turbulence (HIT). Vickery used the Dryden correlation function:

$$R(r) = \exp\left[-r/L_x\right] \qquad \text{... (75)}$$

whereas Harris based his analysis on the reduced spectrum he had proposed earlier (§1.2.2 Equation 16). Both produce very similar results but for this study the coherence function was derived in Appendix C using the von Karman spectrum (Equation 17) which was shown in Chapter 4 to accurately model the experimental observations.

The general outcome from all three analyses is that the coherence function could be expressed in terms of a single parameter, η, where:

$$\eta = f\left(\frac{r}{L_x}, \frac{nL_x}{\bar{U}}\right) \qquad \text{... (76)}$$

and, whereas Equation 74 tends to unity when n tends to zero, η does not - it tends to $c \cdot r/L_x$; where c is a constant, the value of which depends upon which analysis is used.

Using von Karman's spectrum the theoretically derived coherence are shown, for comparison with experimental values, in Fig.41. In general, the behaviour of the theoretical results at long wavelengths is similar to that of the experimental results. They do not collapse to a common curve, as predicted by Equation 74 but attain a definite maximum which decreases with increasing values of separation, r. For eddies with smaller wavelengths the theoretical analysis correctly predicts that the coherence will progressively decrease. At the small wavelengths the theory predicts that the coherence is independent of separation r and the results collapse to a common curve. The general trends observed in Fig.41 also help to explain how for atmospheric measurements, where r/L_x is usually O(0.1), the empirical expression of Equation 74 appears to be valid.

Although the theory in Appendix C correctly predicts the overall behaviour of the measured coherence it does not achieve great accuracy. In nearly all cases the predicted values at the long wavelengths are smaller than the measured. The exceptions were $r/B = 0.375$, 0.5 and 0.75 with $L_x/B = 1.98$. For the smallest turbulence scale, $L_x/B = 0.57$, the measured values are drastically under-estimated, and the discrepancy progressively gets worse with increased separation, r. At the shorter wavelengths, even with $L_x \approx 2B$ and the smallest separation, $r \approx 0.125B$ the measured values are still under-estimated. The theory tends to predict a faster drop-off rate for the coherence at the short wavelengths than is observed from measurement. It of course makes no allowance for the distortion caused by the models to the turbulence, the effects of which on the coherence were discussed earlier. The derivation in Appendix C is based on the assumption that the turbulence is HIT, which is only valid at the short wavelengths. Full details about HIT, including its limitations are in Refs.29 & 71.

In general therefore, although HIT predicts results which are consistent in behaviour with experiments, particularly good agreement has been achieved with atmospheric measurements[35], it requires further development to achieve the accuracy necessary in analyses of wind loading of buildings. Such development was considered to be outside the scope of this study.

The influence that a two-dimensional bluff body has in modifying the incident turbulence has been investigated theoretically by Hunt[46] and experimentally by Petty[84] and Bearman[77], whose experimental results are shown reproduced in Fig.39. A similar but limited investigation was made of the approach flow in the present study. A hot-wire anemometer upstream of the stagnation line of the model was used to measure the mean and fluctuating components of the longitudinal turbulence. The results are shown in Figs.47 to 49, where it is observed that the incident turbulence is affected by the presence of the model. The velocity fluctuations are attenuated as the model is approached and the turbulence progressively deviates from a Gaussian distribution, with large negative values of skewness and increasing values of Kurtosis. There is some indication of the fluctuations being amplified at $x/B = -0.5$; however, this is only slight and it is occurring at a position much further from the model than would be expected, using measurements by Petty and Bearman. In the present study the flow was surveyed using coarse incremental spacing, therefore the observed trend has to be viewed with this in mind. In general, the results conform with observations by Petty and Bearman for comparable turbulence scale/model size ratio, L_x/B.

Comparing the spectra of the u-component of turbulence in Fig.48 for different positions upstream of the model shows that there is a significant redistribution of energy taking place as the flow approaches the model, with the proportion being increased at the short wavelengths.

In addition to the point measurements, cross-correlations of the u-component of turbulence at a number of positions upstream of the model, and the fluctuating pressures on the stagnation line of the model were determined. Typical coherence results, obtained for the mid-height and top level of the models, are presented in Figs.50 & 51, respectively. It is observed that although the coherence is fairly constant for large wavelengths, it is not unity and the correlation is increased for larger separations. With the hot-wire at an upstream distance of $x/B = -1.0$ the $(\text{coherence})^{\frac{1}{2}}$ is about 0.9. This trend is comparable with results reported by Kao[82] for a two-dimensional model in turbulent flow. He measured turbulence upstream of a model of square cross-section at distances of $x/B = -1.0$, -1.25 and -4.0, and found that there was very little variation in the coherence for the u-component of turbulence and fluctuating pressures, at the three upstream positions. There is, however, some doubt about the reliability of Kao's results since he obtained values for the coherence function greater than unity. Since it is not possible for two signals to be more than fully correlated (i.e. $\gamma(n) \ngtr 1.0$), such a result indicates that there must have been an error in his data processing.

An alternative to the cross-correlation approach for relating the fluctuating pressures to the incident turbulence is the aerodynamic admittance approach. In Chapter 5, the concept of an aerodynamic admittance function $\chi_a^2(n)$ was introduced to account for the fact that there is a progressively more rapid loss of correlation for eddies with shorter wavelengths. For the fluctuating pressure at the stagnation line, recovered directly from the incident turbulence, the admittance function $\chi_a^2(n)$ in Equation 69 was the ratio of pressure spectrum to free stream turbulence spectrum non-dimensionalised by $\rho^2\overline{U}^2$. The admittance functions for the pressure spectra in Fig.33 from model mid-height stagnation point 304 have been determined for each turbulence scale using the turbulence spectra in Fig.25, and the results are shown in Fig.53. Many difficulties were experienced in obtaining the admittance values, principally because the pressure and velocity spectra data points were not coincident at the discrete wavelengths, which meant that data values had to be interpolated for selected wavelengths. Combined with the fact that the scatter in the two spectra tended at times to amplify the scatter in admittance values the result achieved was not considered to be totally successful. Nevertheless, there are a few interesting observations which can be made. The first is that the admittance values are not fully correlated at large wavelengths and the maximum correlation occurs at wavelengths of about 10B. Secondly, although the measured $\chi_a^2(n)$ do exhibit a loss in correlation and generally approach zero at very small wavelengths, the admittance values are not solely a function of reduced frequency $nB/\overline{U}$, and independent of L_x/B as proposed by Hunt[78]. Measurements by Bearman[86], however, of $\chi_a^2(n)$ for fluctuating drag of square flat plates generally substantiate Hunt's proposal by demonstrating that $\chi_a^2(n)$, for a range of L_x/B values at high values of $nB/\overline{U}$ do collapse to a common curve. It must be remembered, however, when making comparisons of $\chi_a^2(n)$ for pressure fluctuations with those for drag fluctuations that the spatial correlation of the pressures must also be considered.

Finally, it is observed that for the results in Fig.53 there is no apparent systematic trend with increasing turbulence scale. This is surprising as it had been expected that at large wavelengths with $L_x > B$ the flow would be approximately quasi-steady and with smaller values of L_x/B there would be a reduction in $\chi_a^2(n)$.

Cook[53], in his investigations, also reported that measurements of $\chi_a^2(n)$ for pressure fluctuations on the stagnation line of models of buildings with square section indicated a maximum occurring at $nB/\bar{U} \approx 0.1$, but in contrast to the results from the present study he found that $\chi_a^2(n)$ was independent of turbulence scale for $nB/\bar{U} > 0.1$.

During similar comparison of measured $\chi_a^2(n)$, but for fluctuating drag of flat plates, Bearman[86] also found that there was not total agreement with reported $\chi_a^2(n)$. He suggested that the reasons may be due to the accuracy of the experiments, which may also account for the present discrepancies discussed above. The fact that there is only a small number of measured $\chi_a^2(n)$ reported in the literature may be indicative of the difficulty in accurately measuring $\chi_a^2(n)$, which is substantiated by this study.

Three-dimensionality of the flow at the top of the model and its effect on the velocity-pressure correlations can be assessed by comparing the results from the top of the model with those from the mid-height level in Fig.51. The differences between the two flow regimes, as reflected in the coherence plots, are seen to be mainly on two aspects. The first is that the coherence at the mid-height level is fairly constant for reduced frequencies up to about 0.2 whereas for level 9 the coherence is flat up to about 0.1. This means that the unsteady wind loads on the windward face at the mid-height and the incident turbulence can be approximated by a linear relationship for wavelength/model size ratios greater than about 5, whereas for the top levels this is true for ratios greater than about 10.

The second point concerns the correlations at the small wavelengths. For the mid-height level the coherence could be approximated by an exponential decay curve whereas for the top level of the model this is not the case. Here the correlaions, in some instances, are found to increase slightly in value at wavelengths less than about 20B. This is due to the asymmetry of the cross-correlation function, the magnitude of the quadrature spectra of the velocity-pressure cross-spectra are not zero and were found to be about the same magnitude as the co-spectra.

The flow regime at the top of the models has a vertical component due to the flow over the free-end, which reduces the distortion of turbulence since the w-component of turbulence is not affected to the same extent by vortex stretching. In fact, whereas the w-component of turbulence at the mid-height region is expected to be amplified near the model, at the top levels it will probably be attenuated but depends on L_x/B. This conclusion is drawn from comparisons made between the v- and w-components of turbulence measured by Petty[84] and Bearman[77], whose results are shown reproduced in Fig.39.

The difference between the flows at the top and mid-height regions of the models will also be manifested in the cross-correlation measurements for the pressure fluctuations at levels 3 and 9. Comparing the coherence of pressure fluctuations in Figs.41 & 42 it is found that in all cases the pressures at model mid-height are slightly better correlated than those from similar positions at the top of the model, except at the high wave numbers. For pressure taps with vertical separations the pressure fluctuations are better correlated at the long wavelengths than those with lateral separations. Typical results are shown in Fig.54 for vertical separations of $r/B = 0.5$ and 1.0. Using the exponential function in Equation 74 to represent the behaviour of the coherence measurements in Fig.54 the best fit to the data is achieved with values for the decay constant c_z of about 4.9 and 6.0 for spatial separations of $r/B = 0.5$ and 1.0 respectively. These c_z values fall in between the 3.2 and 10.3 shown by Newberry[15] and Dalgleish[81] for their full-scale measurements, and are on the lower limit normally quoted for velocity correlations from atmospheric measurements. Comparing these c_z values with the results for lateral separations in Fig.52 it is found that they are within the experimental scatter. It had been expected that they would have been smaller in value because of the high frequency eddies being 'piled up' at the stagnation line giving rise to fluctuating pressures with small magnitude and higher coherence. The differences may have been obscured by the experimental scatter.

The general effect of increasing the turbulence scale L_x should be to improve the cross-correlation of the pressure fluctuations. From the results in Figs.41 & 42 this was found to be the case at both the top and mid-height region of the model. An increase in the spatial correlation of the fluctuating pressures, when integrated over the area of the building would result in increased loading, hence increased deflections, stresses, etc. experienced by the building. No attempt has been made to quantify what the significance of the observed differences in the cross-correlations has on the along-wind response; the reason being that the differences are small and the errors that would be introduced into the calculations by attempting to describe the coherence results using a universal function (for example Equation 74 or HIT theory) would invalidate any conclusions drawn from the results of the computation.

Finally, there were no effects on the windward face pressure correlations which could be attributed to having been caused by model geometry.

6.3.2 Leeward face

The coherence measurements for the pressure fluctuations on the leeward face at levels 3 and 9 are shown in Figs.43 & 44 respectively and the peak coefficients of the cross-correlation functions are listed in Table 7.

At model mid-height the pressure correlations, particularly for the pressure taps near the edges, are seen to be influenced by vortex shedding. There is strong correlation between the pressures at the vortex shedding frequency, the strength of the correlation being a function of both model geometry and turbulence scale. These effects are better illustrated in Fig.55 where all the results from the nine model-grid combinations are shown together for pressure tap pairs 13-19, 14-18 and 15-17.

Model 2, with section ratio B/D = 2, is seen to produce the strongest correlations at the vortex shedding frequency whilst in general Model 1 with section ratio B/D = 4 the weakest. Increasing the scale of turbulence improves the correlation, presumably by the formation of more coherent vortices. In Chapter 5 it was argued that the base pressure increased when the ratio of turbulence scale to model size was reduced because of increased rate of entrainment of the shear layers which reduced the radius of curvature of the shear layers and significantly altered the wake width. Increased rate of entrainment of the shear layers has also been found tends to thicken the shear layers more rapidly causing them to dissipate energy by generating turbulence soon after separation and the formation of weaker vortices. It is suggested that this mechanism is also responsible for the reduction in the correlations at the vortex frequency with $L_x<B$. The effects of model geometry on the correlations can similarly be explained in terms of shear layer and after body interaction, and vortex formation using the arguments in Chapter 5.

The shed vortices are not contained within a narrow frequency band as is the case with smooth flow, the free stream turbulence has caused the, normally periodic and coherent, shedding of vortices to break down into the broad range of shedding frequencies which is apparent in Figs.33 and 34.

It should be noted that it is the normalised co-spectrum, not the square root of the coherence function, which affects the dynamic wind loading in the along-wind direction (see Appendix B). The assumption commonly made that the two functions are nearly identical was found to be generally valid for the windward face but comparing typical measurements for the two functions in Fig.56 it is seen that for the leeward face this is not the case.

The negative values for the normalised co-spectrum at the vortex shedding frequency suggests that there are strong fluctuating crosswind and torsional forces acting on the models. For pairs of pressure taps further towards the centre of the leeward face the normalised co-spectrum at the vortex shedding frequency increases from large negative values to nearly zero, whilst at twice the vortex shedding frequency it has increased in value from about zero to about 0.8 for pressure taps 15-17.

At level 9 the correlations at the vortex shedding frequency are not discernible from broad band random fluctuations. At the top region of the models the low pressure in the wake bleeds in air from the free stream, over the free end, inhibiting the shear layers from forming into coherent vortices. It is only with $L_x/B \approx 2.0$ that there is any evidence of vortex shedding at the Strouhal number.

The empirical relationships given by Equations 74 & 76 or that by Vellozzi and Cohen[18] do not adequately describe the coherence measurements at model mid-height for the leeward face. This is not surprising since such expressions were not completely satisfactory when applied to the windward face data, and the leeward face data has the complication that the wake pressure is a function of both model geometry and free stream flow conditions.

The observations of coherence for level 9 differ from those for level 3 with the coherence measurements for wavelengths larger than 4B collapsing to a common curve and the pressure fluctuations being very nearly fully correlated. There is, however, a small but discernable reduction in the correlation with decreased model depth, and is particularly evident for large spatial separations. For wavelengths less than 4B the coherence values progressively decrease but the high variability at these frequencies makes it impractical to establish precisely what effect, if any, turbulence scale, model geometry or spatial separation are having. From the general characteristics of the curves in Fig.44 the coherence appears to have been reduced to a common curve with a broad band of scatter. To test whether a simple empirical relationship, such as the exponential function given by Equation 74, would adequately describe the curve, data from Model 1 (B/D = 4) with $L_x/B = 0.57$ was replotted using log-linear scales and the decay constant, C_y, determined. A mean value of about 4 was obtained with upper and lower limits of about 6 and 2.5, respectively for the band of scatter. It was found however that the exponential function could not be made to apply over the entire frequency band. Up to reduced frequencies of about 0.05 the exponential function under-estimates the experimental data, and although at the higher frequencies the data falls within the lower and upper limits defined by $C_y = 2.5$ and 6, the general trend is the experimental data decreases at a faster rate than predicted.

Similar to the windward face pairs of pressure taps with vertical separations are found to have poorer correlated pressures than those from lateral separations. Typical results are shown in Fig.57 for vertical separations of $r/B = 0.5$ and 1.0. Using the exponential function to represent the behaviour of the coherence data the best fit is achieved with $C_z = 6.8$ for $r/B = 0.5$. For $r/B = 1.0$ it was found to be impractical to use Equation 74 and no value was determined.

The general effect of turbulence scale and model geometry at large wavelengths are fluctuating pressures at level 3 on Model 1 ($B/D=4$) are the highest correlated whilst those on Model 3 ($B/D=1$) are the lowest. The exception is with the combination Model 2 ($B/D=2$) and $L_x/B \simeq 2$ which produces the lowest correlation. In all other combinations $L_x/B \simeq 2$ produced the highest correlations and $L_x/B \simeq 0.5$ the lowest.

For measurements from the top level of the models the results for large wavelengths are summarised as $L_x/B \simeq 0.5$ producing the highest correlations and $L_x/B \simeq 1$ the lowest. This is significantly different to the above observations for level 3 and also to those on the windward face which experienced the highest correlations with $L_x/B \simeq 2$ and the lowest with $L_x/B \simeq 0.5$. In making comparisons with the windward face measurements it is noted that the pressures on the leeward face are generally better correlated. For a given scale of turbulence, at level 9 on the leeward face, Model 3 ($B/D=1$) experiences the highest correlations and Model 1 ($B/D=4$) the lowest.

6.3.3 Windward-leeward face correlations

Measurements of cross-spectra between fluctuating pressures on the two faces have been normalized to the coherence function and are shown in Figs.45 & 46 for levels 3 and 9, respectively. Peak coefficients of the cross-correlation functions are listed in Table 8.

For the frequency range investigated ($0.01<nB/\bar{U}<1$) there is no apparent trend which suggests there is a continued loss in spatial correlation with increasing wavenumber. The measurements in fact appear to be quite intractable and in general the coherences are low in comparison with those from the windward and leeward faces discussed earlier. It is envisaged that if the frequency range was to have extended to include very much longer wavelengths, the coherence measurements would have shown signs of increasing in value. This, however, would have no significant consequence to the outcome from calculations of wind loads on buildings, since for most tall buildings their natural frequency, n_o, or more precisely their reduced frequency, $n_oB/\bar{U}$, will be within the range examined, or higher. Therefore, the contribution from the cross-correlation of forces between the two faces, towards the dynamic loading at the resonant frequency, can be determined and the contribution from the cross-correlation of forces from the two faces to the quasi-steady along-wind response will be negligible, relative to the contributions from the windward and leeward faces.

The coherence data in Figs.44 & 45 are for the four pressure taps from the centre of the front face towards the corner, paired with the pressure taps directly opposite on the leeward face. For each of the nine model/grid combinations there are differences between the coherence from each pair of pressure taps but because of the variability interpretation of these is impossible. Therefore, a generalisation of the results is made so that overall trends and general differences can be made between the nine model/grid combinations permitting conclusions of the effects of section ratio and turbulence scale.

At model mid-height the coherence values do not vary to any set pattern and can be considered to be approximately uniform within the frequency range examined. On this basis, Model 1 ($B/D=4$) with turbulence scale ratios $L_x/B \simeq 0.5$ and 1.0 has the strongest correlations and Model 3 ($B/D=1$) the weakest. With the largest turbulence scale examined $L_x/B \simeq 2.0$ the strongest correlations are from Model 2 (B/D=2) and the weakest is again with Model 3. In general the strongest correlations, surprisingly, are with the smallest turbulence scale, $L_x/B \simeq 0.5$. The exception is with the combination B/D=2 and $L_x/B \simeq 2.0$, where there is an increase in correlation at the vortex shedding frequency. A few other combinations also exhibit an increase in correlation at the vortex shedding frequency but they are generally only slight.

At the top level of the model the coherence is found to increase in value over a very broad frequency band at the short wavelengths and has a maximum occurring at about a reduced frequency of $nB/\bar{U} \simeq 0.4$. At this frequency there was also a slight increase in the energy level with some pressure spectra in Fig.34, particularly evident for the leeward face. The physical cause of these observations is not known for certain but a possible explanation is that they are due to vortices being shed from the model free-end. If it is caused by vortex shedding, then from the spectra and cross-correlations, including those from Fig.44, it is concluded that they must be very broad band in character and not very coherent. In this broad frequency band the effect of increasing the section ratio, B/D, is to improve the correlation. The general effect of turbulence scale is not so straightforward with $L_x/B \simeq 0.5$ and 2.0 producing very similar results and $L_x/B \simeq 1.0$ resulting in the weakest correlations.

At longer wavelengths the effect of turbulence scale is to increase correlation as turbulence scale ratio is increased in value.

The peak coefficients of the cross-correlation function, of pressures on the centre line, from Table 8 have been plotted and the distributions are shown in Fig.58. These graphically illustrate some of the general observations which have been made and discussed above.

Correlations between the incident turbulence and pressure fluctuations on the leeward face have not been presented because the results were found to be virtually identical to the windward-leeward pressure correlations and therefore would have contributed very little new information.

CHAPTER 7

DISCUSSION AND FINAL CONCLUSIONS

7.1 General Discussion

Buildings are, aerodynamically, bluff bodies and as such analytical solutions of the flow field around them and therefore the pressures, loads, deflections, etc. that they experience are not generally feasible. The lattice theory proposed by Vickery, when applied to bluff bodies is found to agree with experimental observations for $L_x \gg B$, but for $L_x/B = O(1)$ the theory consistently under-estimates the measured values, particularly at the long wavelengths. It was assumed that HIT theory was applicable to the incident turbulence of a bluff body but as demonstrated in Chapter 6, for the cross-correlation of pressures, this was not a valid assumption.

A more mathematically precise approach to the problem by Hunt correctly predicts the general behaviour of dynamic wind loads on the windward face of bluff bodies. Results from Hunt's analytical model have furthered the understanding of the mechanisms involved and as such has opened up avenues for investigation of a very complex process. However, even if the refinement and development of this, or any other, analytical model is ever fully realised, which is doubtful, it will probably not be accepted by designers because of its complexity.

The author considers that the simpler gust factor approach will become more widely accepted and is also more suited to building Codes of Practice. The main purpose of this research has therefore been to provide experimental information on the effects of turbulence scale on wind loading and the cross-correlation of fluctuating pressures on faces of tall buildings in order to improve present Codes of Practice and future design of tall buildings.

7.2 Conclusions

The main conclusions to be drawn from the experimental work were as follows:

(1) The pressure fluctuations on the windward face were recovered directly from the incident turbulence with an average pressure coefficient of about 0.85, whereas those on the leeward face were a function of wake characteristics.

(2) Both the mean and fluctuating components of surface pressure on the leeward face are strongly dependent on turbulence scale. The effect is for the base pressure coefficient to decrease from about -0.4 to -0.7 and the magnitude of the pressure fluctuations to increase as L_x/B is increased from about 0.5 to 2.0. For the top half of the models the lowest base pressure is achieved when the turbulence scale ratio L_x/B is about 1.0.

(3) The current UK Code of Practice recommends using drag coefficients which could significantly under-estimate the total wind load on a tall building, particularly for buildings with section ratios B/D=1 to 2.

(4) Measurements of pressure coherence on the windward face show that the coherence does not tend to unity for very long wavelengths unless $r \ll L_x$ and the simple exponential function proposed by Davenport is found in general not to be adequate. The coherence is not solely a function of $nr/\bar{U}$ but also r/L_x.

With the best fit to the exponential function the empirical constant for the pressure coherence is smaller in value than the commonly accepted values. These values however have principally been based on the assumption that results from atmospheric measurements are directly applicable to buildings. The results from this investigation and that from Royex House indicate that the scale of gusts on the building is much larger than the undisturbed wind and is due to a cushioning effect on the front of the building.

HIT theory correctly predicts the observed trends but the results are not within acceptable accuracy. It is the author's opinion that with suitable modification to account for the cushioning effect, this theory could also provide accurate results and would prove a useful analytical model.

(5) The coherence between pressures on the windward and leeward faces is only weakly dependent on turbulence scale and section ratio and can be considered to be approximately 0.3 and constant for wavelengths 1B-100B. With typical values of $C_{p_\omega} = 0.85$ and $C_{p_\ell} = -0.72$ the cross-correlation function $\chi_a^2(n)$ is estimated to be about 0.65.

For a typical building with height of 184 m, breadth of 73 m, natural frequency 0.2 Hz and damping of 0.01 situated in a city environment, the British Code of Practice[8] gives $C_{p_\omega} = 0.8$ and $C_{p_\ell} = -0.25$, hence $\chi_a^2(n)$ is determined to be approximately 0.75. The gust response factor G, computed in accordance with Davenport's[50] method, is 2.4.

7.3 Future Research

At present it is considered that there is insufficient data with which to validate design calculations. The results contained in this thesis provide some of this information but these and other results from wind tunnel investigations need to be validated against full scale measurements. It is only in recent years that data handling systems have been developed to the level where the volume of data involved in carrying out this type of measurement programme in a full scale investigation can practicably be managed.

Systematic wind tunnel testing of aeroelastic models is also necessary to determine the accuracy of dynamic calculations.

Table 1

Typical values of surface roughness length, Z_o, and power law exponent, α, for various types of terrain

Type of terrain	Z_o (m)	α
Mud flats, ice	$10^{-5} - 3.10^{-5}$	
Smooth sea	$2.10^{-4} - 3.10^{-4}$	
Sand	$10^{-4} - 10^{-3}$	0.10
Snow surface	$10^{-3} - 6.10^{-3}$	
Mown grass	$10^{-3} - 10^{-3}$	0.13
Low grass, steppe	$10^{-2} - 4.10^{-2}$	
Fallow field	$2.10^{-2} - 3.10^{-2}$	
High grass	$4.10^{-2} - 10^{-1}$	0.19
Palmetto	$10^{-1} - 3.10^{-1}$	
Forest and woodland	$10^{-1} - 1$	
Suburb	1 - 2	0.32
City	1 - 4	

Table 2

Dimensions of turbulence generating grids

Grid	M	b	d
1	247	45	19
2	495	95	19
3	740	133	19

(all dimensions in mm)

d-bar depth

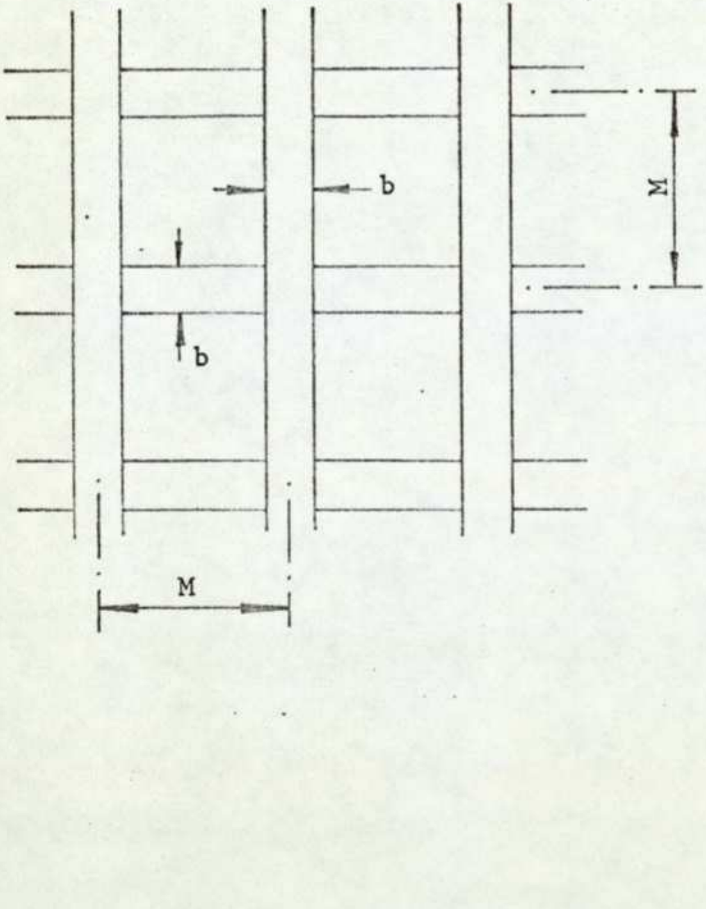

Table 3

Scales and intensities of grid generated turbulence

Grid	x/b	I_u	L_x (mm)
1	34.2	0.13	54
	45.6	0.10	58
	56.9	0.08	56
	68.3	0.07	59
2	30.5	0.21	103
	41.9	0.15	100
	53.3	0.11	116
	64.8	0.09	124
3	19.9	0.16	194
	29.7	0.12	184
	37.9	0.10	198
	49.3	0.08	206

Table 4

Skew and Kurtosis for pressure fluctuations on level 3

Pressure taps	Grid 1 (L_x=0.57B)		Grid 2 (L_x=1.0B)		Grid 3 (L_x=1.98B)	
	Skew	Kurtosis	Skew	Kurtosis	Skew	Kurtosis
Model 1 (B/D=4)						
01	0.123	3.51	0.430	3.27	0.369	3.18
02	0.136	3.50	0.508	3.56	0.324	3.02
03	0.219	3.21	0.511	3.36	0.394	3.22
04	0.202	3.21	0.526	3.41	0.364	3.22
13	-0.415	4.22	-0.230	4.15	0.042	3.87
14	-0.278	3.97	-0.076	3.95	0.024	3.94
15	-0.110	3.71	+0.059	3.89	0.049	3.59
16	-0.003	3.70	+0.046	3.89	-0.048	3.74
Model 2 (B/D=2)						
01	0.193	3.14	0.459	3.40	0.365	3.35
02	0.158	3.12	0.521	3.36	0.352	3.19
03	0.206	3.02	0.529	3.41	0.389	3.24
04	0.213	3.11	0.485	3.51	0.394	3.17
13	-0.632	4.46	-0.666	4.83	-0.789	4.71
14	-0.460	4.27	-0.444	4.76	-0.771	4.99
15	-0.317	4.16	-0.201	4.16	-0.500	4.58
16	-0.191	4.00	-0.068	4.33	-0.318	4.45
Model 3 (B/D=1)						
01	0.150	3.10	0.354	3.32	0.300	3.18
02	0.246	3.24	0.329	3.26	0.359	3.25
03	0.199	3.22	0.384	3.27	0.381	3.22
04	0.192	3.24	0.350	3.22	0.379	3.17
13	-0.691	4.19	-0.432	3.62	-0.823	4.56
14	-0.697	4.58	-0.309	3.64	-0.714	4.67
15	-0.605	4.45	-0.226	3.76	-0.529	4.29
16	-0.514	4.09	-0.044	3.36	-0.574	4.28

Table 5

Skew and Kurtosis for pressure fluctuations on level 9

Pressure taps	Grid 1 (L_x=0.57B)		Grid 2 (L_x=1.0B)		Grid 3 (L_x=1.98B)	
	Skew	Kurtosis	Skew	Kurtosis	Skew	Kurtosis
Model 1 (B/D=4)						
01	0.399	3.30	0.372	3.40	0.306	3.09
02	0.302	3.25	0.429	3.54	0.343	3.22
03	0.369	3.27	0.392	3.41	0.367	3.25
04	0.373	3.31	0.431	3.48	0.344	3.20
13	-0.097	2.77	-0.215	3.14	-0.273	3.22
14	-0.161	3.03	-0.310	3.34	-0.271	3.12
15	-0.131	2.96	-0.228	3.21	-0.276	3.10
16	-0.129	2.84	-0.267	3.44	-0.390	3.19
Model 2 (B/D=2)						
01	0.367	3.30	0.323	3.22	0.318	3.16
02	0.380	3.25	0.361	3.31	0.392	3.38
03	0.352	3.23	0.394	3.31	0.365	3.16
04	0.393	3.31	0.374	3.31	0.376	3.30
13	-0.272	3.26	-0.384	3.67	-0.478	3.67
14	-0.315	3.35	-0.313	3.48	-0.363	3.66
15	-0.312	3.34	-0.329	3.65	-0.381	3.47
16	-0.370	3.37	-0.077	3.44	-0.337	3.38
Model 3 (B/D=1)						
01	0.319	3.23	0.530	3.49	0.325	3.25
02	0.382	3.28	0.271	3.25	0.315	3.19
03	0.419	3.29	0.374	3.36	0.396	3.31
04	0.418	3.31	0.434	3.32	0.410	3.29
13	-0.348	3.27	-0.183	3.38	-0.351	3.31
14	-0.295	3.04	-0.374	3.52	-0.395	3.40
15	-0.300	3.17	-0.367	3.45	-0.417	3.40
16	-0.344	3.23	-0.405	3.43	-0.416	3.36

Table 6

Peak cross-correlation coefficients of leeward face pressure fluctuations

	Pressure taps	Separation $\delta y/B$	Grid 1 (L_x=0.57B)			Grid 2 (L_x=1.0B)			Grid 3 (L_x=1.98B)		
			Model 1 B/D=4	Model 2 B/D=2	Model 3 B/D=1	Model 1 B/D=4	Model 2 B/D=2	Model 3 B/D=1	Model 1 B/D=4	Model 2 B/D=2	Model 3 B/D=1
Level 3	01-07	0.75	0.47	0.56	0.40	0.56	0.52	0.59	0.58	0.43	0.42
	02-06	0.50	0.72	0.73	0.72	0.80	0.78	0.75	0.82	0.78	0.79
	03-05	0.25	0.92	0.92	0.91	0.94	0.93	0.93	0.95	0.94	0.94
	04-01	0.375	0.81	0.79	0.78	0.88	0.77	0.02	0.84	0.81	0.79
	04-02	0.25	0.92	0.91	0.90	0.92	0.73	-0.10	0.94	0.93	0.93
	04-03	0.125	0.97	0.97	0.97	0.98	0.89	-0.09	0.98	0.98	0.98
Level 9	01-07	0.75	0.38	0.34	0.30	0.46	0.38		0.50	0.47	0.45
	02-06	0.50	0.64	0.62	0.60	0.70	0.67		0.75	0.76	0.75
	03-05	0.25	0.85	0.86	0.85	0.89	0.88		0.92	0.92	0.92
	04-01	0.375	0.74	0.72	0.69	0.75	0.70		0.82	0.82	0.80
	04-02	0.25	0.86	0.85	0.85	0.89	0.82		0.92	0.92	0.92
	04-03	0.125	0.95	0.95	0.96	0.96	0.83		0.98	0.97	0.97

Table 7

Peak cross-correlation coefficients of leeward face pressure fluctuations

	Pressure taps	Separation $\delta y/B$	Grid 1 (L_x=0.57B)			Grid 2 (L_x=1.0B)			Grid 3 (L_x=1.98B)		
			Model 1 B/D=4	Model 2 B/D=2	Model 3 B/D=1	Model 1 B/D=4	Model 2 B/D=2	Model 3 B/D=1	Model 1 B/D=4	Model 2 B/D=2	Model 3 B/D=1
Level 3	13-19	0.75	0.28	0.14	0.02	0.12	-0.14	-0.14	0.06	-0.32	-0.10
	14-18	0.50	0.49	0.27	0.23	0.39	0.16	0.15	0.33	-0.05	0.13
	15-17	0.25	0.74	0.73	0.64	0.76	0.59	0.58	0.69	0.46	0.60
	16-13	0.375	0.68	0.57	0.57	0.61	0.40		0.56	0.34	0.54
	16-14	0.25	0.80	0.73	0.72	0.80	0.55		0.71	0.56	0.69
	16-15	0.125	0.91	0.90	0.89	0.90	0.71		0.90	0.83	0.88
Level 9	13-19	0.75	0.85	0.70	0.60	0.82	0.59		0.72	0.40	0.46
	14-18	0.50	0.90	0.80	0.70	0.87	0.66		0.84	0.61	0.63
	15-17	0.25	0.95	0.89	0.85	0.91	0.79		0.92	0.85	0.85
	16-13	0.375	0.93	0.83	0.75	0.88	0.66		0.88	0.75	0.80
	16-14	0.25	0.95	0.90	0.84	0.92	0.76		0.94	0.84	0.87
	16-15	0.125	0.98	0.96	0.93	0.94	0.94		0.97	0.95	0.95

Table 8

Peak cross-correlation coefficients of windward-leeward face pressure fluctuations

		Grid 1 (L_x = 0.57B)			Grid 2 (L_x = 1.0B)			Grid 3 (L_x = 1.98B)		
	Pressure taps	Model 1 B/D=4	Model 2 B/D=2	Model 3 B/D=1	Model 1 B/D=4	Model 2 B/D=2	Model 3 B/D=1	Model 1 B/D=4	Model 2 B/D=2	Model 3 B/D=1
Level 3	01-19	0.11	0.10 -0.08	-0.06	0.07 -0.09	0.13 -0.10	-0.11	-0.12	-0.19	-0.15
	02-18	0.15 -0.13	0.08 -0.17	-0.10	0.06 -0.10	0.07 -0.10	-0.10	-0.17	-0.17	-0.11
	03-17	-0.16	0.08 -0.16	-0.15	-0.14	0.09 -0.13	-0.19	-0.18	-0.14	-0.18
	04-16	0.14 -0.16	-0.20	-0.15	-0.17	-0.17	-0.21	-0.21	-0.17	-0.21
Level 9	01-19	0.08	0.12	-0.25	0.14	0.11	0.25	-0.18	-0.18	-0.17
	02-18	0.10 -0.11	0.08 -0.09	-0.11	0.15	0.11	-	-0.23	-0.25	-0.26
	03-17	0.12 -0.11	-0.13	-0.14	0.14 -0.12	0.10 -0.13	-0.14	-0.27	-0.24	-0.22
	04-16	0.08 -0.06	0.11 -0.08	-0.13	0.13 -0.15	0.10 -0.11	-0.17	-0.26	-0.24	-0.27
Pressure Taps 04-16	Level 3	0.14 -0.16	-0.20	-0.15	-0.17	-0.17	-0.21	-0.21	-0.17	-0.21
	Level 4	-0.21	-0.19	-	-0.19	-0.16	-0.20	-0.18	-0.15	-0.18
	Level 5	-0.24	-0.17	-0.16	-0.22	-0.15	-	-0.24	-0.18	-0.22
	Level 7	-0.13	-0.17	-0.19	-0.25	0.14 -0.16	-0.35	-0.28	-0.25	-0.30
	Level 8	-0.15	-0.14	-0.19	-0.20	-0.18	-0.29	-0.32	-0.24	-0.34
	Level 9	-0.06	0.11 -0.08	-0.13	0.13 -0.15	0.10 -0.11	0.17	-0.26	-0.24	-0.27

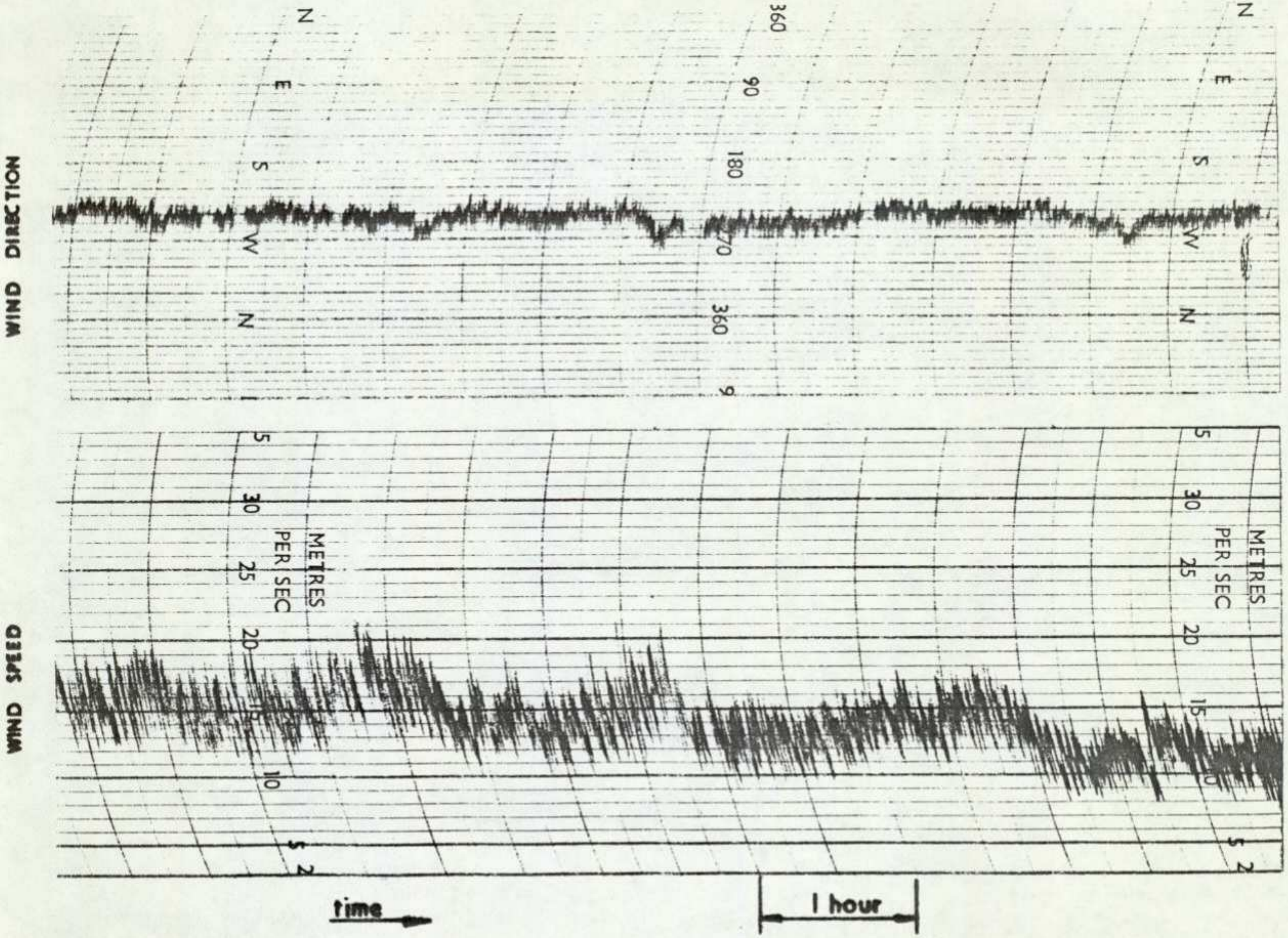

FIG 1 Typical anemograph recording of wind speed and direction.

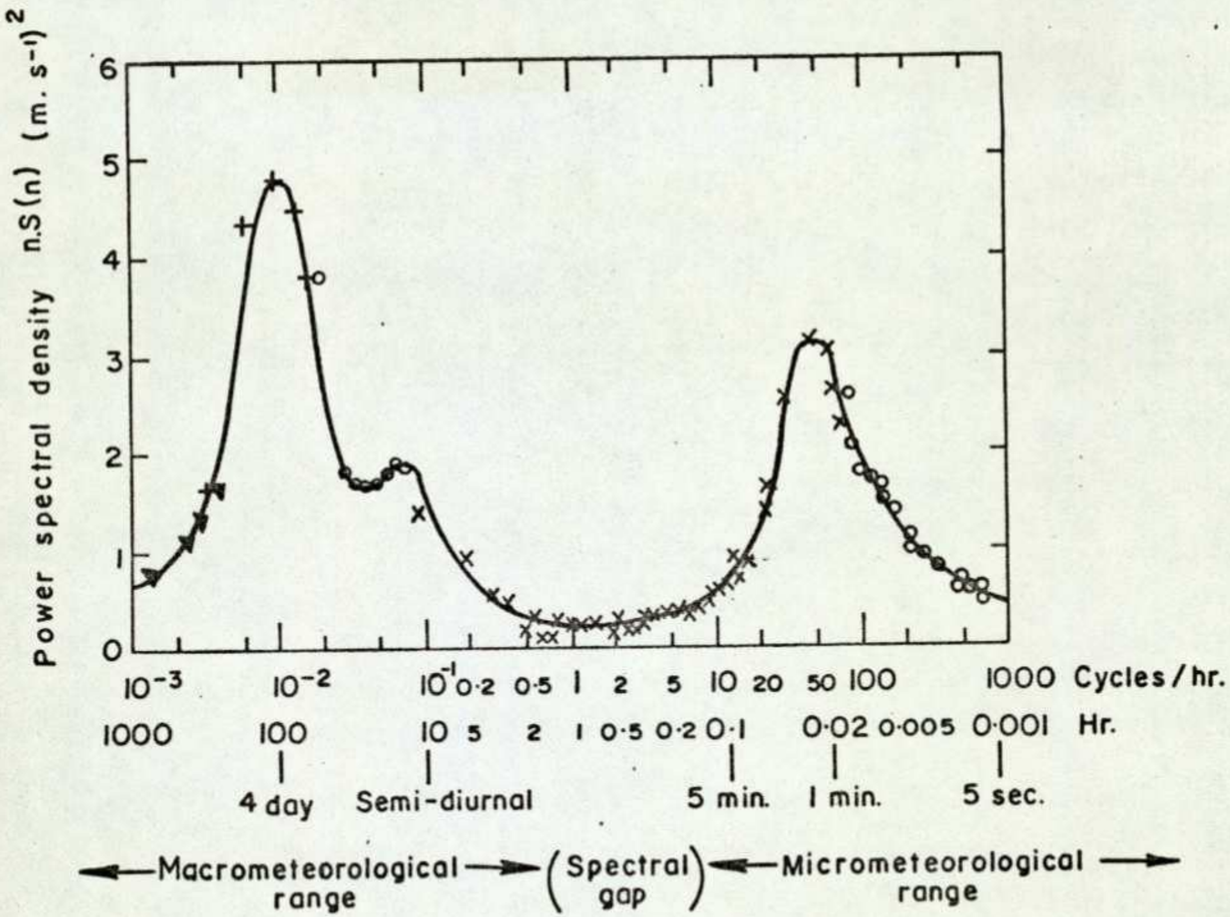

FIG. 2. SPECTRUM OF HORIZONTAL WIND SPEED AT BROOKHAVEN NATIONAL LABORATORY (REF. 23)

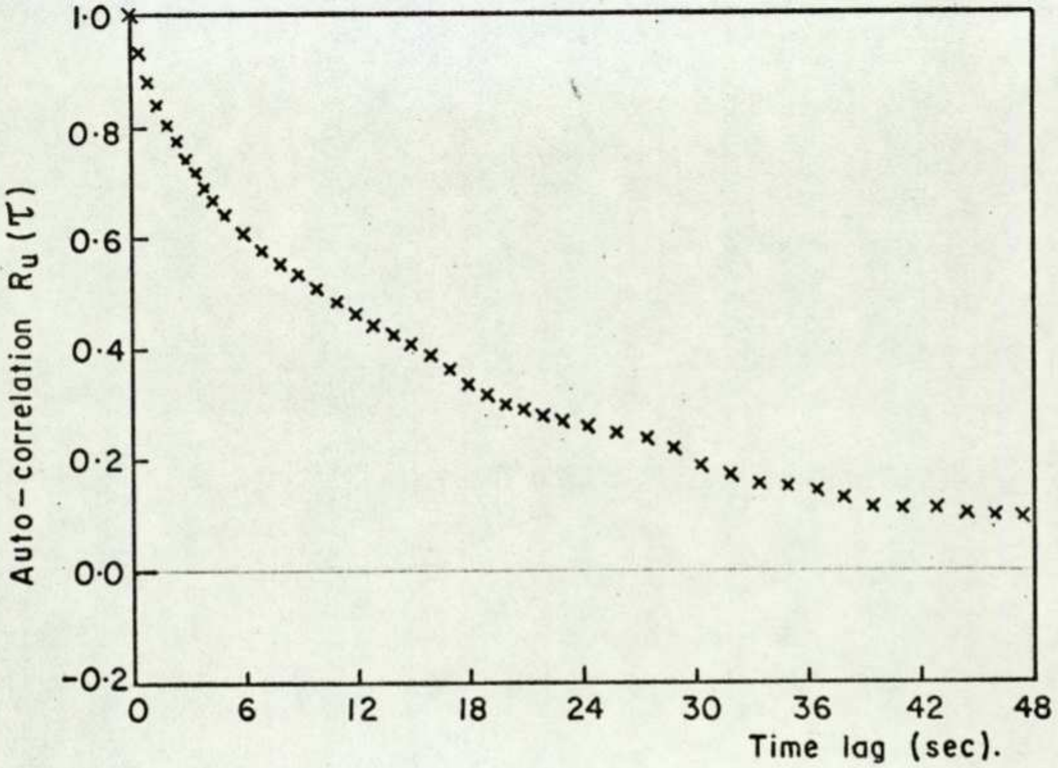

FIG. 3. TYPICAL AUTO-CORRELATION OF THE HORIZONTAL WIND COMPONENT (REF 35).

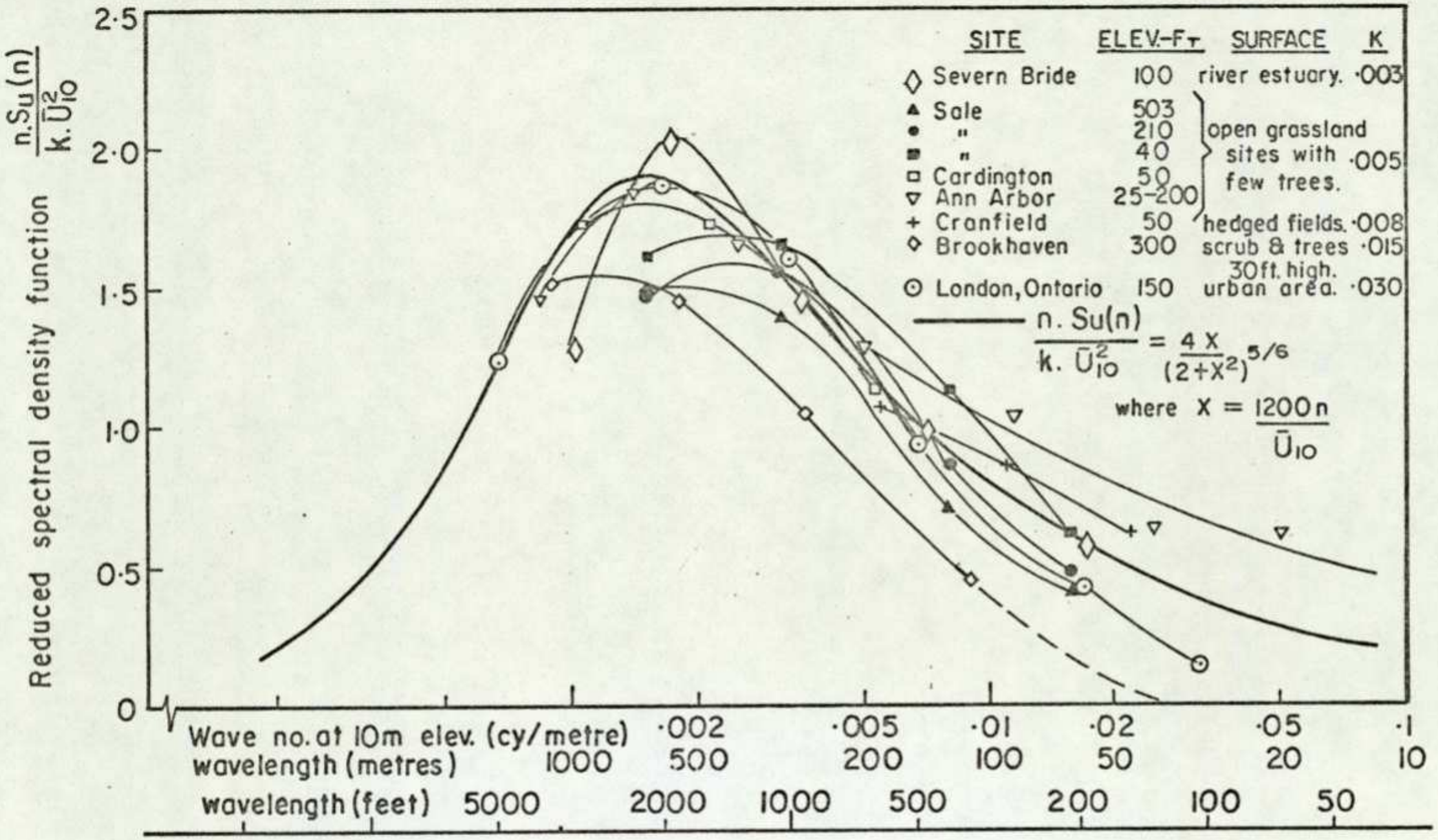

FIG. 4. SPECTRUM OF HORIZONTAL TURBULENCE (REF. 30)

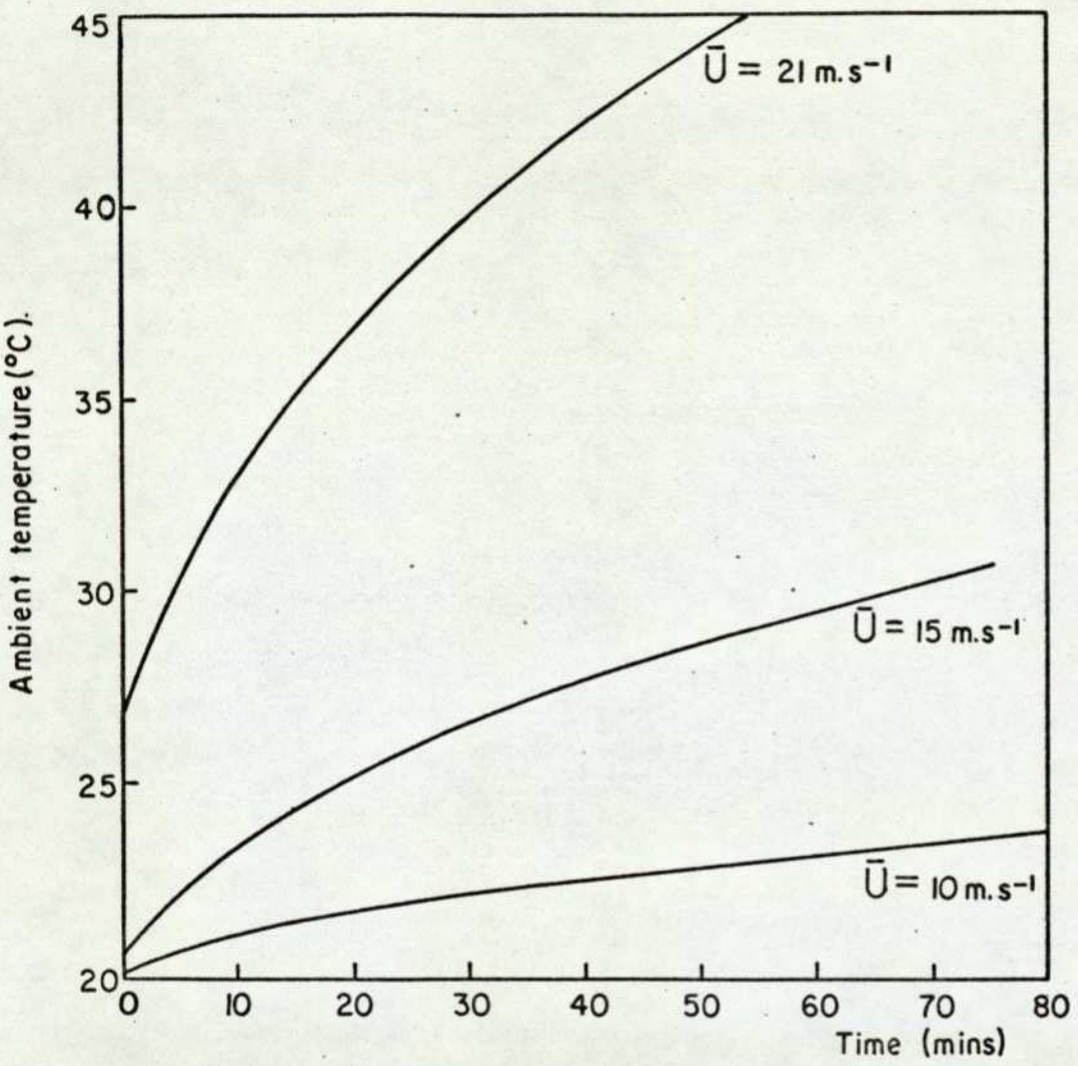

FIG. 5. VARIATION OF AMBIENT AIR TEMPERATURE IN WIND TUNNEL WITH DURATION OF RUN (REF. 54)

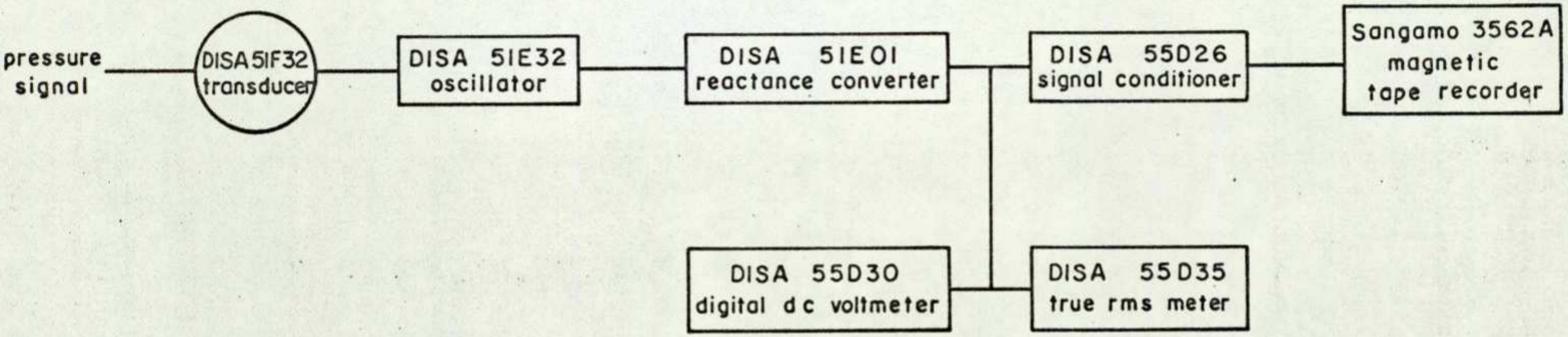

FIG. 6. BLOCK DIAGRAM OF PRESSURE RECORDING SYSTEM

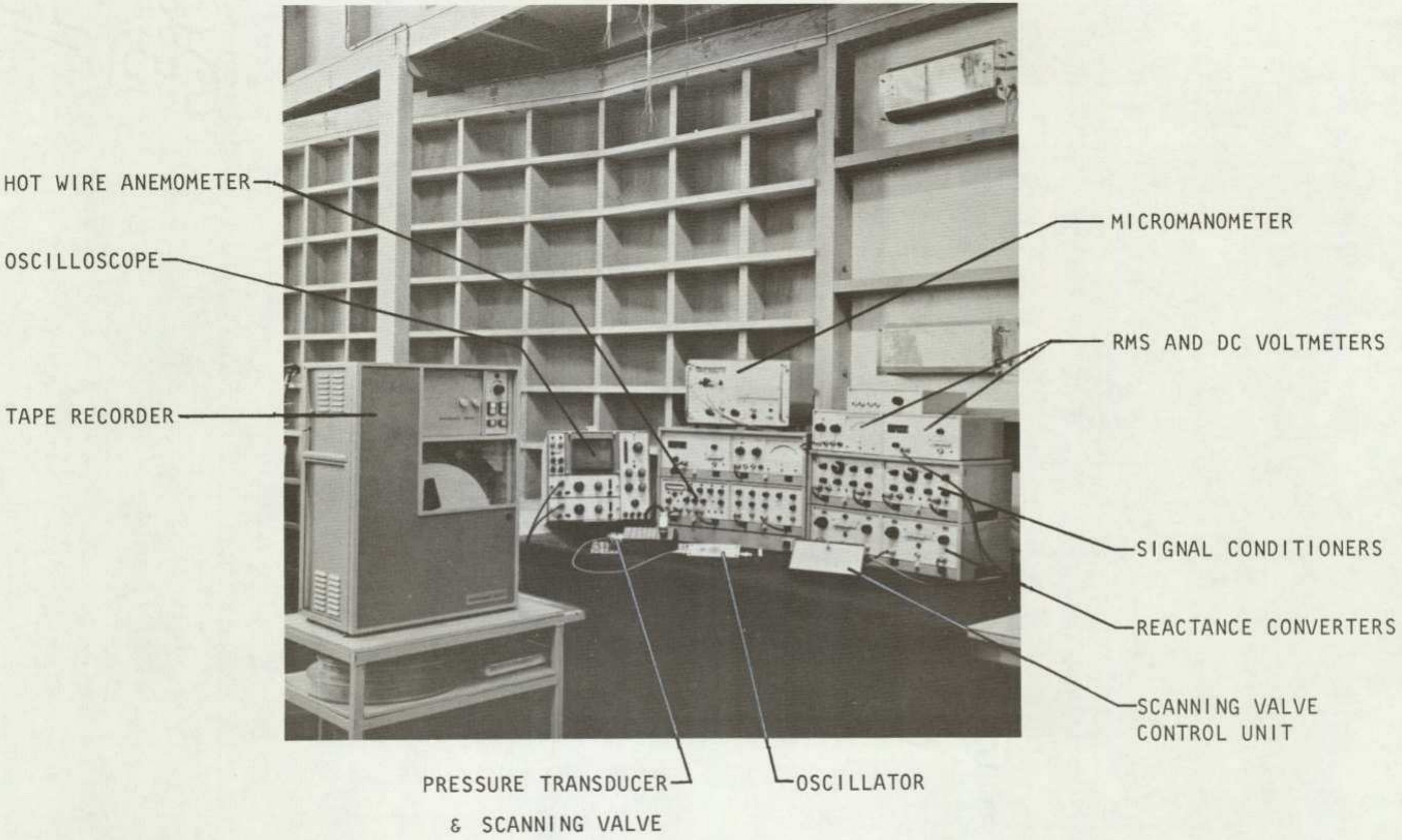

FIG. 7 SURFACE PRESSURE AND TURBULENCE ACQUISITION AND RECORDING EQUIPMENT

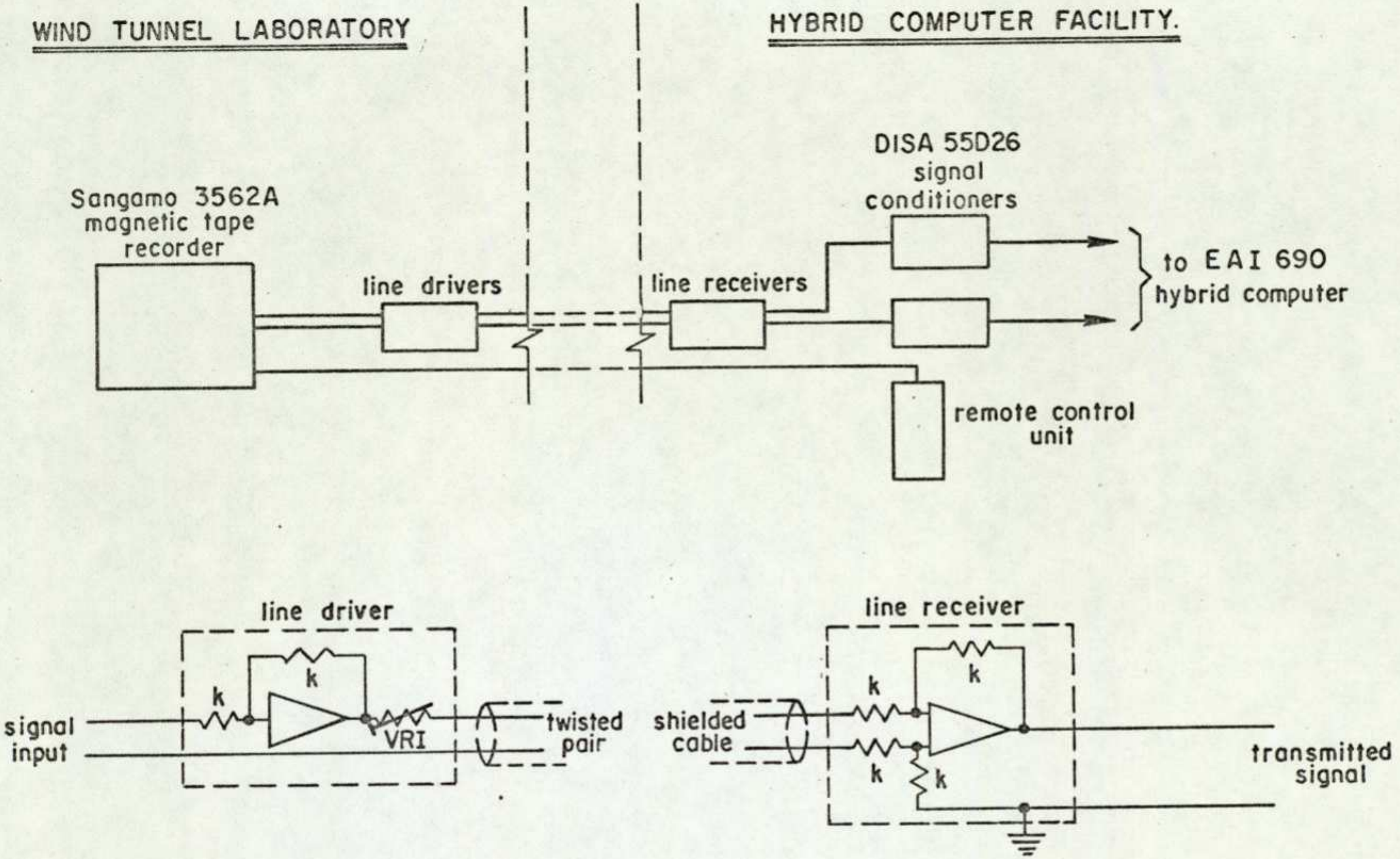

FIG. 8. BLOCK DIAGRAM OF DATA TRANSMISSION SYSTEM.

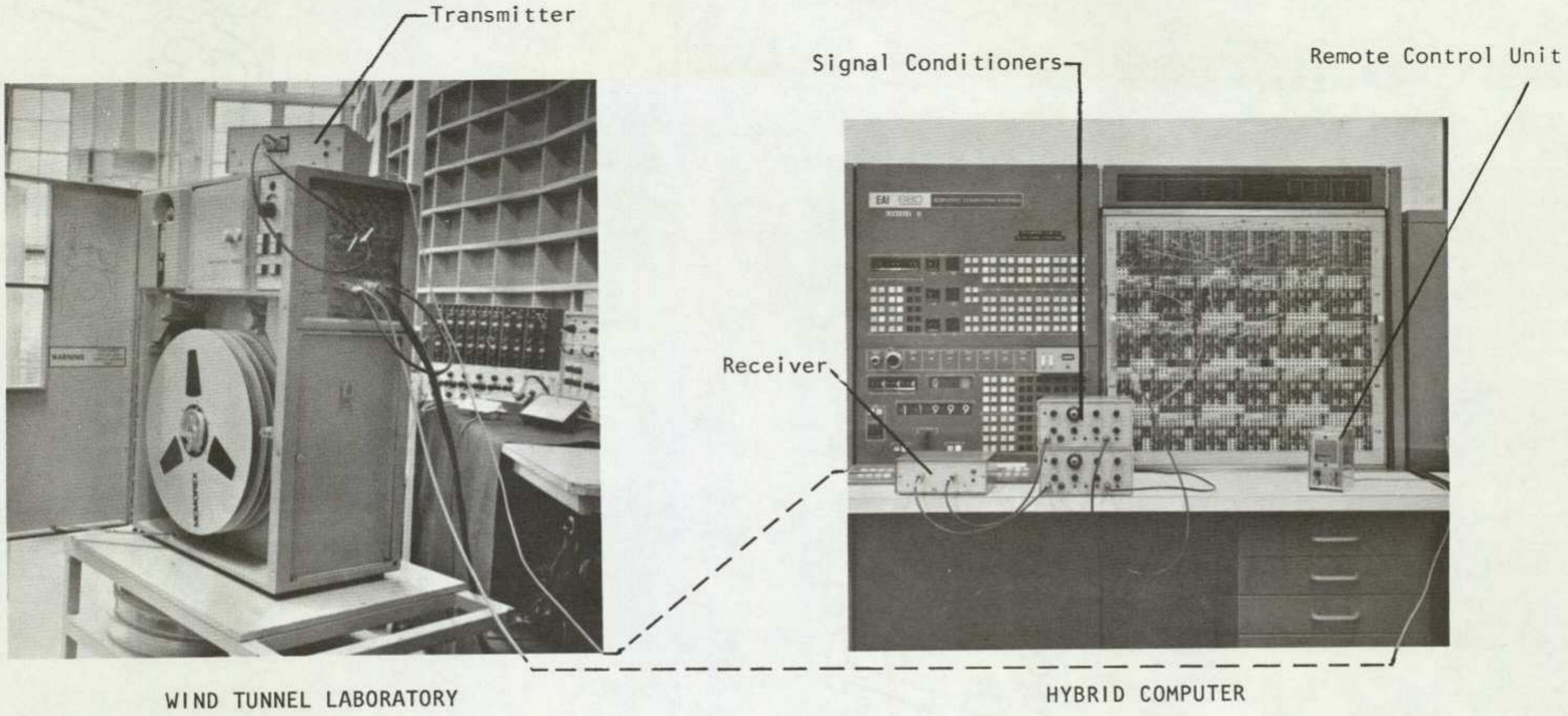

FIG. 9 DATA TRANSMISSION EQUIPMENT FOR ANALOGUE TO DIGITAL CONVERSION OF RECORDED DATA

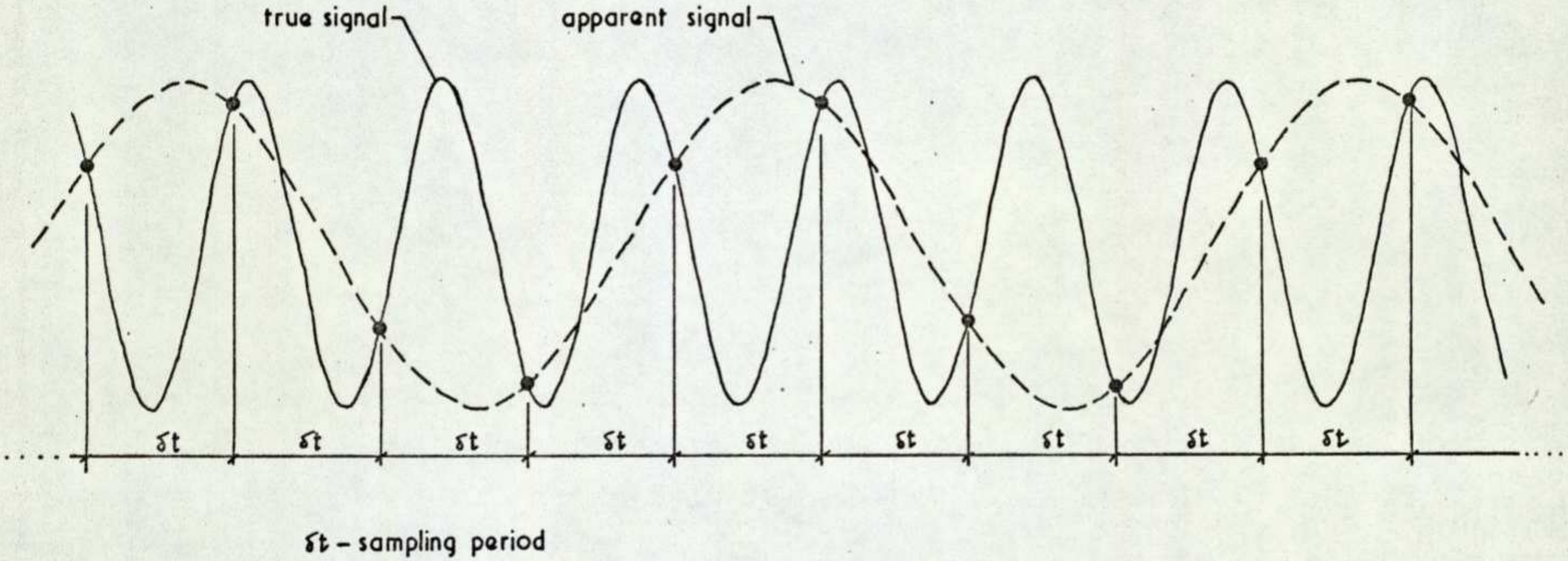

FIG 10 Aliasing

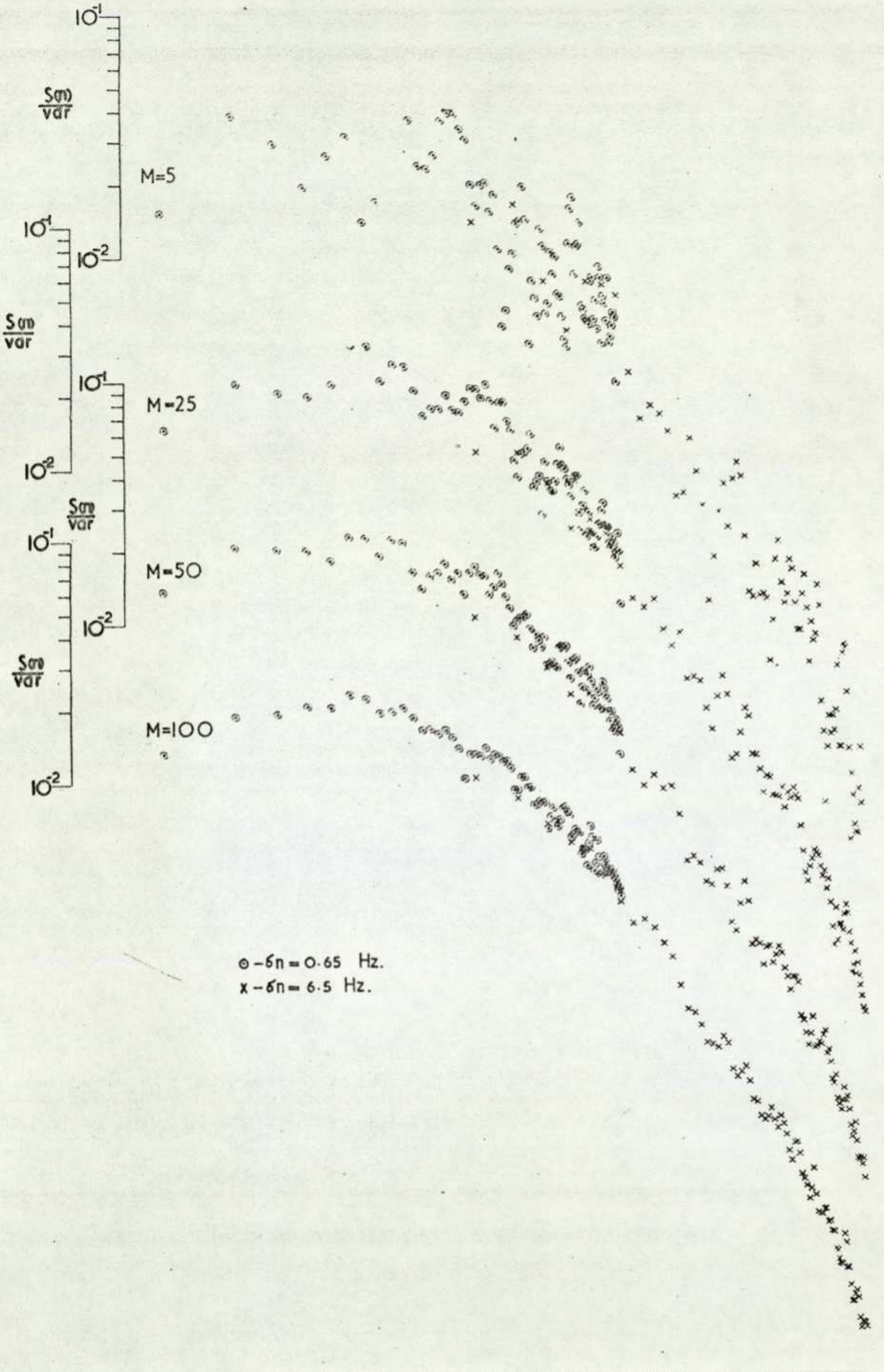

FIG 11 Example of spectral smoothing for grid generated turbulence.

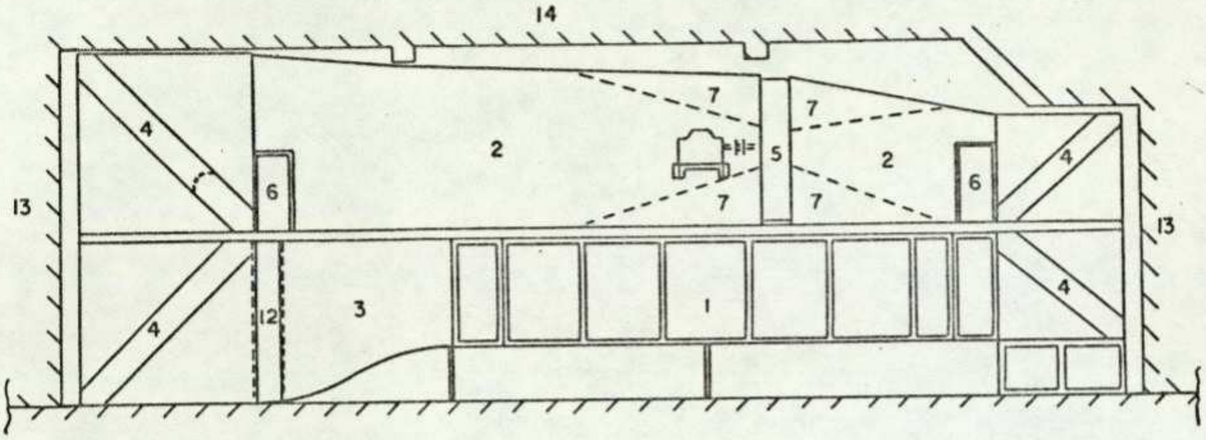

SIDE ELEVATION

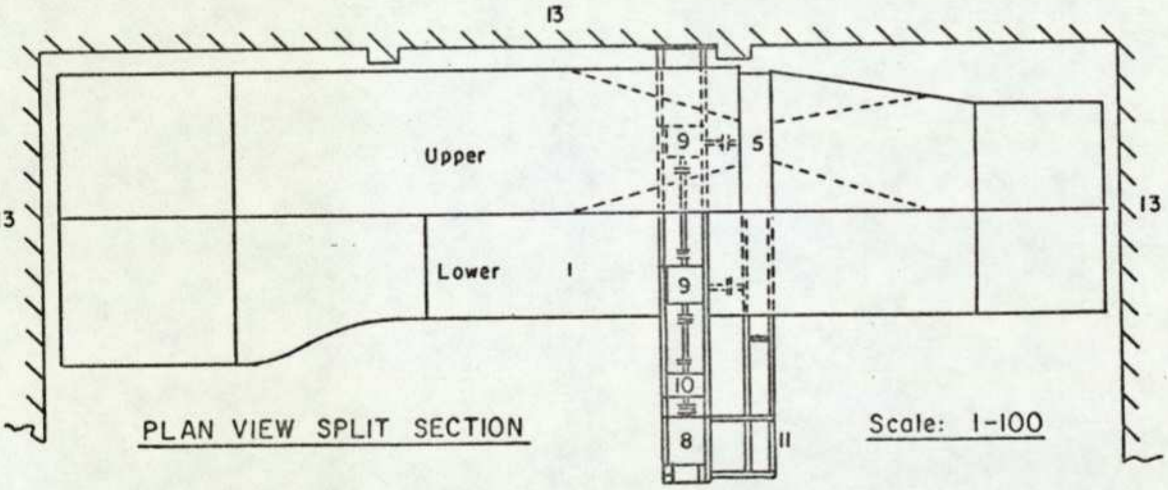

PLAN VIEW SPLIT SECTION

Scale: 1-100

1. Working section, 1·5m x 3·0m x 8m long.
2. Return duct.
3. Contraction = 2 to 1 area ratio.
4. Turning vanes
5. 2 – fans, 1·82m dia.
6. Access doors.
7. Fairings.
8. 77 HP motor.
9. 1 to 1 gearboxes.
10. 3 to 1 gearbox.
11. Support tower for motor & fans.
12. Screens.
13. Laboratory walls.
14. Laboratory ceiling.

FIG. 12. LAYOUT OF INDUSTRIAL AERODYNAMICS WIND TUNNEL
(REF. 65)

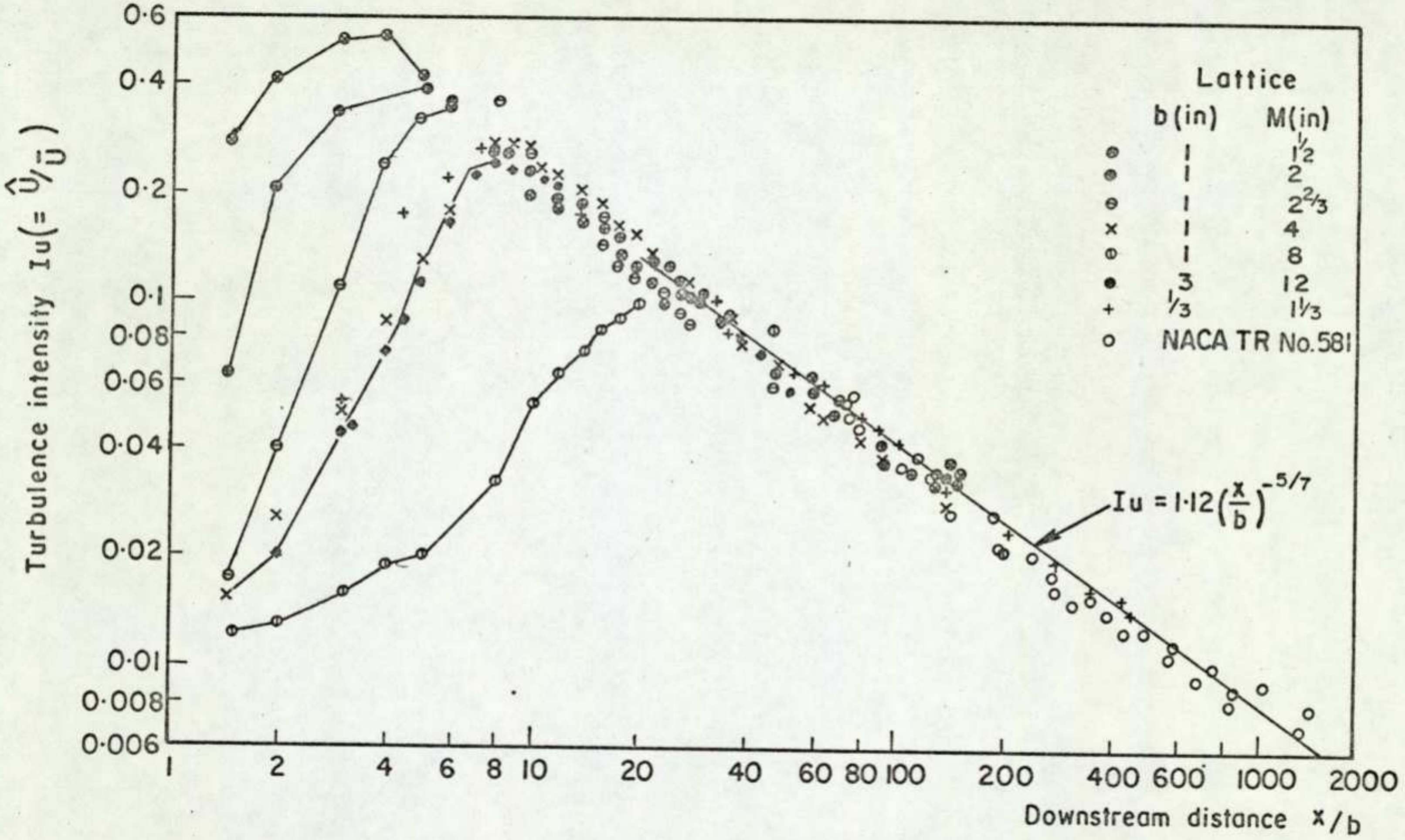

FIG. 13. VARIATION IN TURBULENCE INTENSITY DOWNSTREAM OF LATTICE GRIDS. (REF. 66)

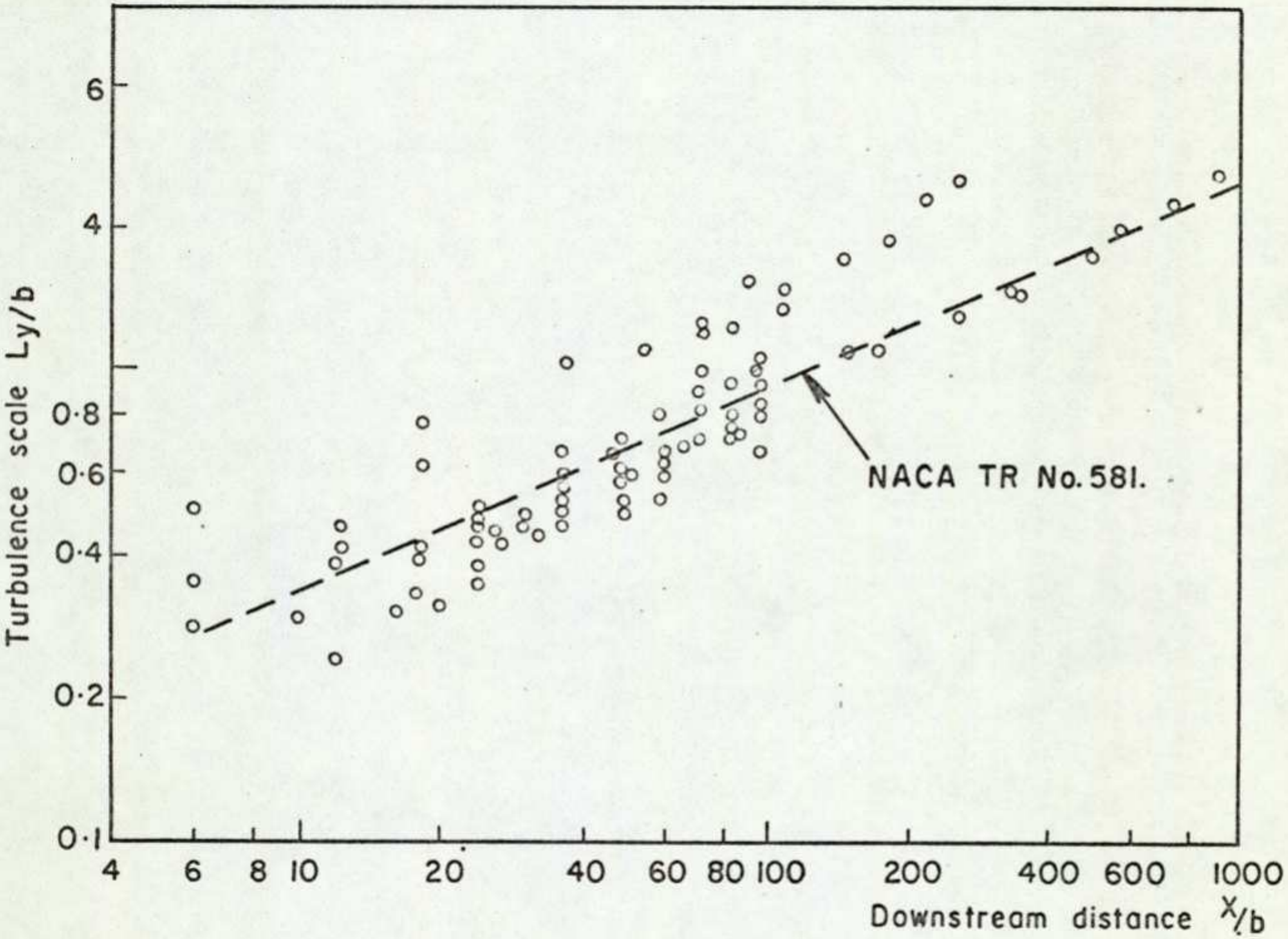

FIG. 14. VARIATION IN LATERAL TURBULENCE SCALE DOWNSTREAM OF LATTICE GRIDS (REF. 66)

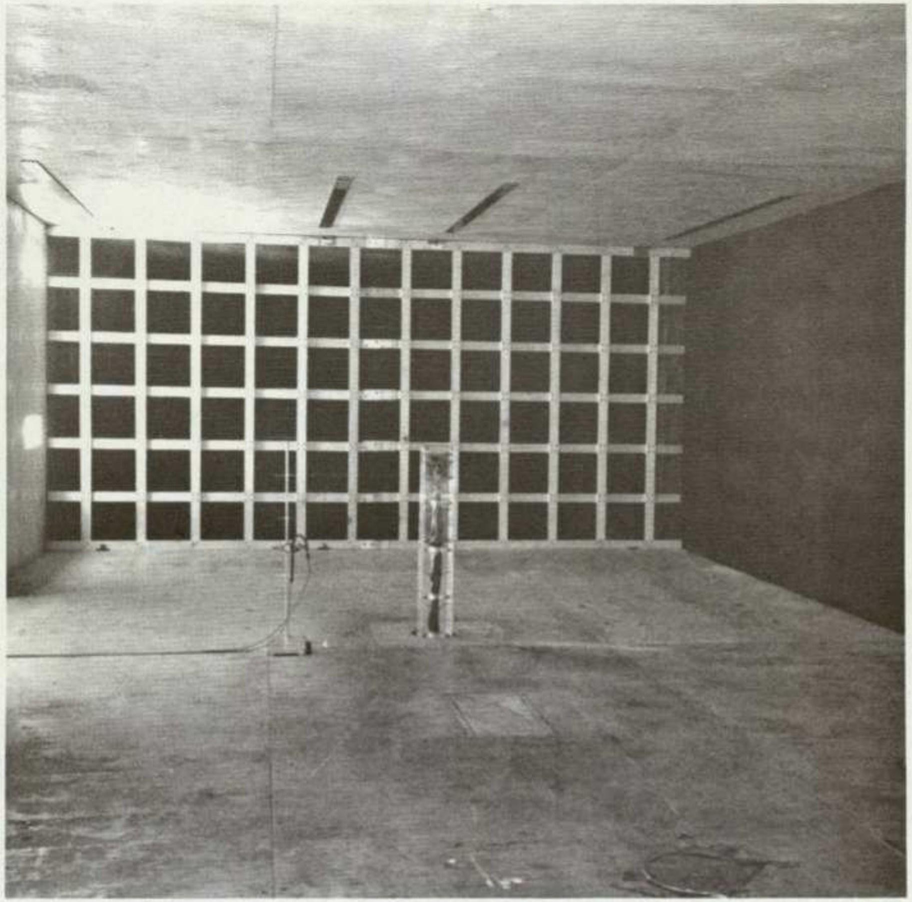

FIG. 15 MODEL 2 AND GRID I POSITIONED IN THE WIND TUNNEL

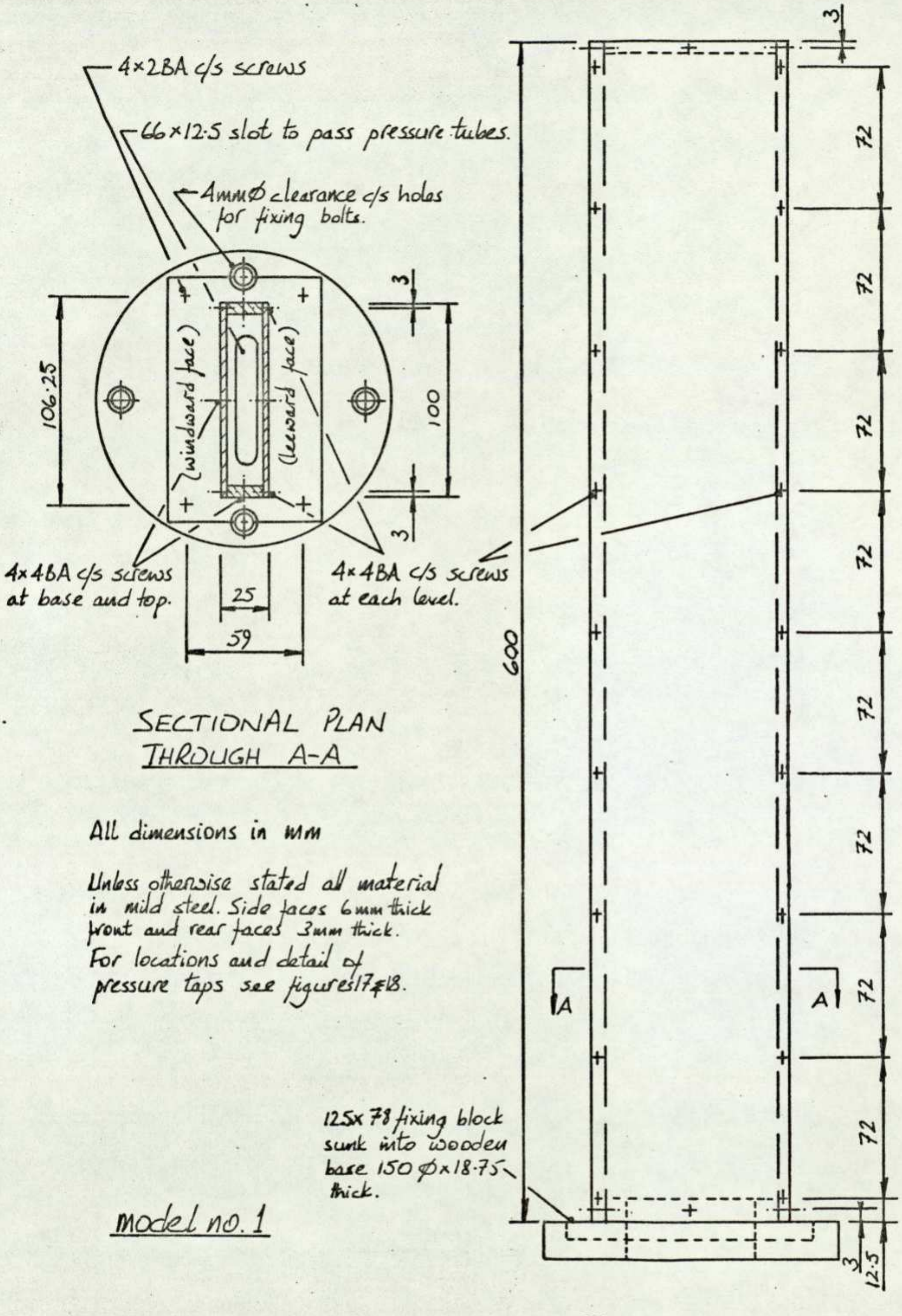

SECTIONAL PLAN
THROUGH A-A

All dimensions in mm

Unless otherwise stated all material in mild steel. Side faces 6mm thick front and rear faces 3mm thick.
For locations and detail of pressure taps see figures 17 & 18.

model no. 1

FRONT VIEW

FIG. 16 CONSTRUCTION DETAILS OF MODELS.

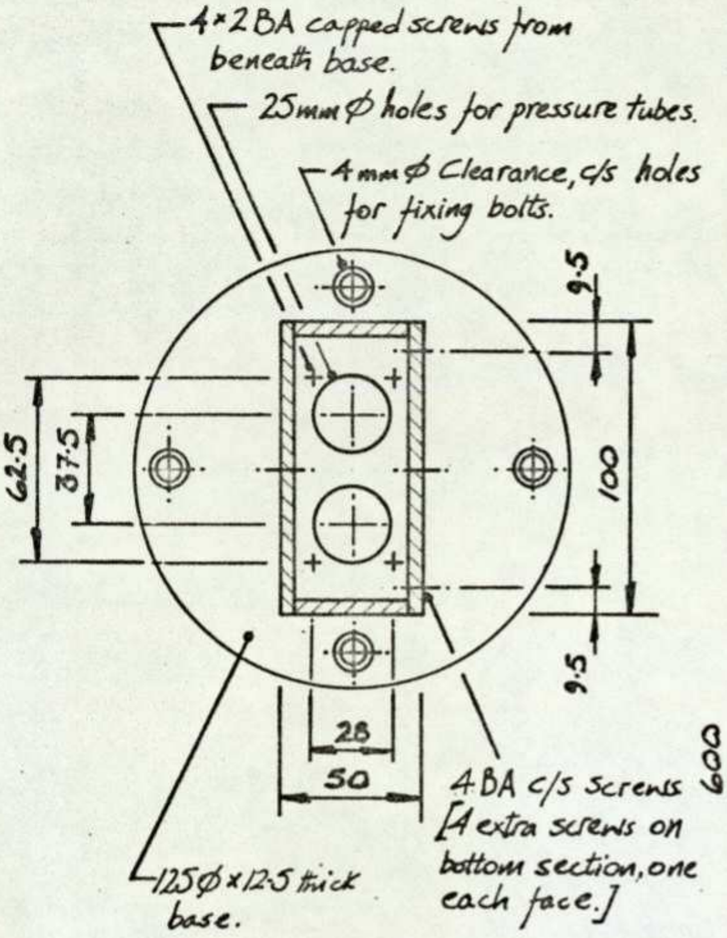

SECTIONAL PLAN
THROUGH A-A

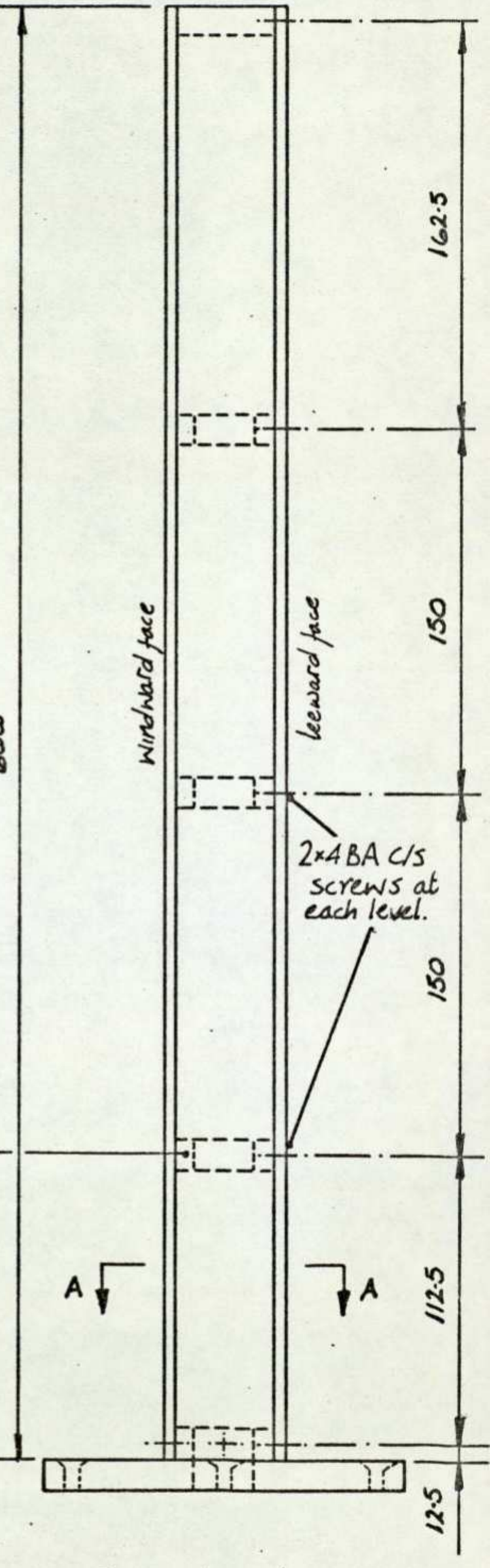

All dimensions in mm

Unless otherwise stated all material in perspex 4·8mm thick.

For locations and detail of pressure taps see figures 17 & 18

Windward and side faces glued at edges and to spacers with perspex adhesive.

model no. 2

SIDE VIEW

FIG. 16. (continued)

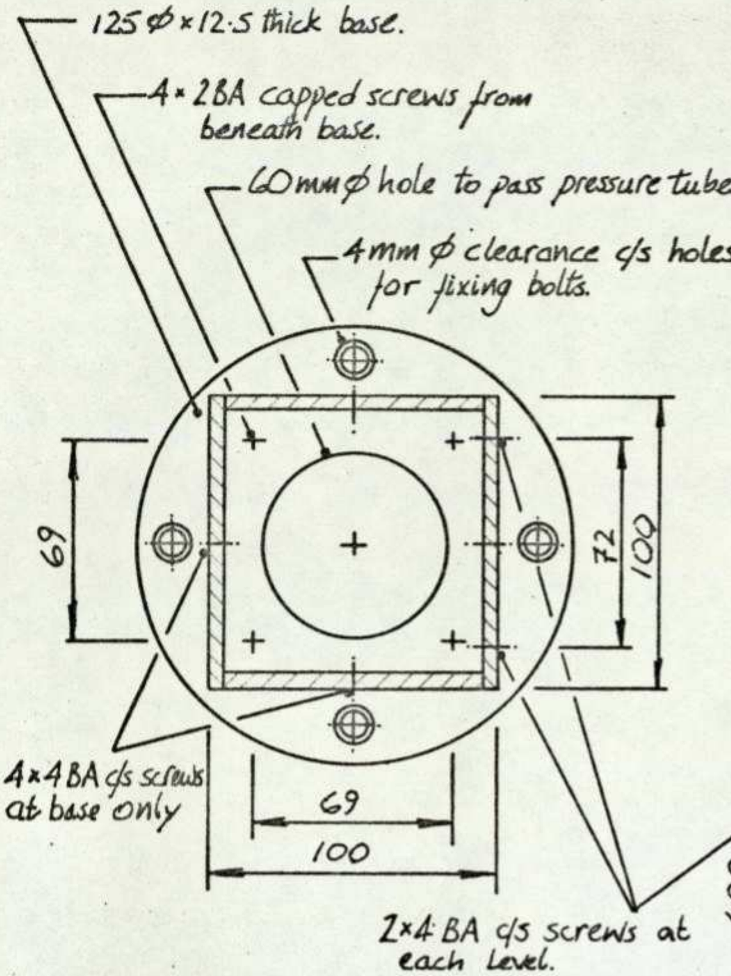

SECTIONAL PLAN THROUGH A-A

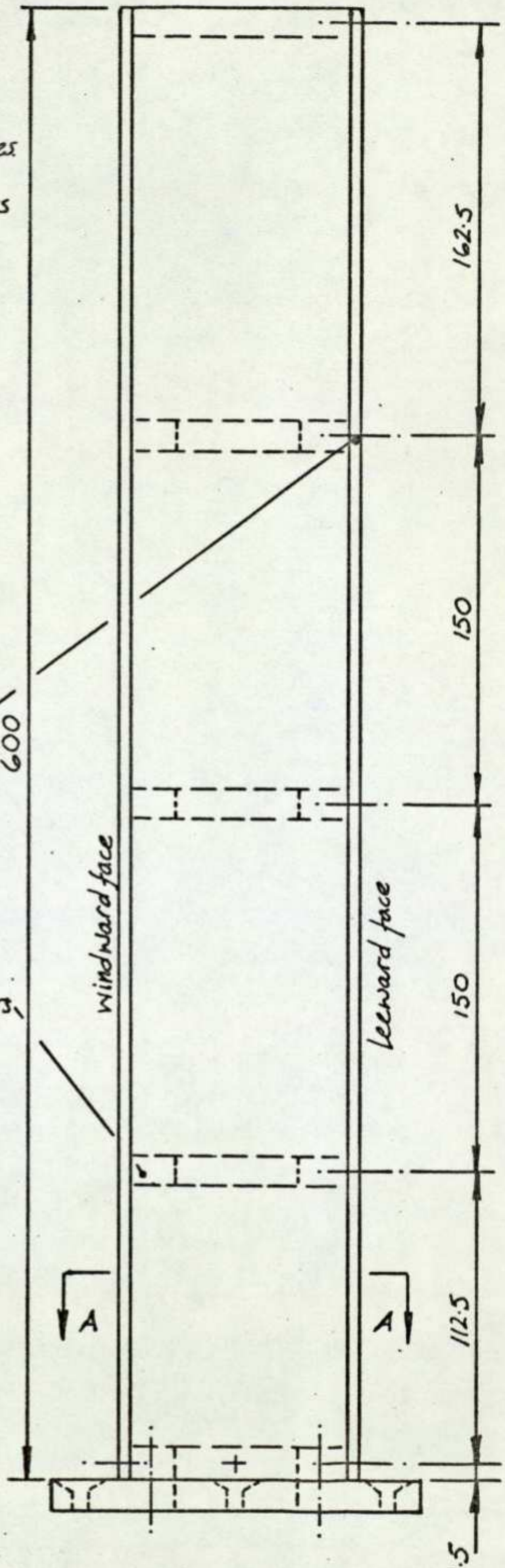

SIDE VIEW

All dimensions in mm.

Unless otherwise stated all material in perspex 4·8mm thick.

Windward and sidefaces glued at edges and to spacers with perspex adhesive.

For locations and detail of pressure taps see figures 17 & 18

model no. 3

FIG. 16 (concluded)

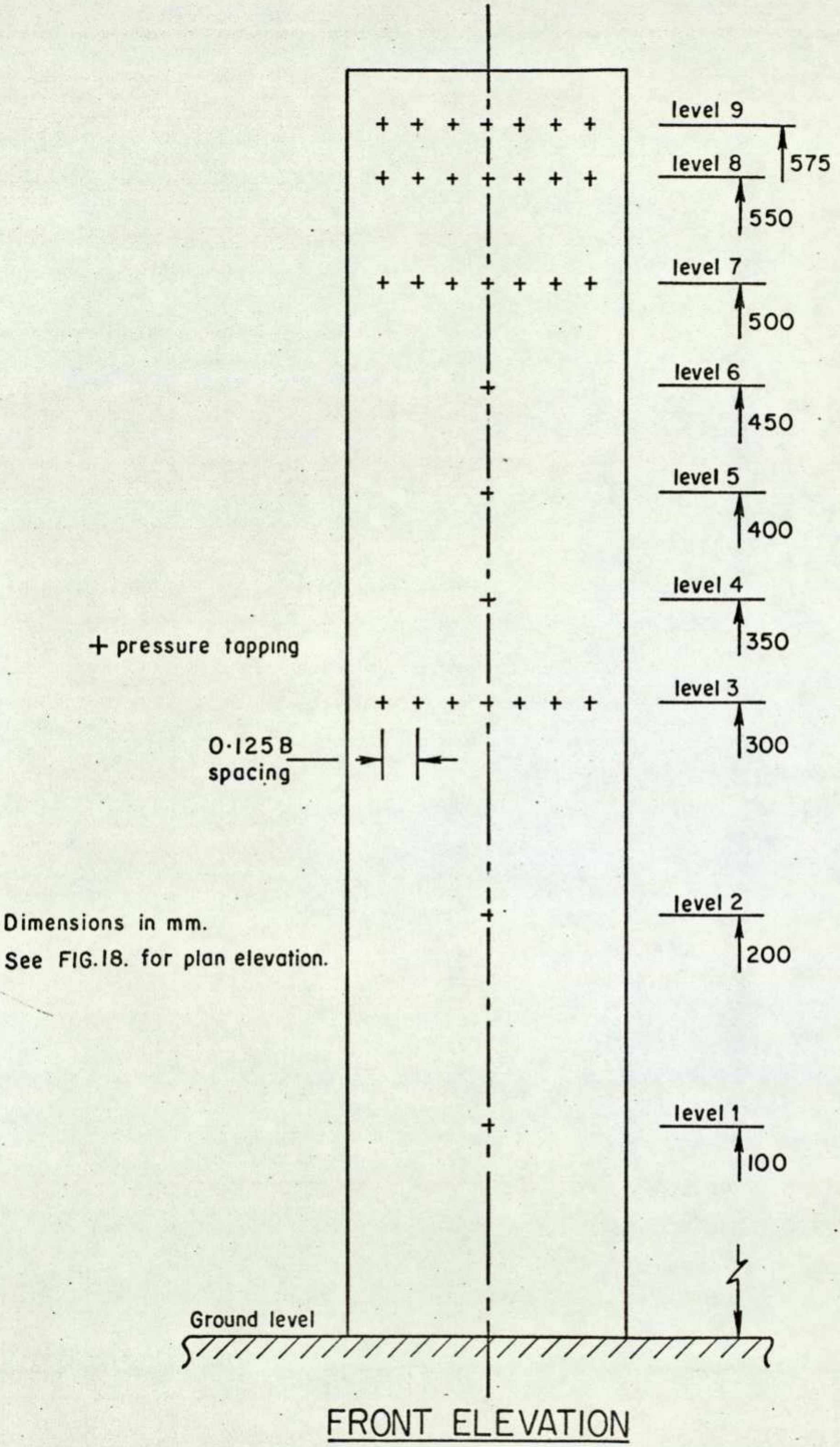

FIG. 17. SURFACE PRESSURE TAPPING POSITIONS.

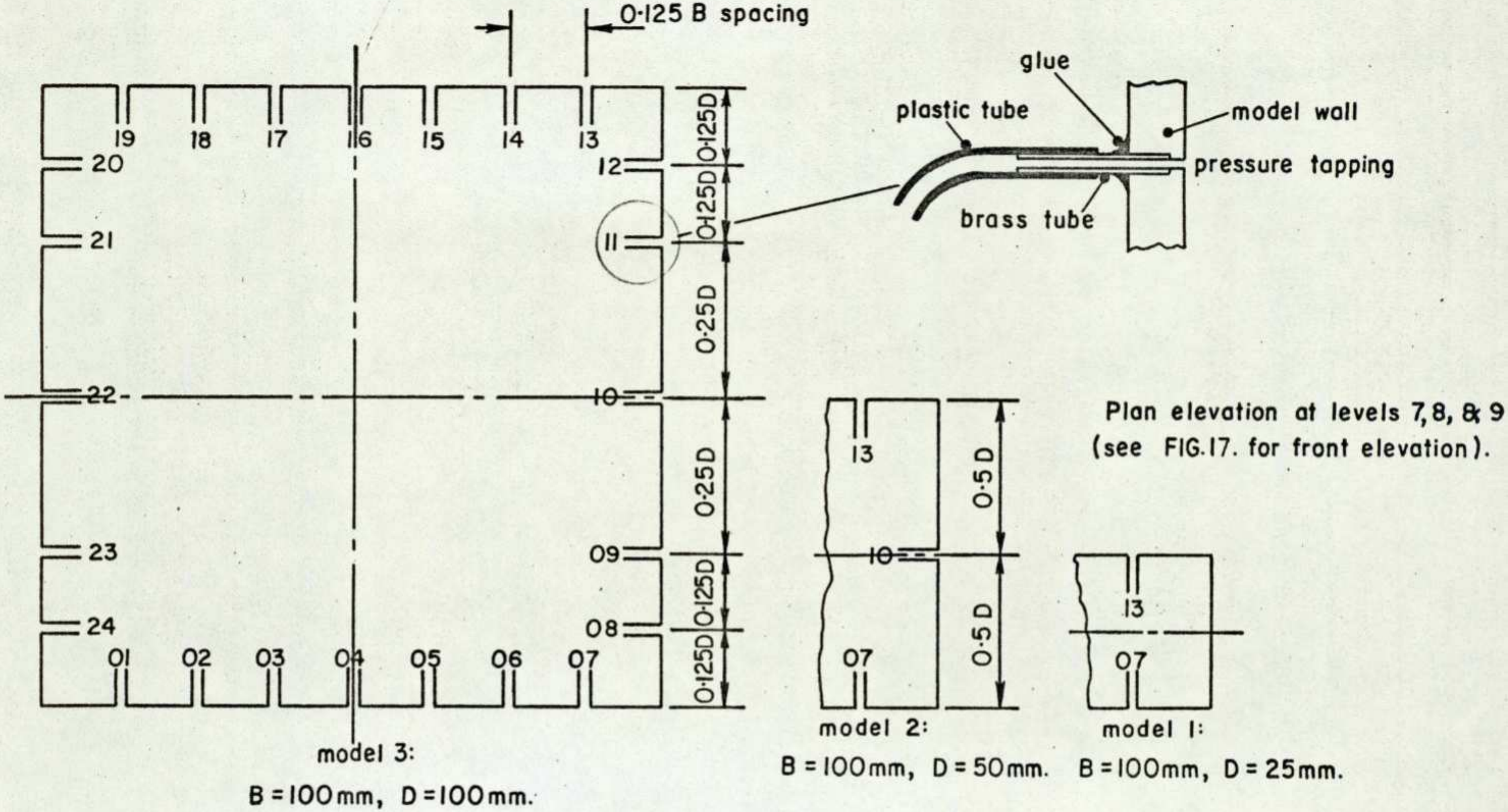

Plan elevation at levels 7, 8, & 9
(see FIG. 17. for front elevation).

model 3:
B = 100 mm, D = 100 mm.

model 2:
B = 100 mm, D = 50 mm.

model 1:
B = 100 mm, D = 25 mm.

Note:- Pressure tappings on models 1 & 2, and at levels 1, 2, 4, 5 & 6 for all models, are numbered according to position and referenced to positions shown on model 3.

FIG. 18. SURFACE PRESSURE TAPPING POSITIONS.

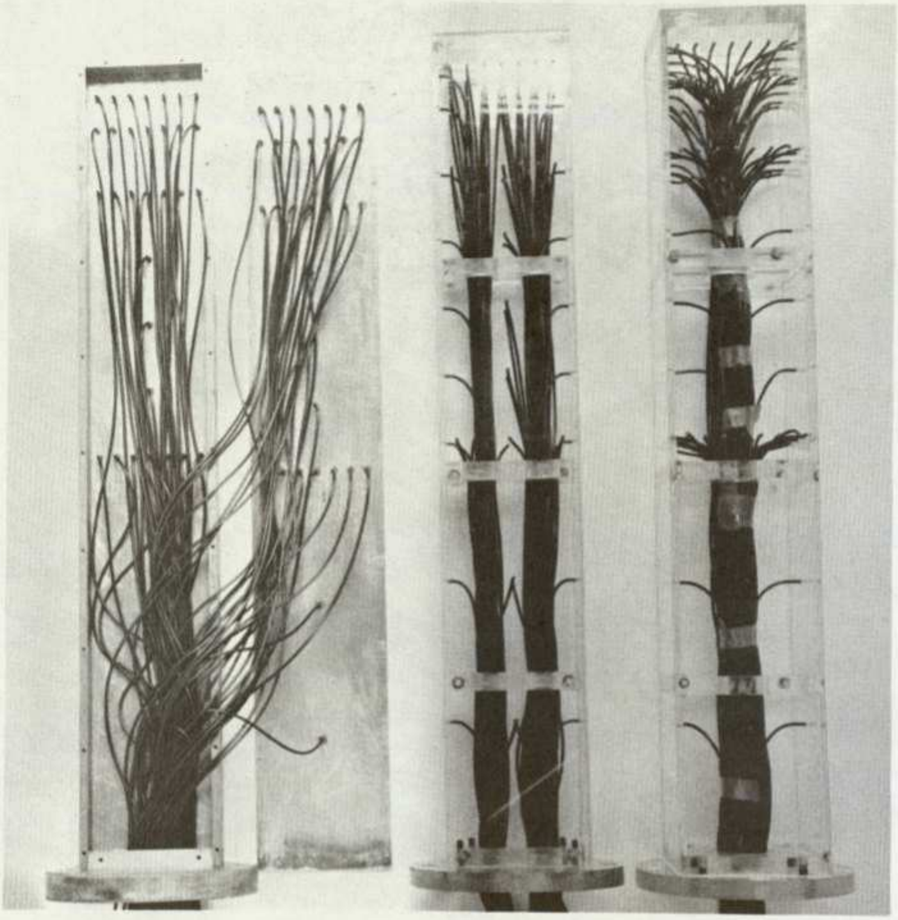

Model 1 Model 2 Model 3

FIG. 19 MODELS USED IN THE INVESTIGATIONS

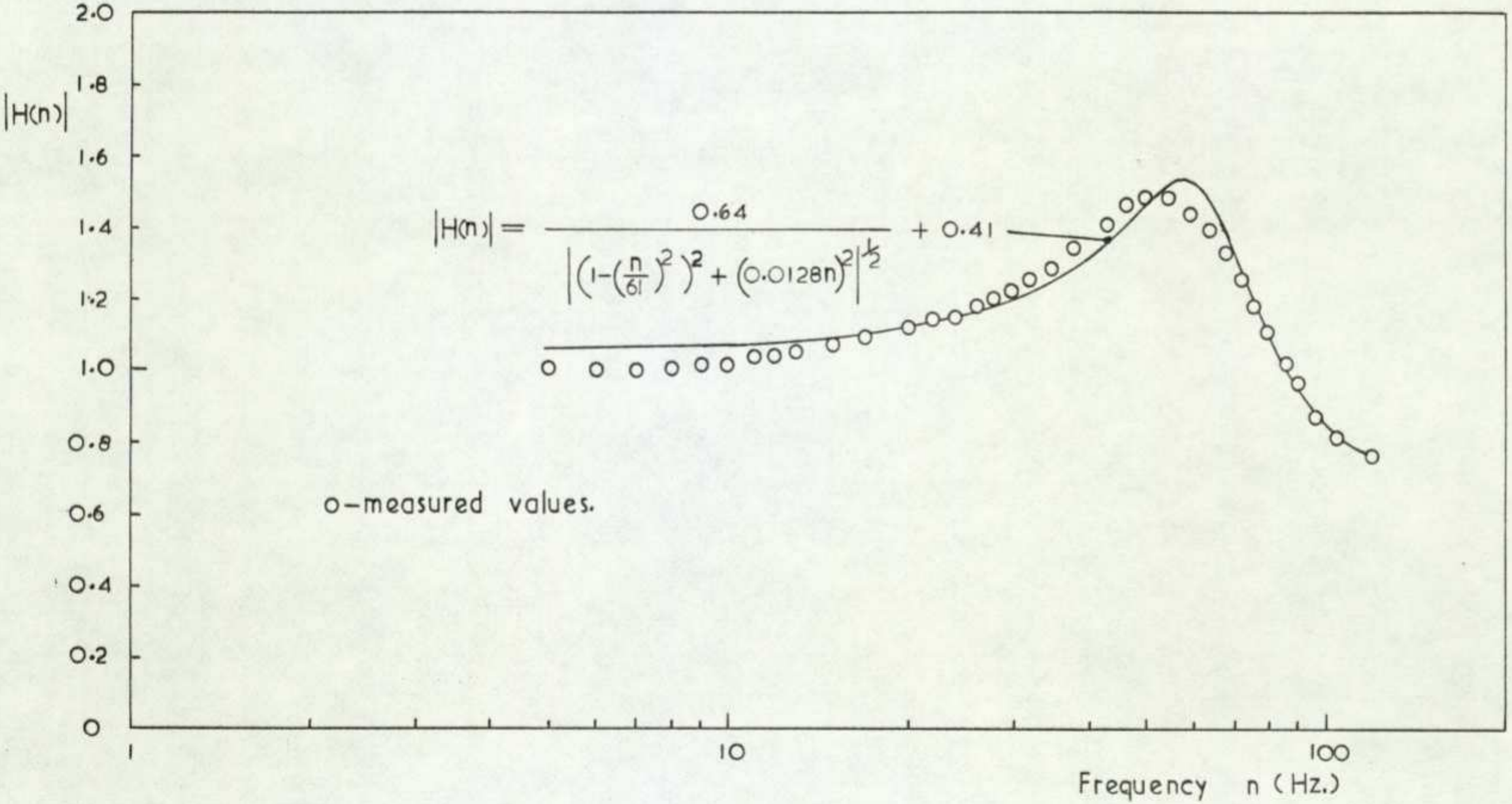

FIG 20 Amplitude response function of 90cm pressure tube Scanivalve system.

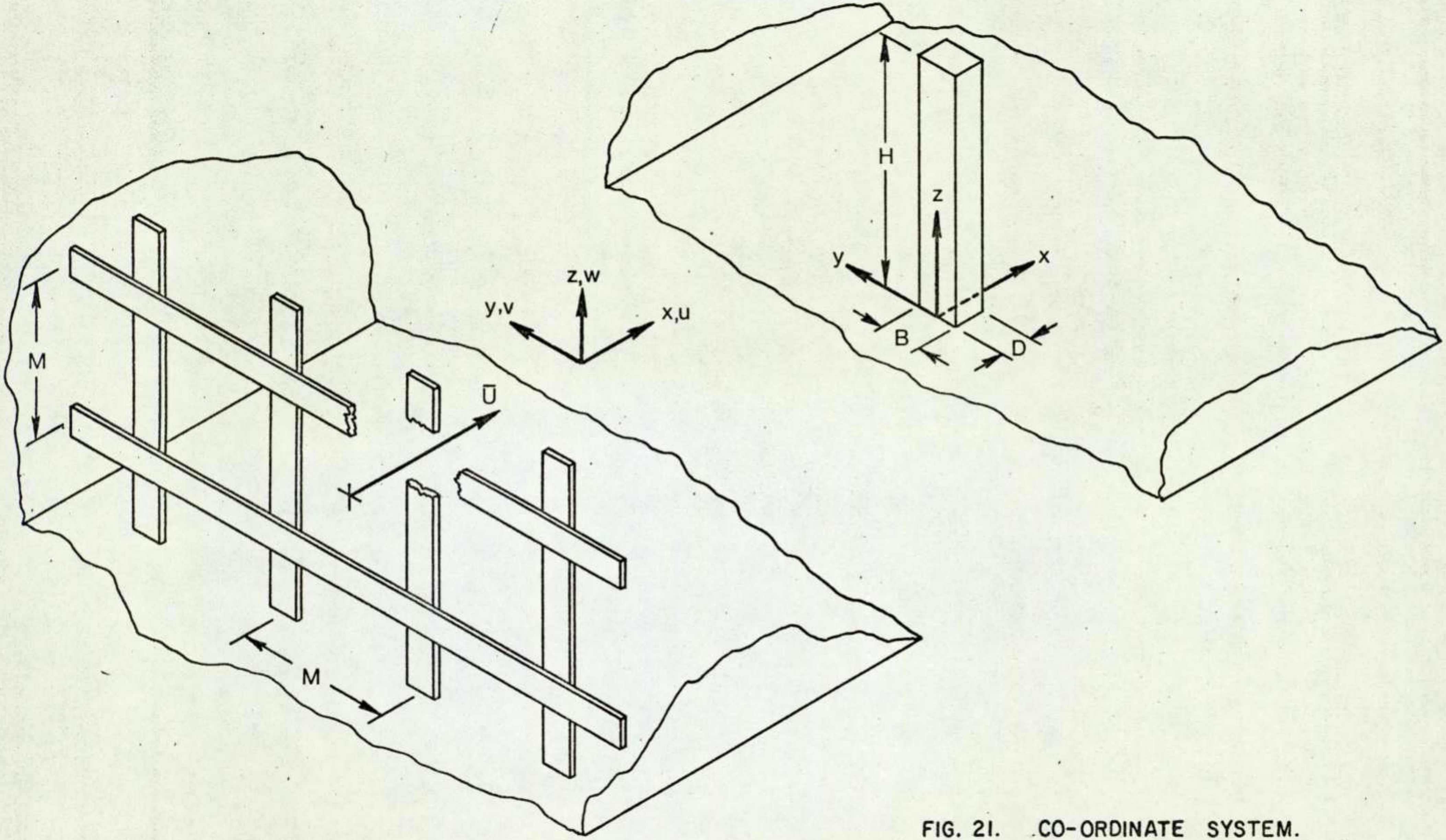

FIG. 21. CO-ORDINATE SYSTEM.

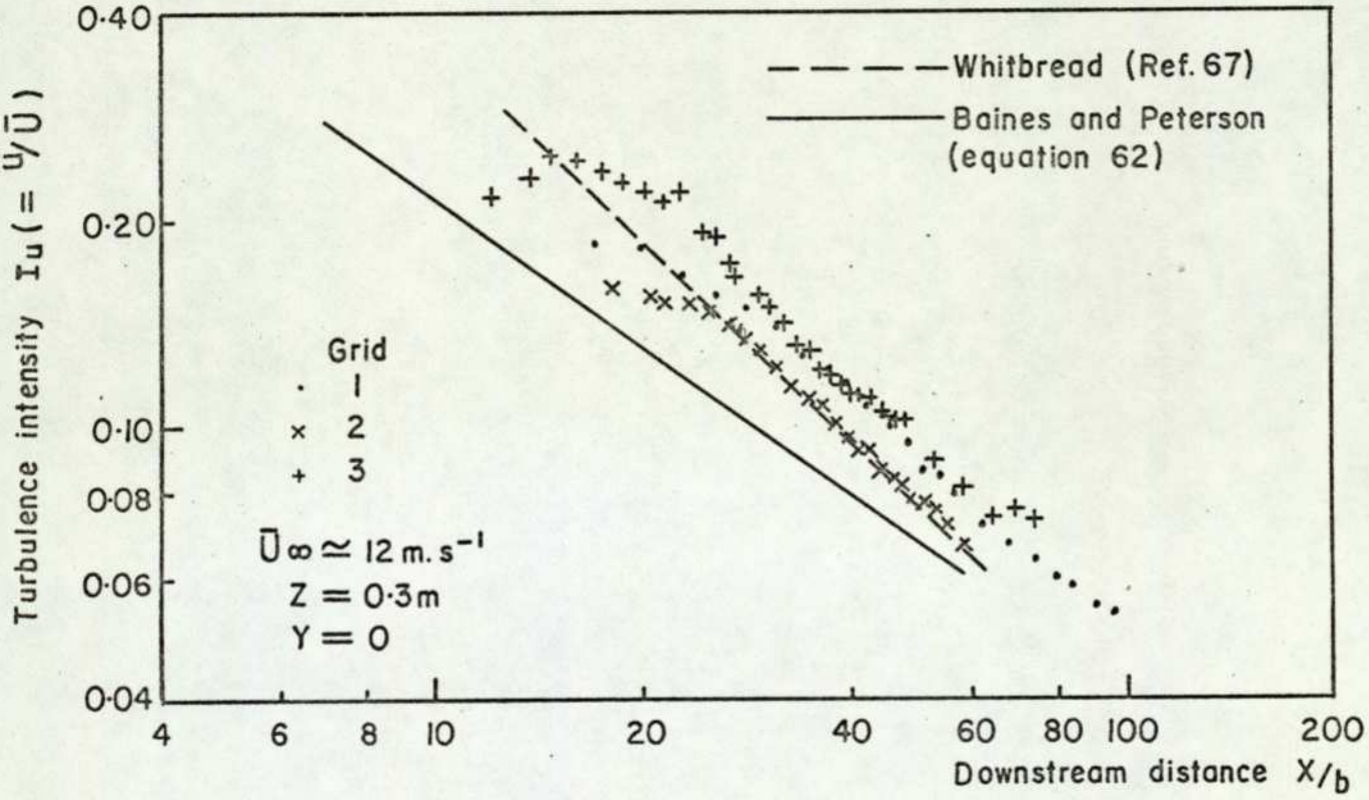

FIG. 22. VARIATION IN TURBULENCE INTENSITY DOWNSTREAM OF TURBULENCE GRIDS.

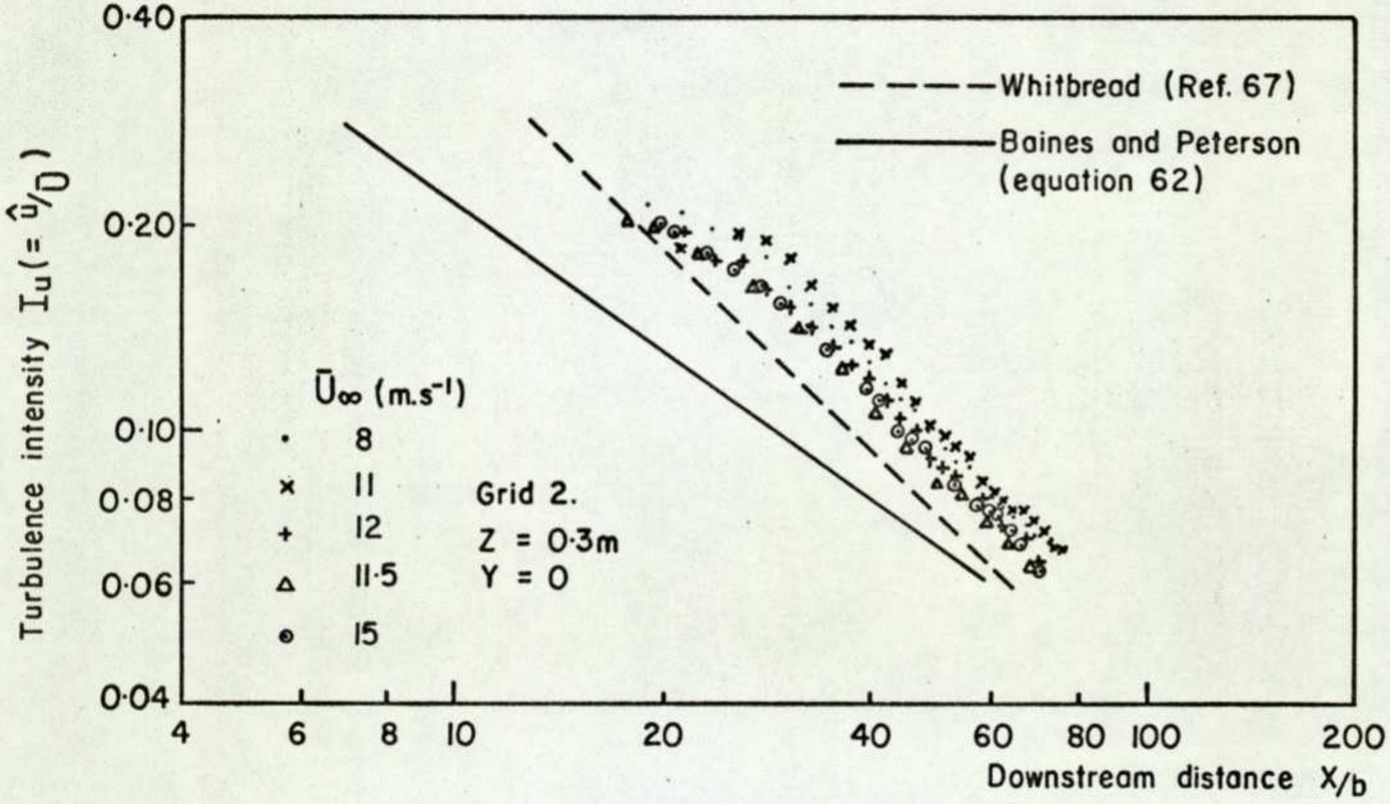

FIG. 23. VARIATION IN TURBULENCE INTENSITY DOWNSTREAM OF GRID 2 FOR DIFFERENT WIND SPEEDS.

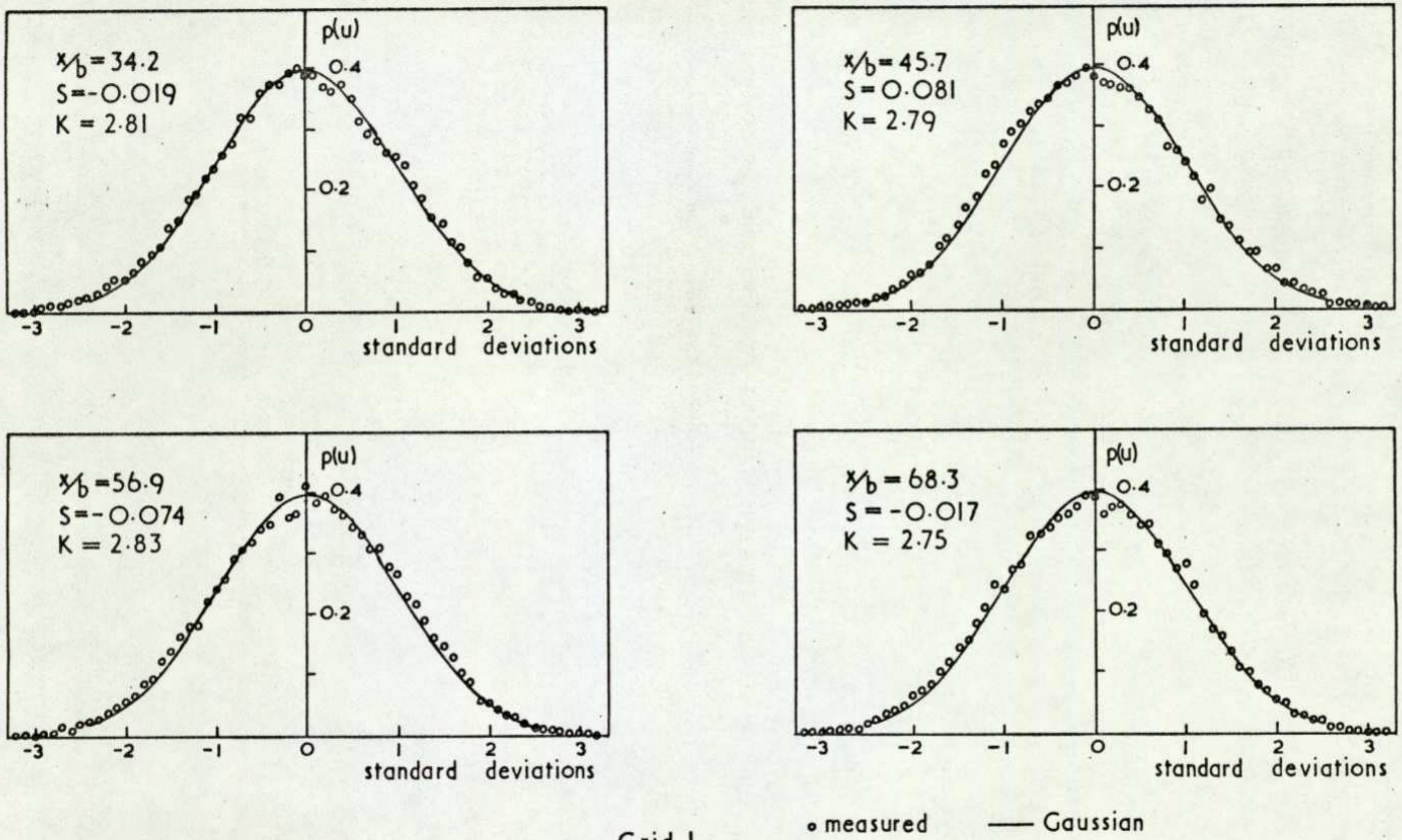

Grid I

FIG 24 Probability density distribution for longitudinal component of turbulence downstream of lattice grids.

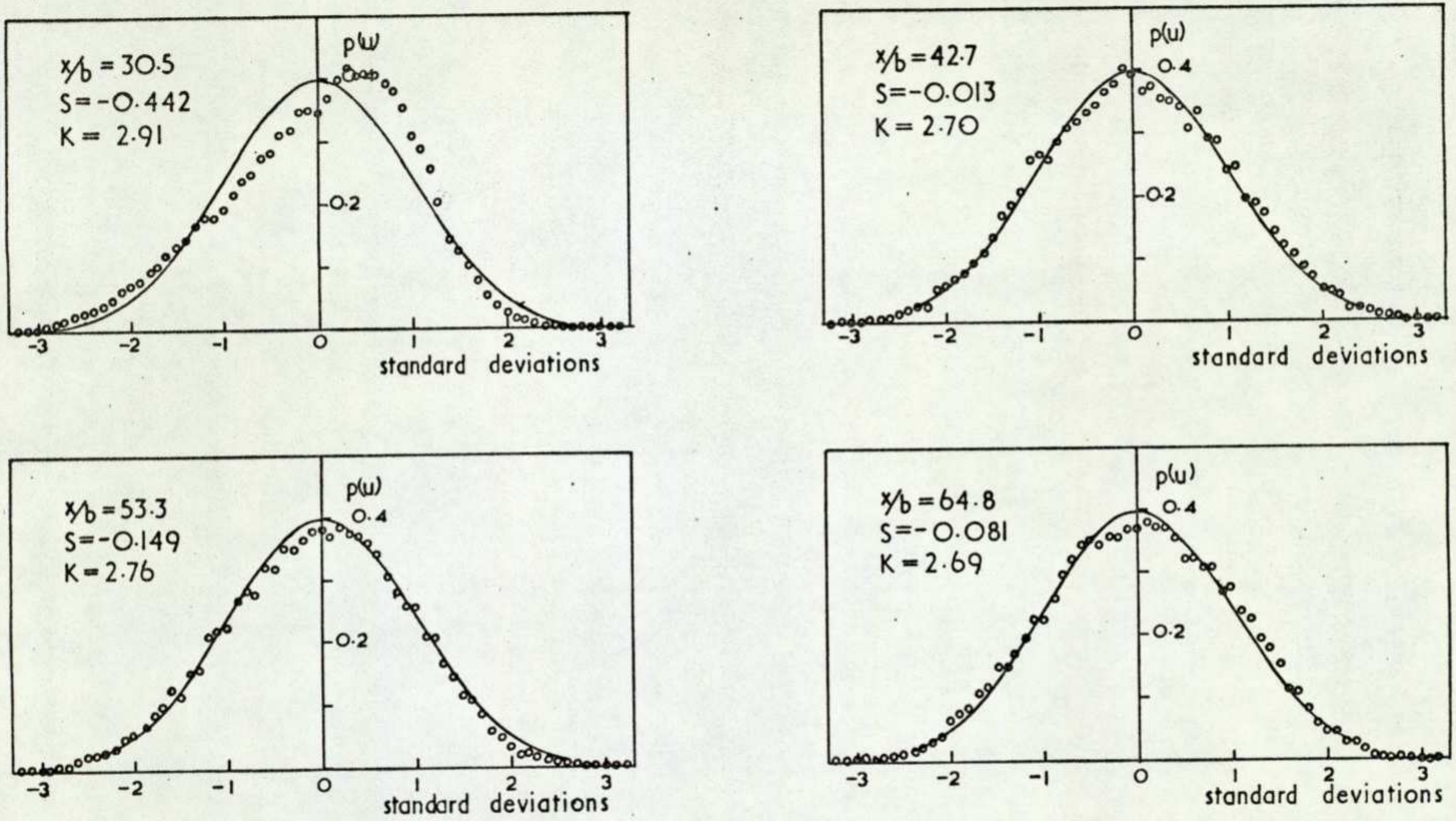

Grid 2

FIG 24 (continued)

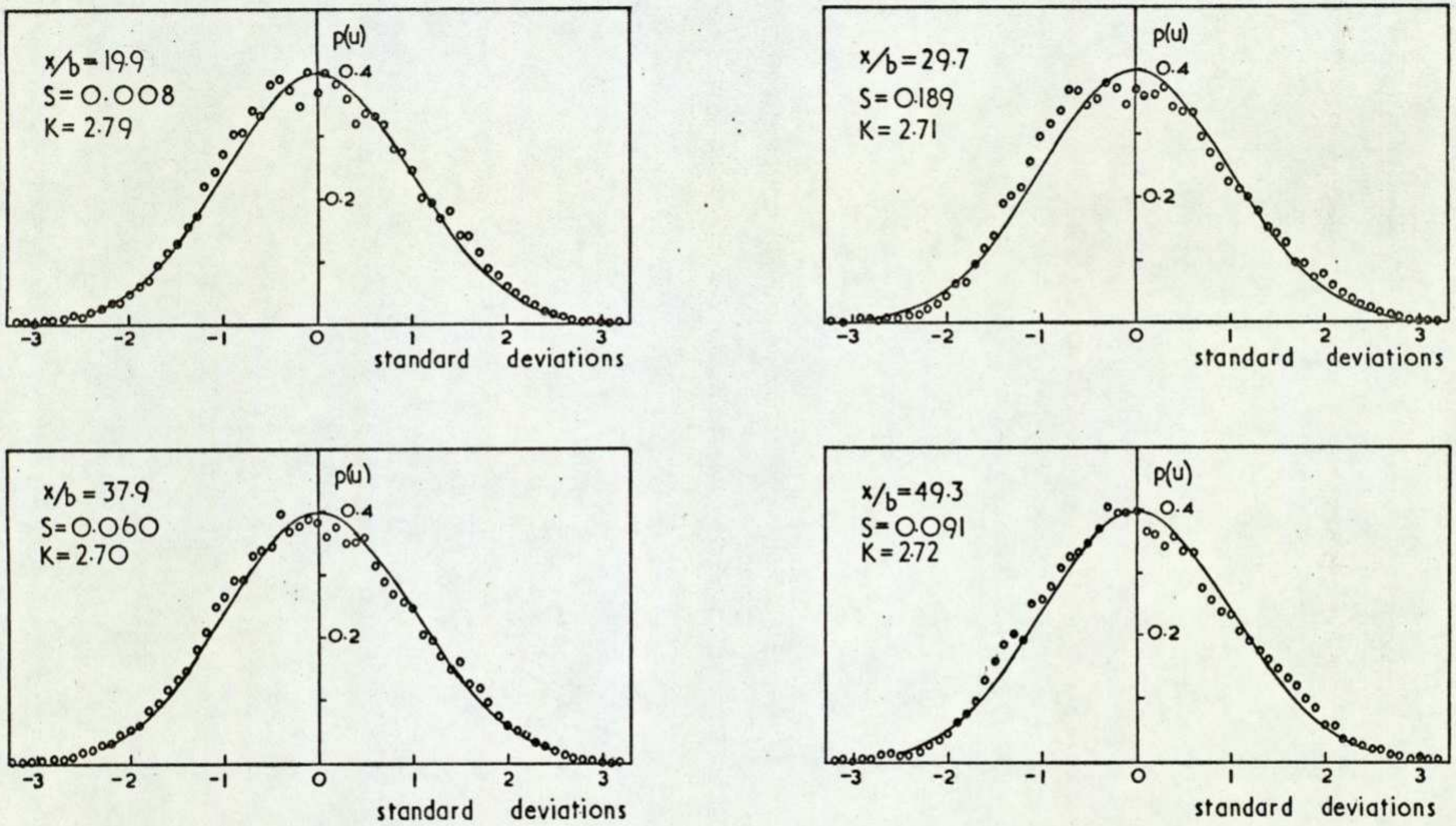

Grid 3

FIG 24 (concluded)

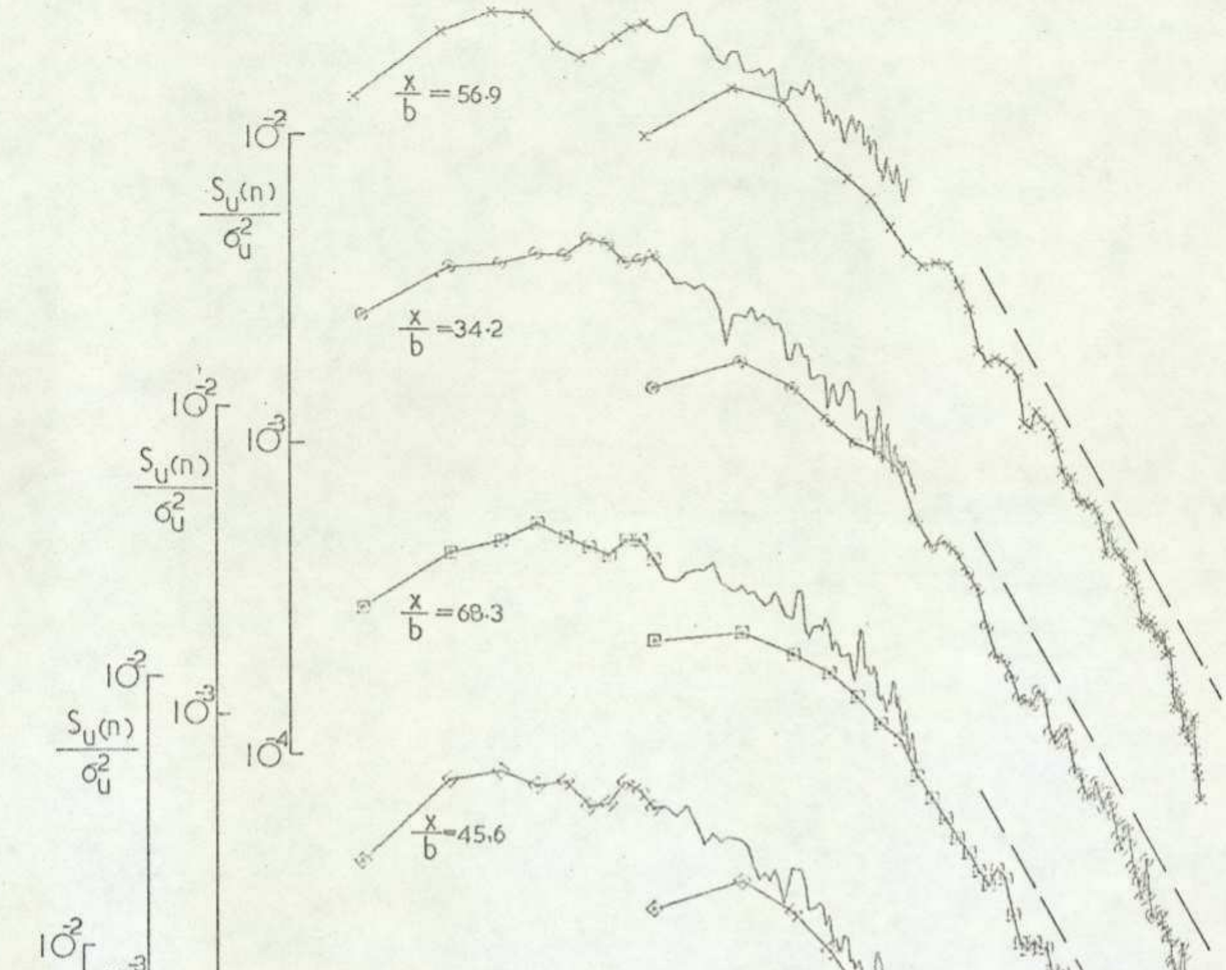

FIG 25 Spectra of longitudinal component of grid generated turbulence.

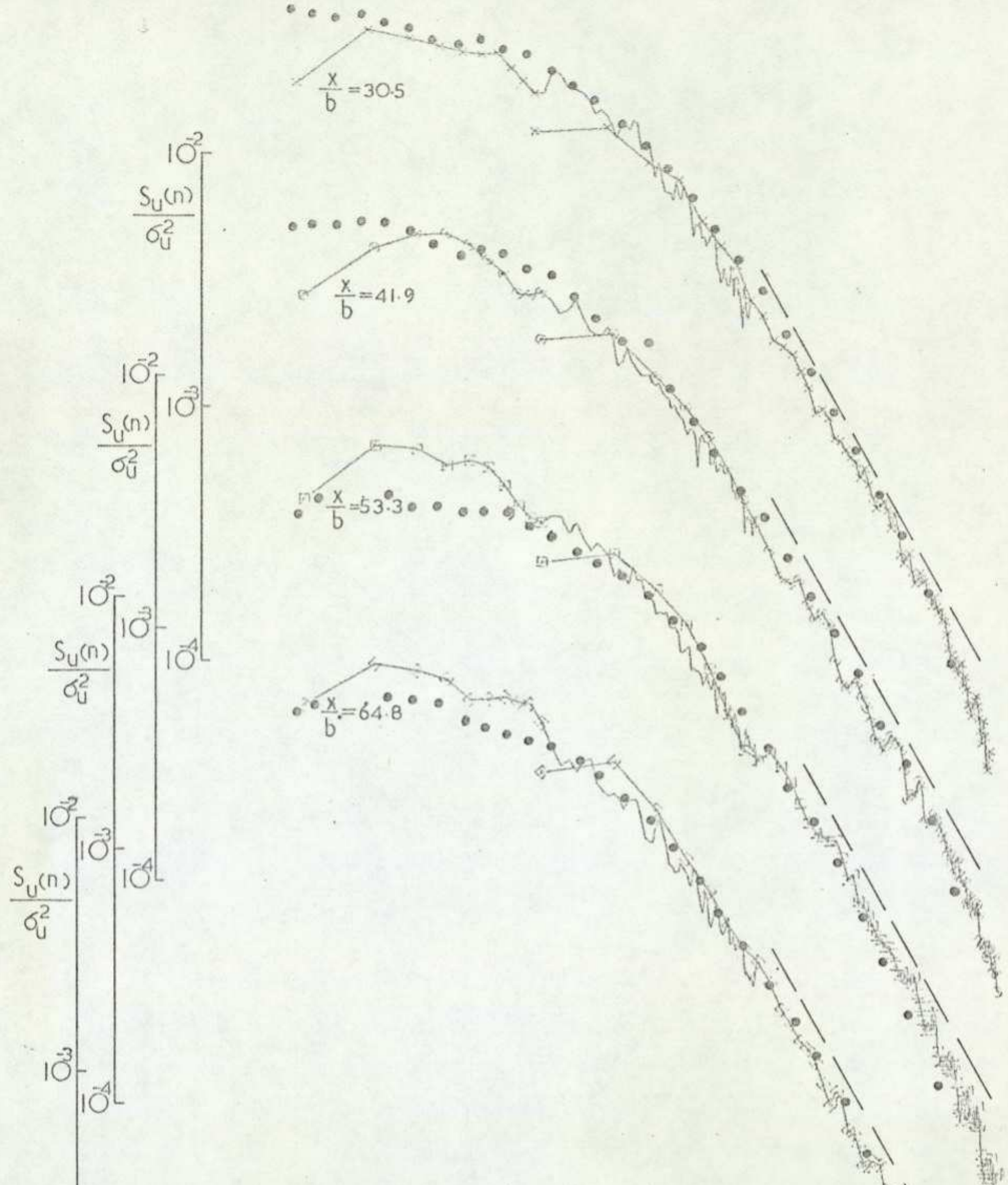
x/b = 30.5
x/b = 41.9
x/b = 53.3
x/b = 64.8
S_u(n)/σ_u^2
S_u(n)/σ_u^2
S_u(n)/σ_u^2
S_u(n)/σ_u^2
10^-2
10^-3
10^-4
10^-2
10^-3
10^-4
10^-2
10^-3
10^-4
10^-2
10^-3
10^-4
10^-2
10^-1
1
10
n/U (m^-1)
Grid 2

FIG 25 (cont.)

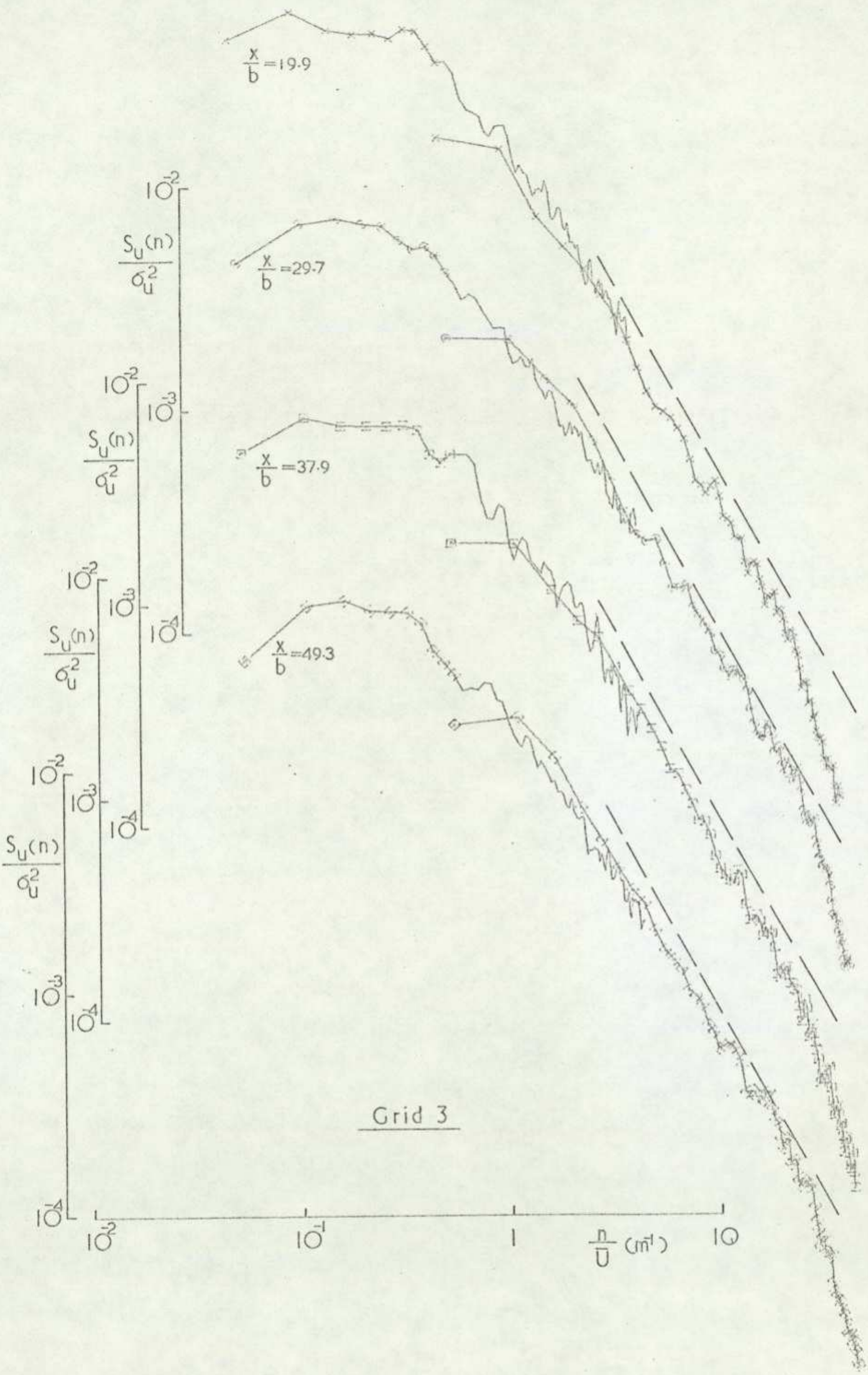

FIG 25 (concluded)

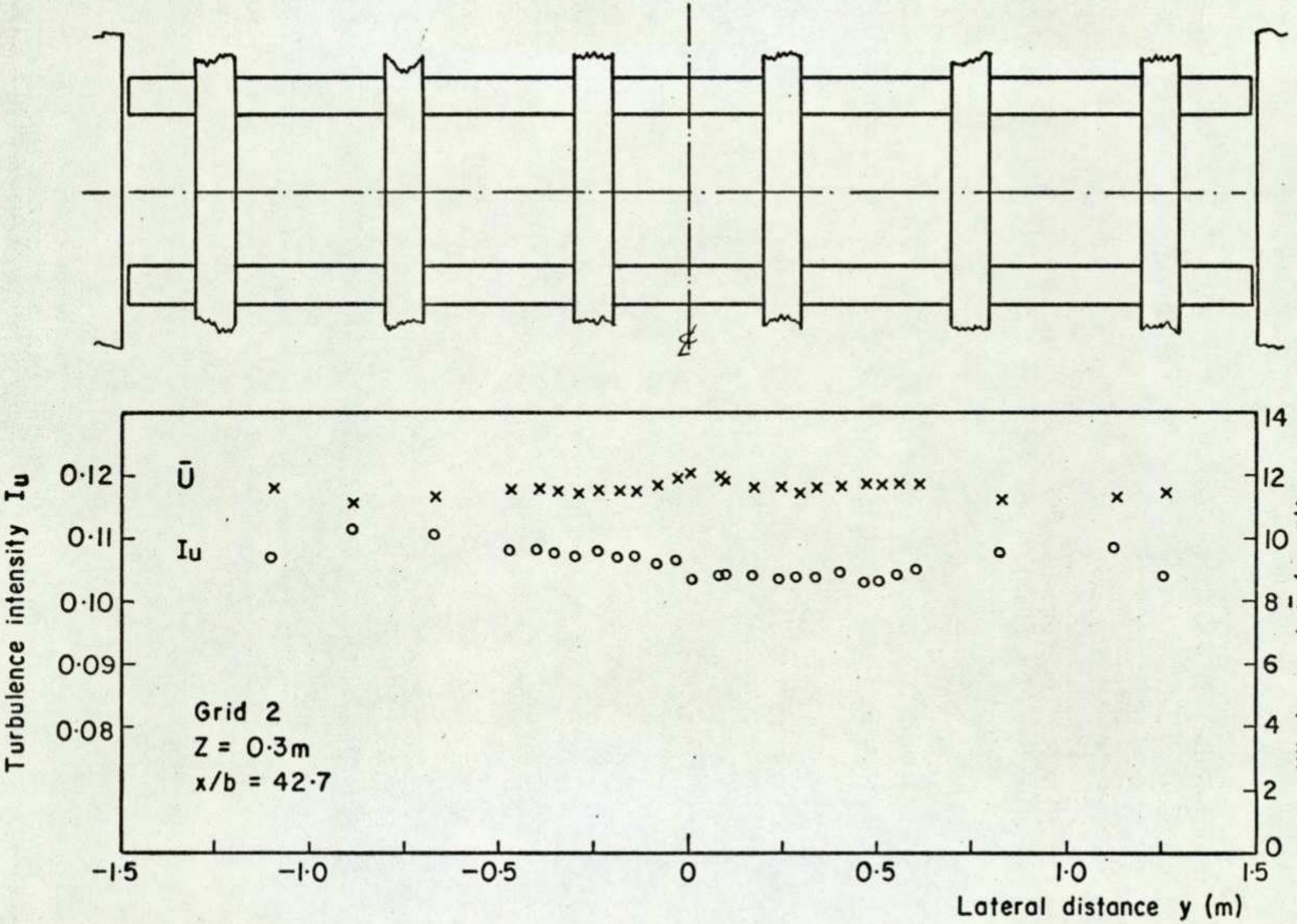

FIG. 26. MEAN FLOW CONDITIONS AT MODEL POSITION.

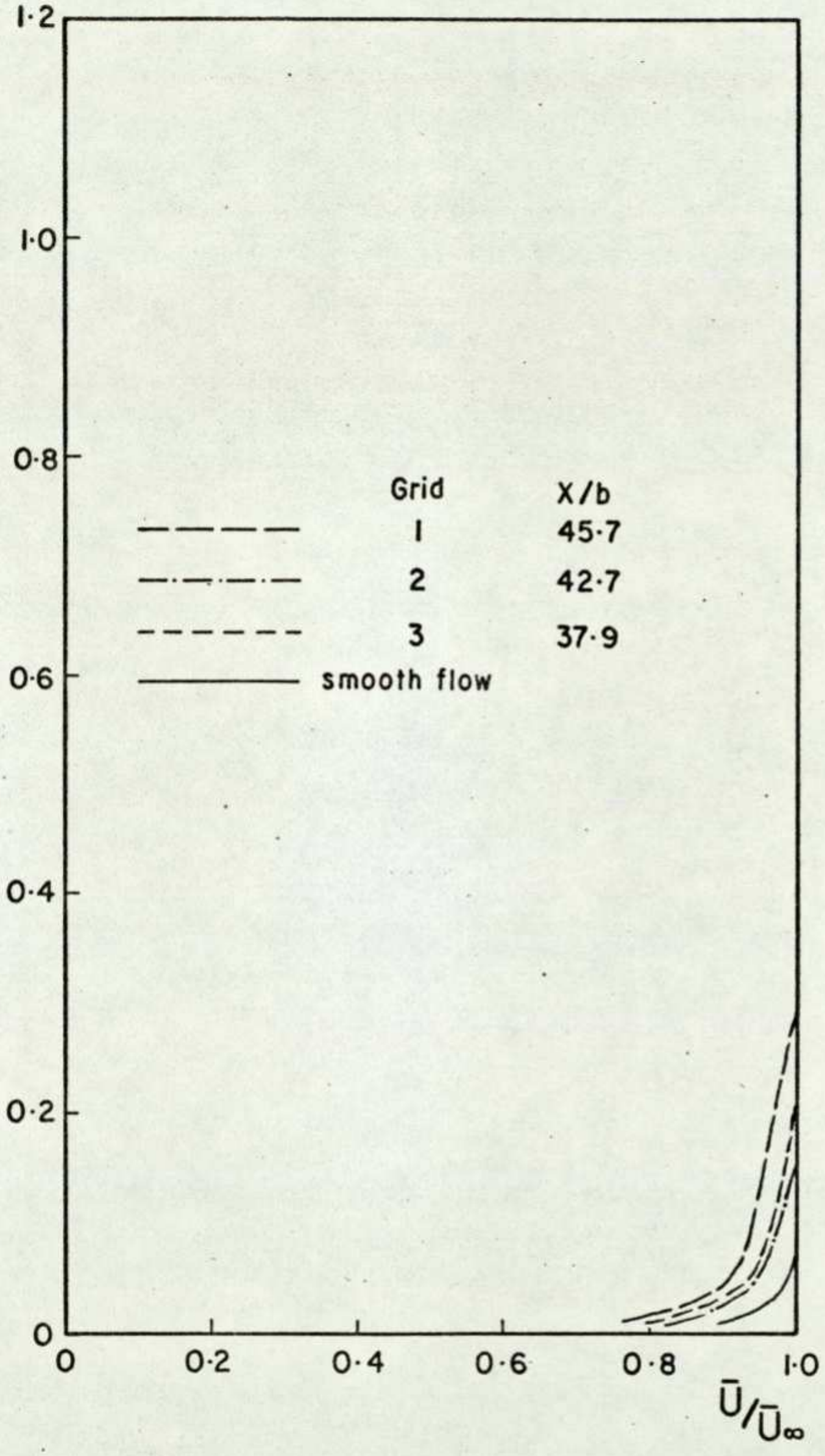

FIG. 27. VELOCITY DISTRIBUTION AT MODEL POSITIONS.

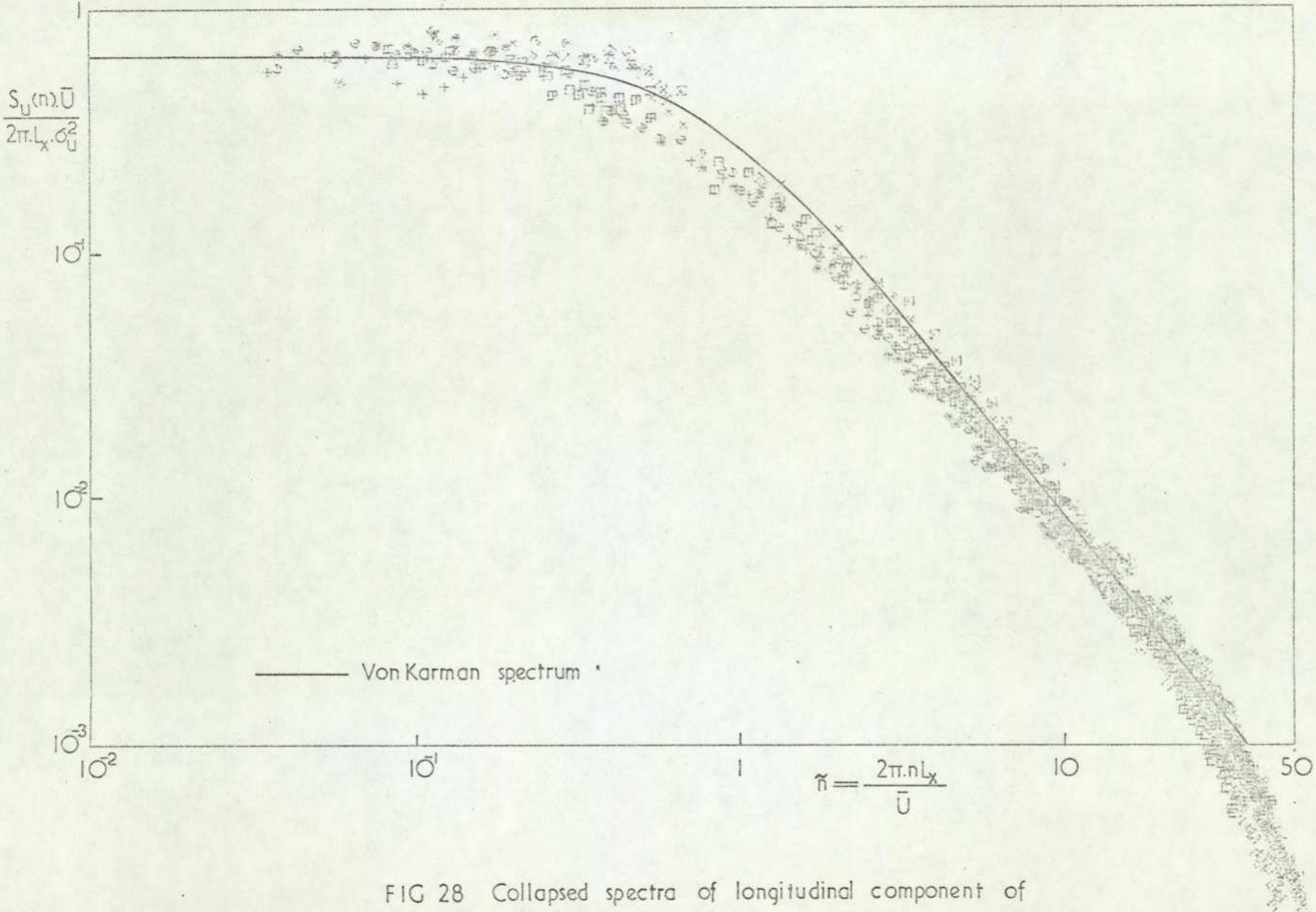

FIG 28 Collapsed spectra of longitudinal component of grid generated turbulence.

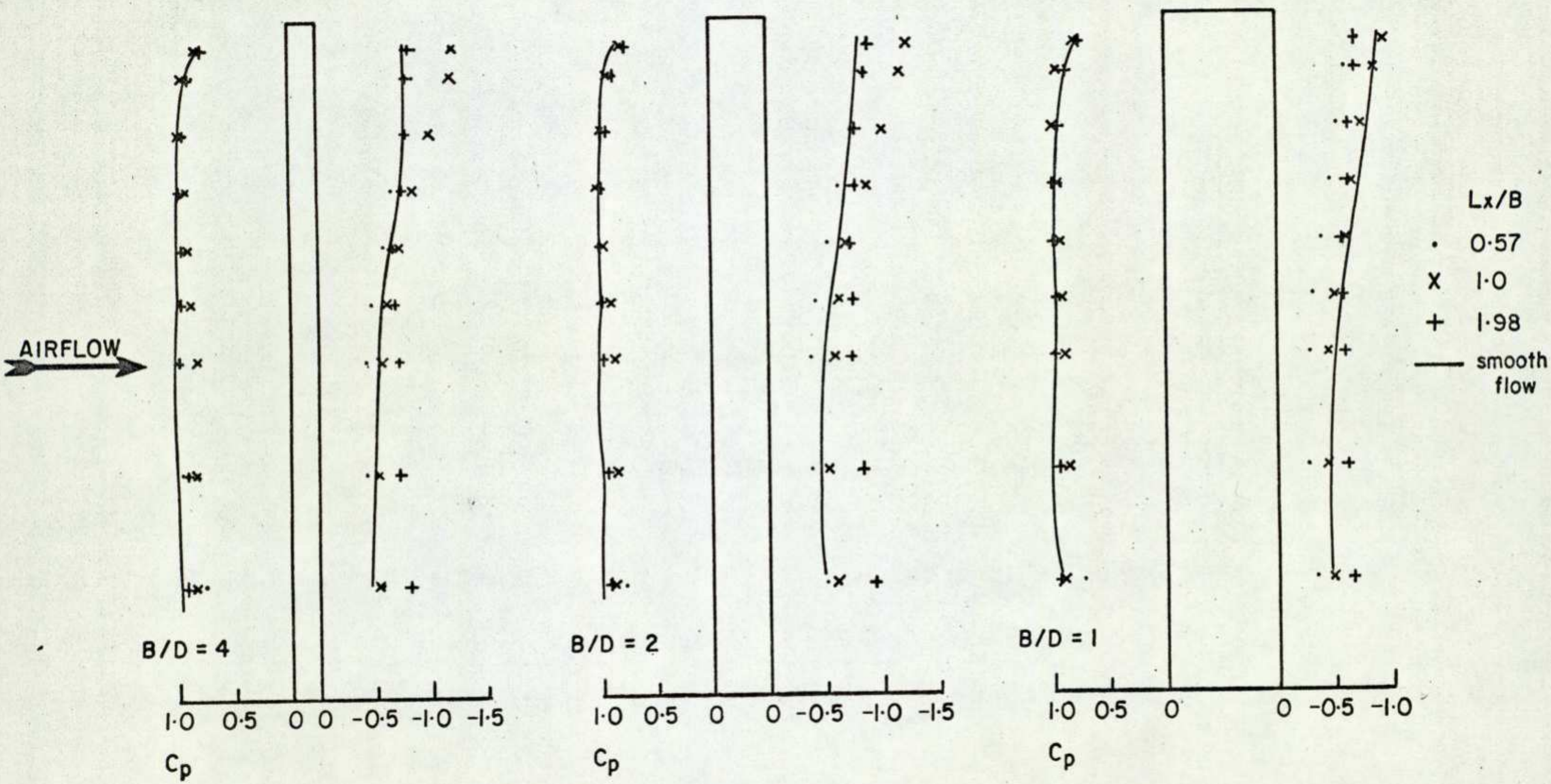

FIG. 29. DISTRIBUTION OF MEAN SURFACE PRESSURE ALONG THE CENTRE-LINE OF THE MODELS.

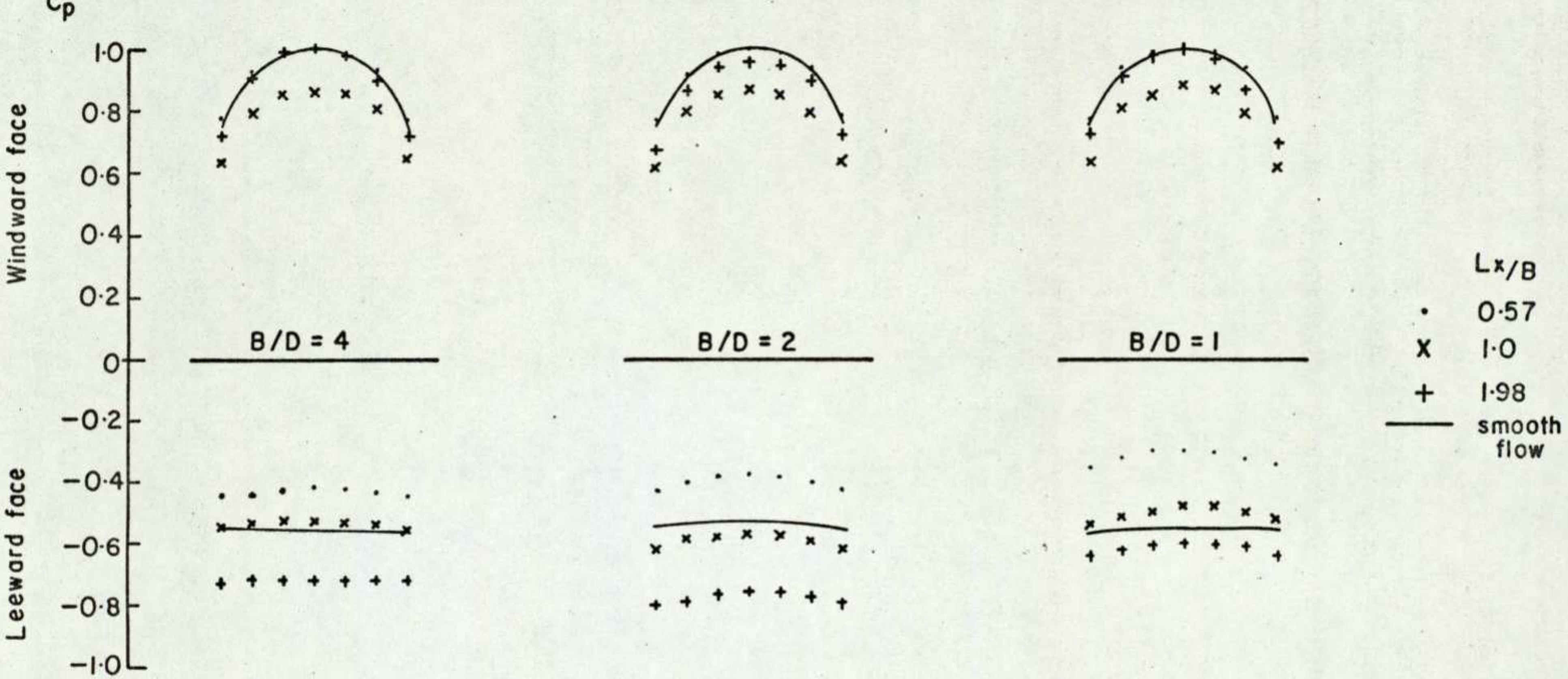

FIG. 30. DISTRIBUTION OF MEAN SURFACE PRESSURE AT LEVEL 3.

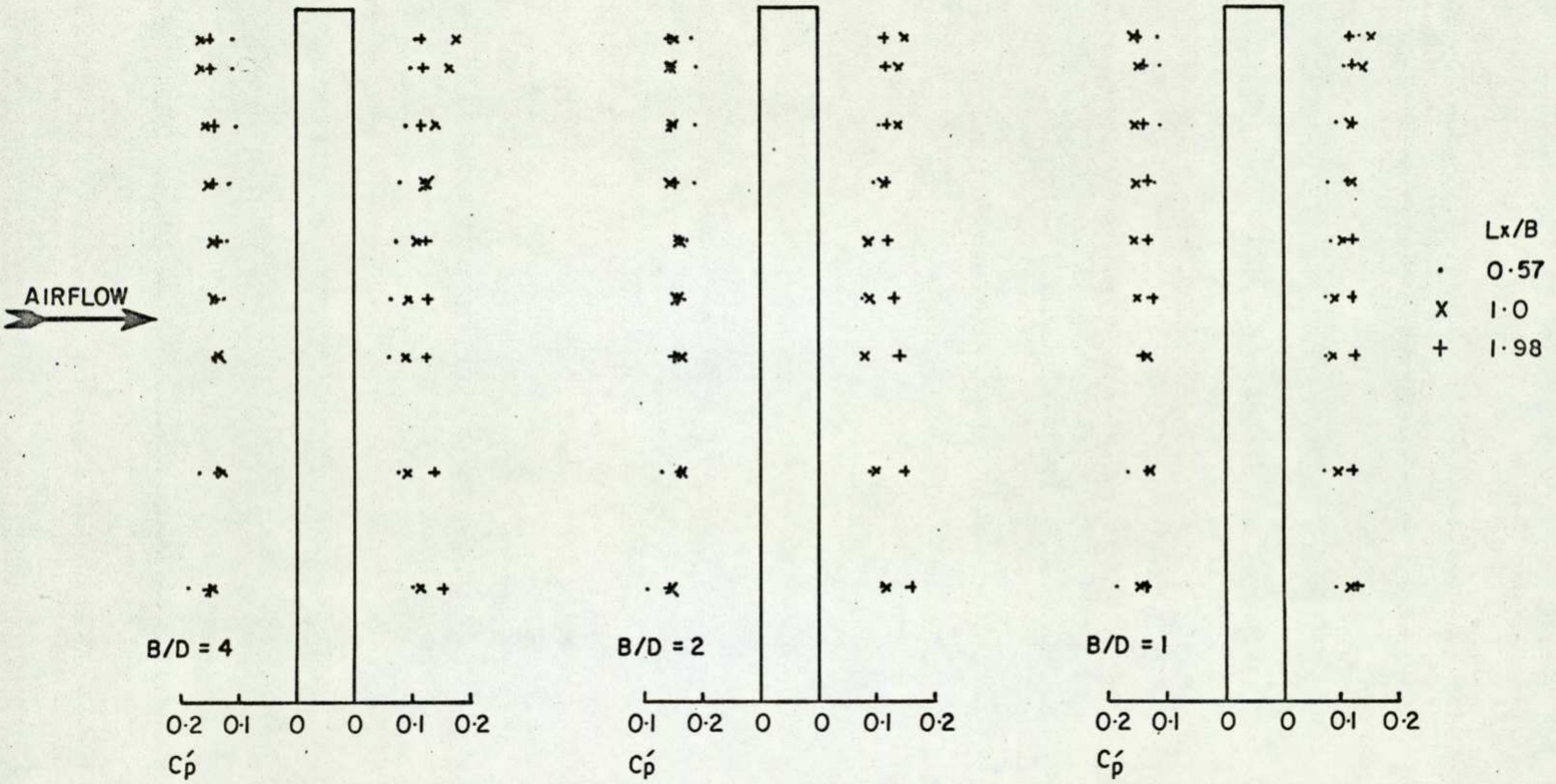

FIG. 31. DISTRIBUTION OF RMS PRESSURE COEFFICIENT ALONG THE CENTRE-LINE OF THE MODELS. (cont.,)

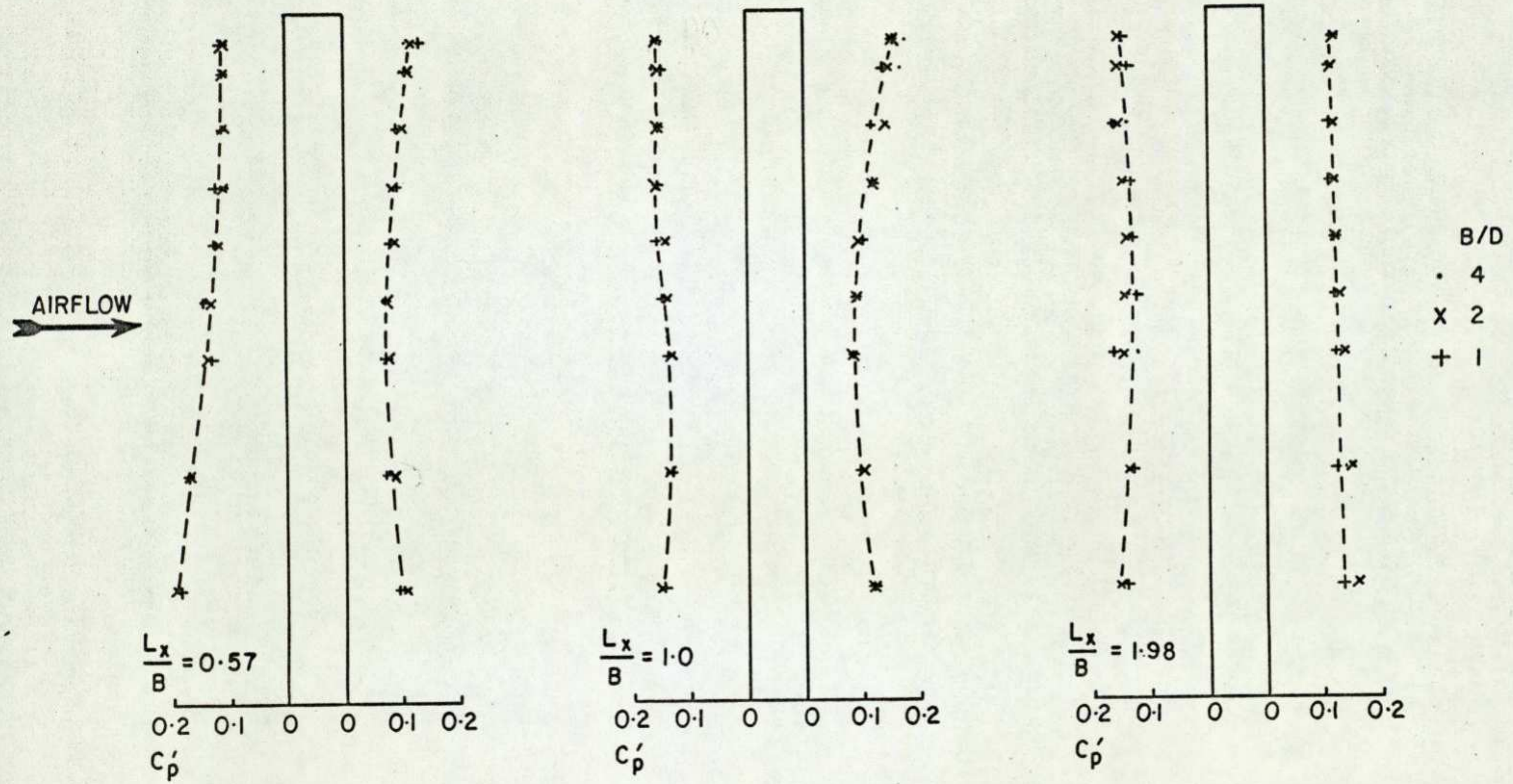

FIG. 31. (concluded)

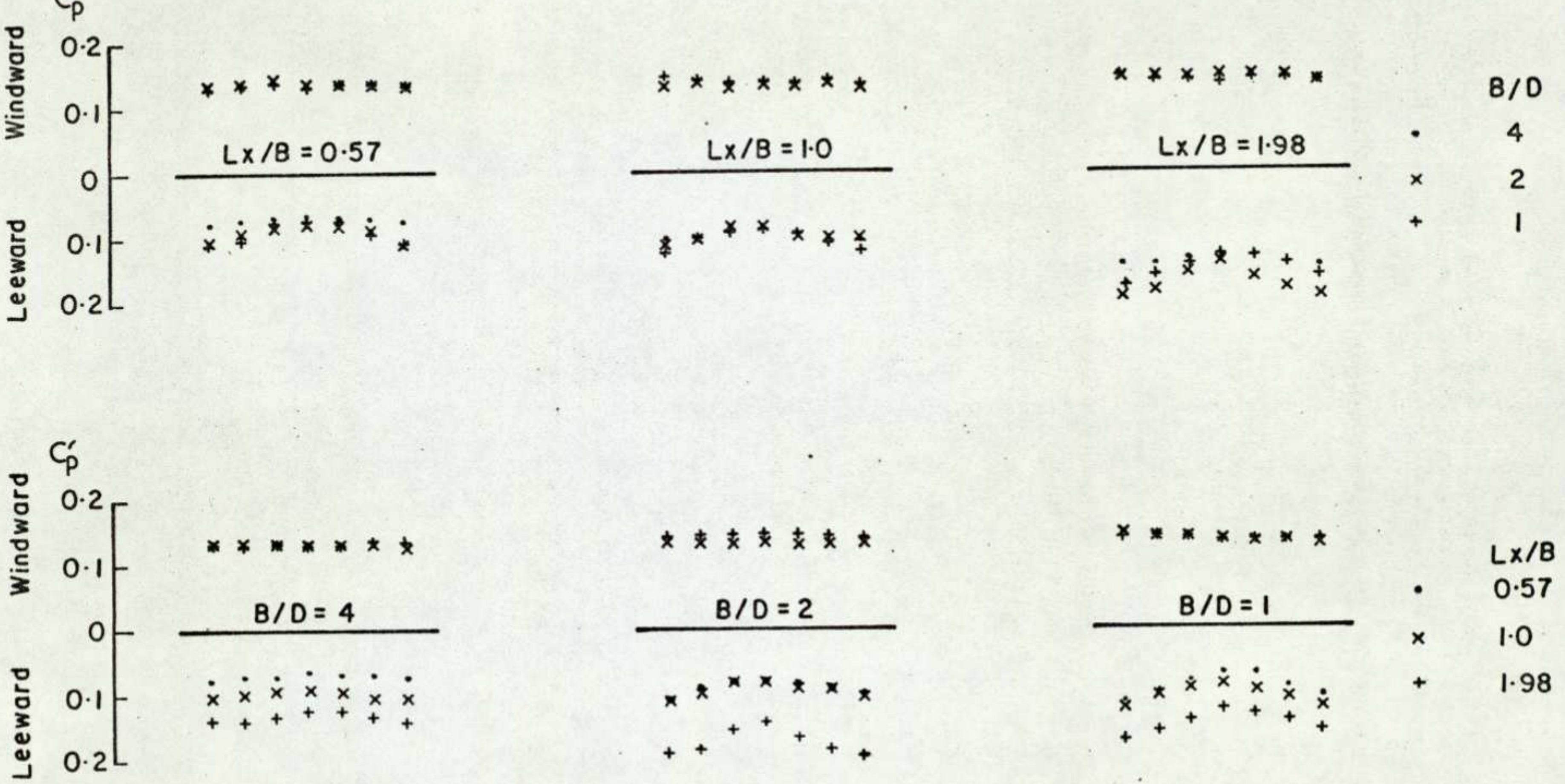

FIG. 32. DISTRIBUTION OF RMS PRESSURE COEFFICIENT AT LEVEL 3.

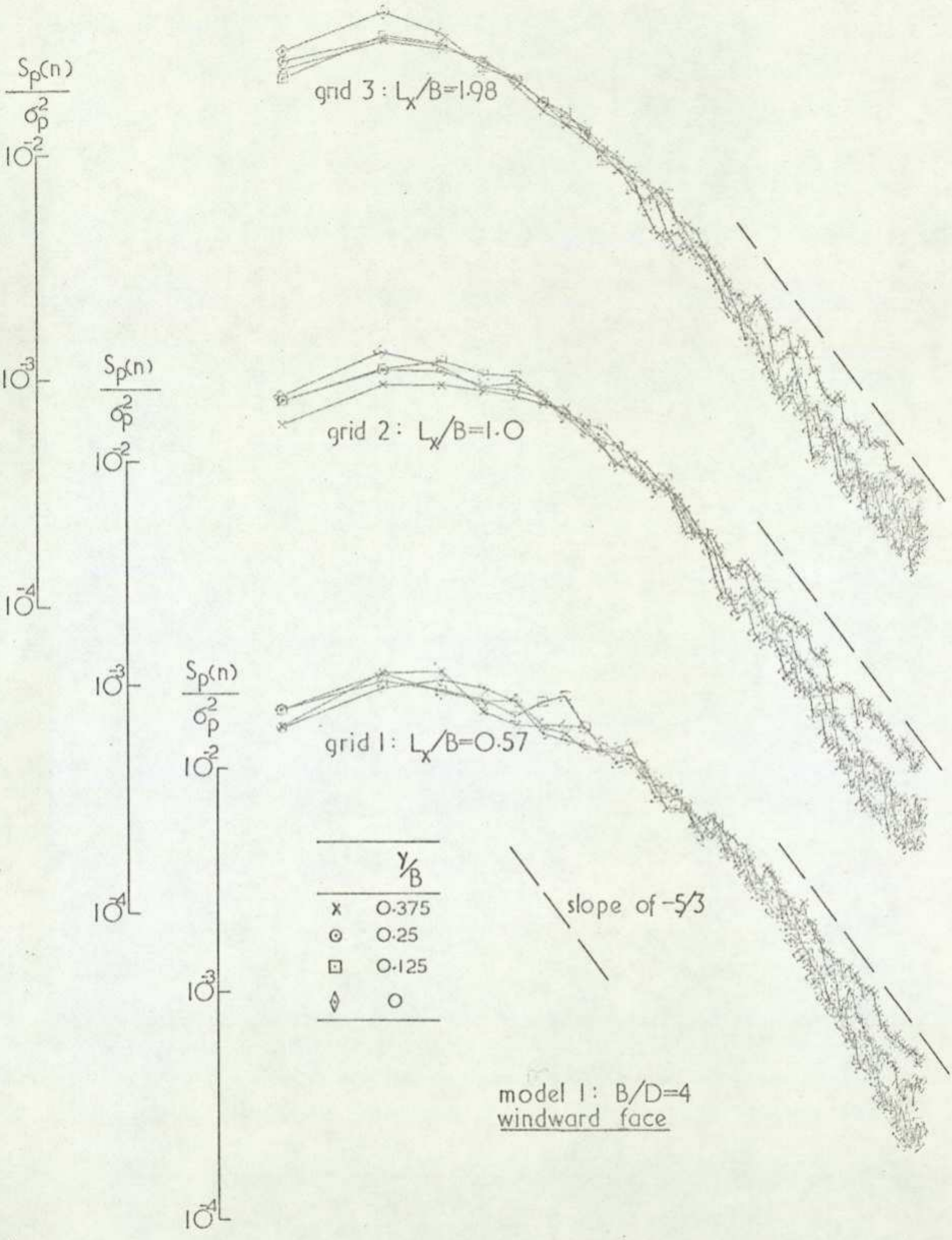

FIG 33 Spectra of pressure fluctuations on models at $z/H=0.5$

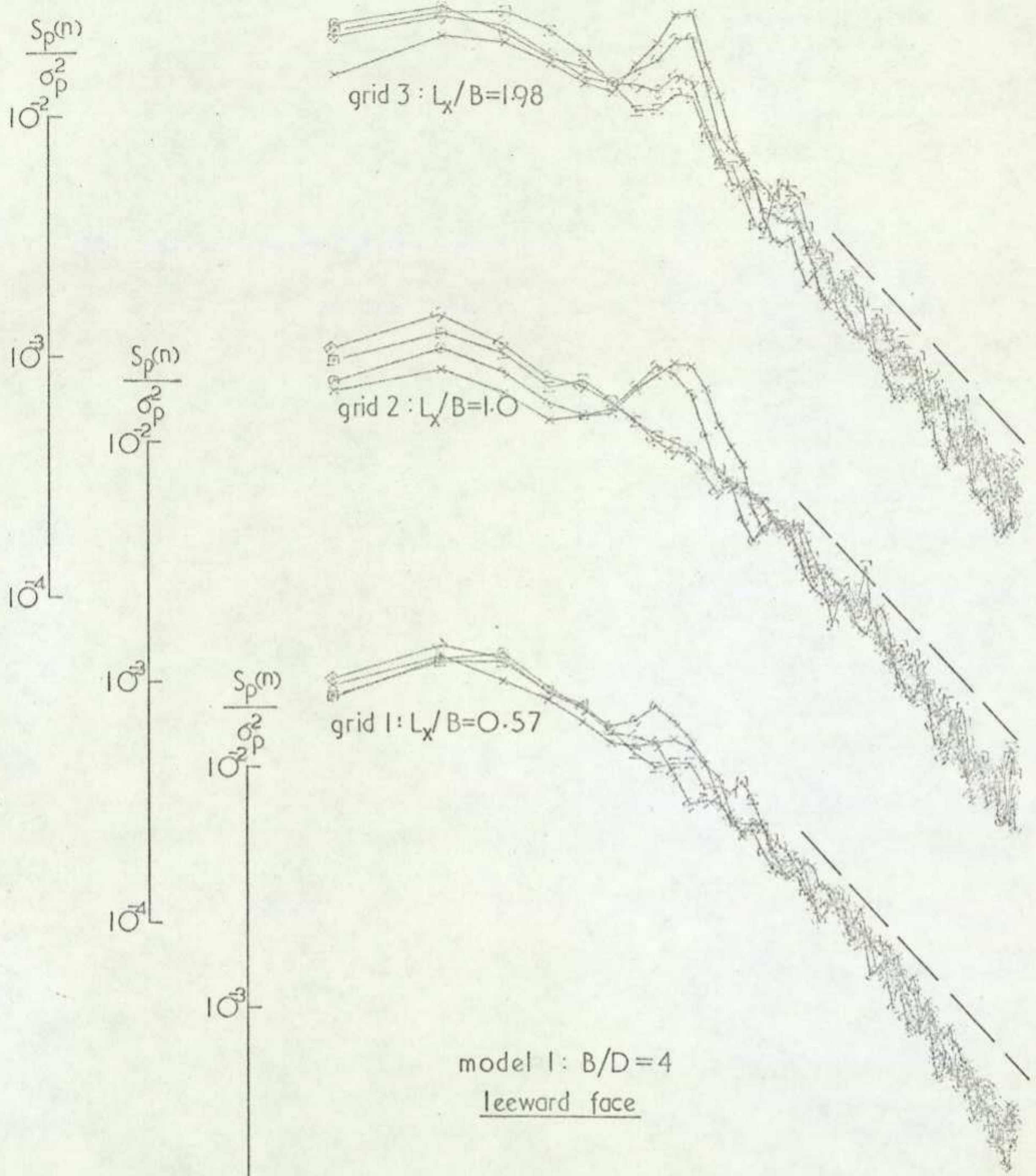
$\frac{S_p(n)}{\sigma_p^2}$
10^{-2}
10^{-3}
10^{-4}
grid 3 : $L_x/B=1.98$
$\frac{S_p(n)}{\sigma_p^2}$
10^{-2}
10^{-3}
10^{-4}
grid 2 : $L_x/B=1.0$
$\frac{S_p(n)}{\sigma_p^2}$
10^{-2}
10^{-3}
10^{-4}
grid 1 : $L_x/B=0.57$
model 1 : B/D = 4
leeward face
10^{-2}
10^{-1}
1
$\frac{nB}{\bar{U}}$

FIG 33 (cont.)

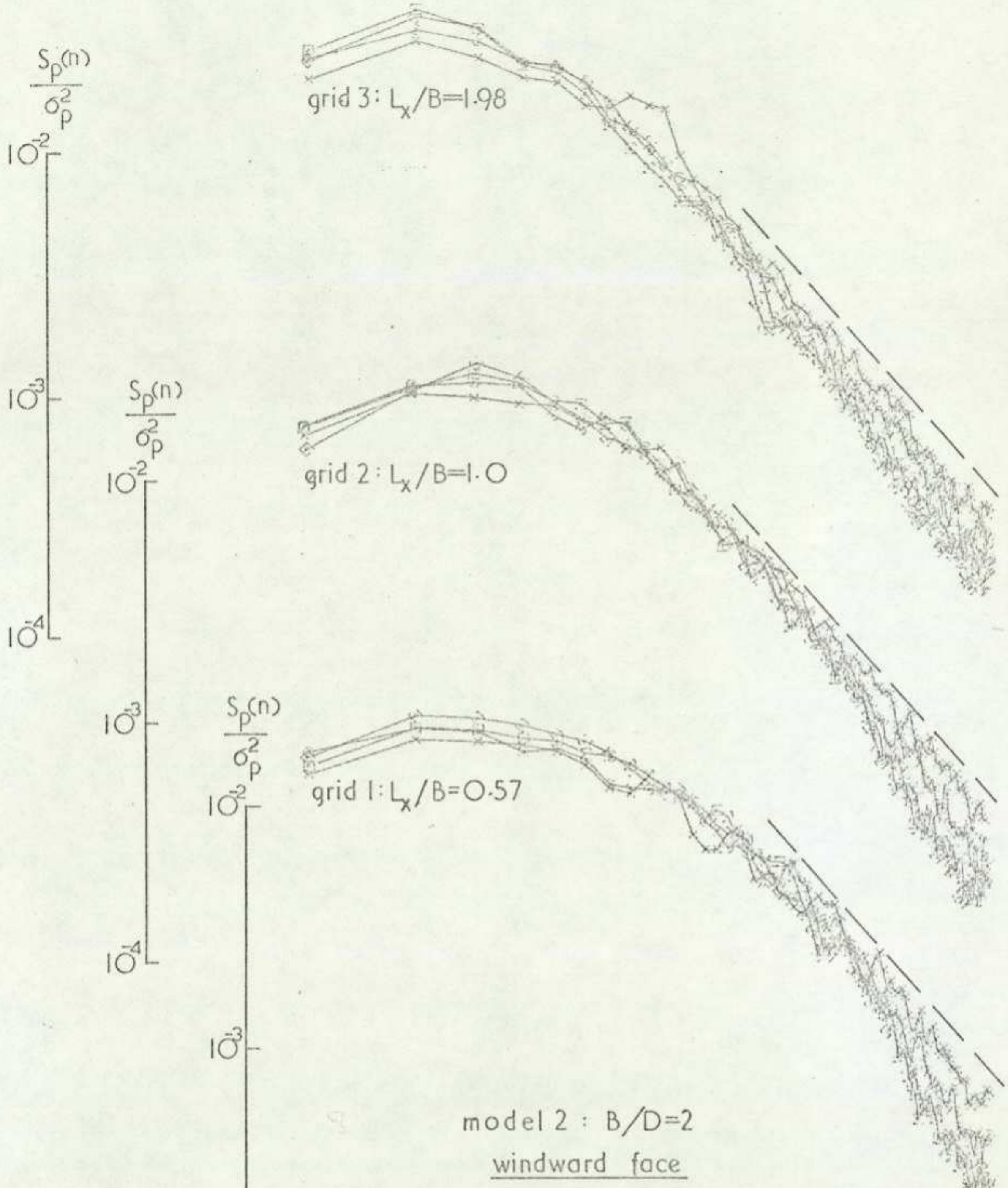
$\frac{S_p(n)}{\sigma_p^2}$
10^{-2}
10^{-3}
10^{-4}
grid 3: L_x/B=1.98
$\frac{S_p(n)}{\sigma_p^2}$
10^{-2}
10^{-3}
10^{-4}
grid 2: L_x/B=1.0
$\frac{S_p(n)}{\sigma_p^2}$
10^{-2}
10^{-3}
10^{-4}
grid 1: L_x/B=0.57
model 2 : B/D=2
windward face
10^{-2}
10^{-1}
$\frac{nB}{\bar{U}}$
1

FIG. 33 (cont.)

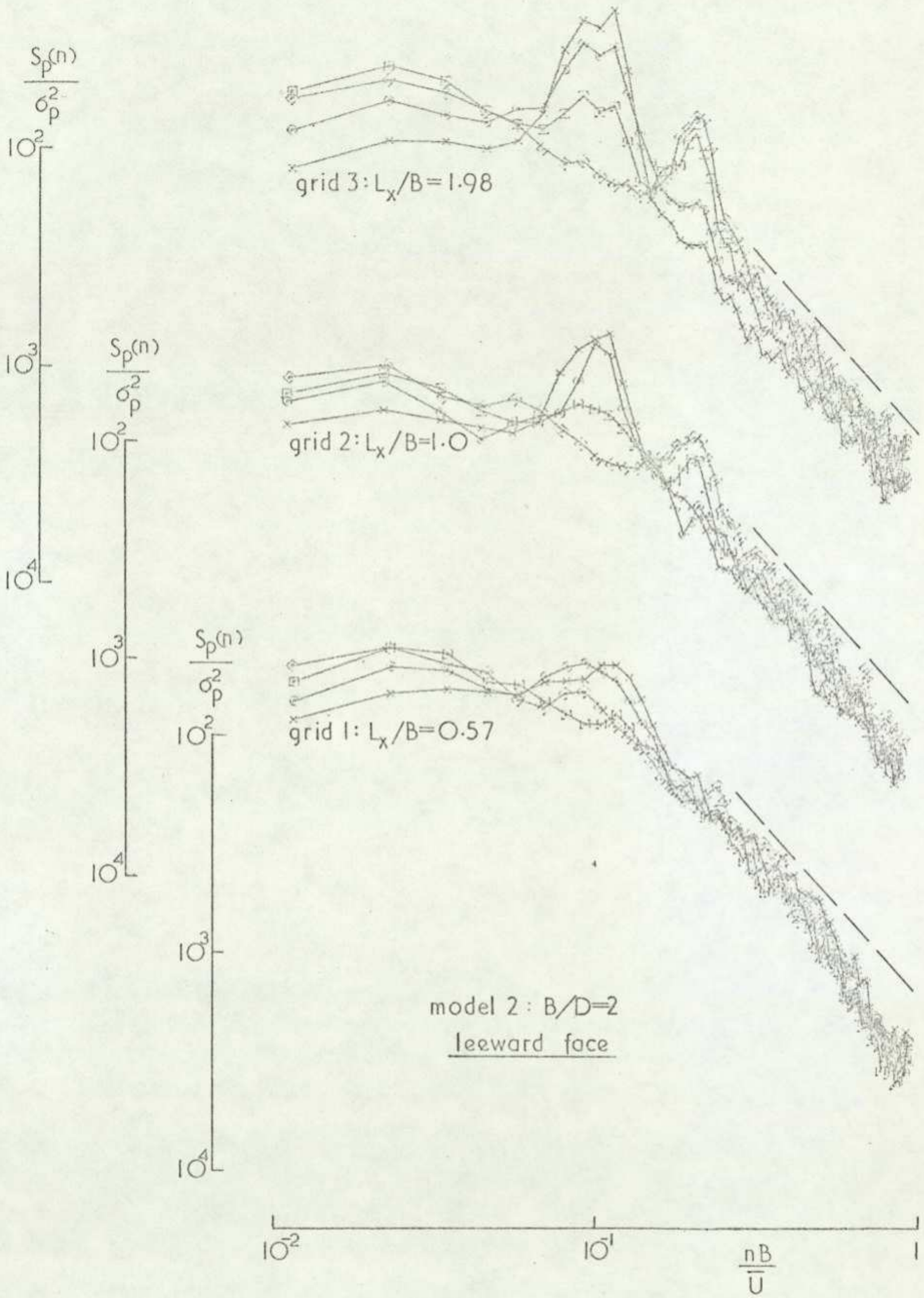
$\frac{S_p(n)}{\sigma_p^2}$
10^2
10^3
10^4
$\frac{S_p(n)}{\sigma_p^2}$
10^2
10^3
10^4
$\frac{S_p(n)}{\sigma_p^2}$
10^2
10^3
10^4
grid 3: $L_x/B=1.98$
grid 2: $L_x/B=1.0$
grid 1: $L_x/B=0.57$
model 2 : B/D=2
leeward face
10^{-2}
10^{-1}
1
$\frac{nB}{\bar{U}}$

FIG 33 (cont.)

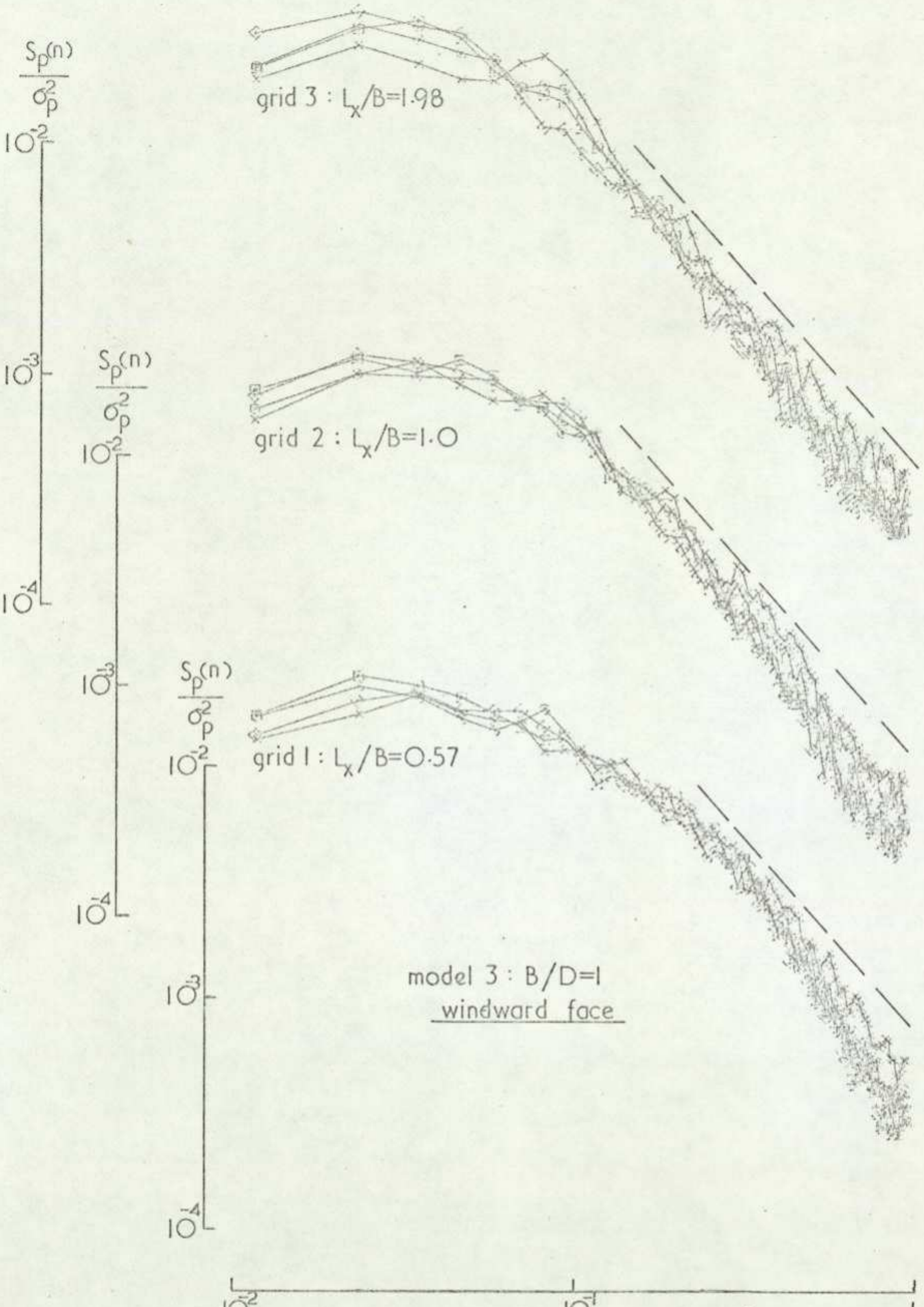
$\frac{S_p(n)}{\sigma_p^2}$
10^{-2}
10^{-3}
10^{-4}
grid 3 : $L_x/B=1.98$
grid 2 : $L_x/B=1.0$
grid 1 : $L_x/B=0.57$
model 3 : B/D=1
windward face
10^{-2}
10^{-1}
1
$\frac{nB}{\overline{U}}$

FIG 33 (cont.)

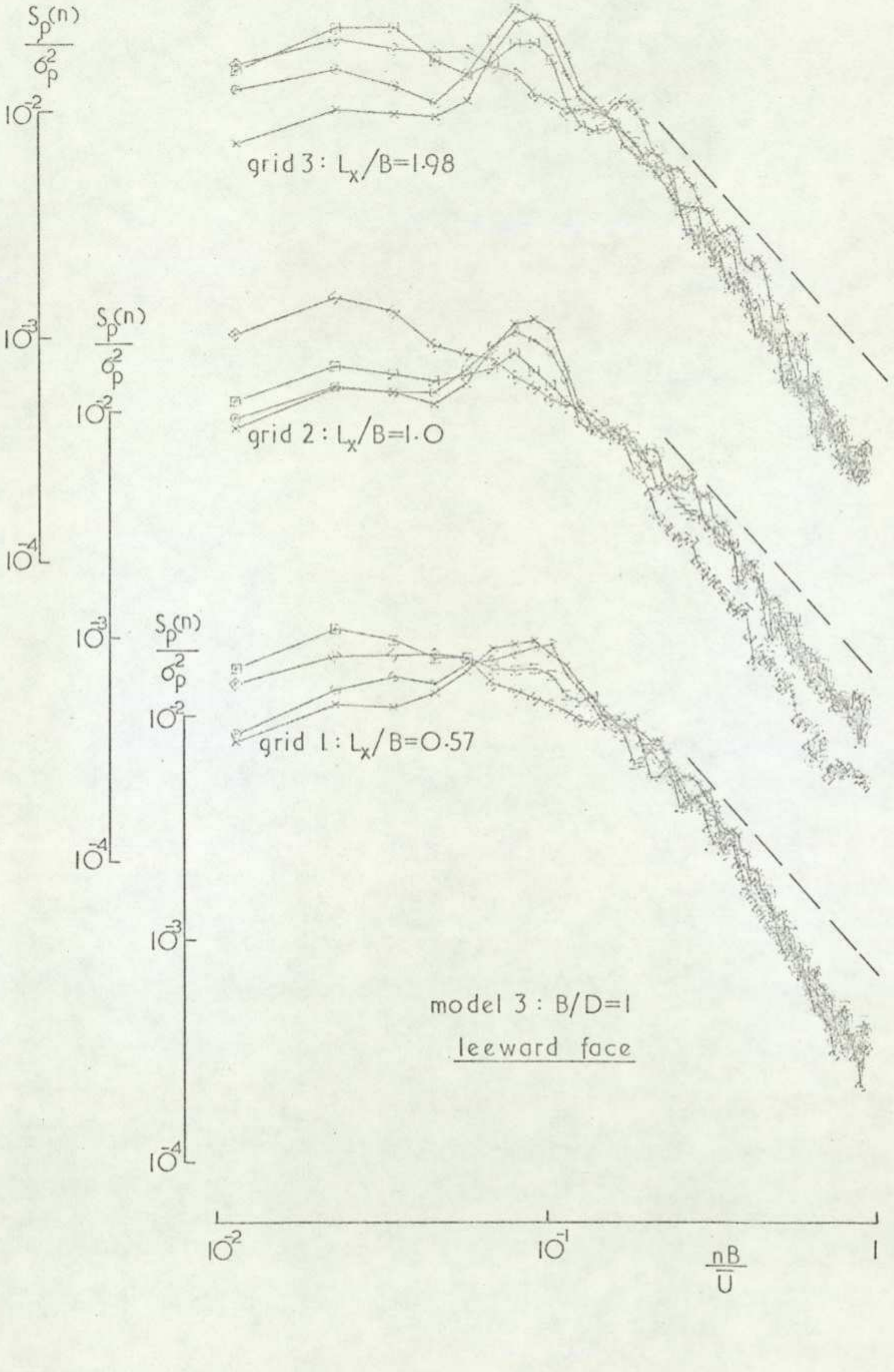

FIG 33 (concluded)

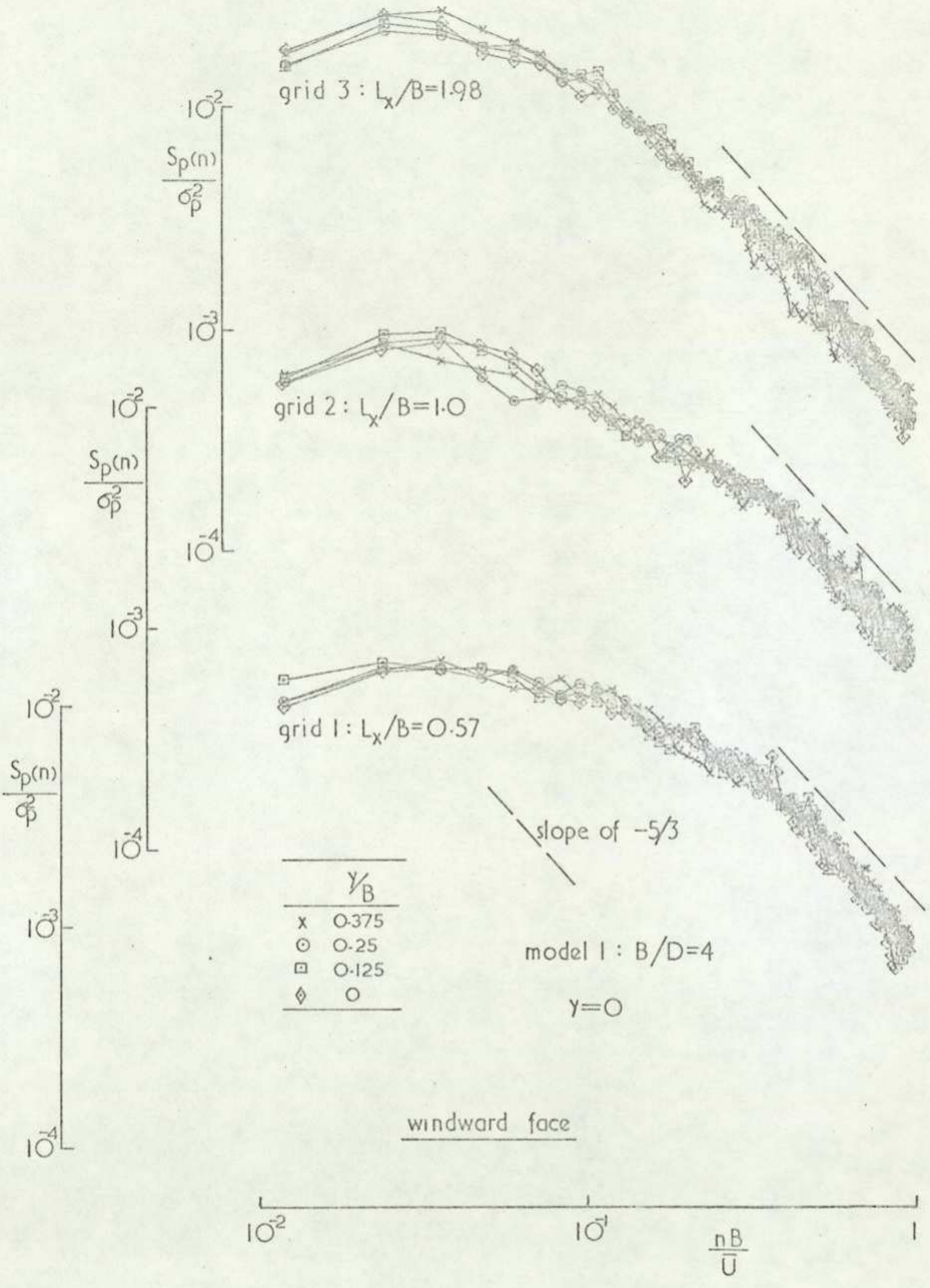

FIG 34 Spectra of pressure fluctuations on models at z/H=0.96

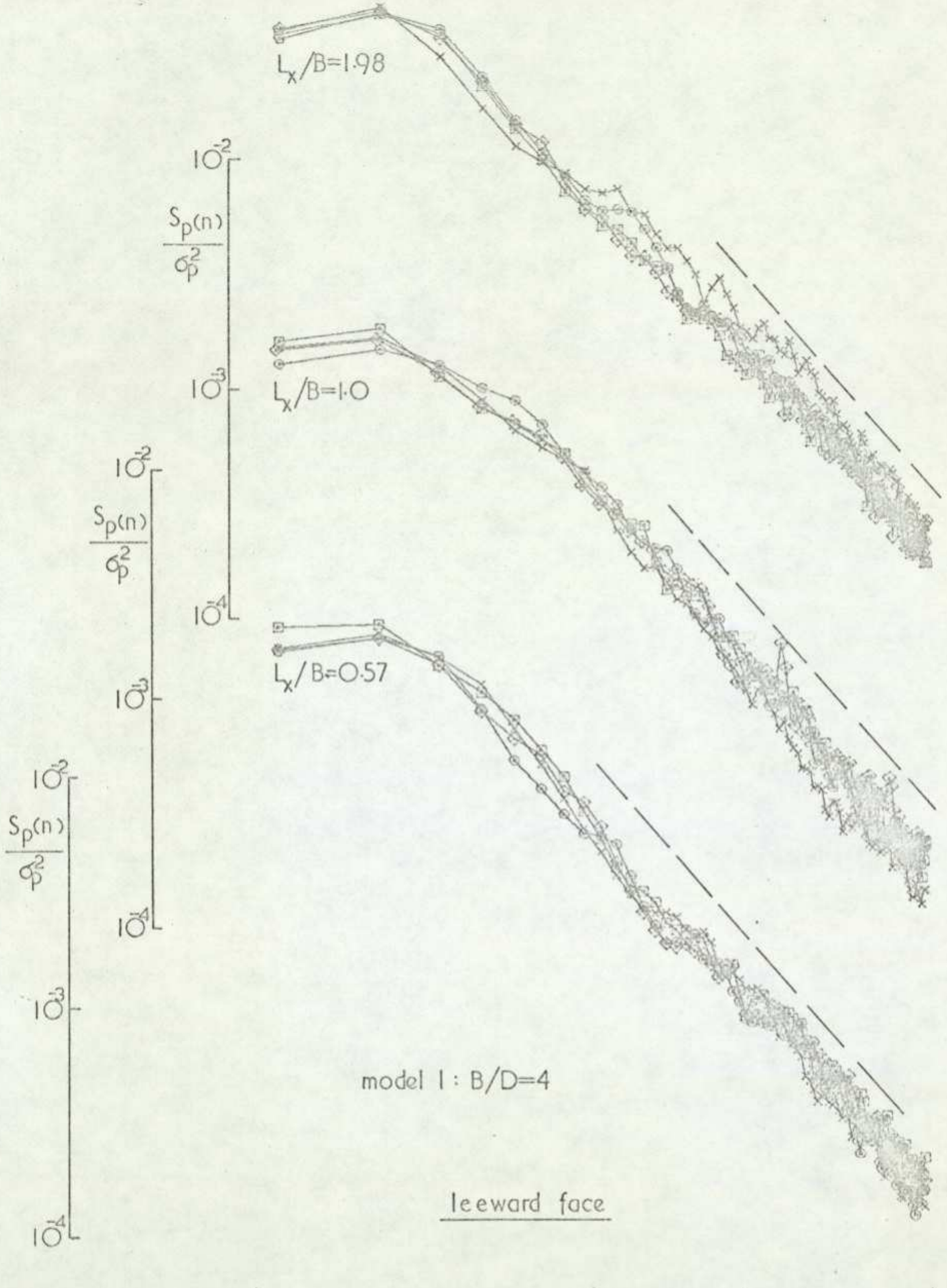
$L_x/B=1.98$
$L_x/B=1.0$
$L_x/B=0.57$
$\frac{S_p(n)}{\sigma_p^2}$
10^{-2}
10^{-3}
10^{-4}
model 1 : B/D=4
leeward face
10^{-2}
10^{-1}
1
$\frac{nB}{\bar{U}}$

FIG 34 (cont.)

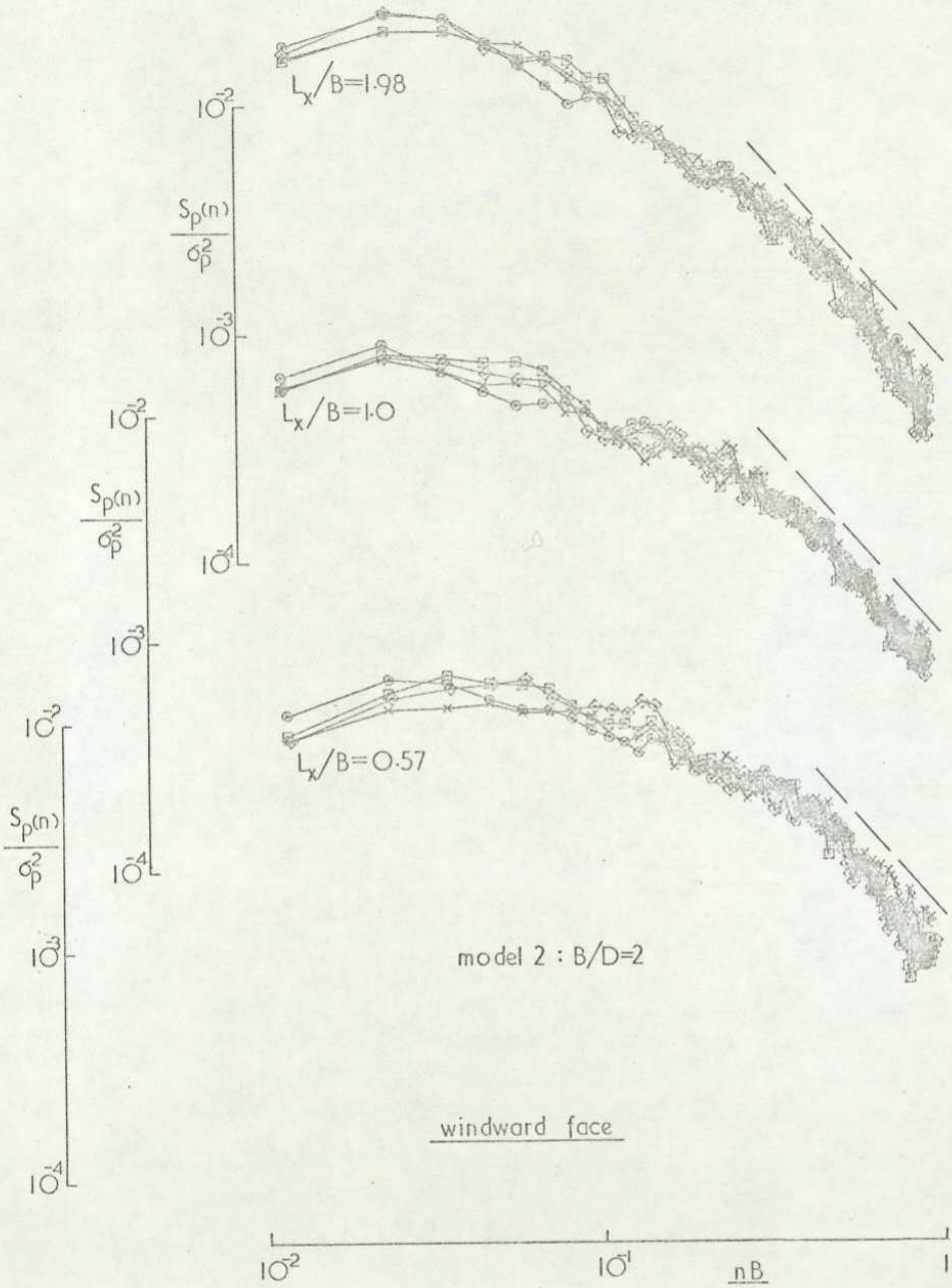
10^{-2}
$\frac{S_p(n)}{\sigma_p^2}$
10^{-3}
10^{-4}
$L_x/B=1.98$
$L_x/B=1.0$
$L_x/B=0.57$
model 2 : B/D=2
windward face
10^{-2}
10^{-1}
1
$\frac{nB}{\overline{U}}$

FIG 34 (cont.)

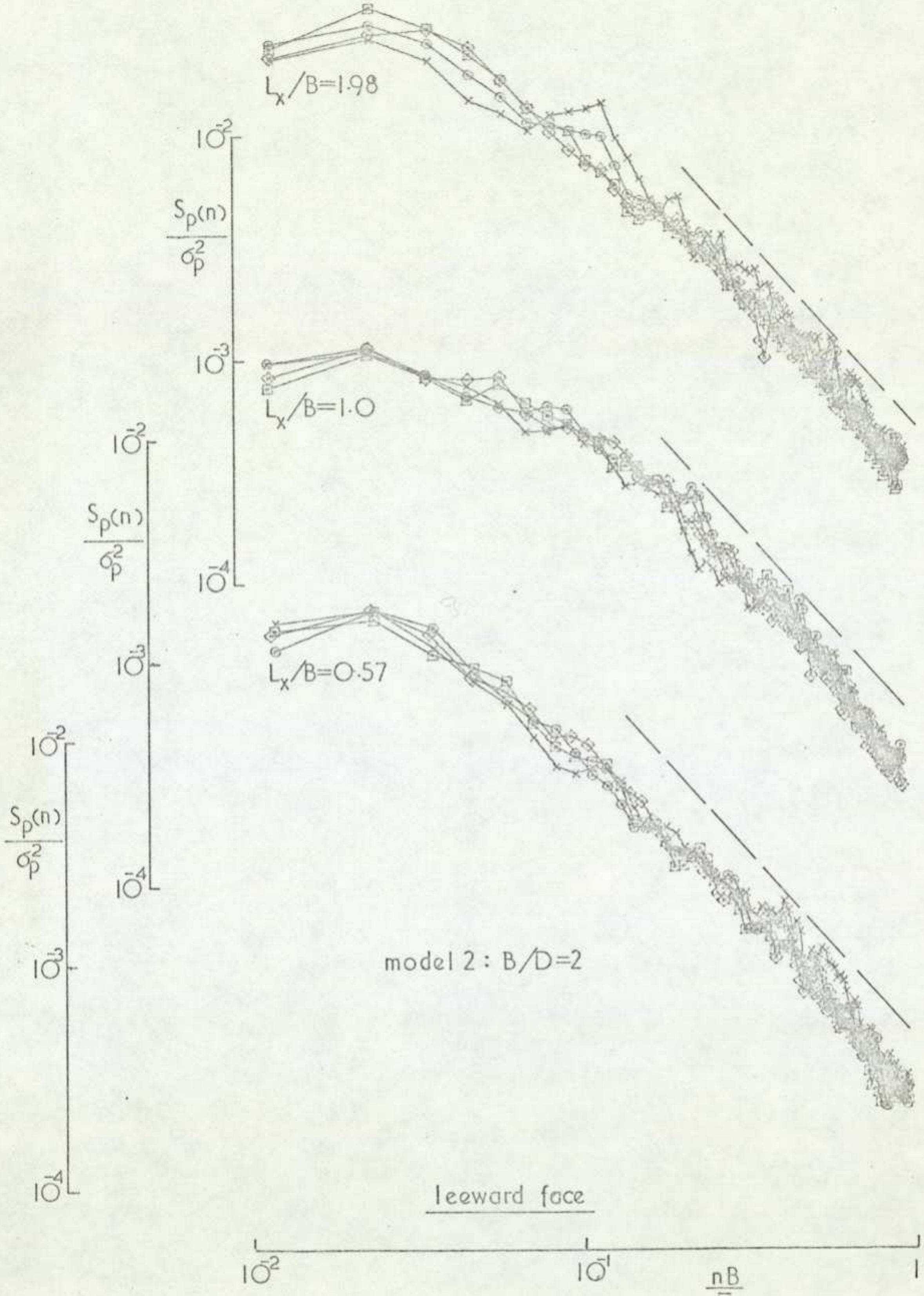
$L_x/B=1.98$
10^{-2}
$\frac{S_p(n)}{\sigma_p^2}$
10^{-3}
$L_x/B=1.0$
10^{-4}
10^{-2}
$\frac{S_p(n)}{\sigma_p^2}$
10^{-3}
$L_x/B=0.57$
10^{-4}
10^{-2}
$\frac{S_p(n)}{\sigma_p^2}$
10^{-3}
model 2 : B/D=2
10^{-4}
leeward face
10^{-2}
10^{-1}
$\frac{nB}{\bar{U}}$
1

FIG 34 (cont.)

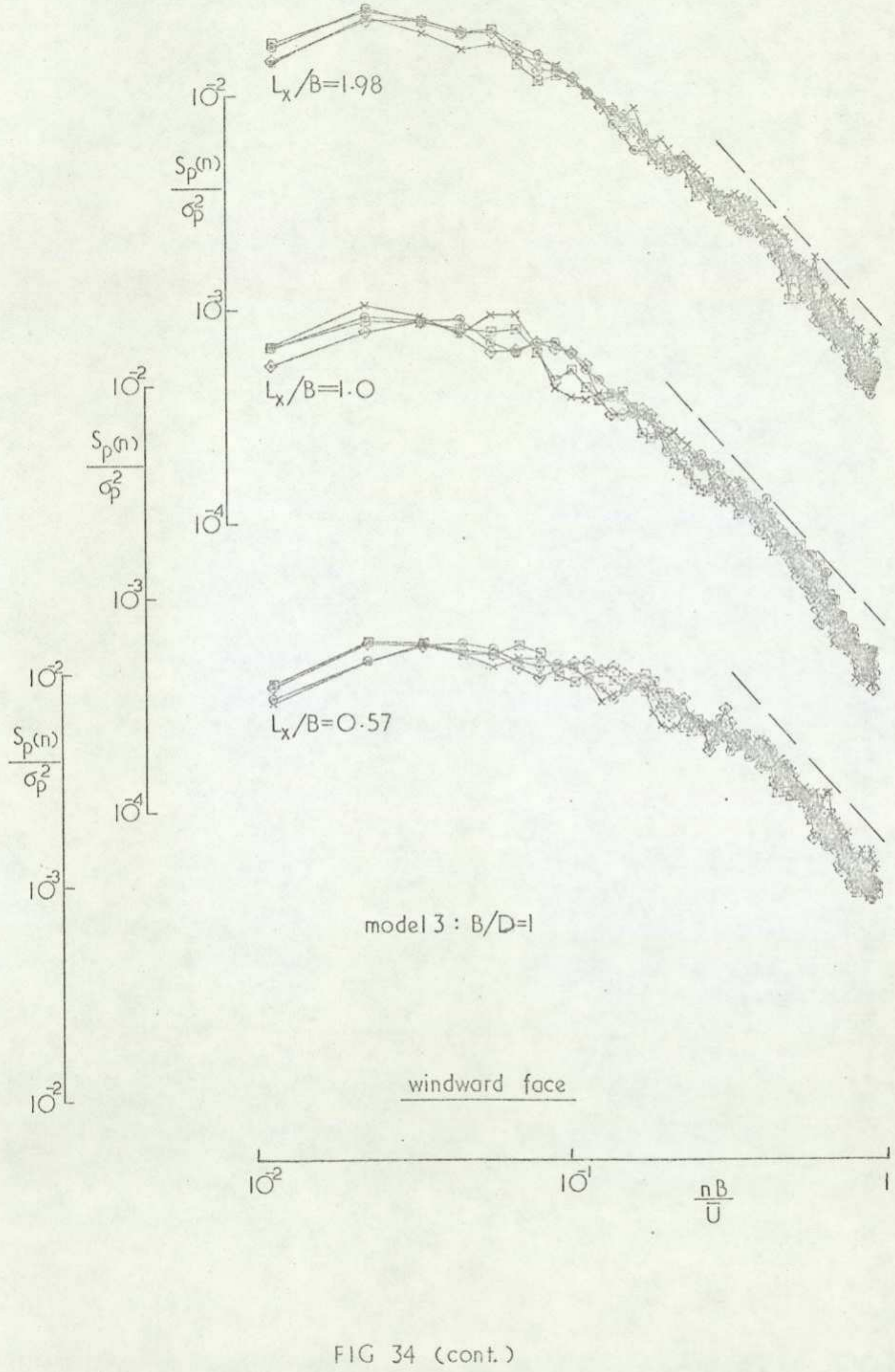
$L_x/B=1.98$
10^{-2}
$\frac{S_p(n)}{\sigma_p^2}$
10^{-3}
10^{-4}
$L_x/B=1.0$
10^{-2}
$\frac{S_p(n)}{\sigma_p^2}$
10^{-3}
10^{-4}
$L_x/B=0.57$
10^{-2}
$\frac{S_p(n)}{\sigma_p^2}$
10^{-3}
10^{-2}
model 3 : B/D=1
windward face
10^{-2}
10^{-1}
1
$\frac{nB}{\bar{U}}$

FIG 34 (cont.)

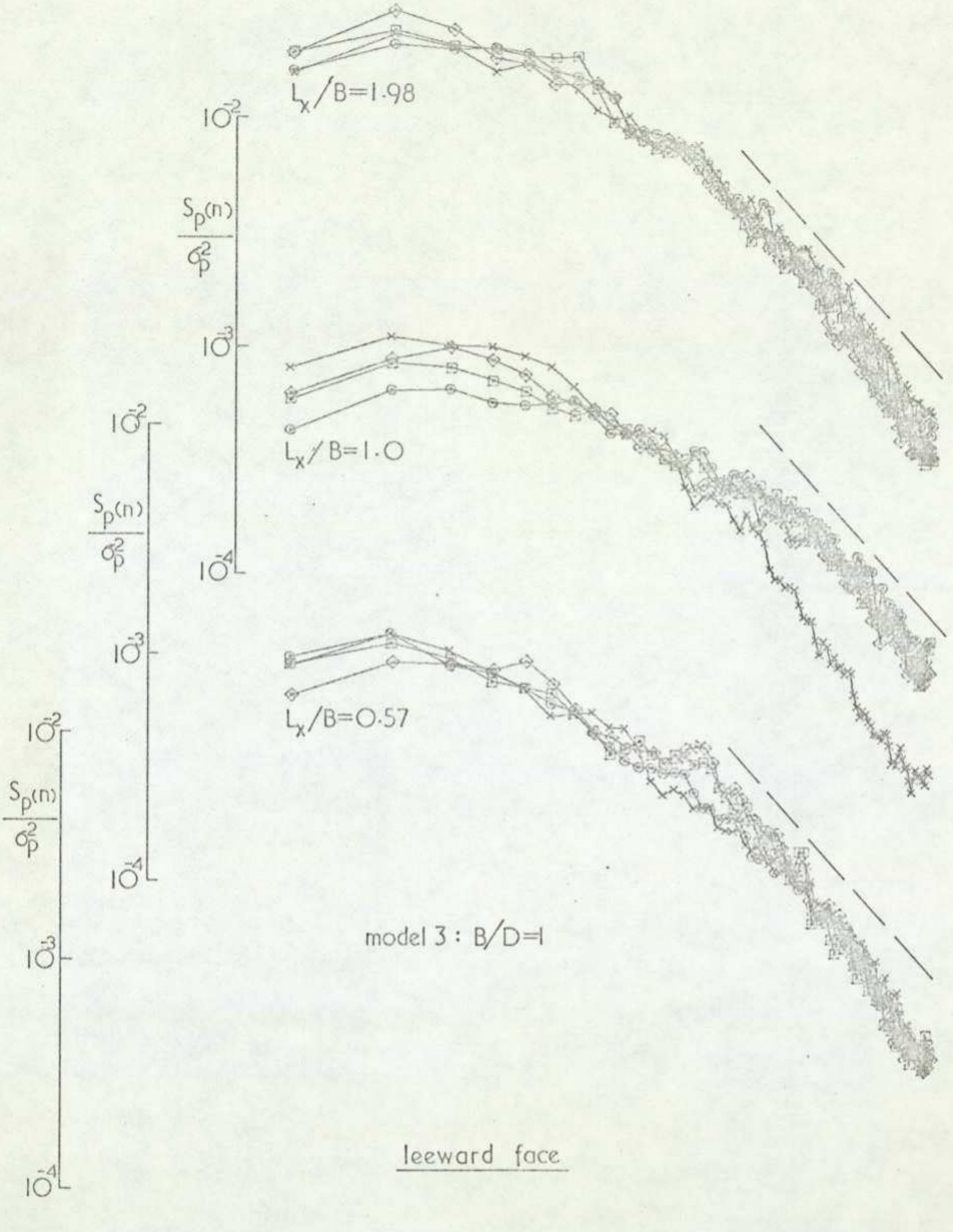

FIG 34 (concluded)

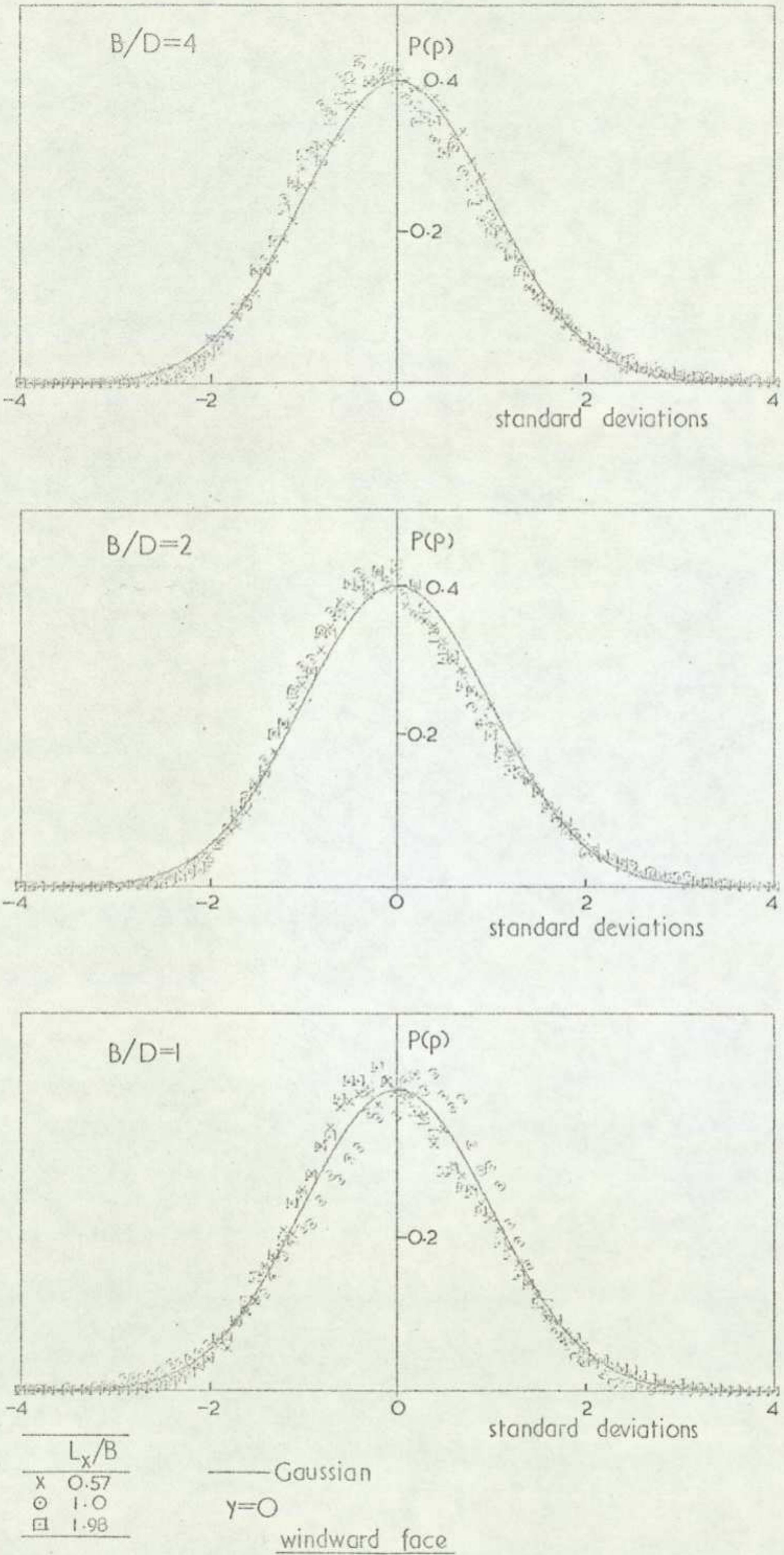

FIG 35 Probability density distribution for pressure fluctuations at $z/H=0{\cdot}5$

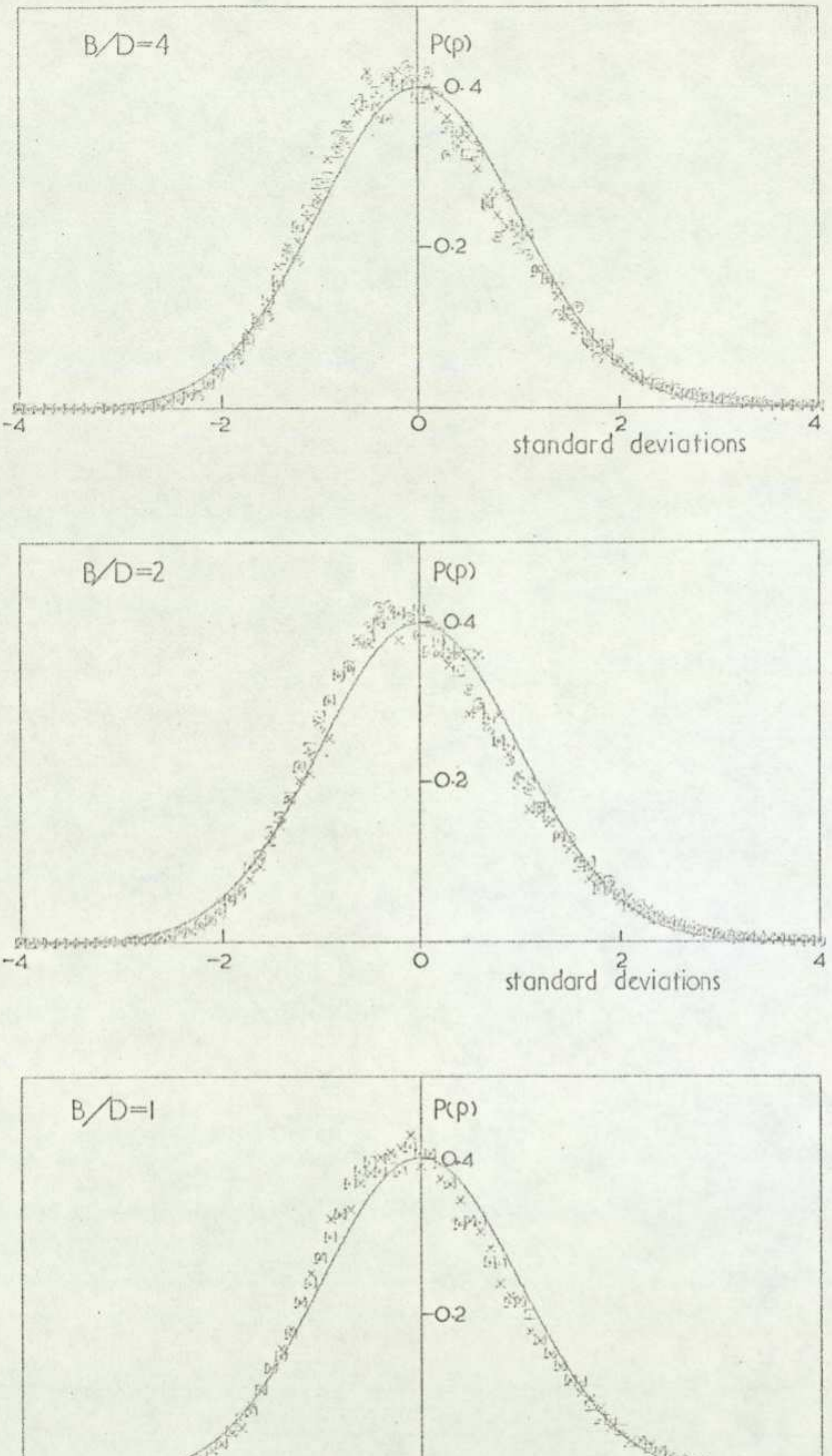

leeward face

FIG 35 (concluded)

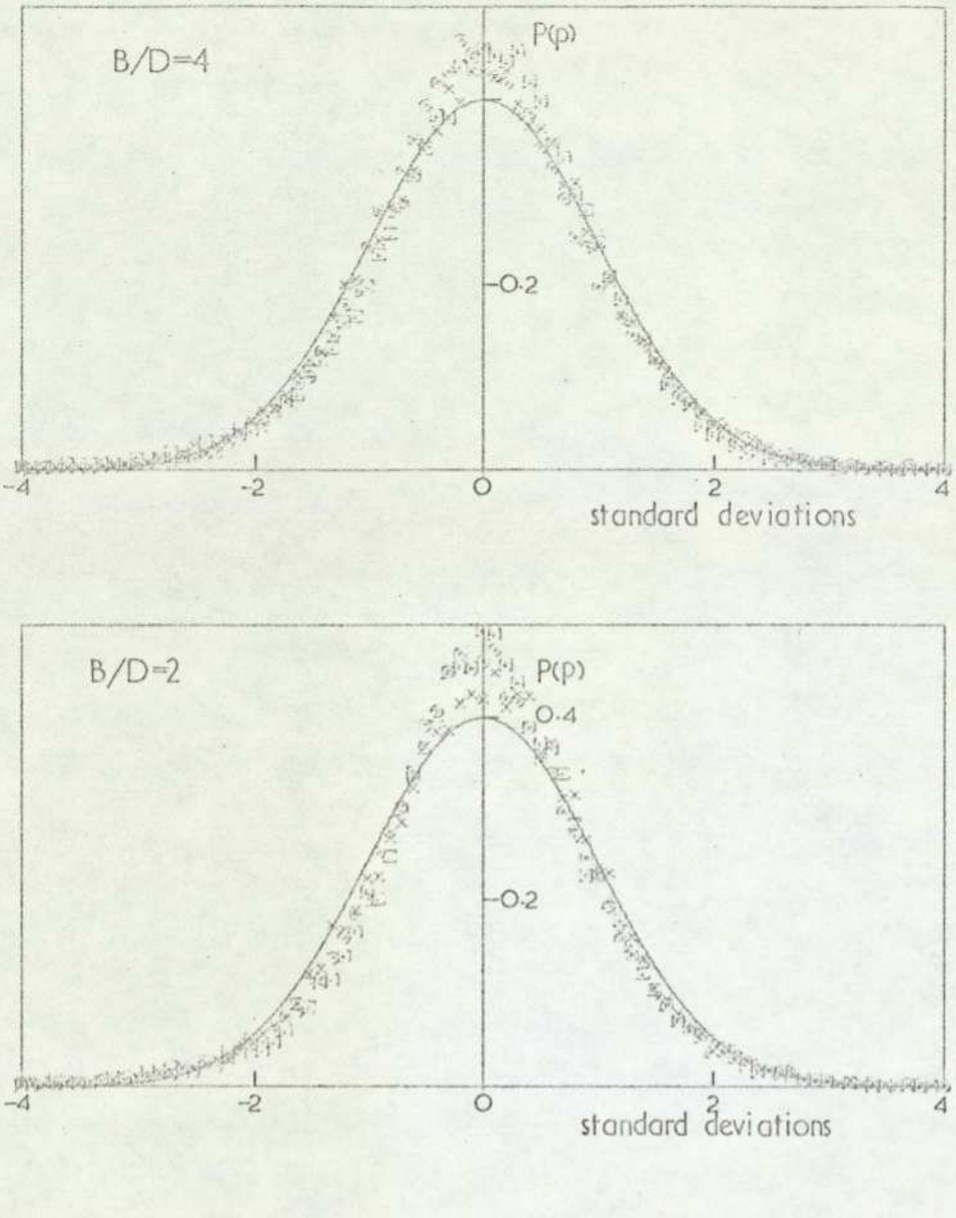

FIG 36 Probability density distribution for pressure fluctuations at $z/H=0.96$

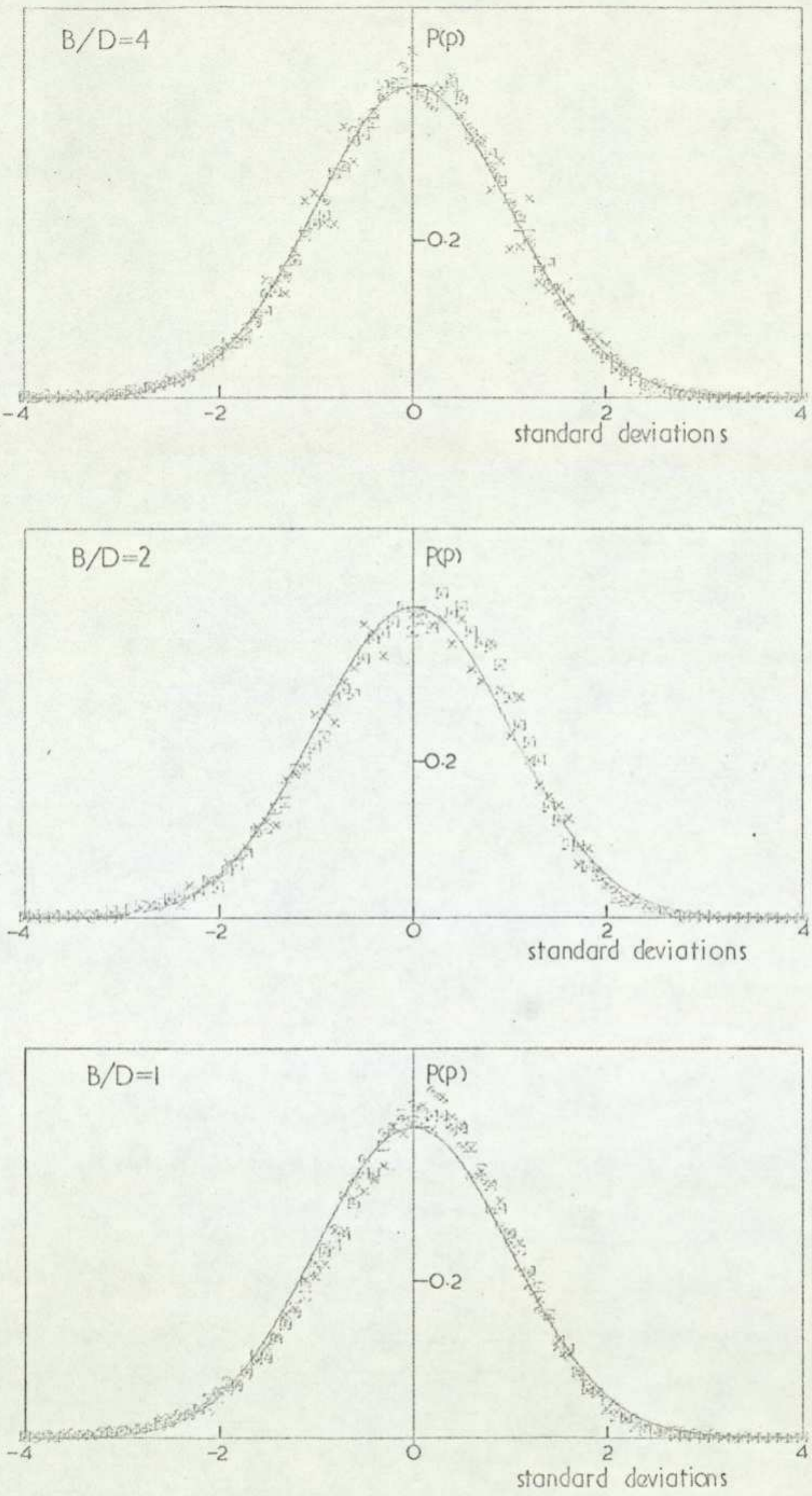

leeward face

FIG 36 (concluded)

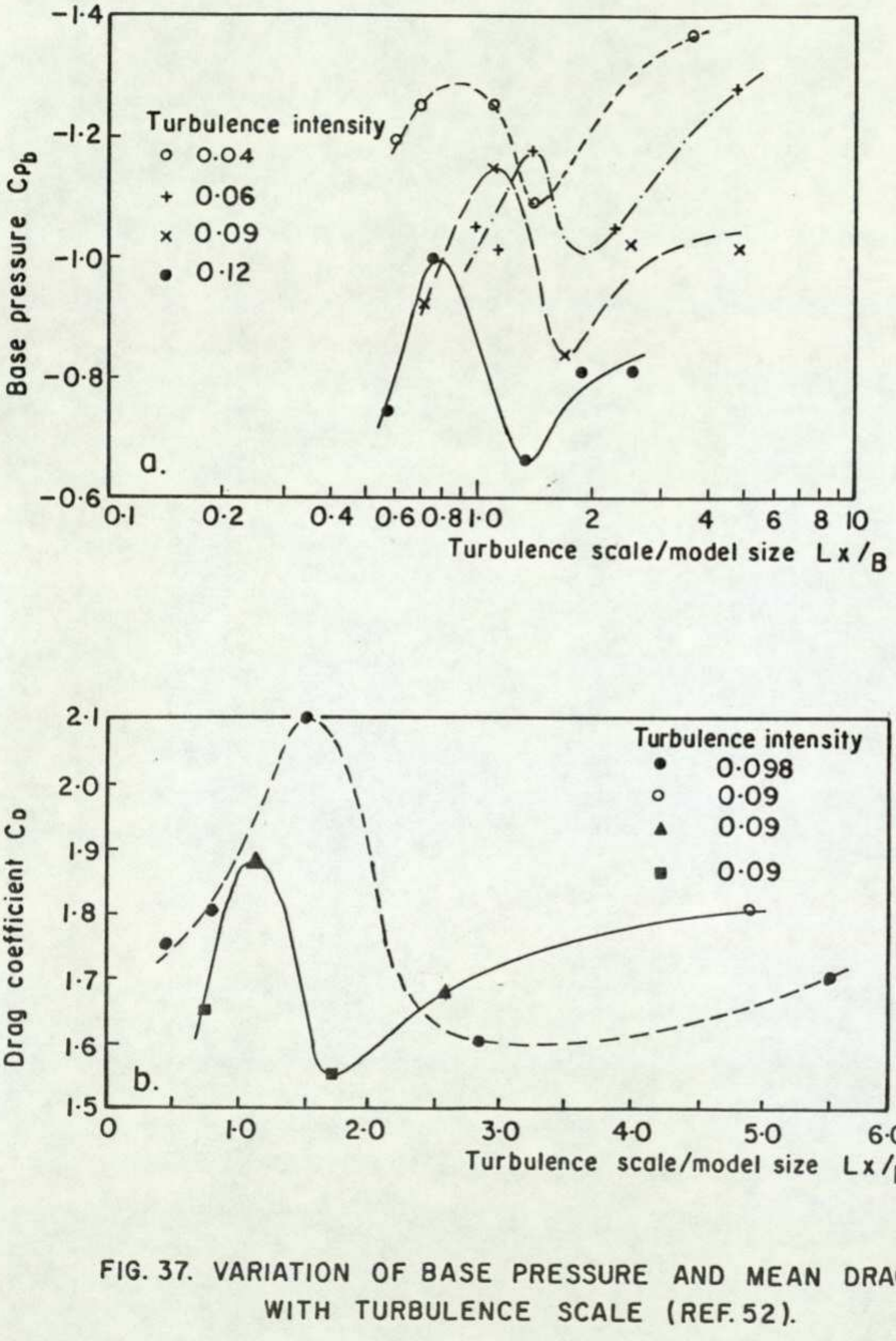

FIG. 37. VARIATION OF BASE PRESSURE AND MEAN DRAG WITH TURBULENCE SCALE (REF. 52).

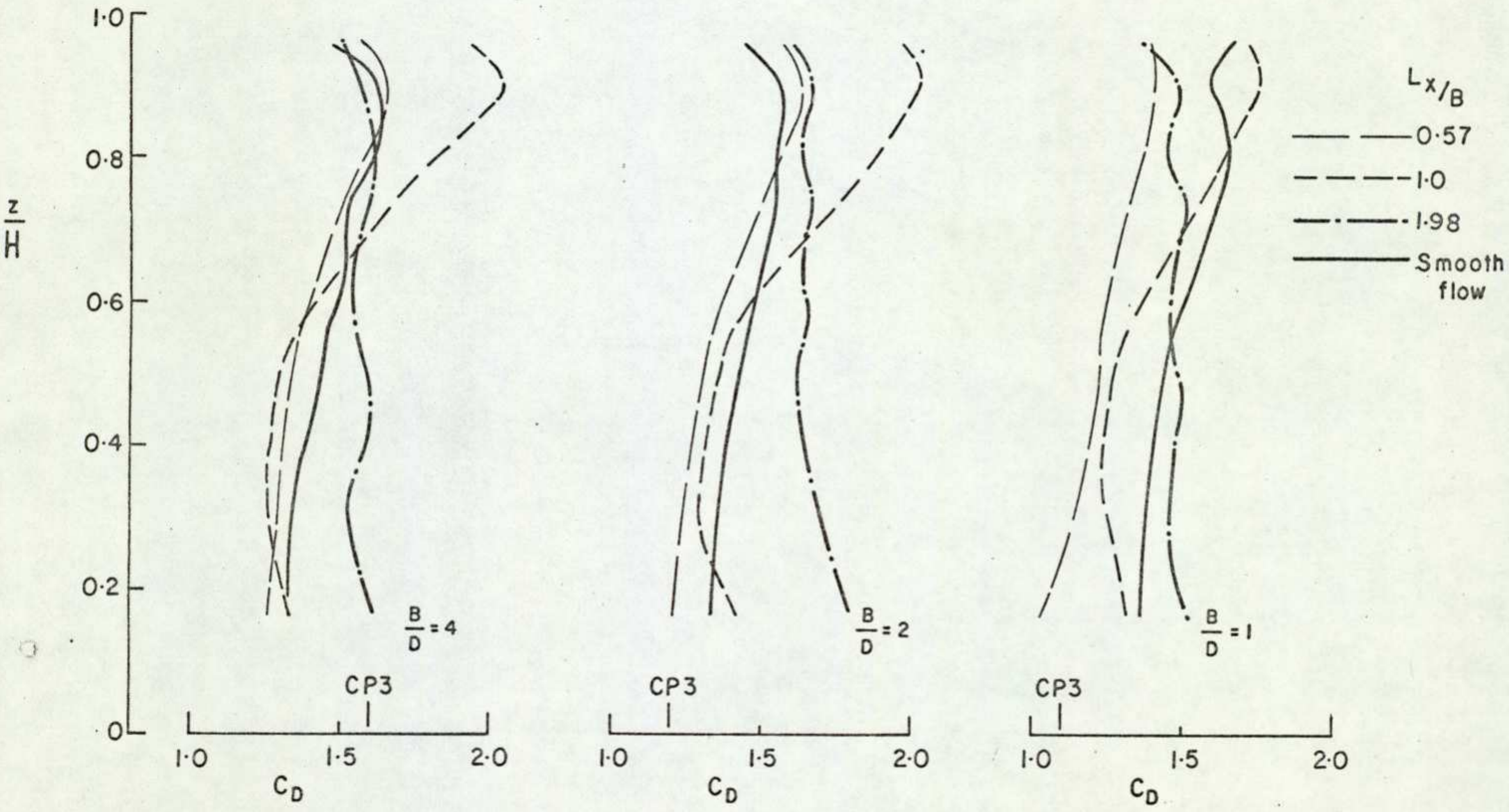

FIG. 38. DISTRIBUTION OF MEAN DRAG COEFFICIENT.

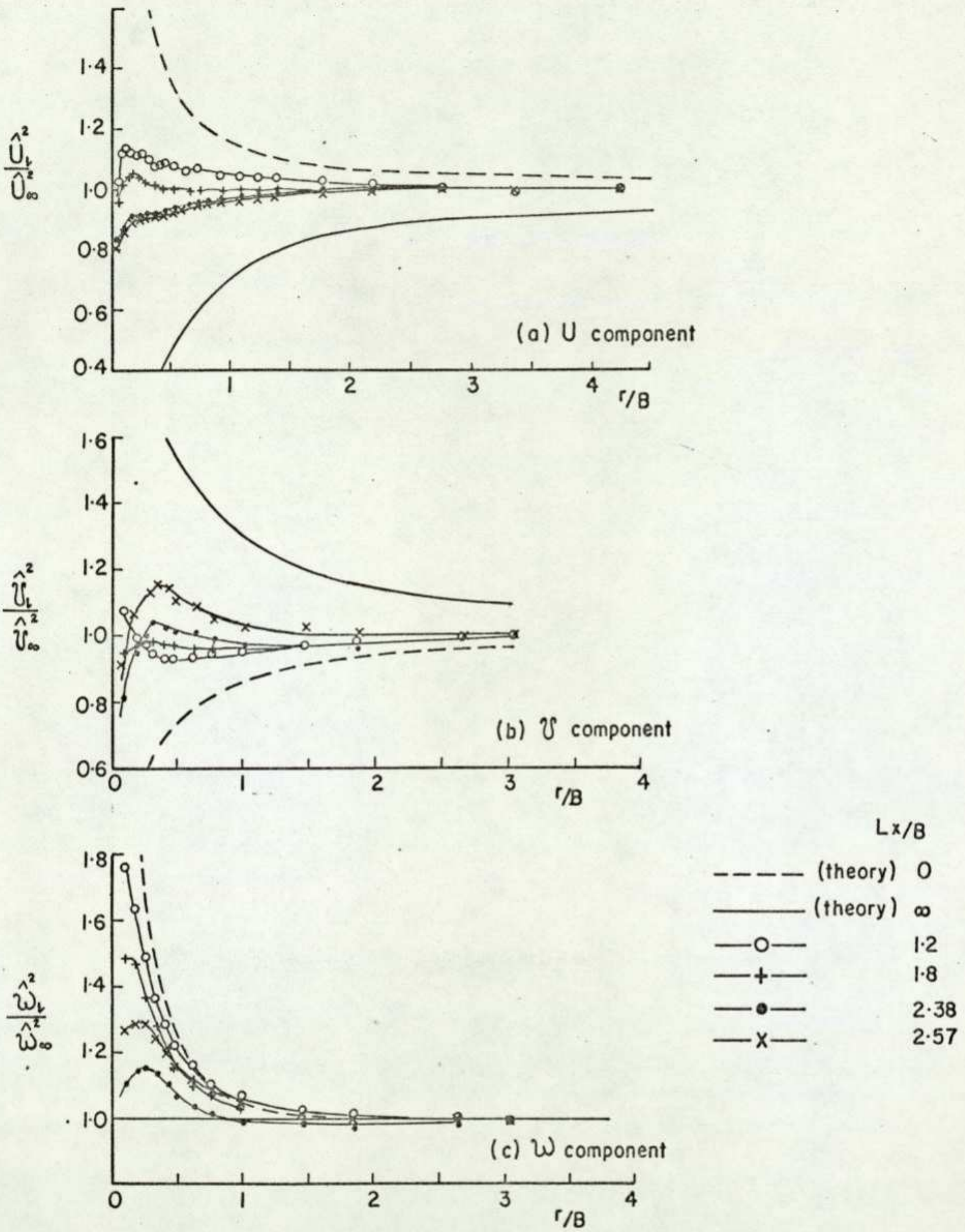

FIG. 39. VELOCITY COMPONENTS OF TURBULENCE APPROACHING STAGNATION. (REF. 77)

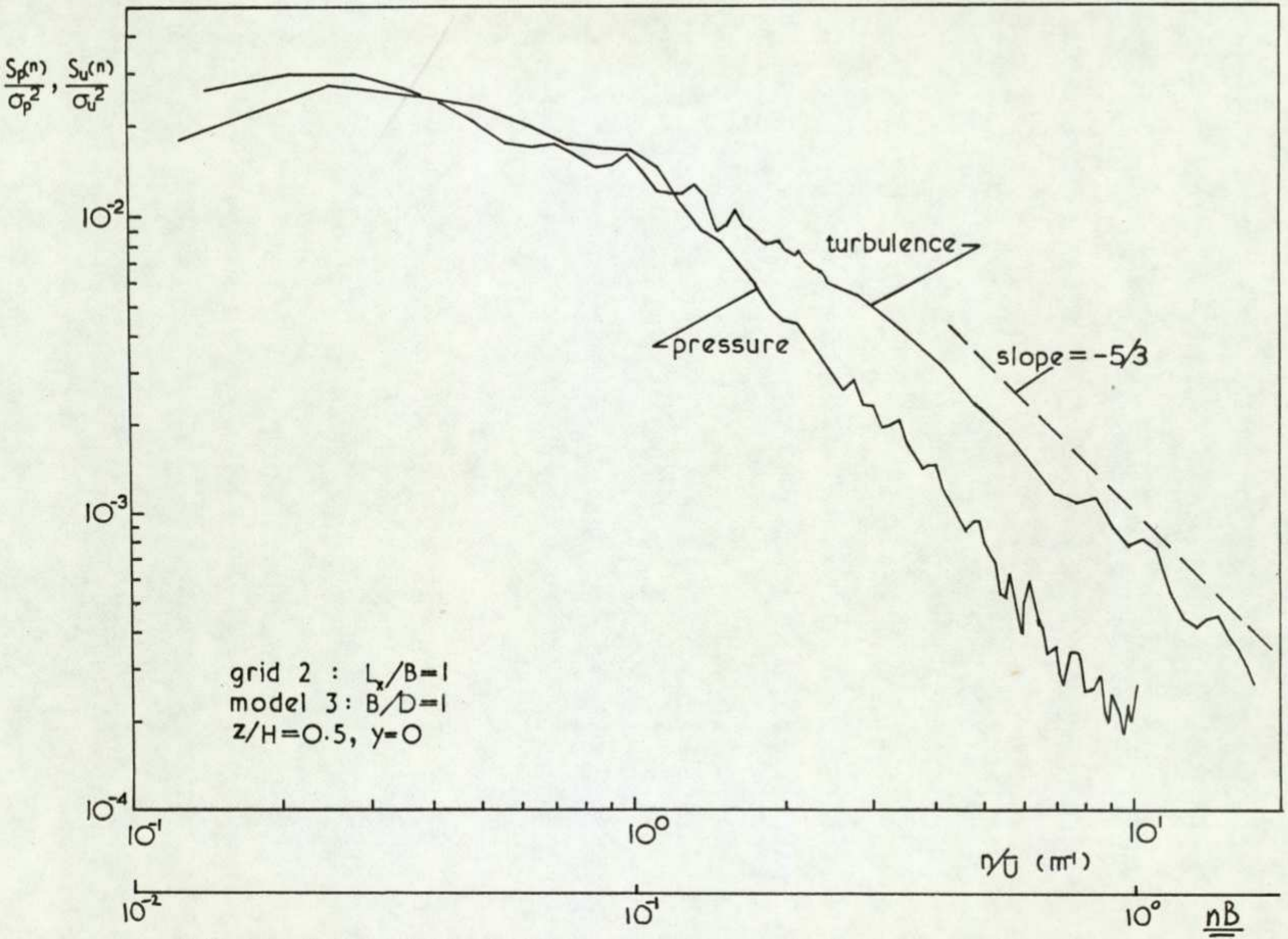

FIG 40 Comparison between spectrum of freestream turbulence and pressure fluctuations on windward face of model.

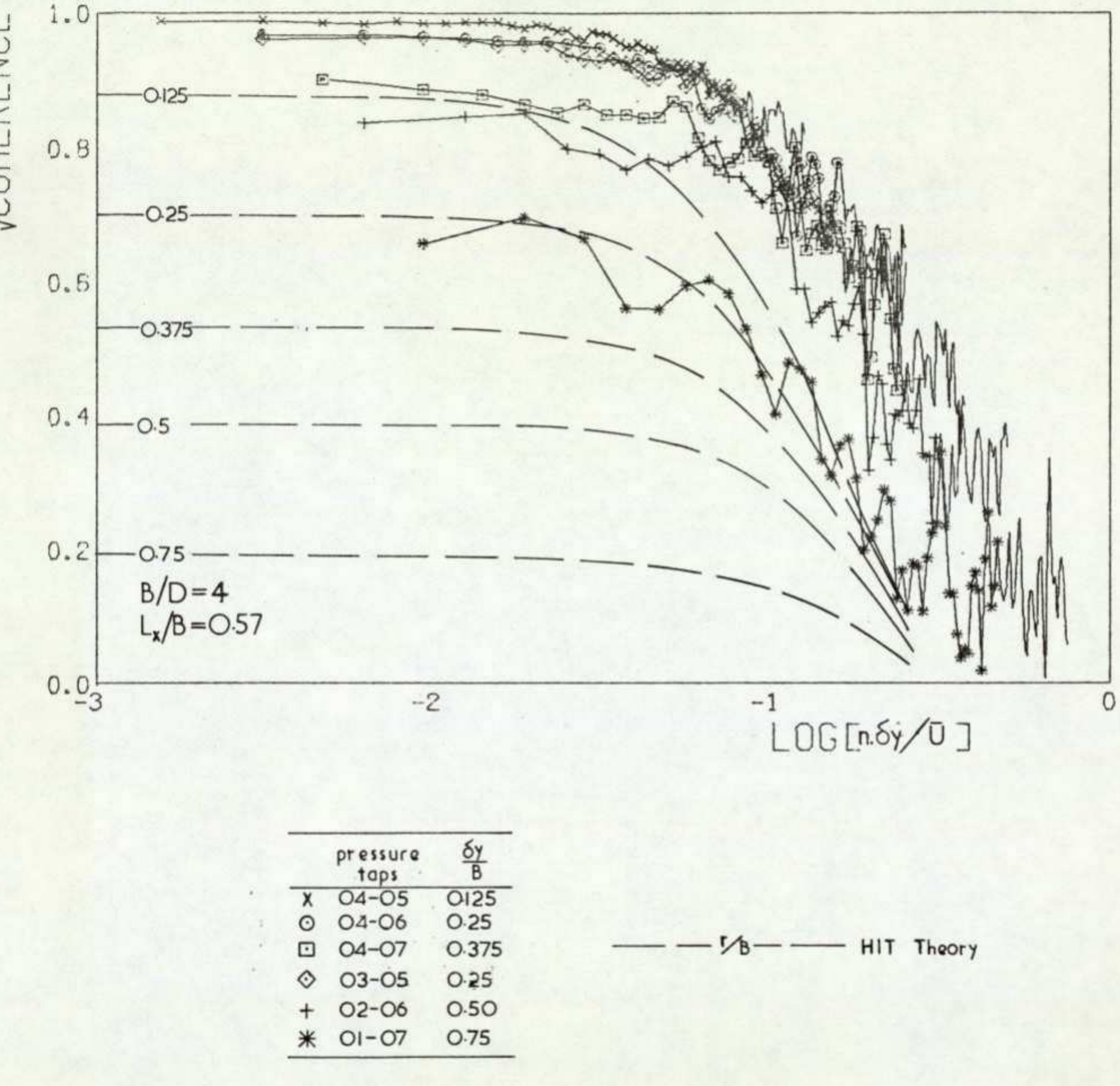

FIG. 41. √Coherence for pressures at z/H=0.5 on windward face (cont.)

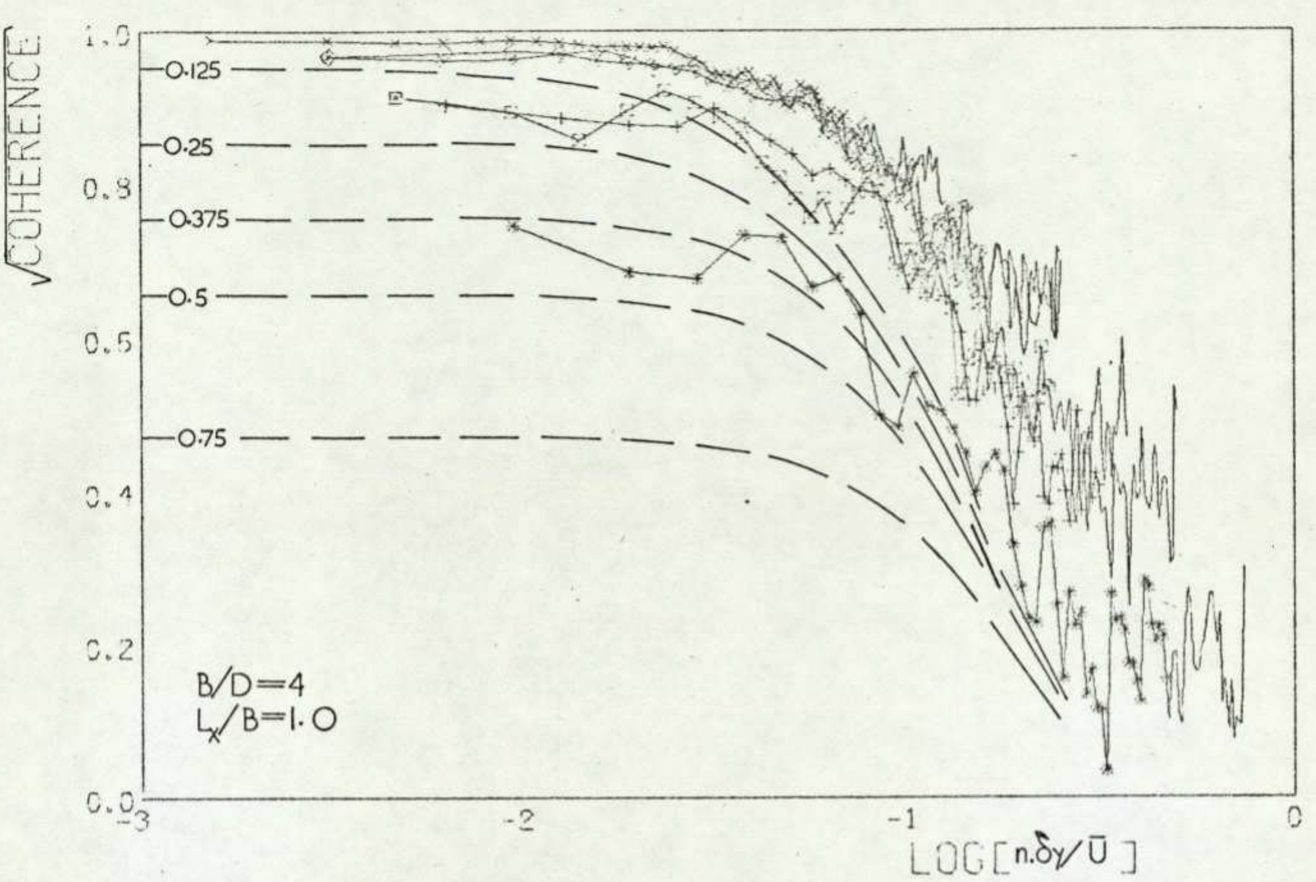
√COHERENCE
1.0
0.8
0.6
0.4
0.2
0.0
-3
-2
-1
0
LOG[n.δy/Ū]
0·125
0·25
0·375
0·5
0·75
B/D=4
L_x/B=1·0

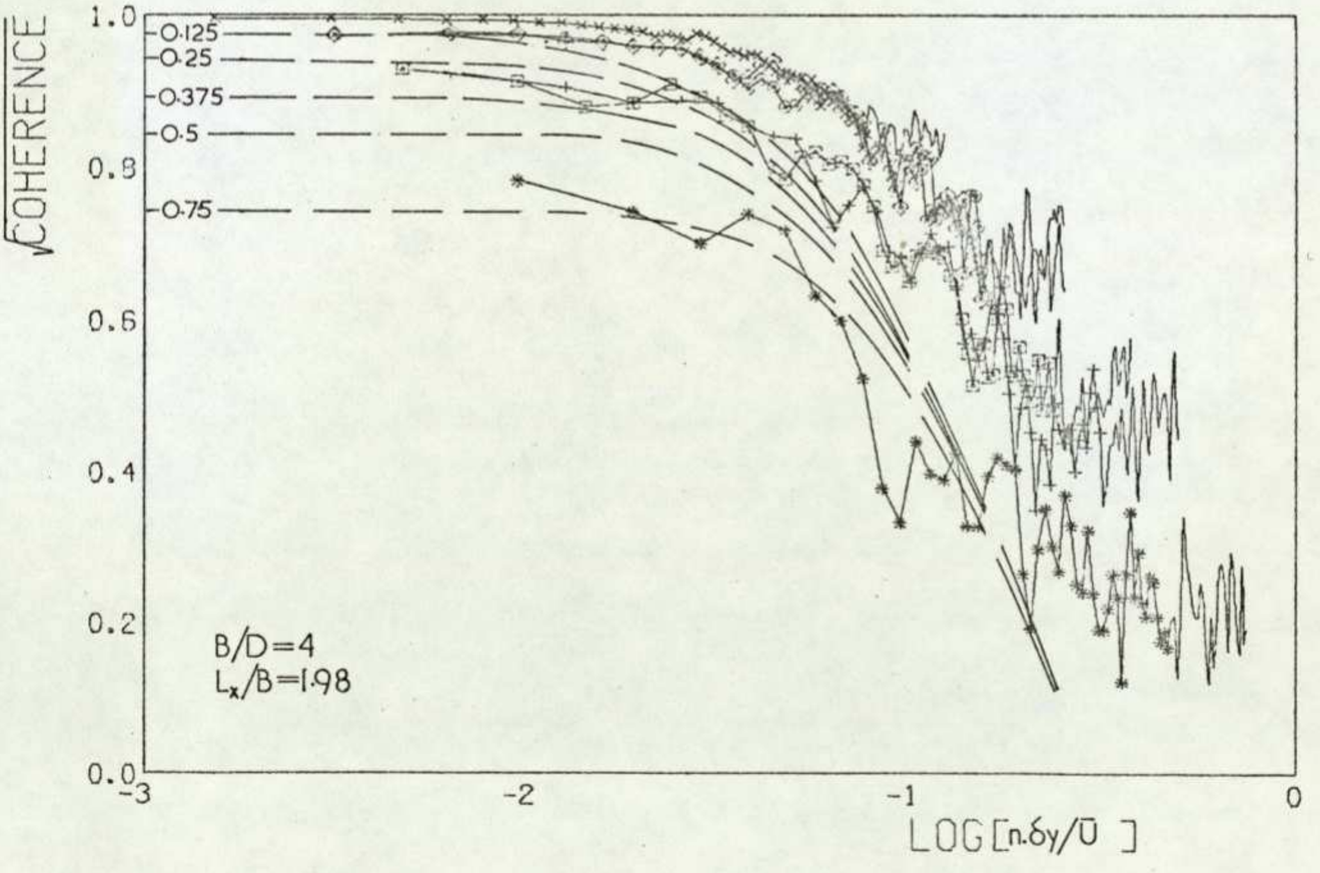
√COHERENCE
1.0
0.8
0.6
0.4
0.2
0.0
-3
-2
-1
0
LOG[n.δy/Ū]
0·125
0·25
0·375
0·5
0·75
B/D=4
L_x/B=1·98

FIG. 41. (cont.)

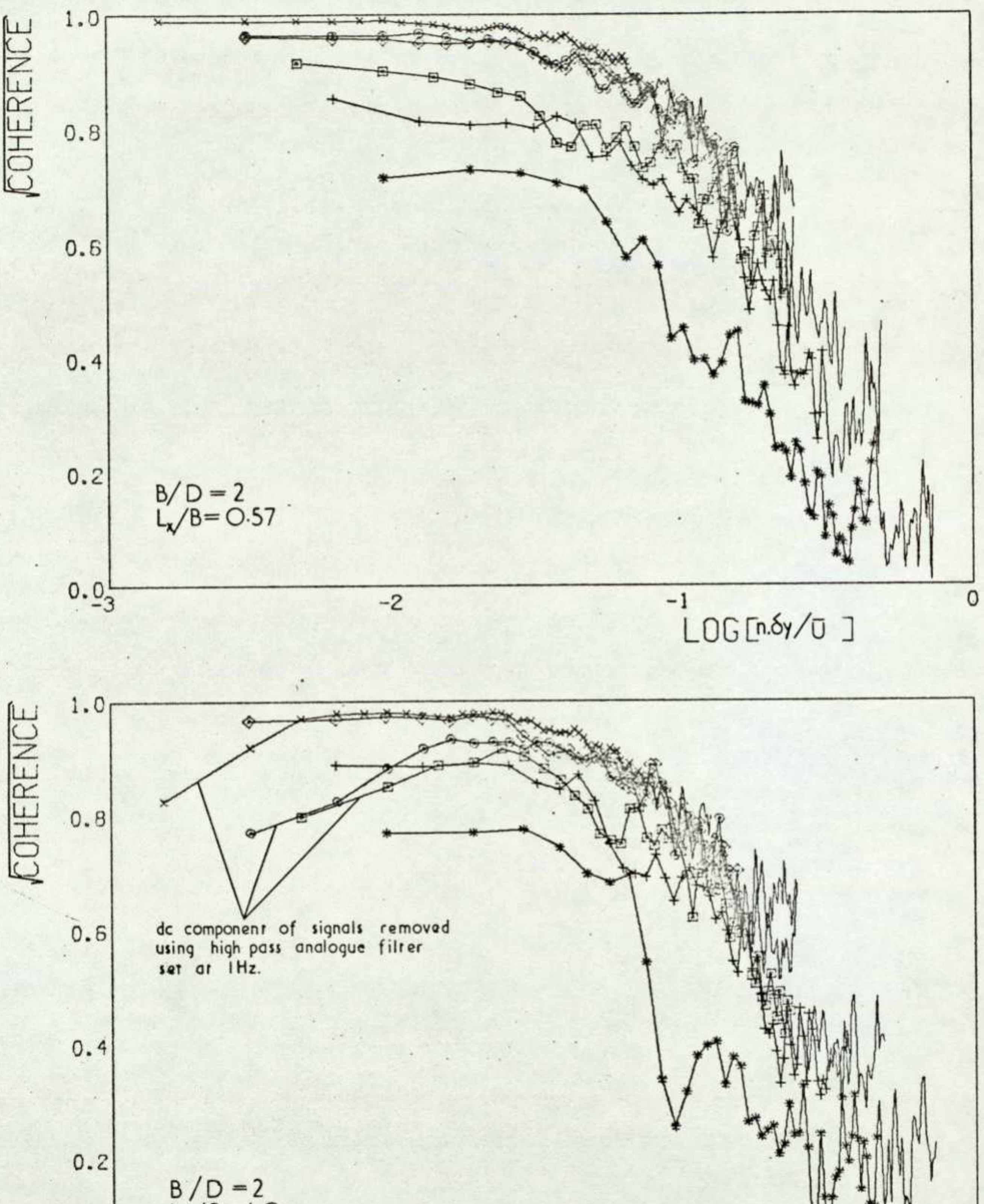
√COHERENCE
1.0
0.8
0.6
0.4
0.2
0.0
-3
-2
-1
0
LOG[n.δy/Ū]
B/D = 2
Lx/B= 0.57
√COHERENCE
1.0
0.8
0.6
0.4
0.2
0.0
-3
-2
-1
0
LOG[n.δy/Ū]
dc component of signals removed
using high pass analogue filter
set at 1Hz.
B/D = 2
Lx/B = 1.0

FIG. 41. (cont.)

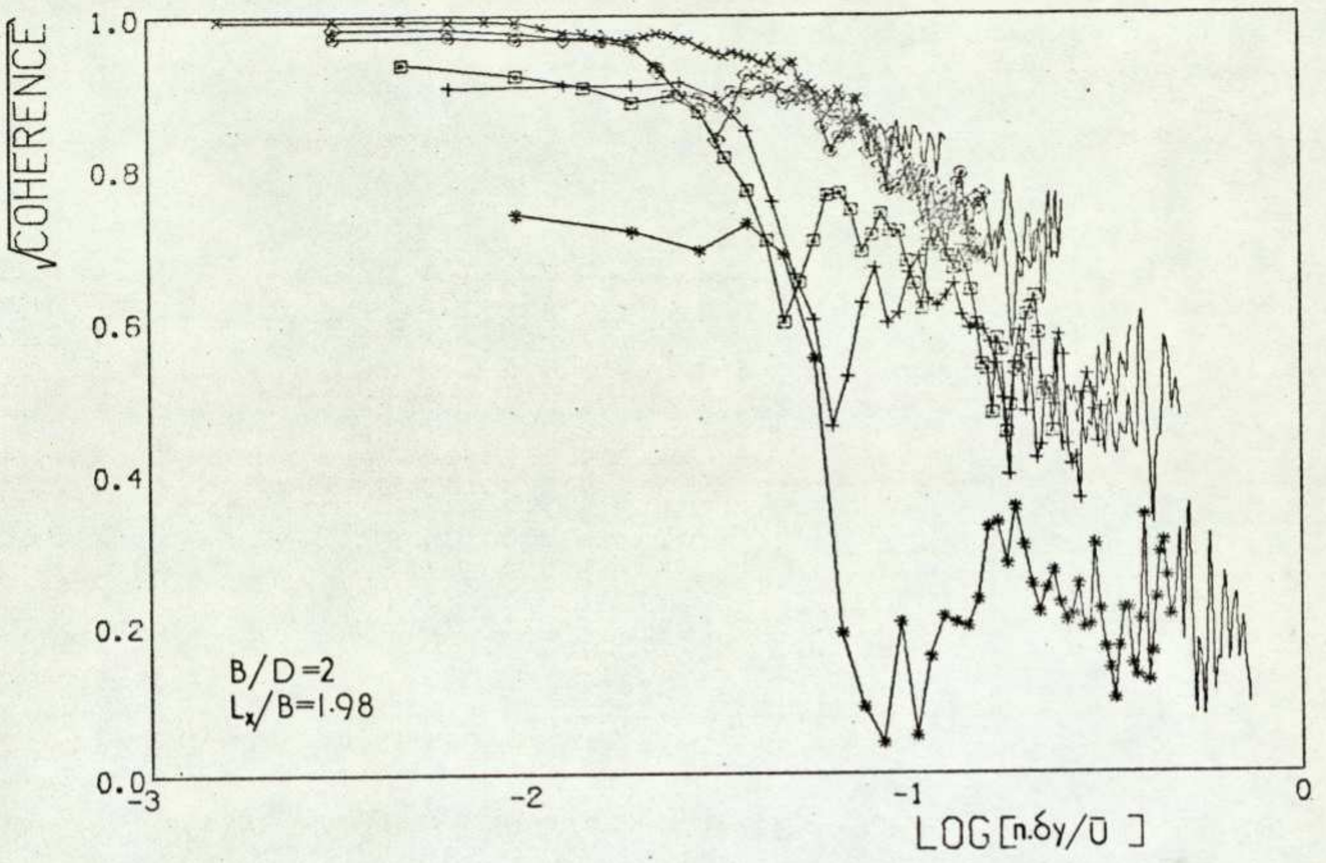
√COHERENCE
1.0
0.8
0.6
0.4
0.2
0.0
-3
-2
-1
0
LOG[n.δy/Ū]
B/D=2
L_x/B=1.98

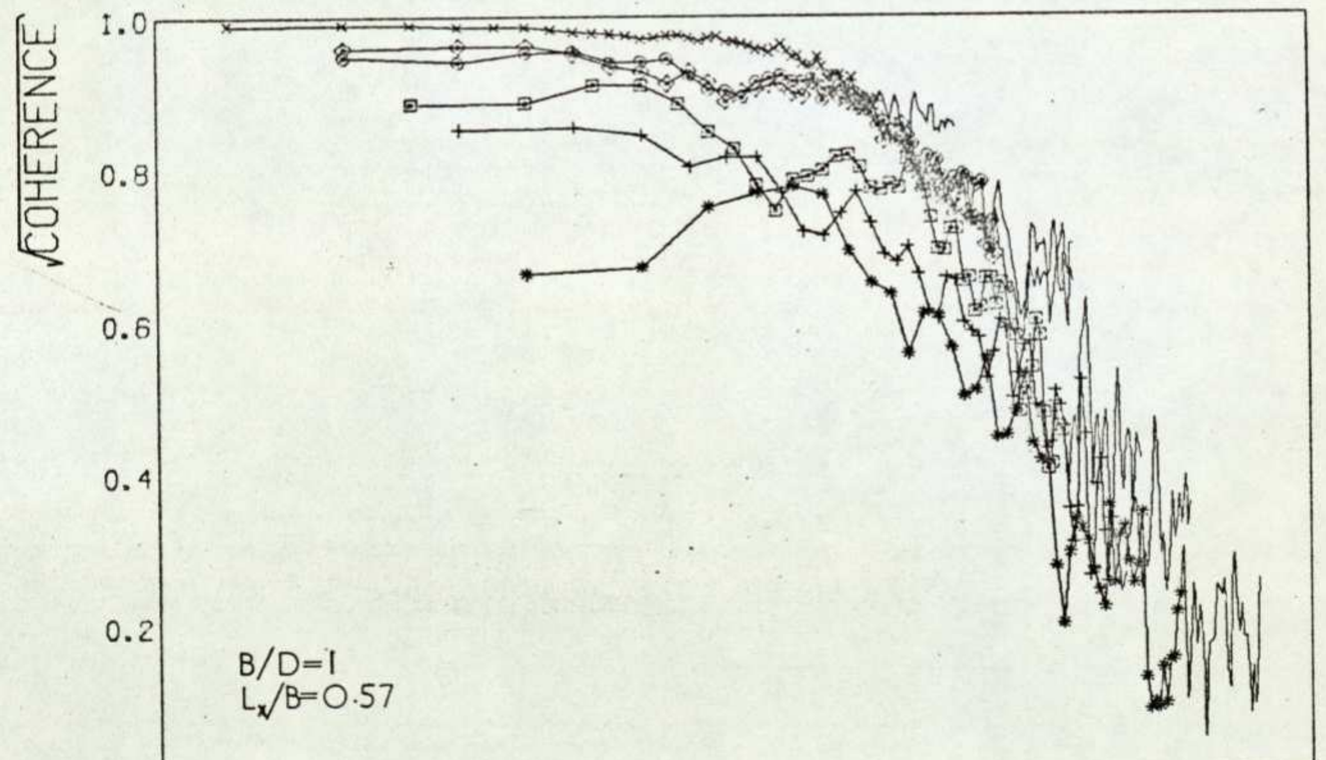
√COHERENCE
1.0
0.8
0.6
0.4
0.2
0.0
-3
-2
-1
0
LOG[n.δy/Ū]
B/D=1
L_x/B=0.57

FIG. 41. (cont.)

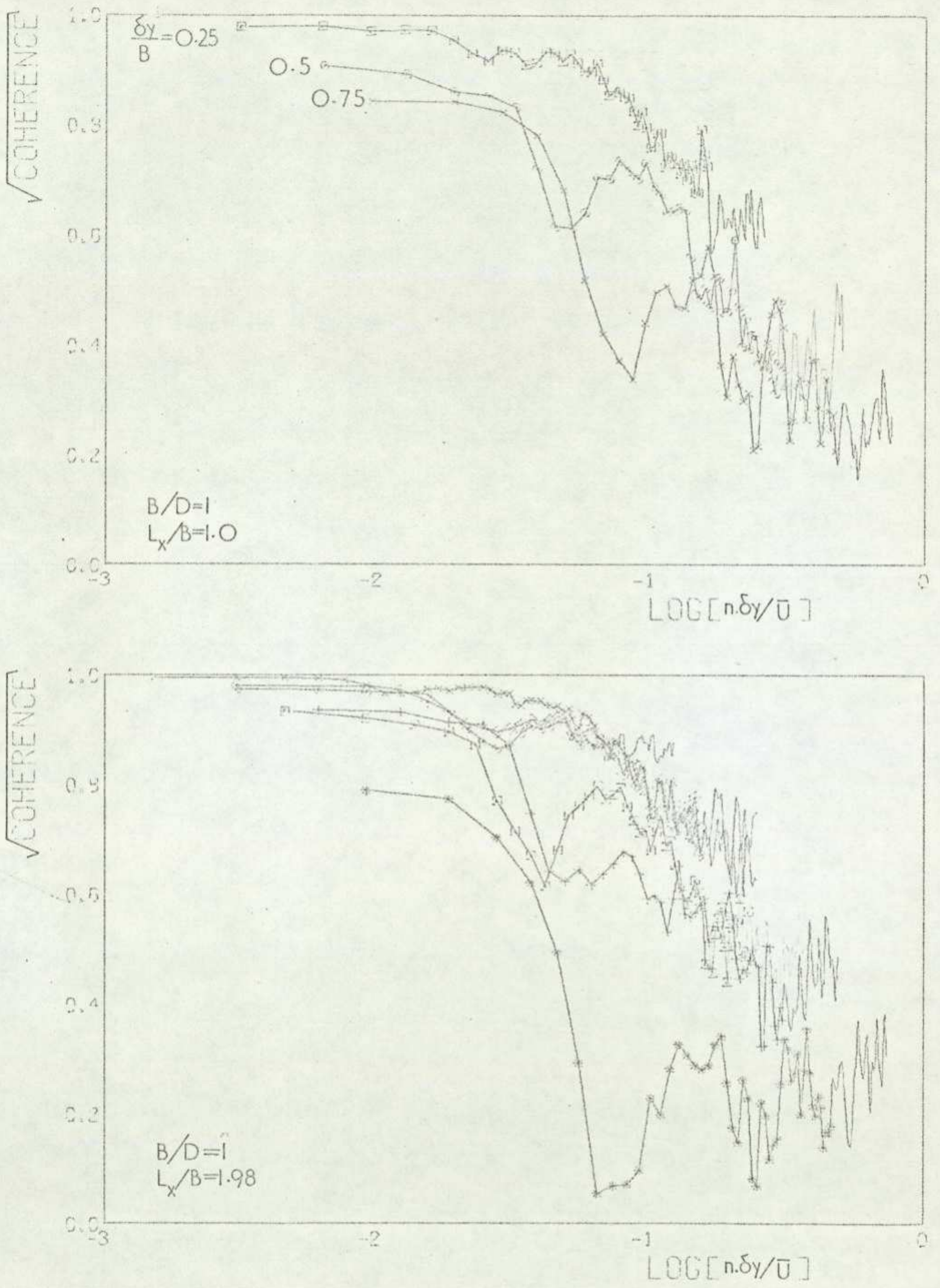

FIG 41 (concluded)

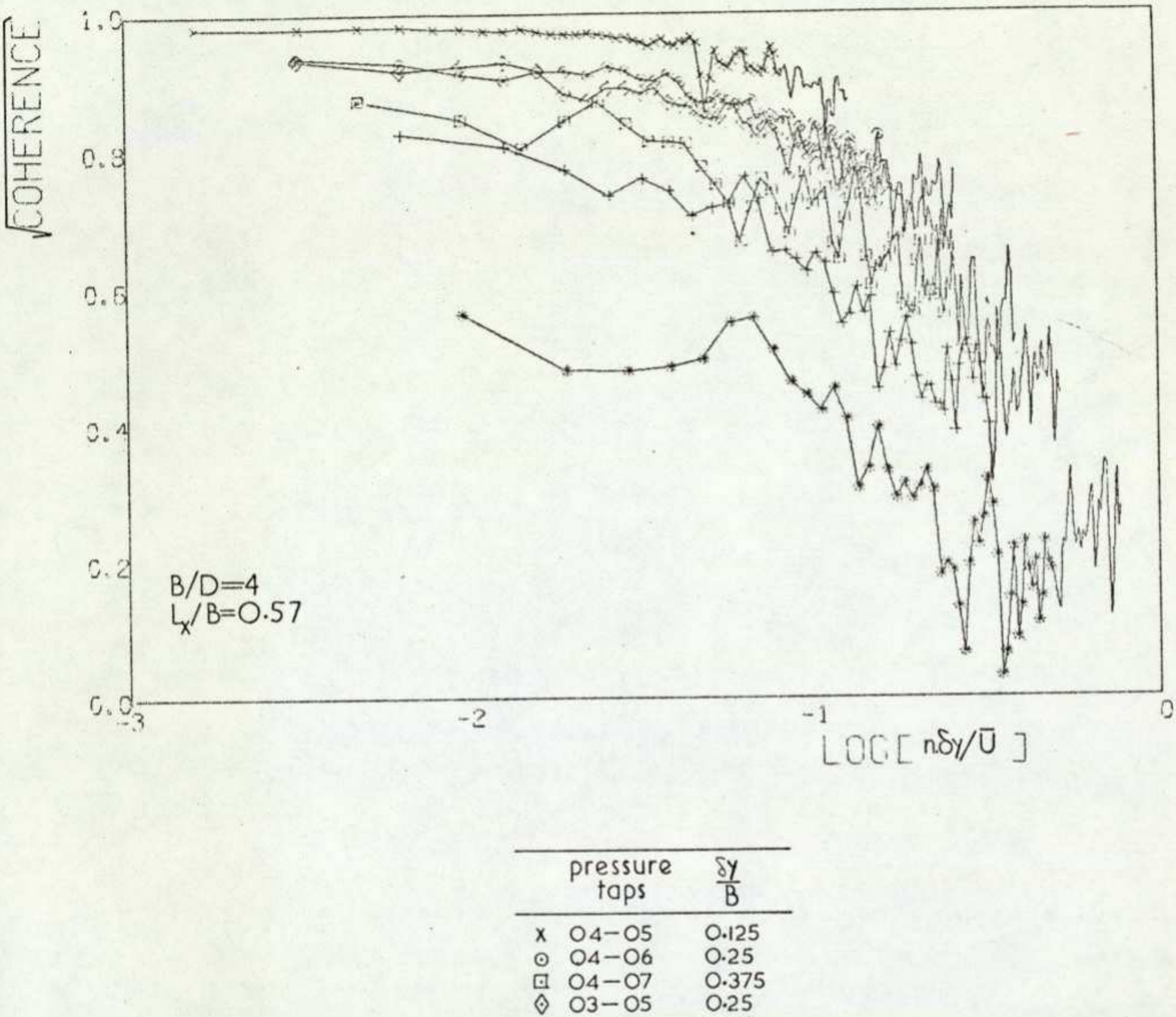

	pressure taps	$\frac{\delta y}{B}$
x	04–05	0·125
⊙	04–06	0·25
⊡	04–07	0·375
◊	03–05	0·25
+	02–06	0·50
✱	01–07	0·75

FIG 42 $\sqrt{\text{Coherence}}$ for pressures at z/H=0·96 on windward face.

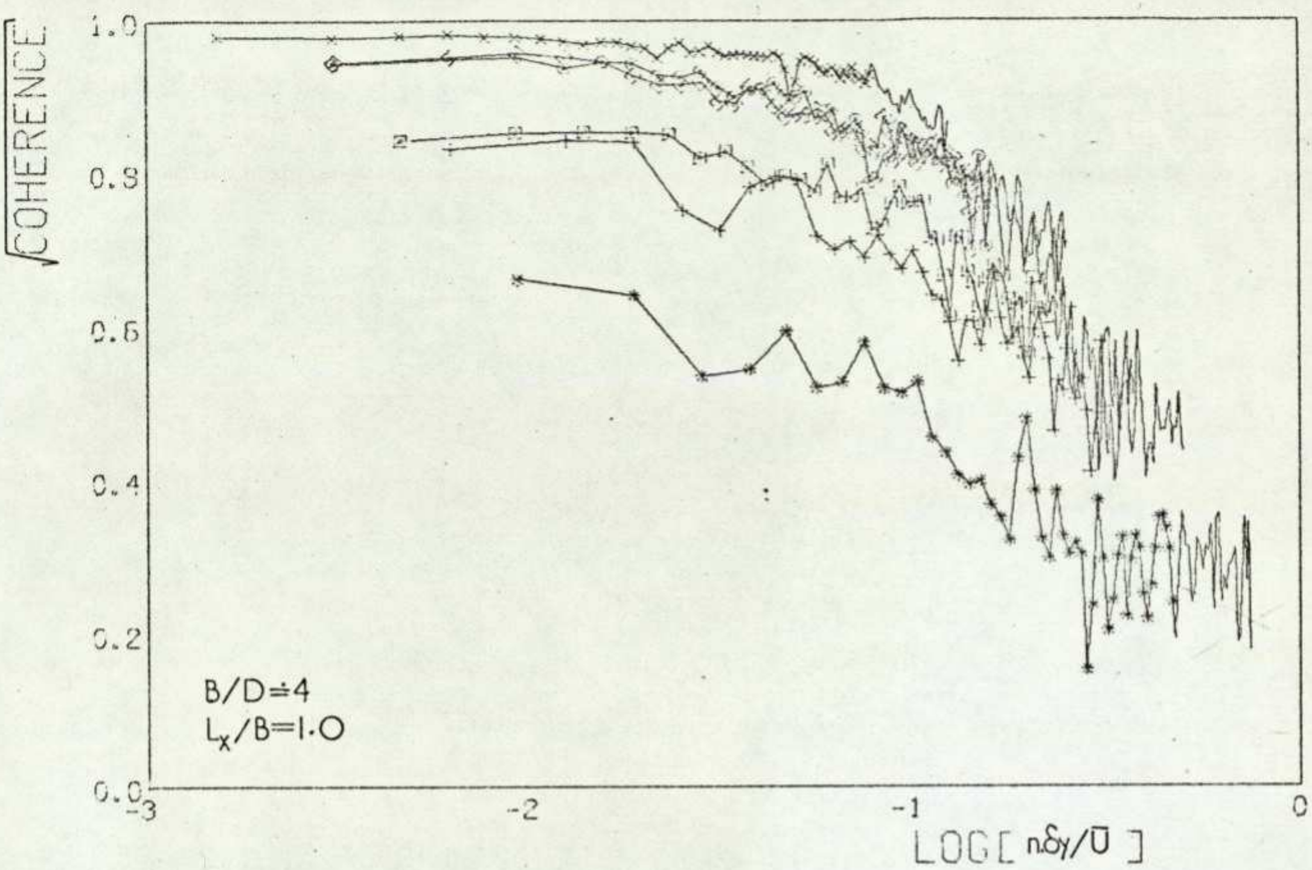

√COHERENCE
1.0
0.8
0.6
0.4
0.2
0.0
-3
-2
-1
0
LOG[n.δy/Ū]
B/D≐4
L_x/B=1.0

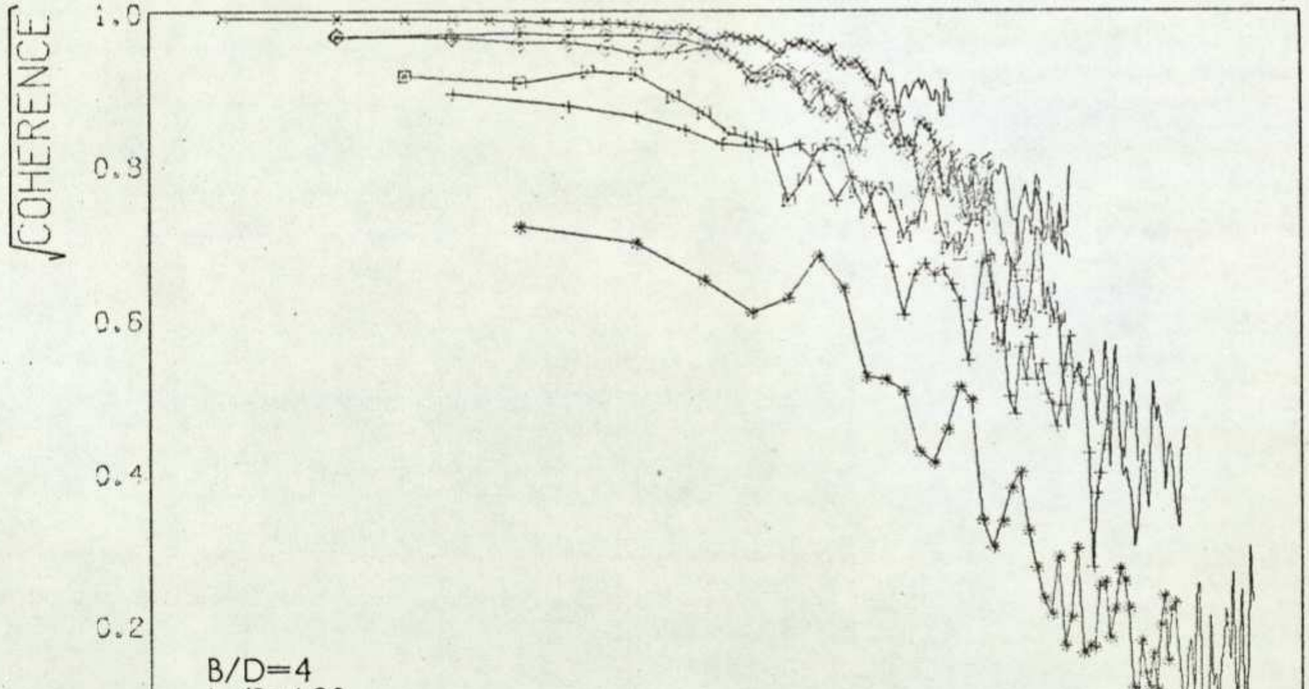

√COHERENCE
1.0
0.8
0.6
0.4
0.2
0.0
-3
-2
-1
0
LOG[n.δy/Ū]
B/D=4
L_x/B=1.98

FIG 42 (cont.)

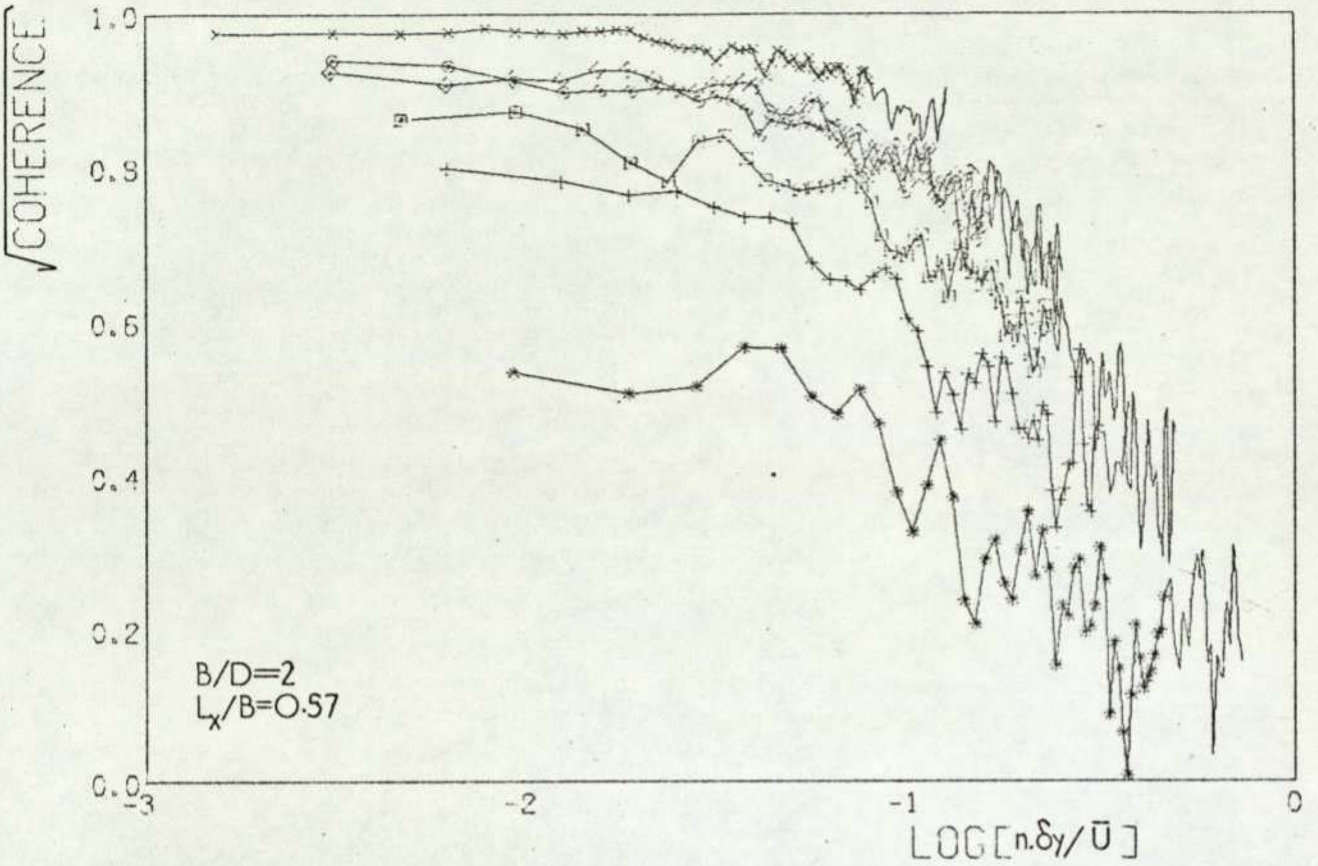
√COHERENCE
1.0
0.8
0.6
0.4
0.2
0.0
-3
-2
-1
0
LOG[n.δy/Ū]
B/D=2
L_x/B=0.57

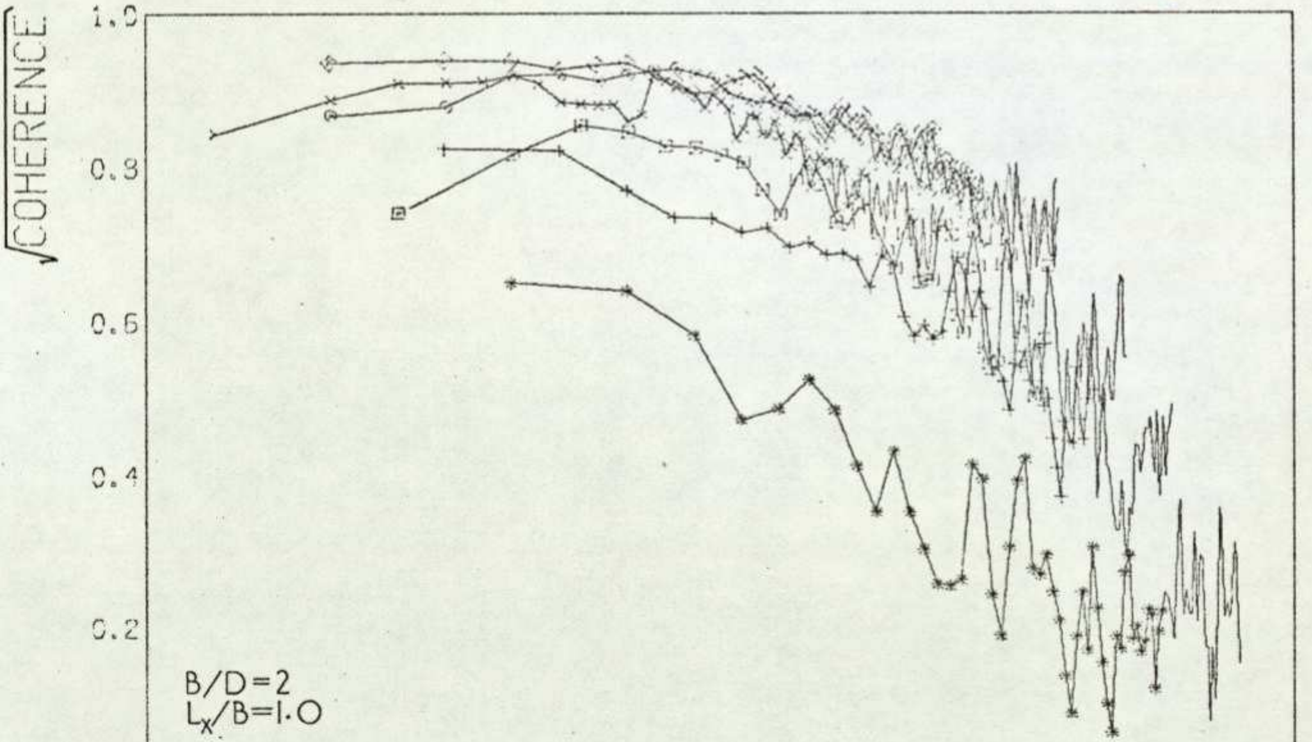
√COHERENCE
1.0
0.8
0.6
0.4
0.2
0.0
-3
-2
-1
0
LOG[n δy/Ū]
B/D=2
L_x/B=1.0

FIG 42 (cont.)

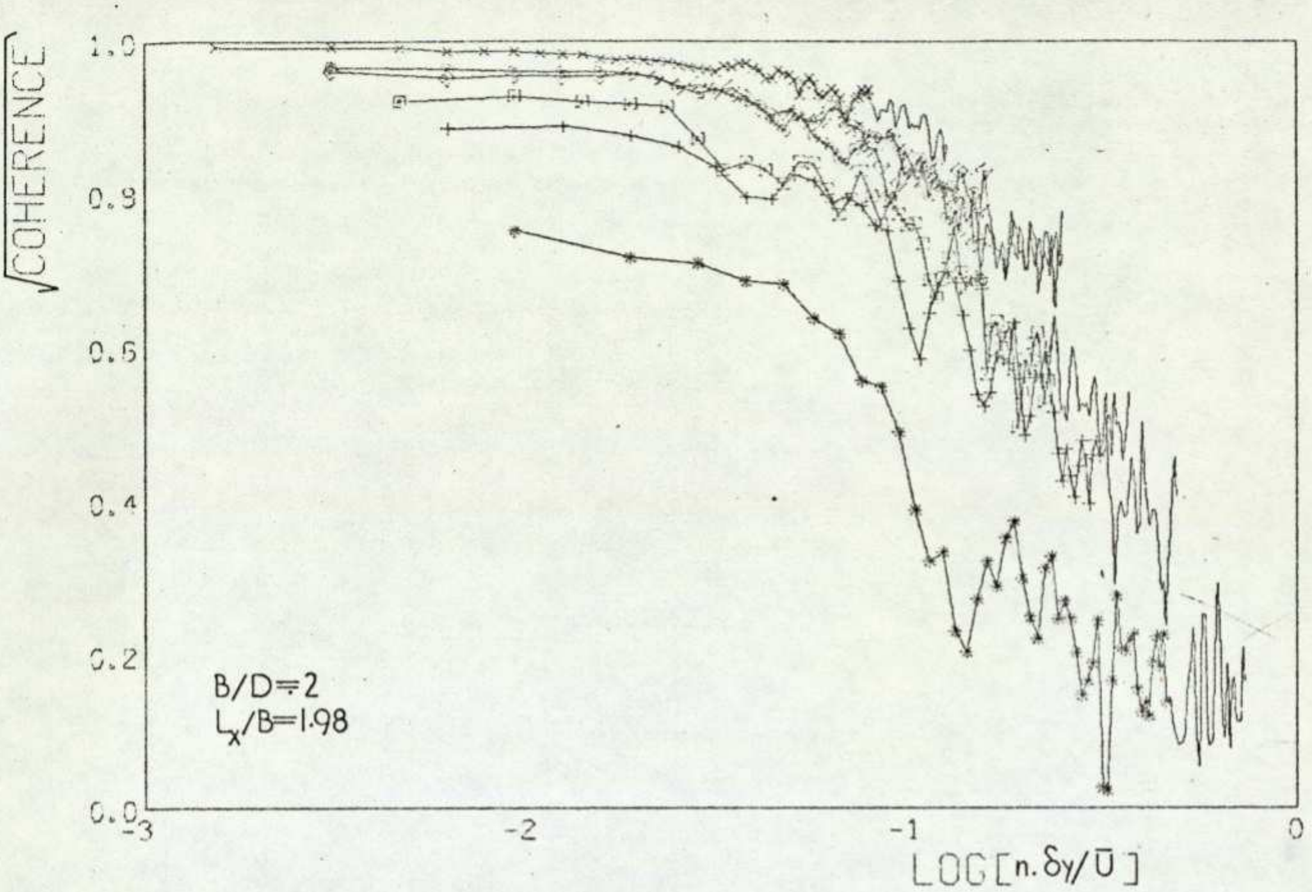
√COHERENCE
1.0
0.8
0.6
0.4
0.2
0.0
-3
-2
-1
0
LOG[n.δy/Ū]
B/D=2
L_x/B=1.98

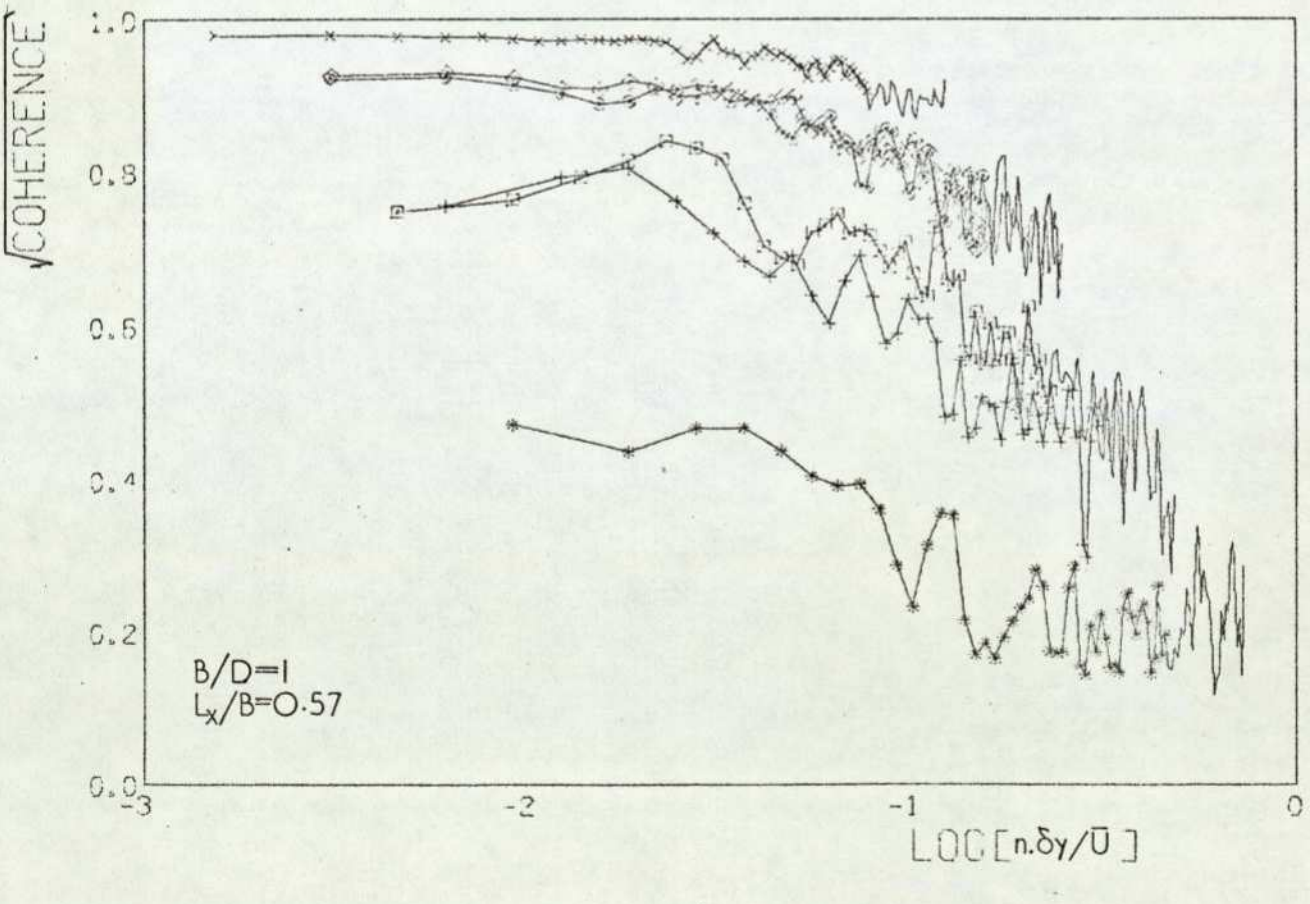
√COHERENCE
1.0
0.8
0.6
0.4
0.2
0.0
-3
-2
-1
0
LOG[n.δy/Ū]
B/D=1
L_x/B=0.57

FIG 42 (cont.)

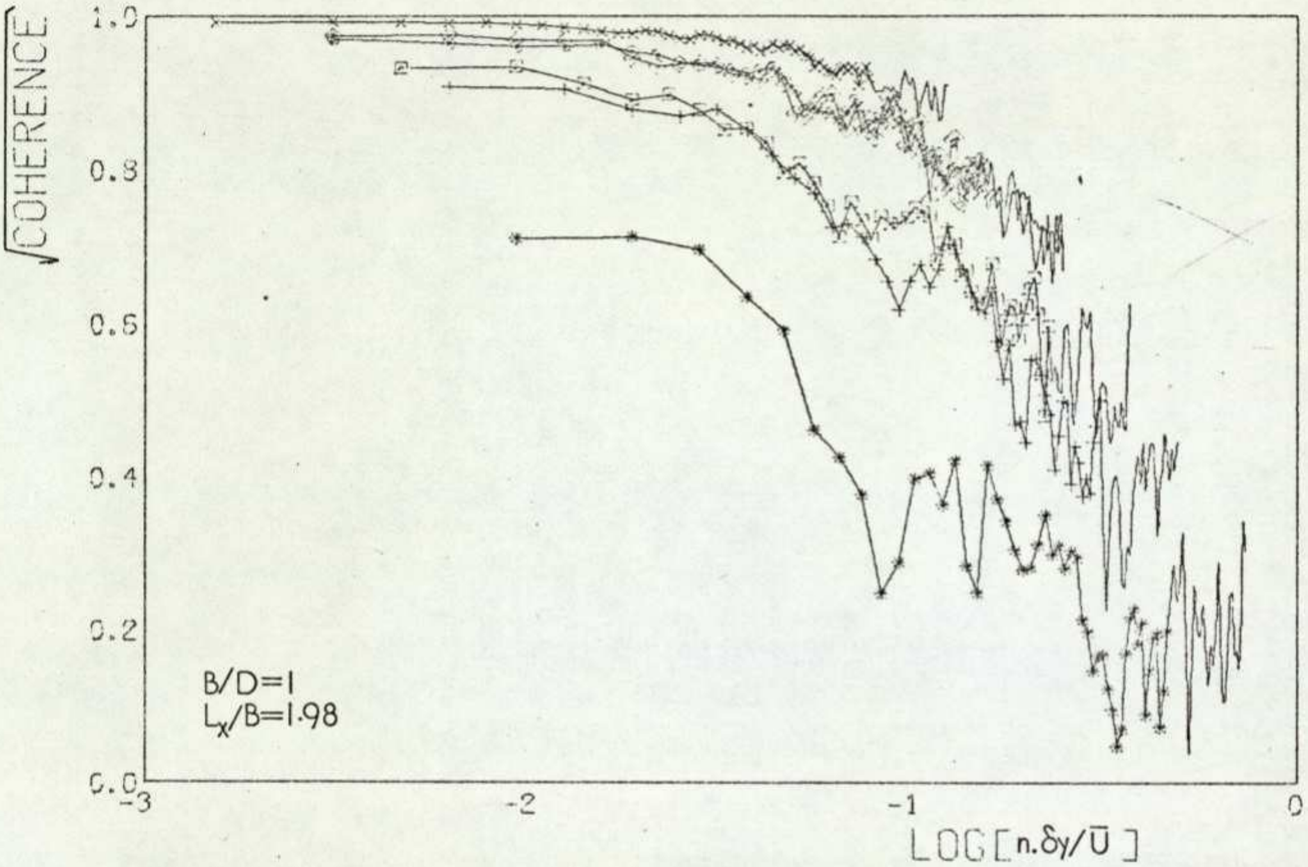

FIG 42 (concluded)

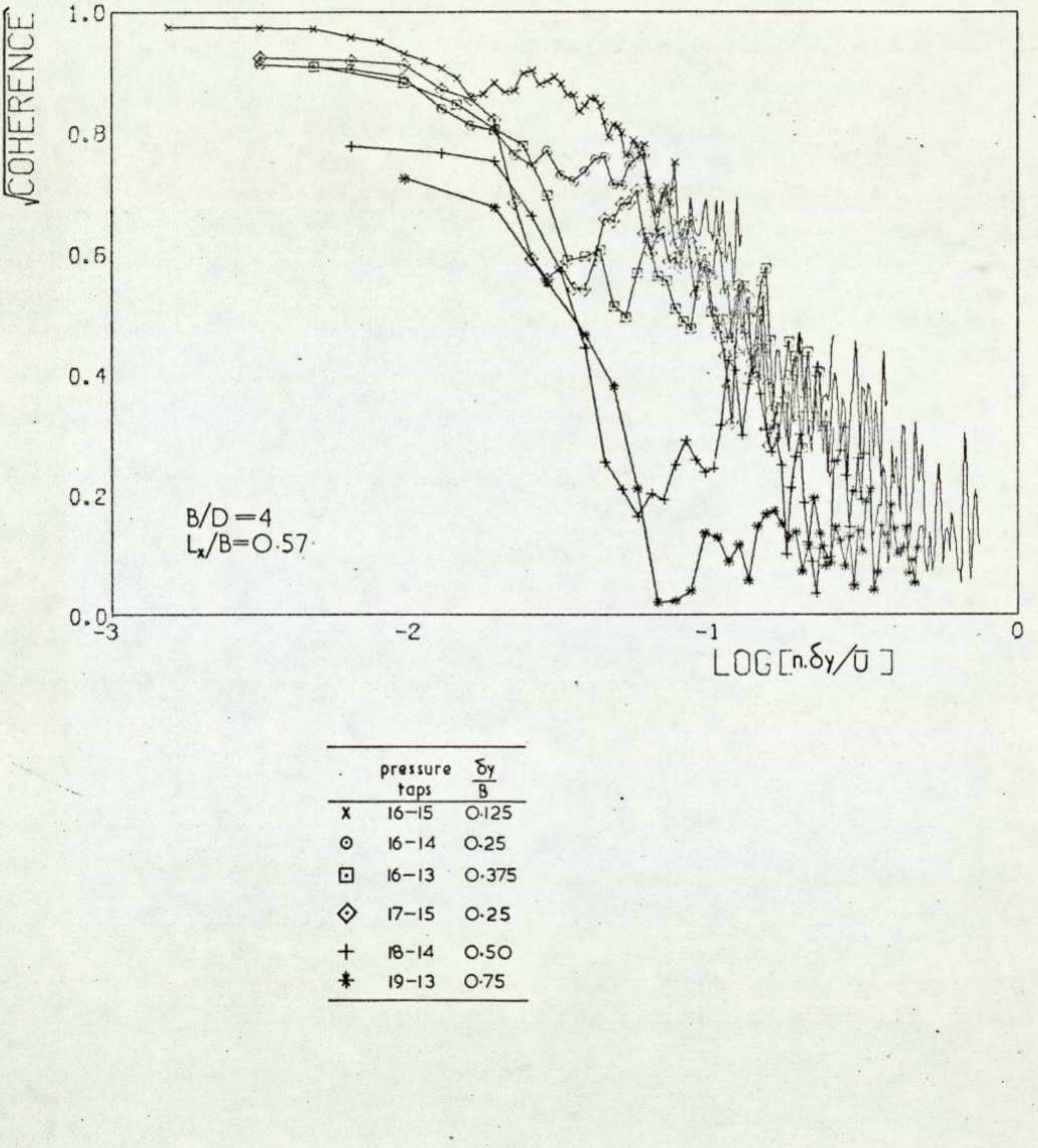

FIG. 43. $\sqrt{\text{Coherence}}$ for pressures at $z/H=0.5$ on leeward face. (cont.)

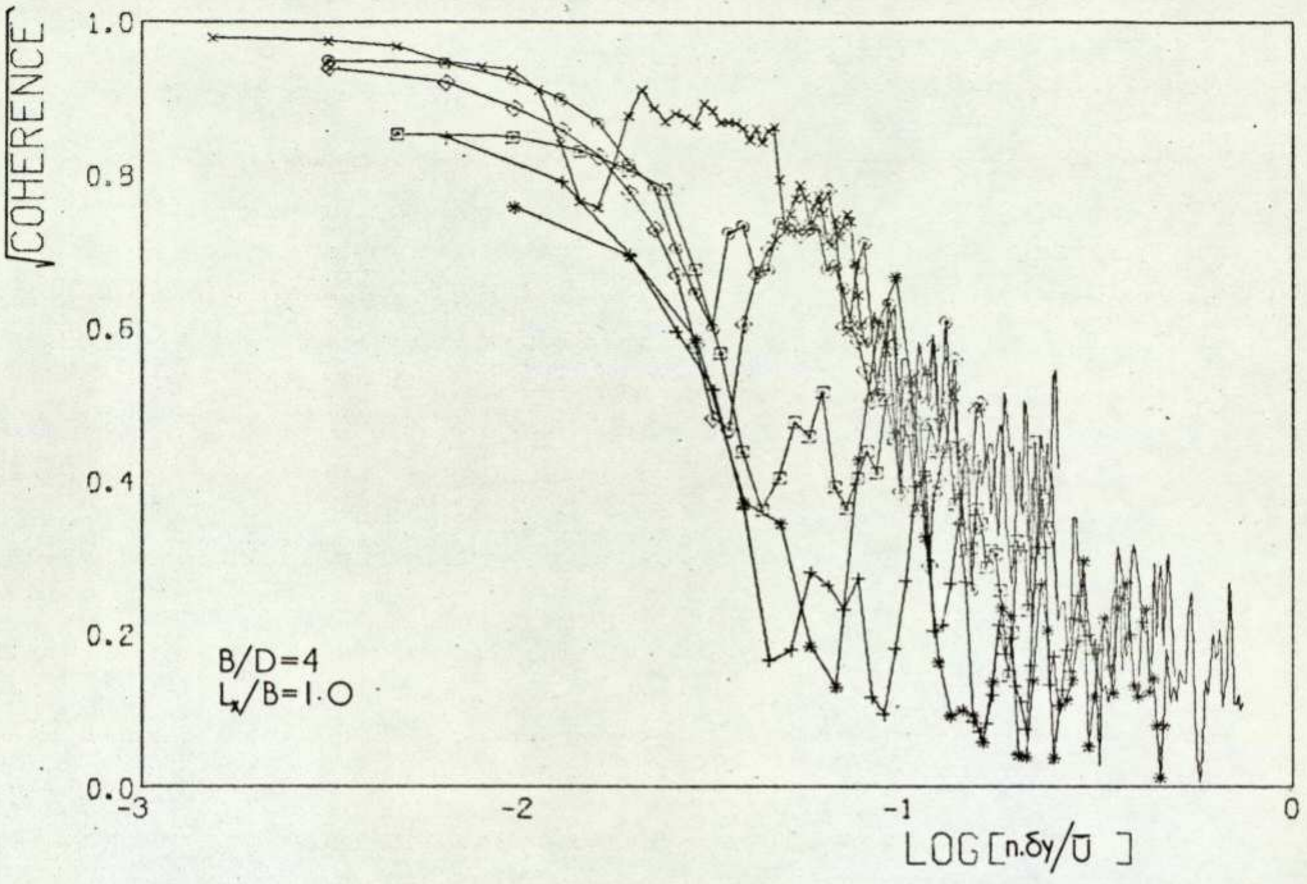

√COHERENCE
1.0
0.8
0.6
0.4
0.2
0.0
-3
-2
-1
0
LOG [n.δy/Ū]
B/D=4
L_x/B=1.0

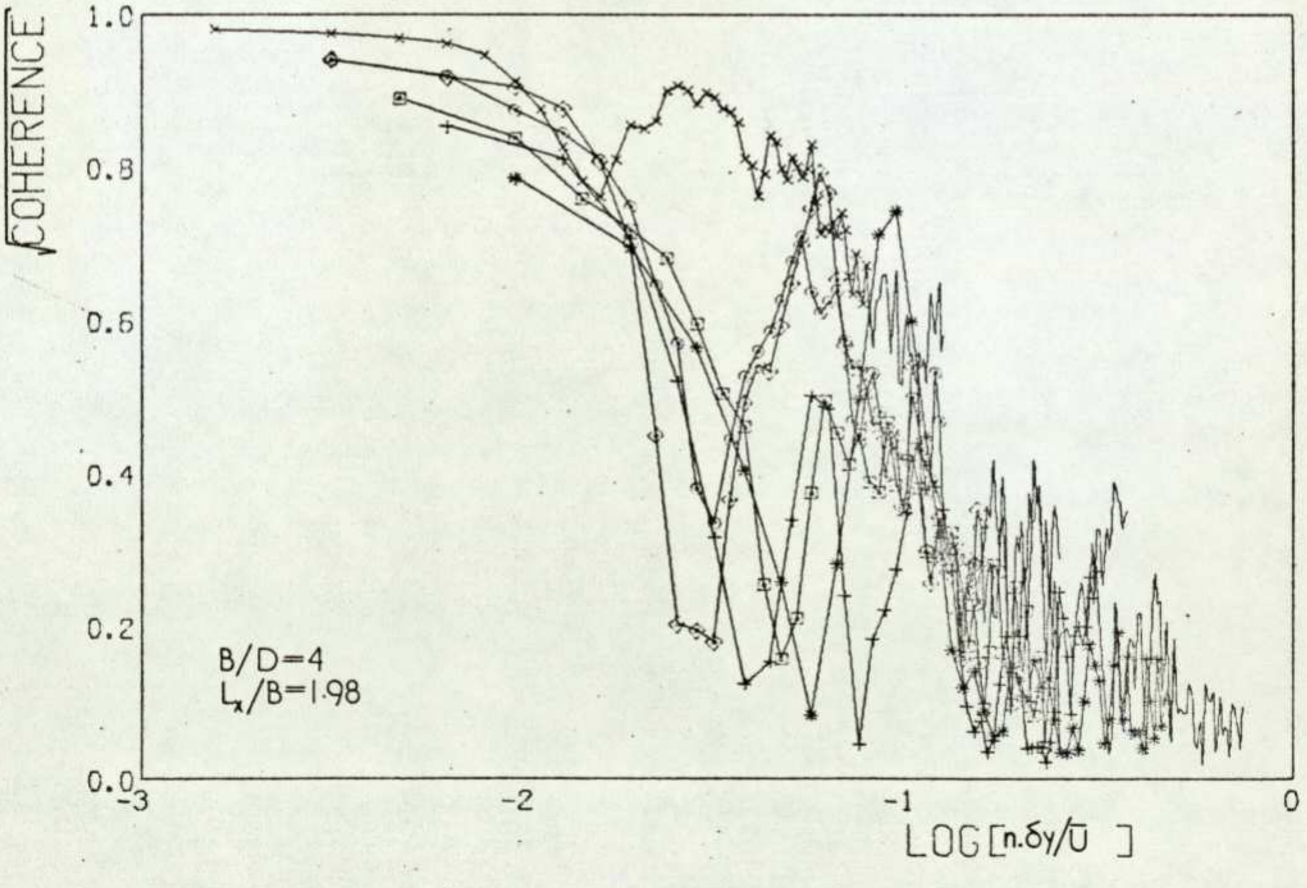

√COHERENCE
1.0
0.8
0.6
0.4
0.2
0.0
-3
-2
-1
0
LOG [n.δy/Ū]
B/D=4
L_x/B=1.98

FIG. 43. (cont.)

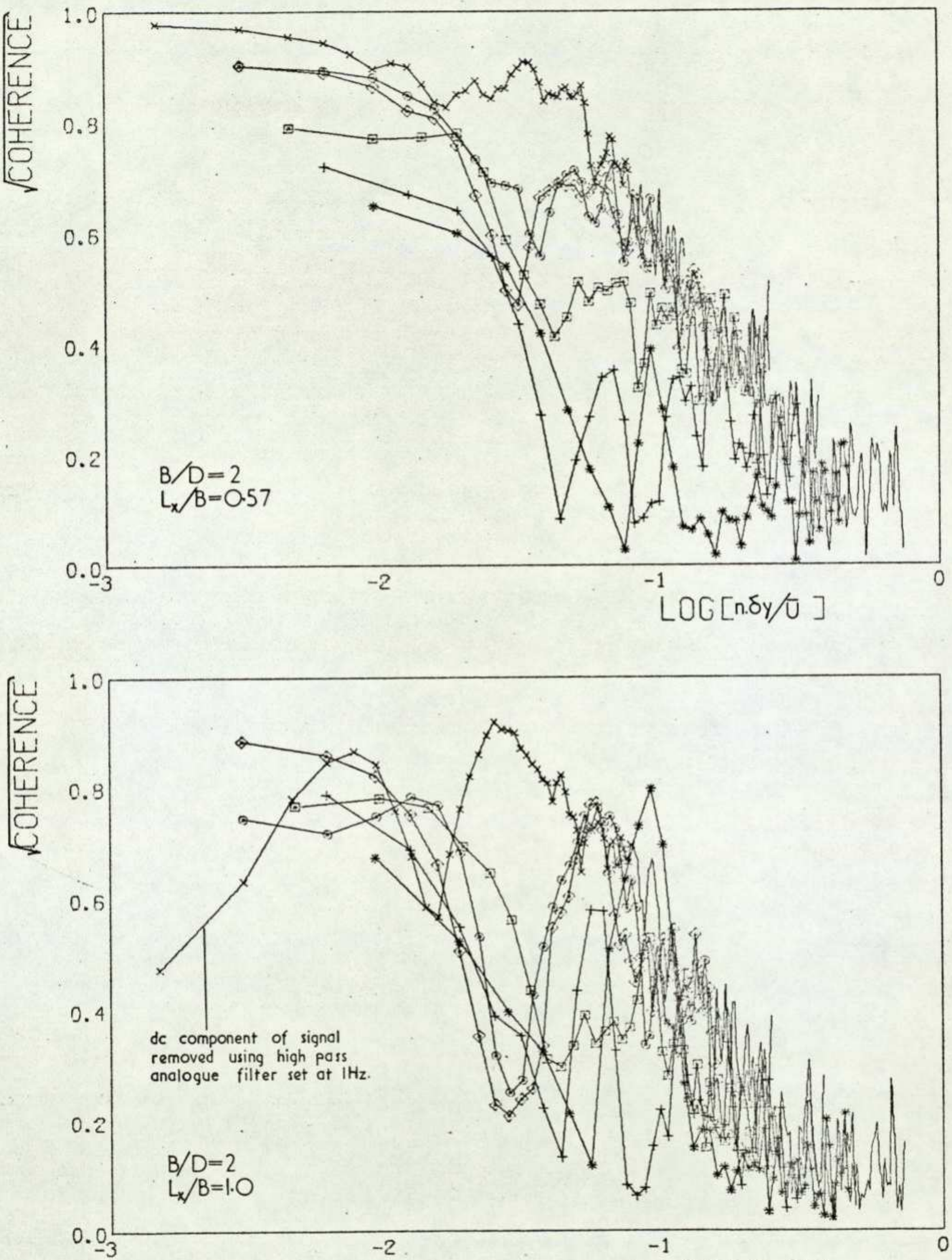
√COHERENCE
1.0
0.8
0.6
0.4
0.2
0.0
-3
-2
-1
0
LOG[n.δy/Ū]
B/D=2
Lx/B=0·57
√COHERENCE
1.0
0.8
0.6
0.4
0.2
0.0
-3
-2
-1
0
LOG[n.δy/Ū]
dc component of signal
removed using high pass
analogue filter set at 1Hz.
B/D=2
Lx/B=1·0

FIG. 43. (cont.)

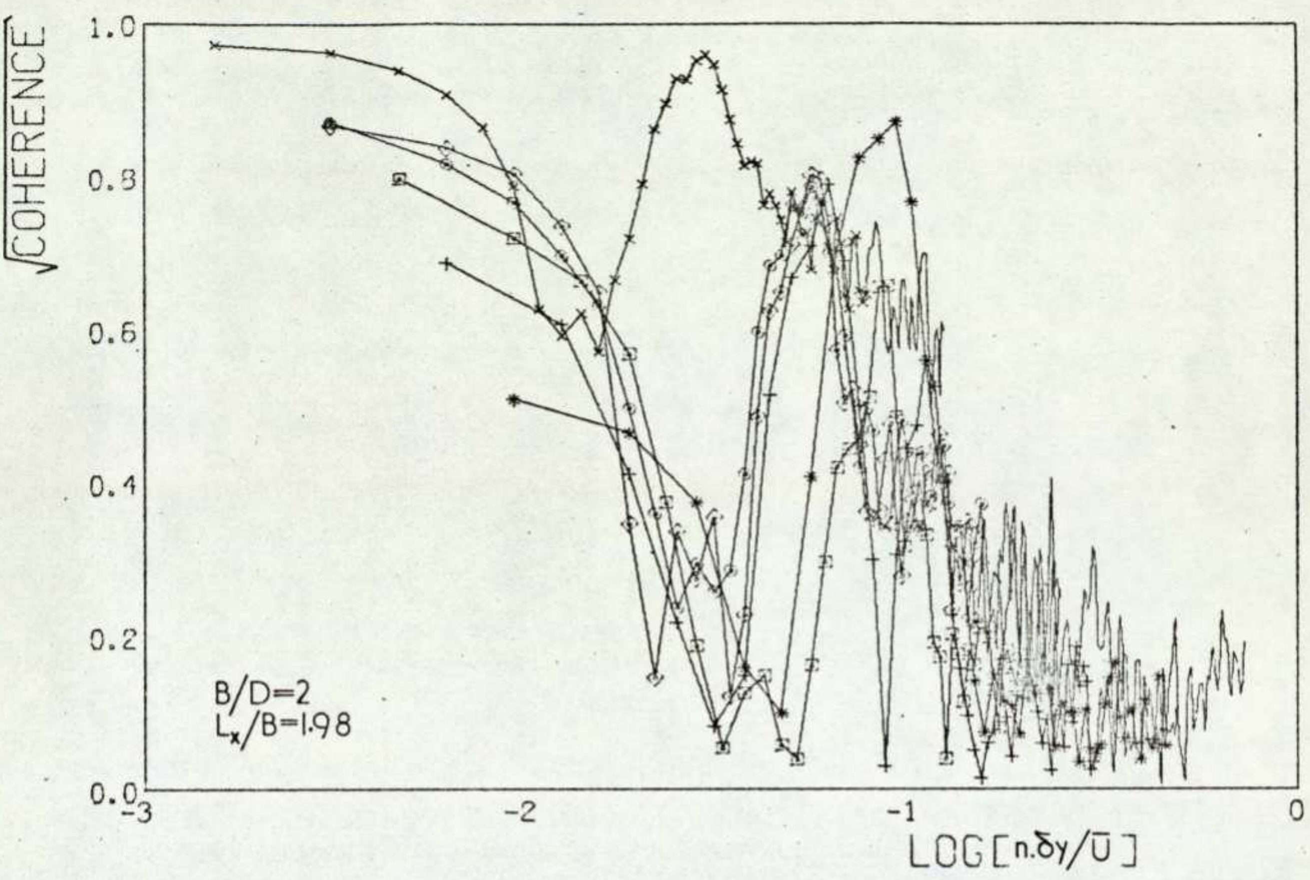

√COHERENCE
1.0
0.8
0.6
0.4
0.2
0.0
-3
-2
-1
0
LOG[n.δy/Ū]
B/D=2
L_x/B=1.98

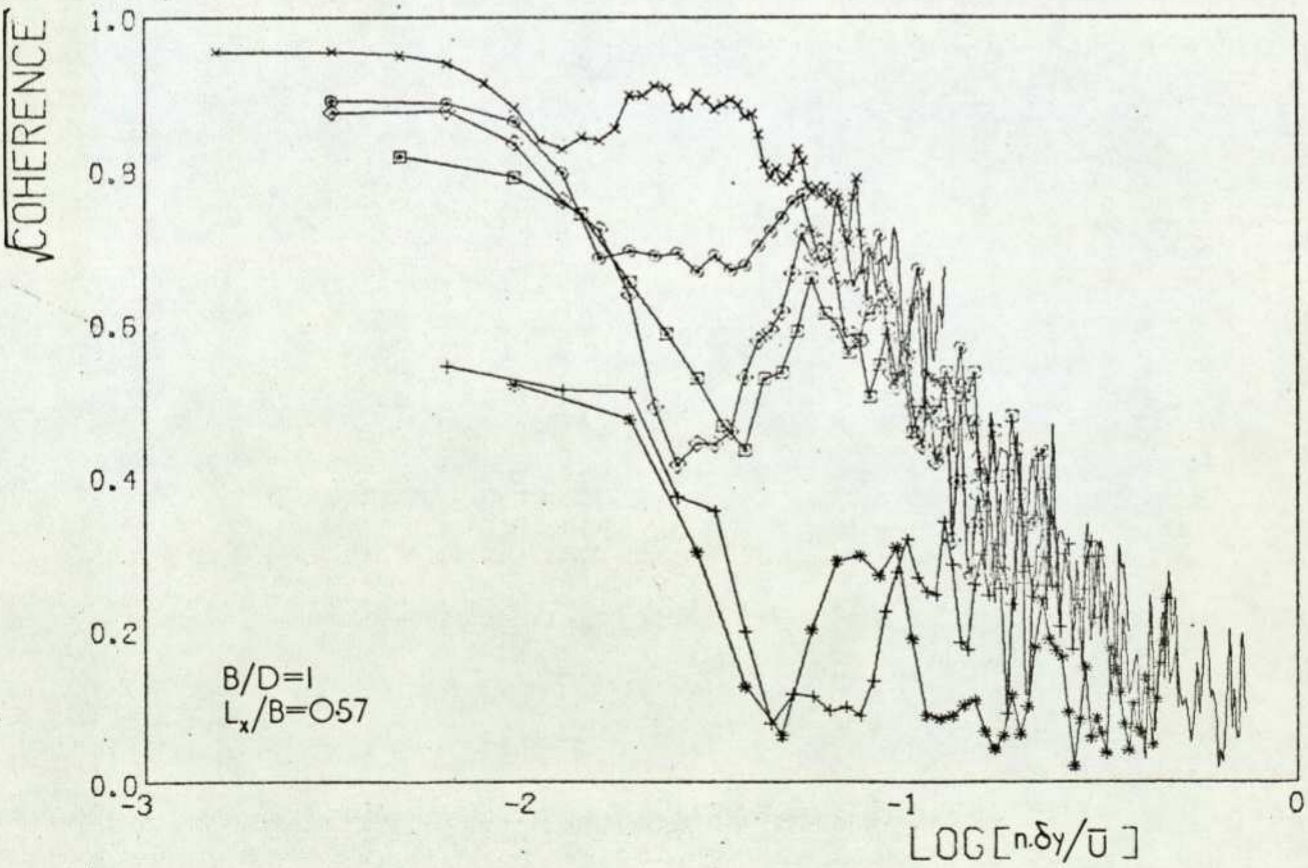

√COHERENCE
1.0
0.8
0.6
0.4
0.2
0.0
-3
-2
-1
0
LOG[n.δy/Ū]
B/D=1
L_x/B=0.57

FIG. 43. (cont.)

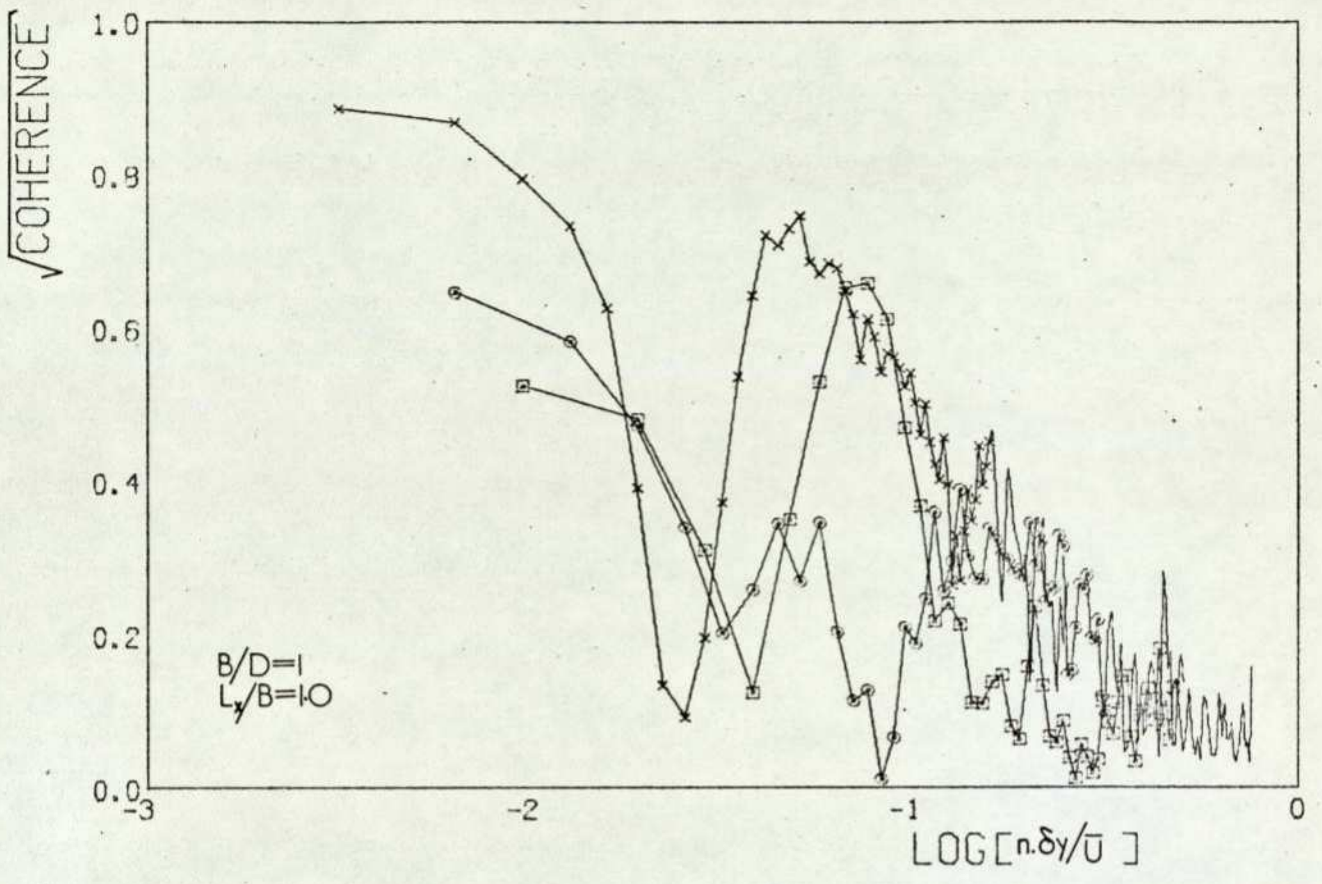

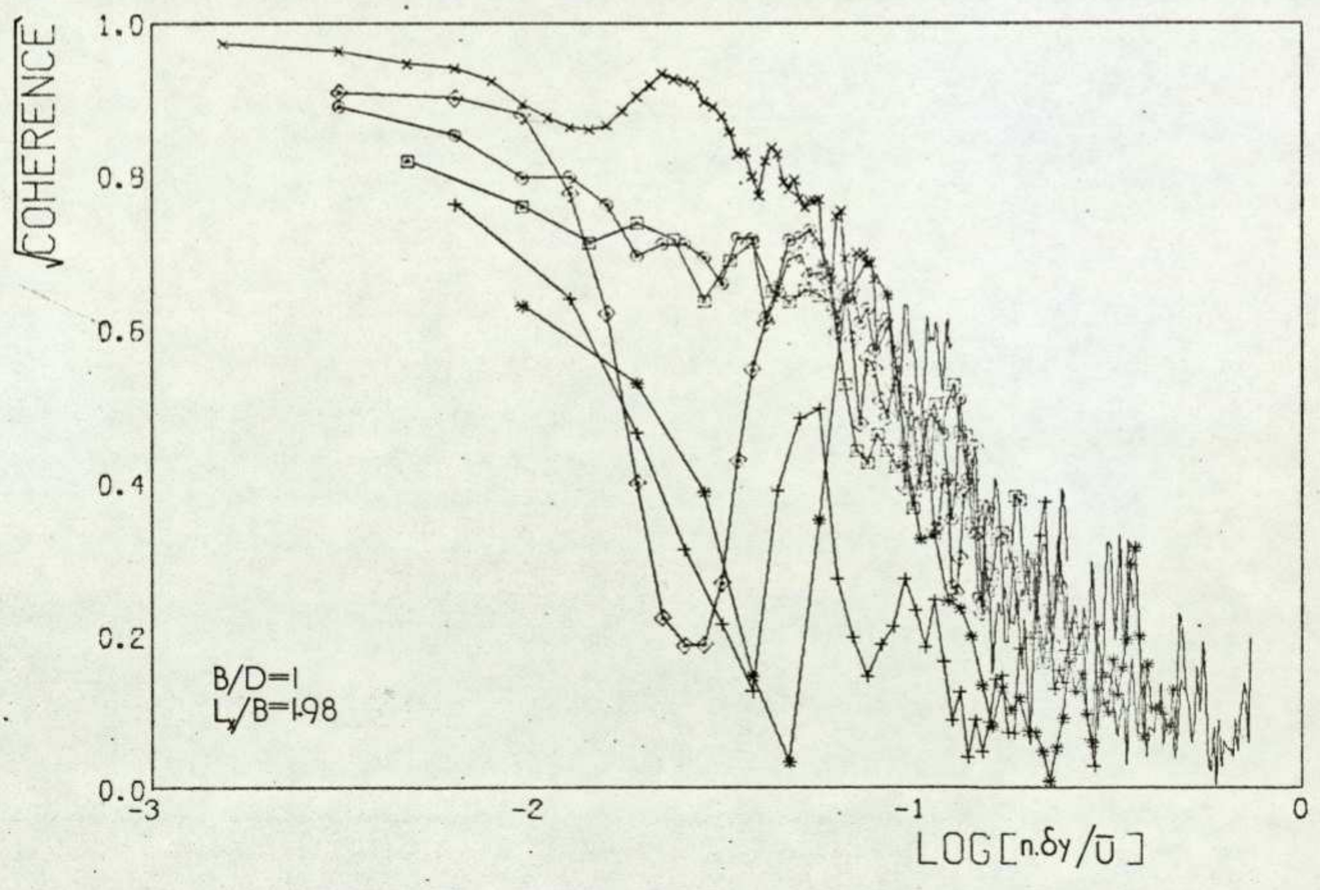

FIG. 43. (concluded)

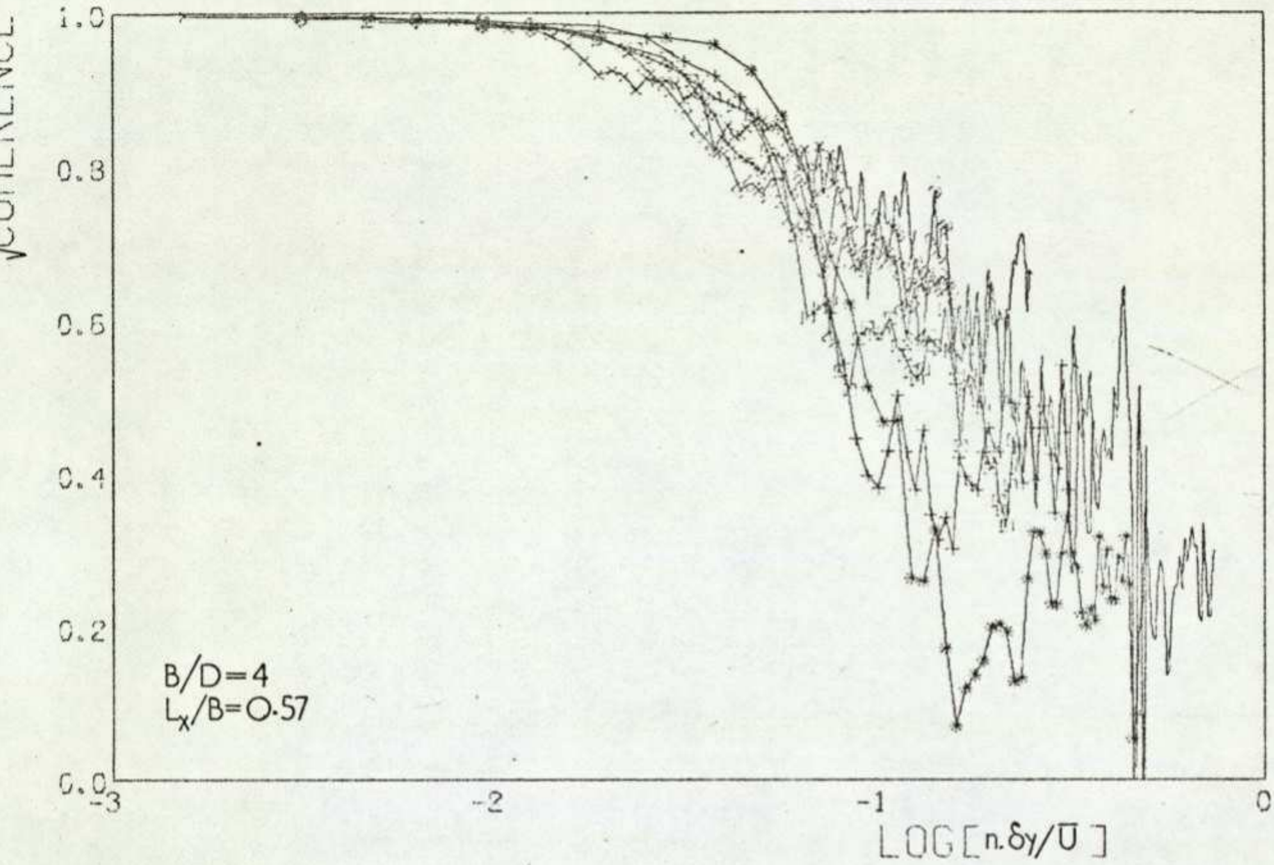

	pressure taps	$\frac{\delta y}{B}$
x	16 – 15	0·125
⊙	16 – 14	0·25
⊡	16 – 13	0·375
◊	17 – 15	0·25
+	18 – 14	0·50
✳	19 – 13	0·75

FIG 44 √Coherence for pressures at z/H=0·96 on leeward face.

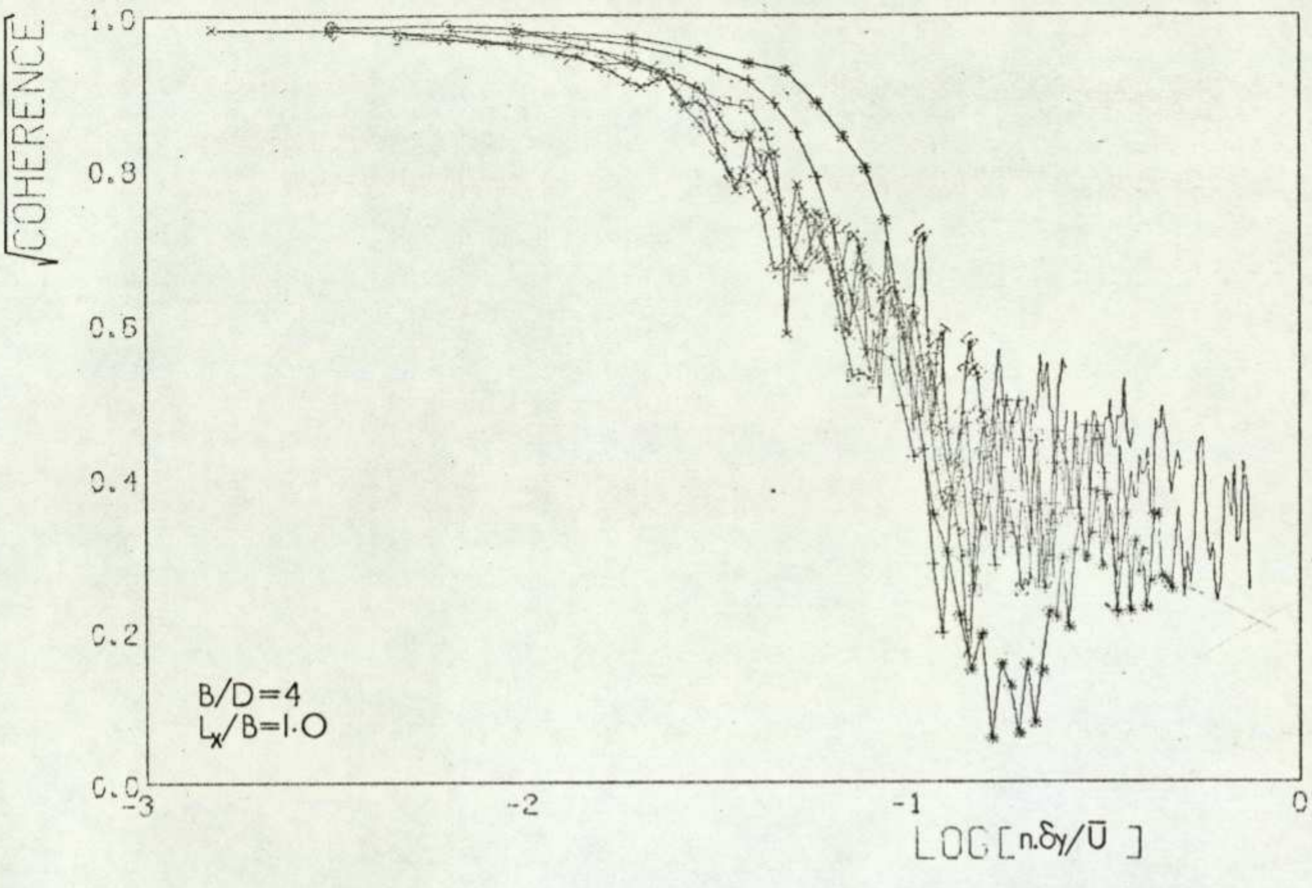

√COHERENCE
1.0
0.8
0.6
0.4
0.2
0.0
-3
-2
-1
0
LOG[n.δy/Ū]
B/D=4
L_x/B=1.0

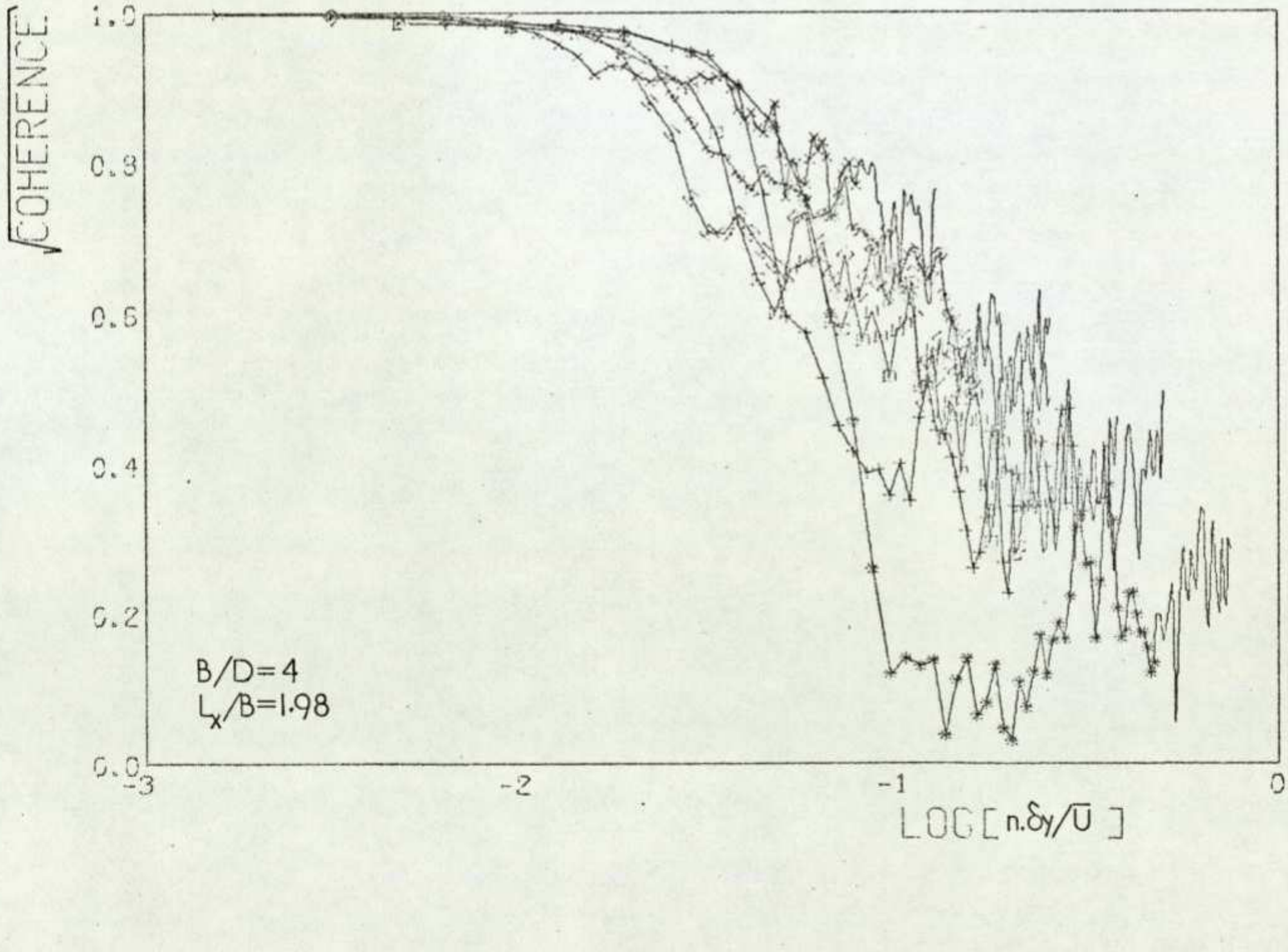

√COHERENCE
1.0
0.8
0.6
0.4
0.2
0.0
-3
-2
-1
0
LOG[n.δy/Ū]
B/D=4
L_x/B=1.98

FIG 44 (cont.)

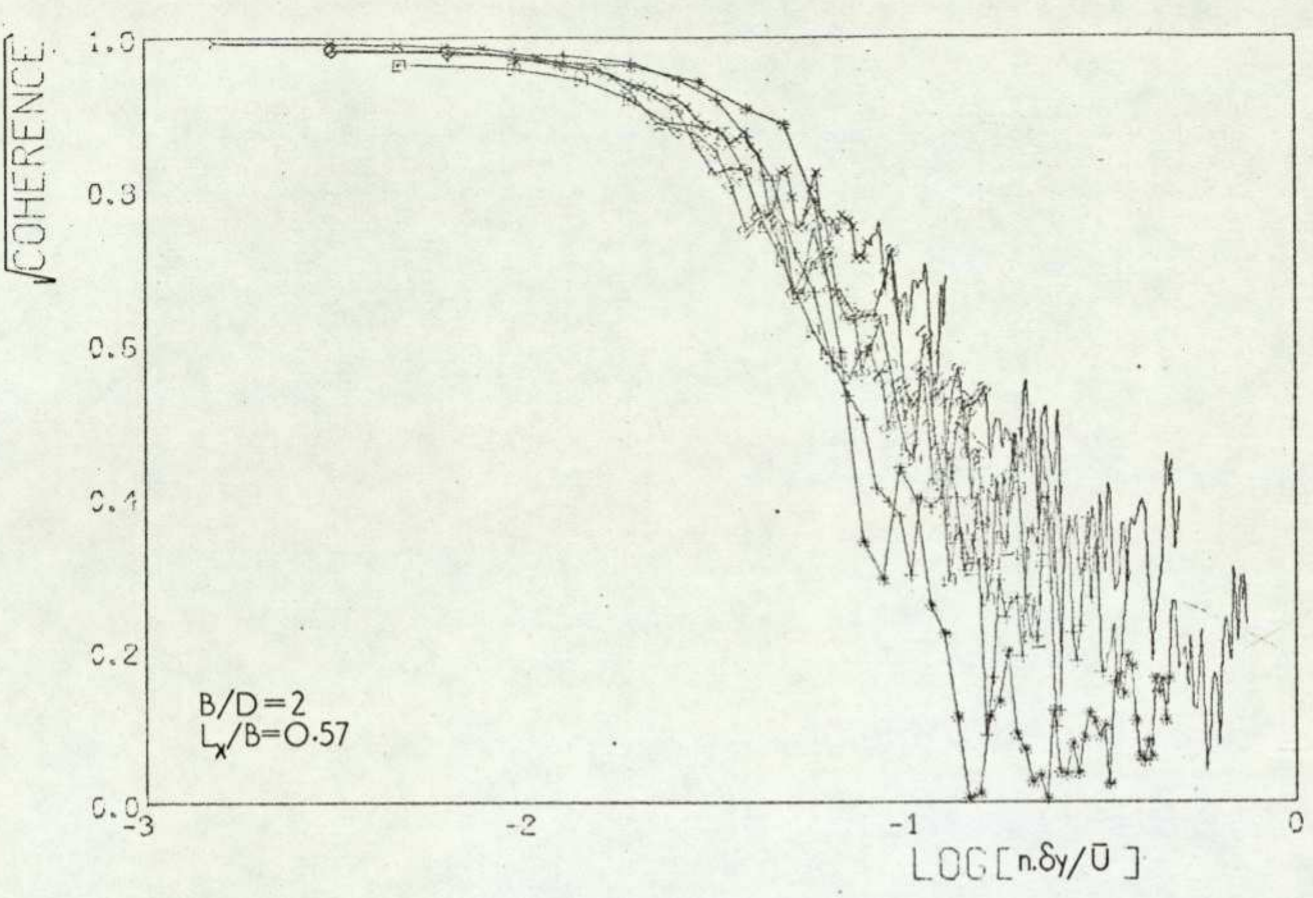
√COHERENCE
1.0
0.8
0.6
0.4
0.2
0.0
-3
-2
-1
0
LOG[n.δy/Ū]
B/D=2
L_x/B=0.57

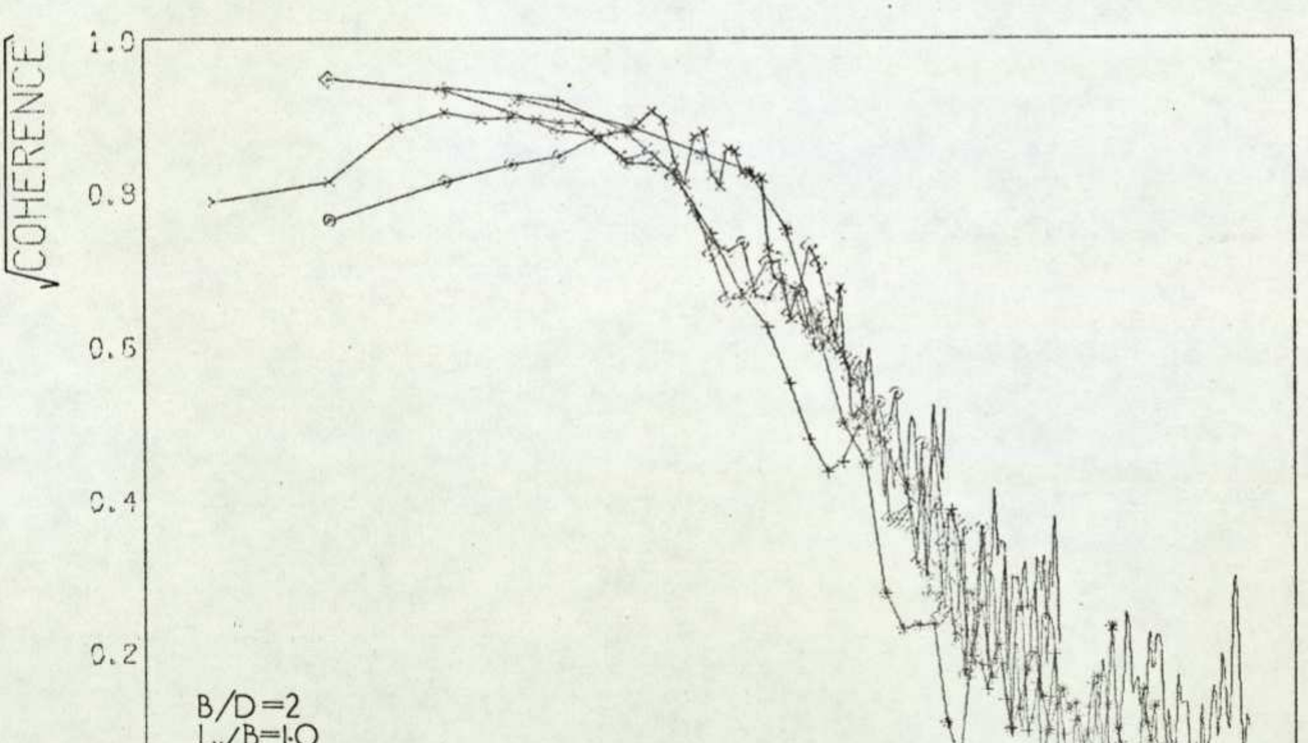
√COHERENCE
1.0
0.8
0.6
0.4
0.2
0.0
-3
-2
-1
0
LOG[n.δy/Ū]
B/D=2
L_x/B=1.0

FIG 44 (cont.)

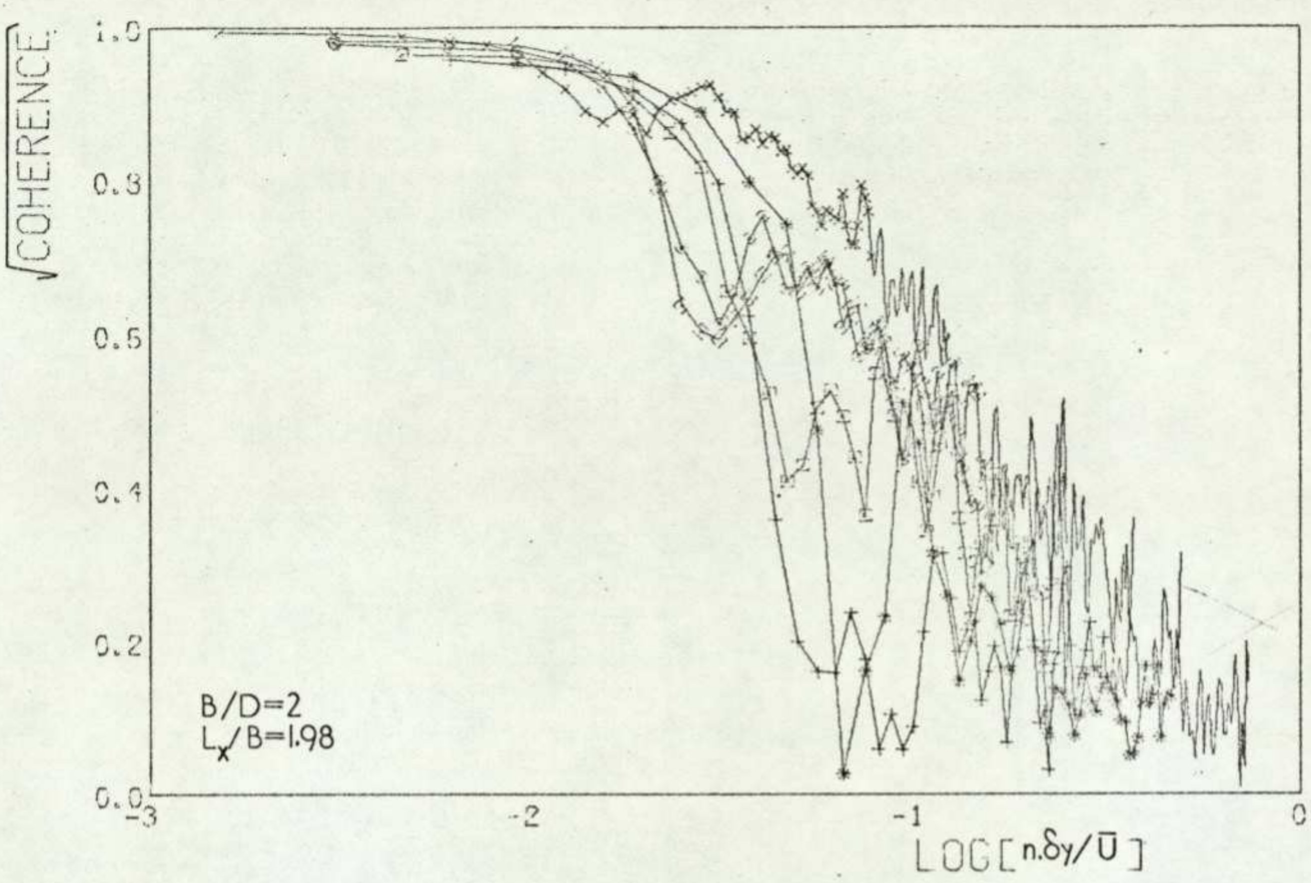

√COHERENCE
1.0
0.8
0.6
0.4
0.2
0.0
-3
-2
-1
0
LOG[n.δy/Ū]
B/D=2
L_x/B=1.98

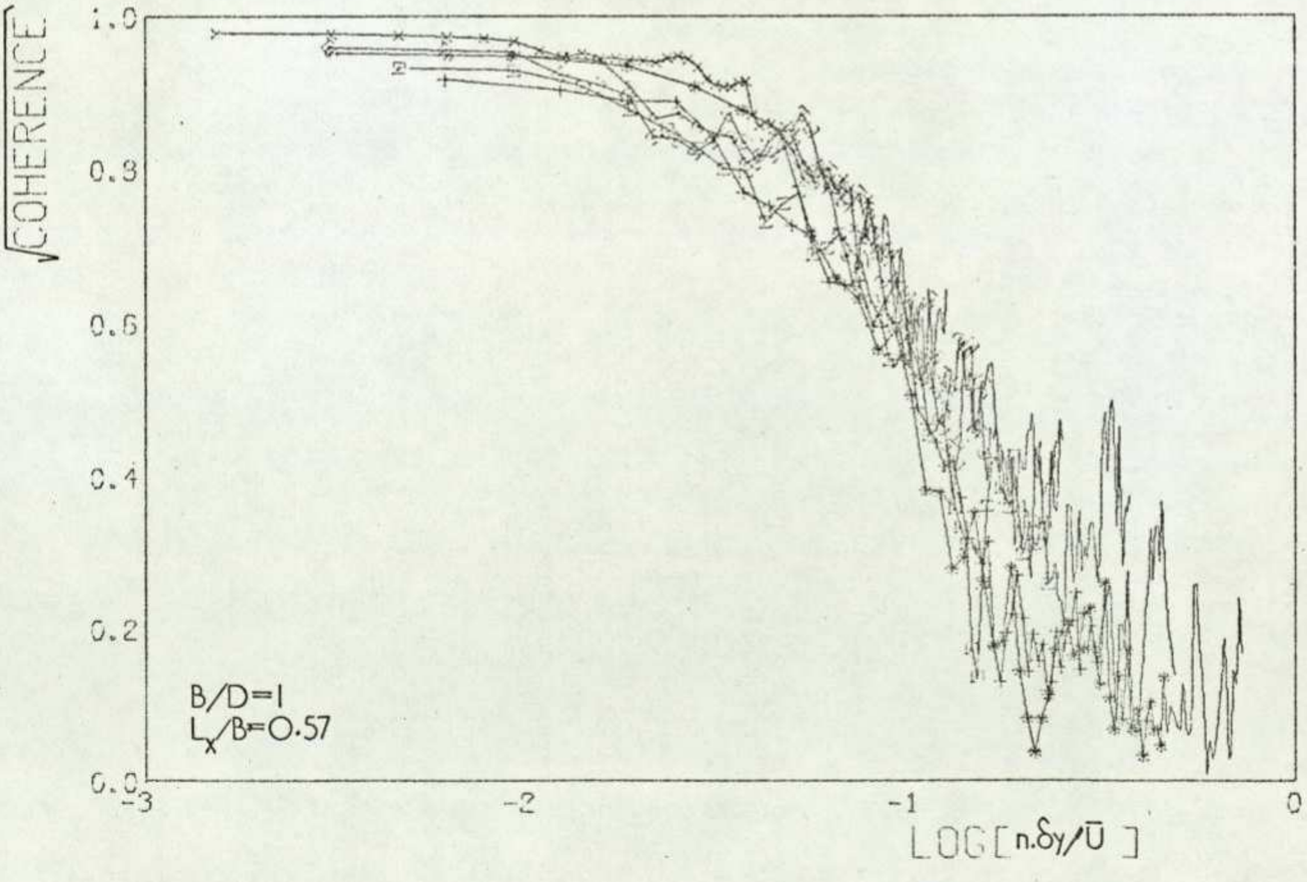

√COHERENCE
1.0
0.8
0.6
0.4
0.2
0.0
-3
-2
-1
0
LOG[n.δy/Ū]
B/D=1
L_x/B=0.57

FIG 44 (cont.)

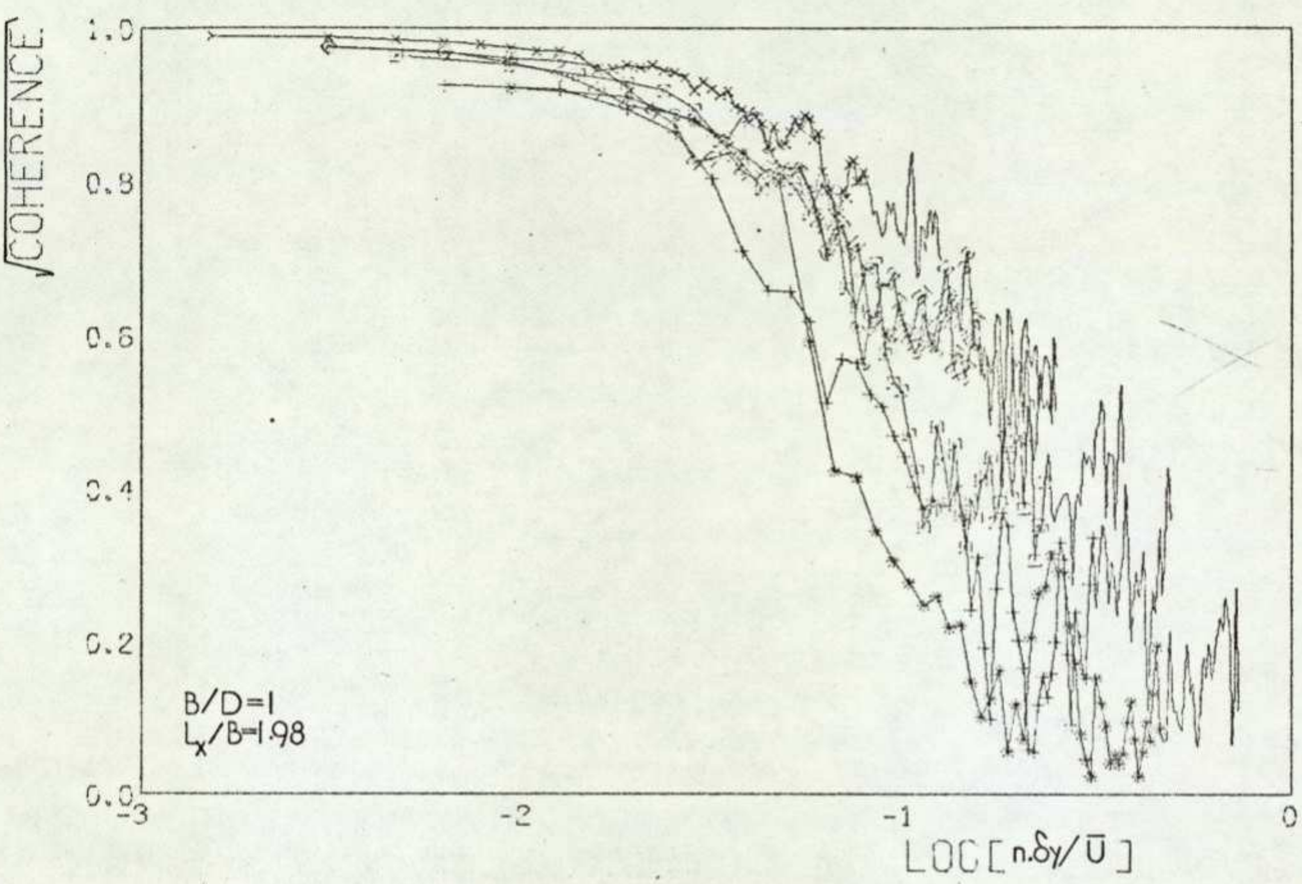

FIG 44 (concluded)

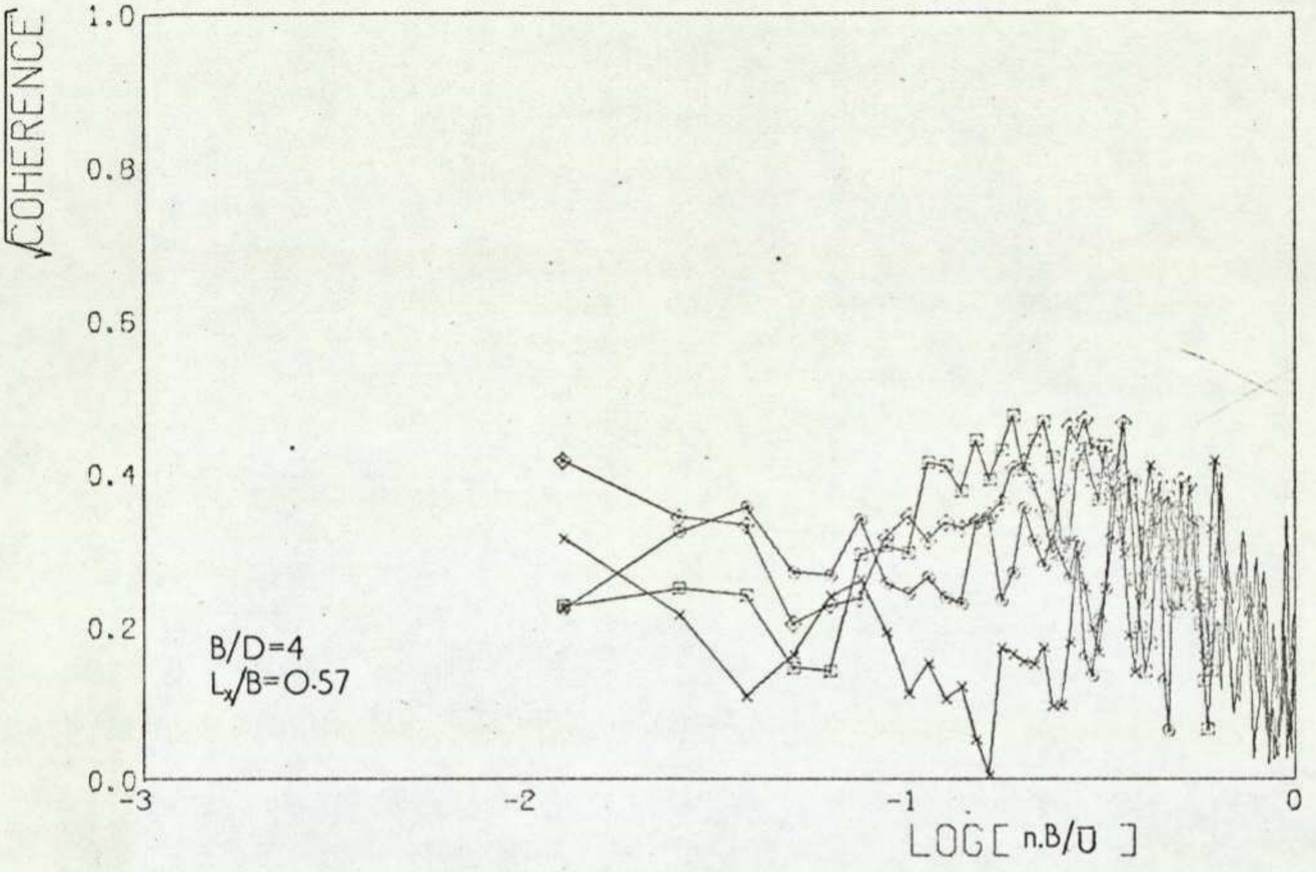

	pressure taps	$\frac{y}{B}$
◇	01–19	0·375
⊡	02–18	0·25
⊙	03–17	0·125
x	04–16	0

FIG 45 √Coherence between windward and leeward face pressures at z/H=0·5

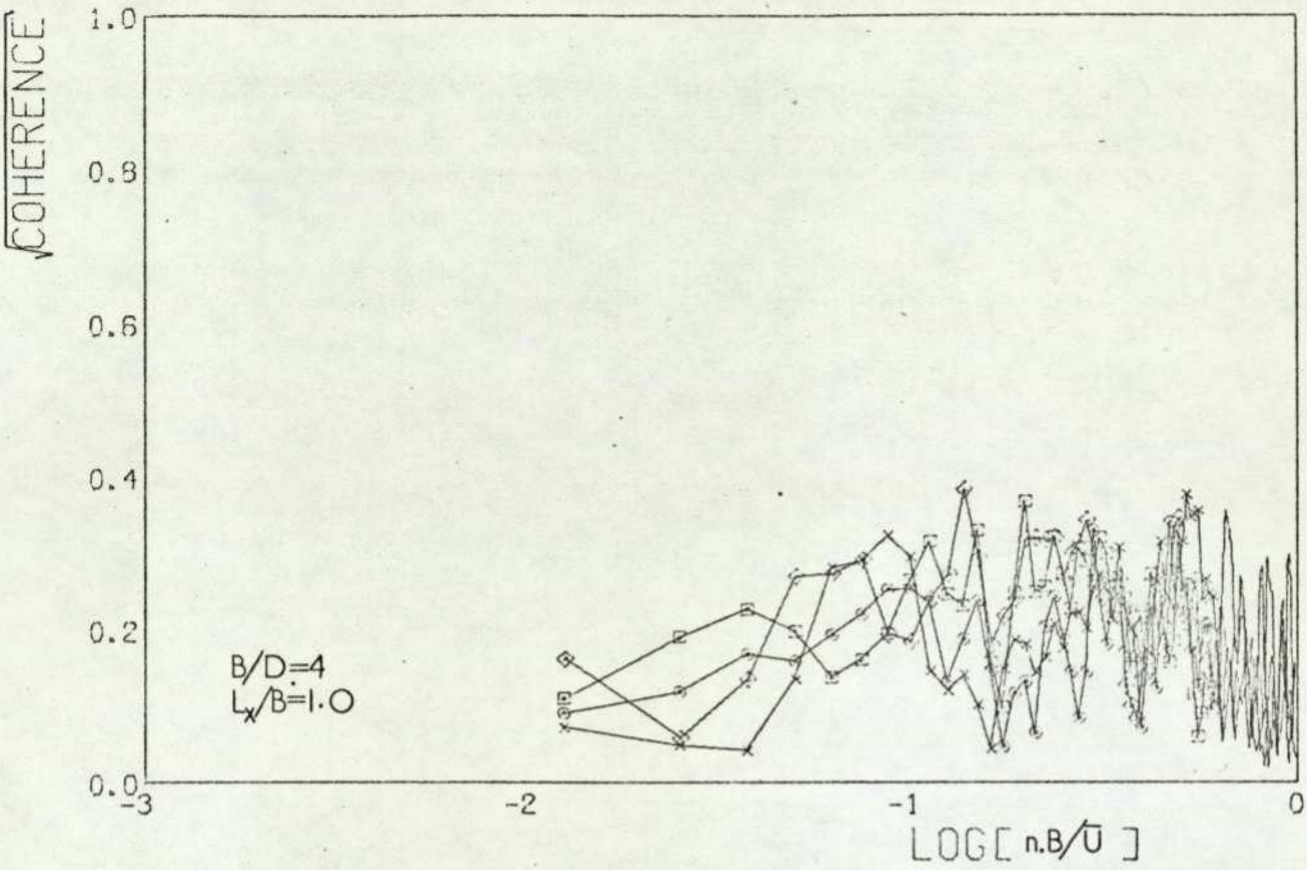
√COHERENCE
1.0
0.8
0.6
0.4
0.2
0.0
-3
-2
-1
0
LOG[n.B/Ū]
B/D=4
L_x/B=1.0

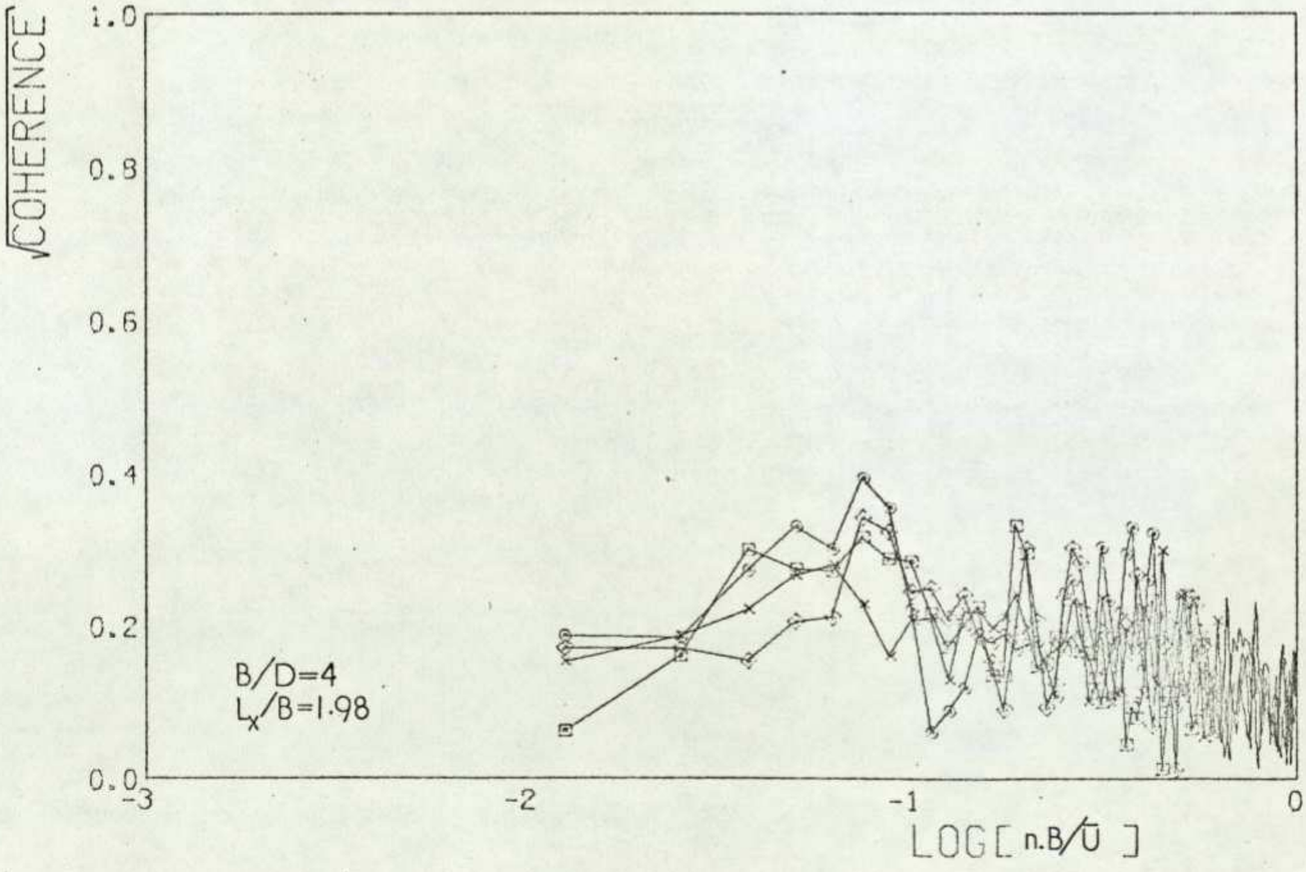
√COHERENCE
1.0
0.8
0.6
0.4
0.2
0.0
-3
-2
-1
0
LOG[n.B/Ū]
B/D=4
L_x/B=1.98

FIG 45 (cont.)

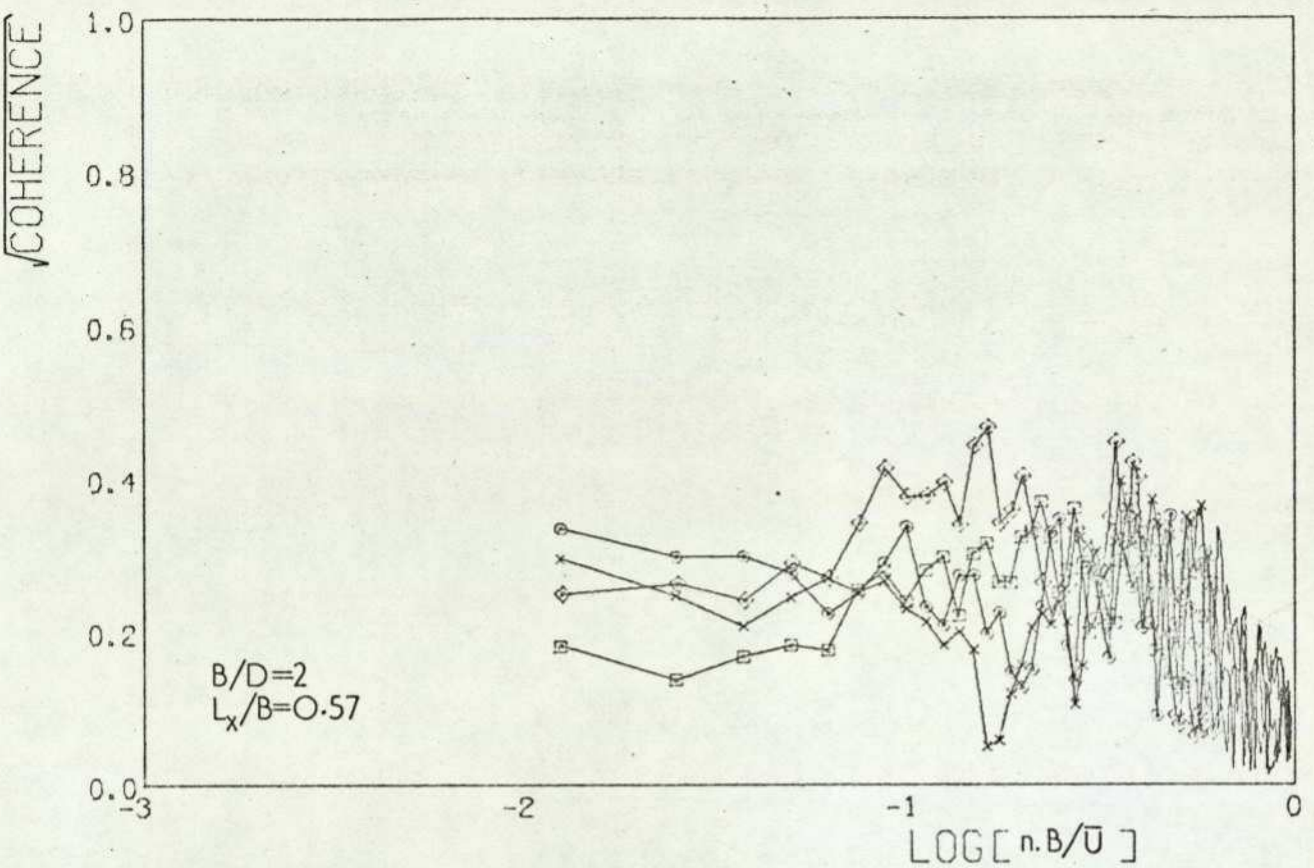

√COHERENCE
1.0
0.8
0.6
0.4
0.2
0.0
-3
-2
-1
0
LOG[n.B/Ū]
B/D=2
L_x/B=0·57

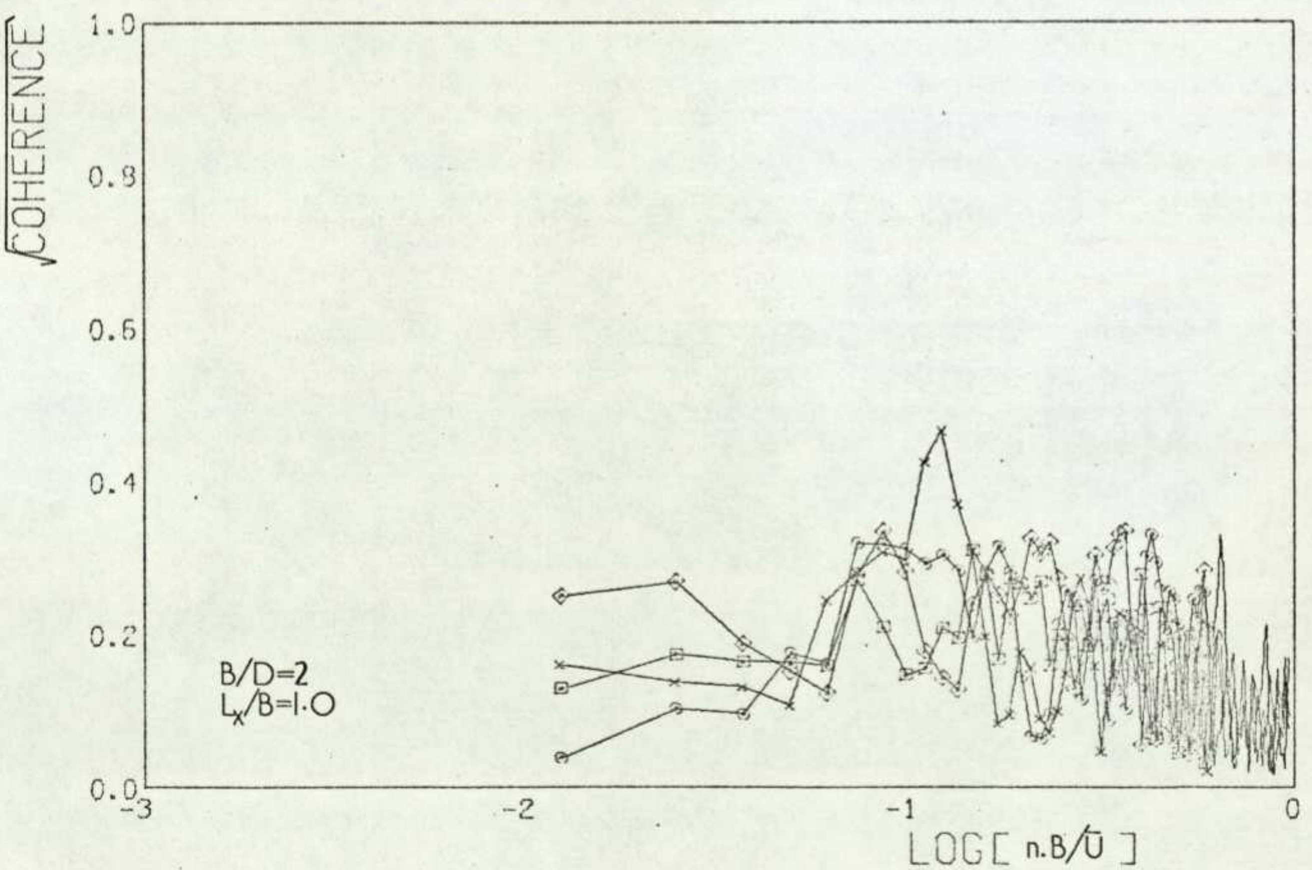

√COHERENCE
1.0
0.8
0.6
0.4
0.2
0.0
-3
-2
-1
0
LOG[n.B/Ū]
B/D=2
L_x/B=1·0

FIG 45 (cont.)

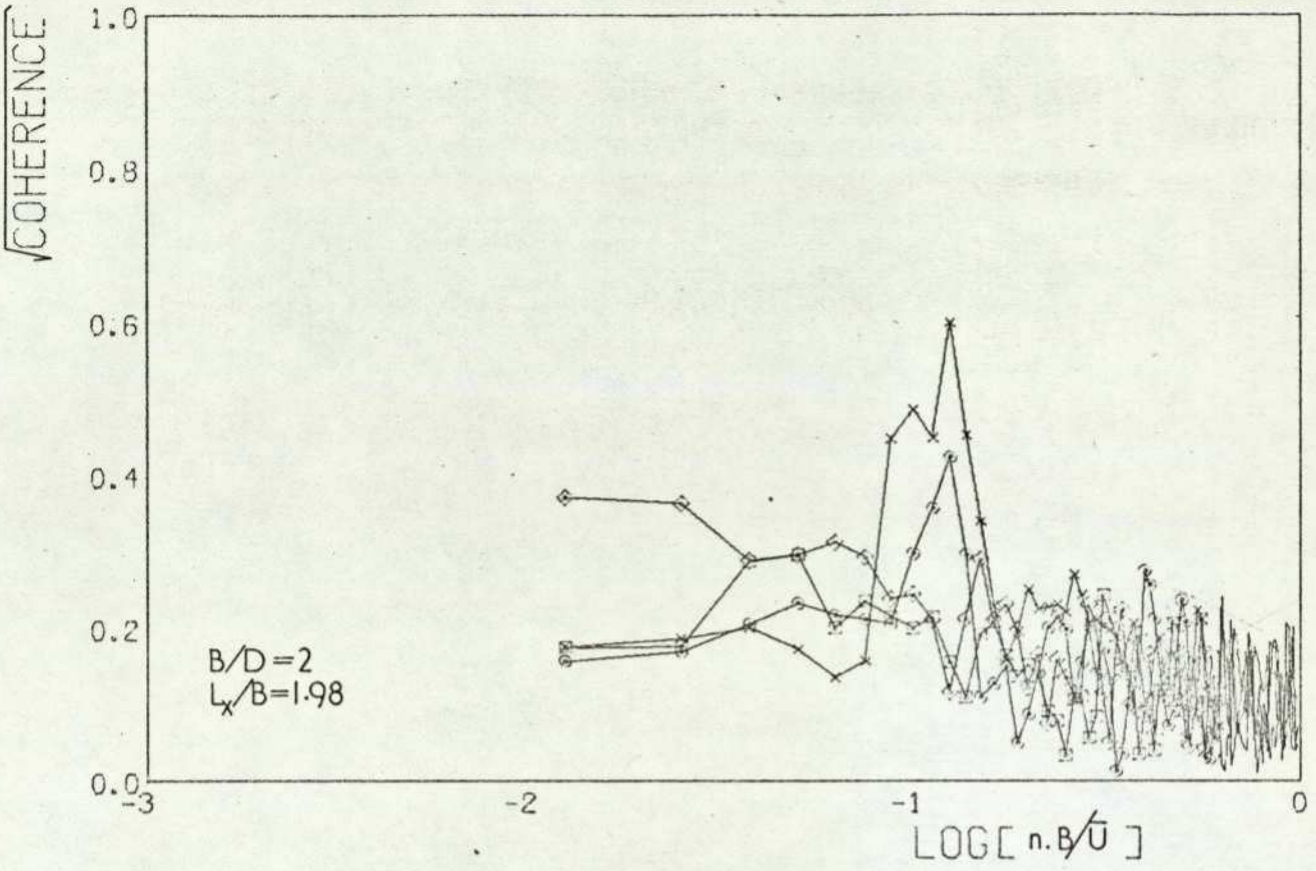
√COHERENCE
1.0
0.8
0.6
0.4
0.2
0.0
-3
-2
-1
0
LOG[n.B/Ū]
B/D = 2
L_x/B=1.98

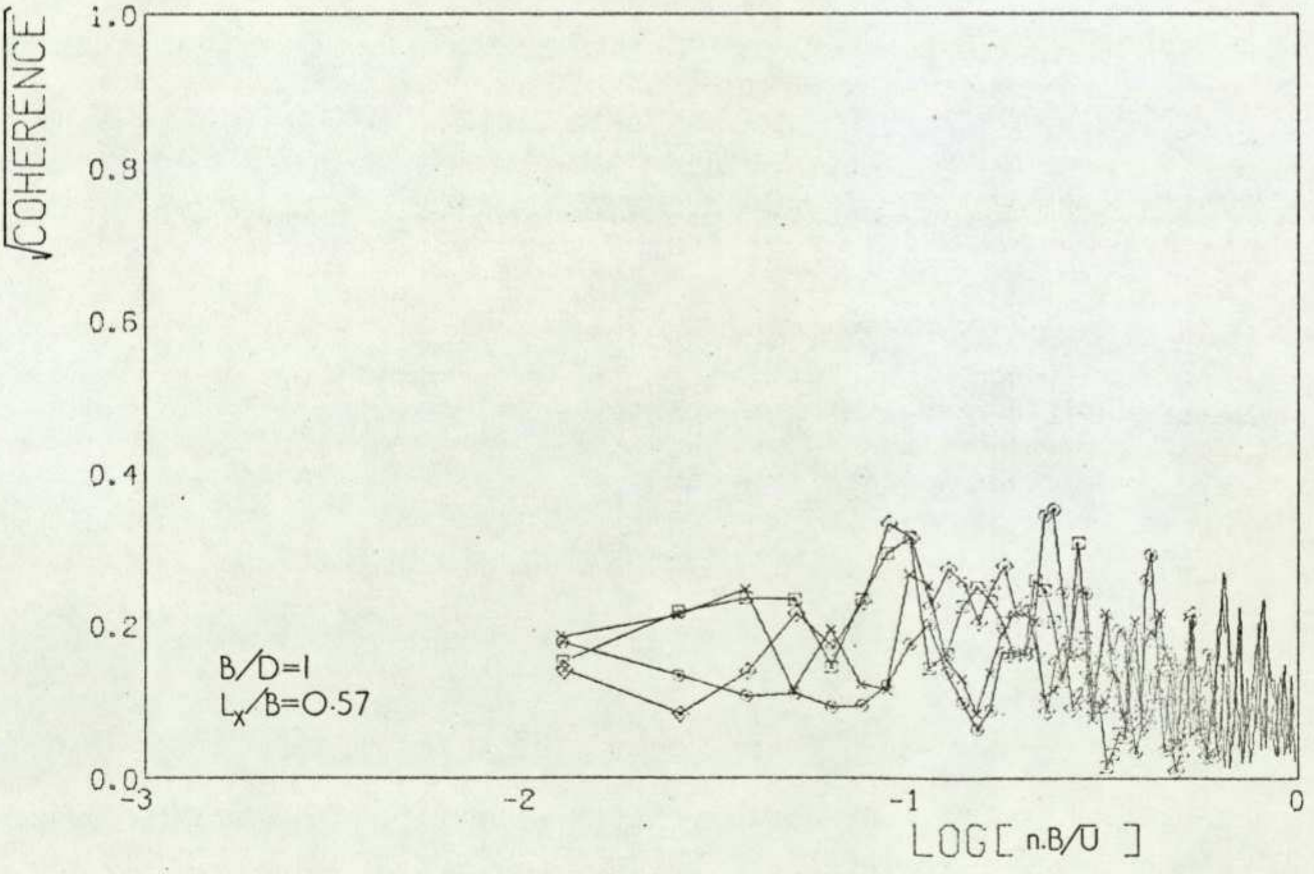
√COHERENCE
1.0
0.8
0.6
0.4
0.2
0.0
-3
-2
-1
0
LOG[n.B/Ū]
B/D=1
L_x/B=0.57

FIG 45 (cont.)

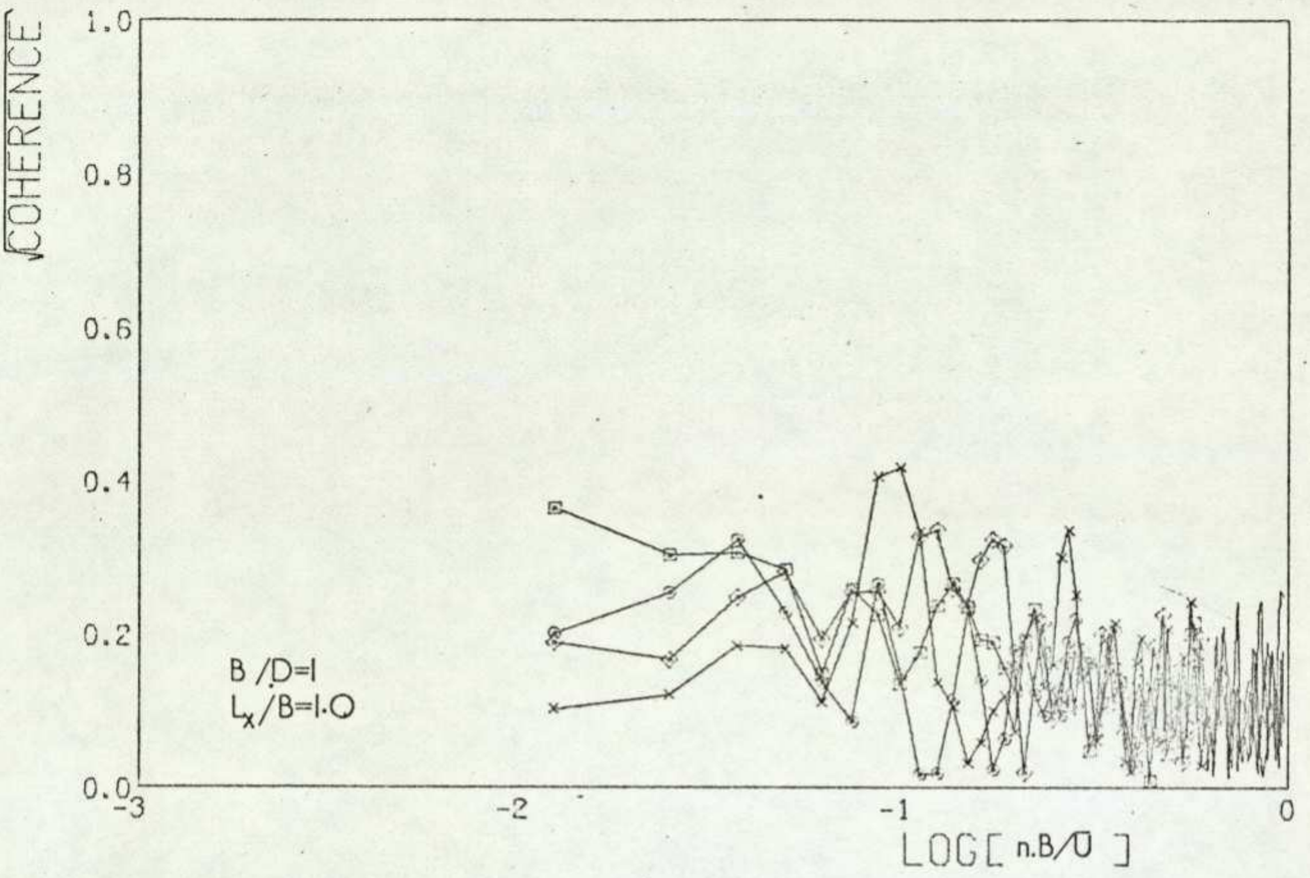

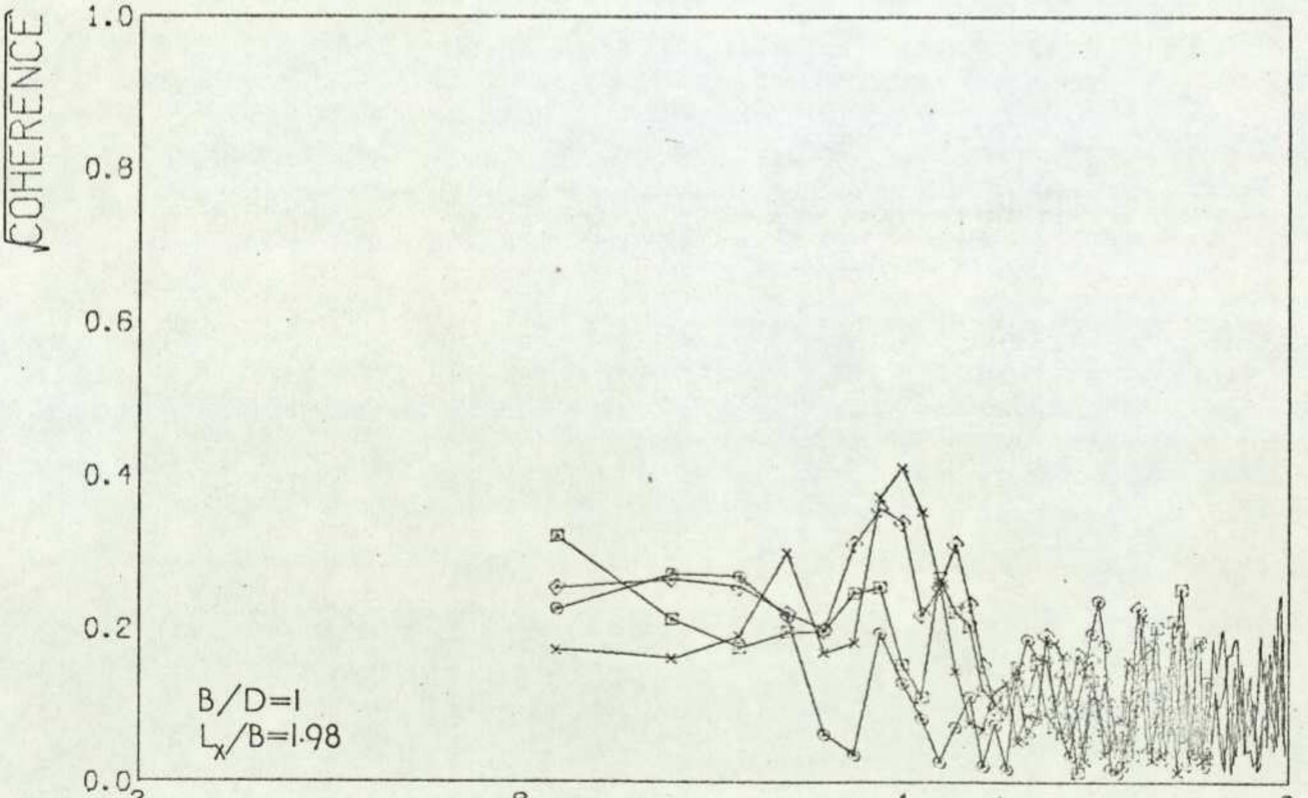

FIG 45 (concluded)

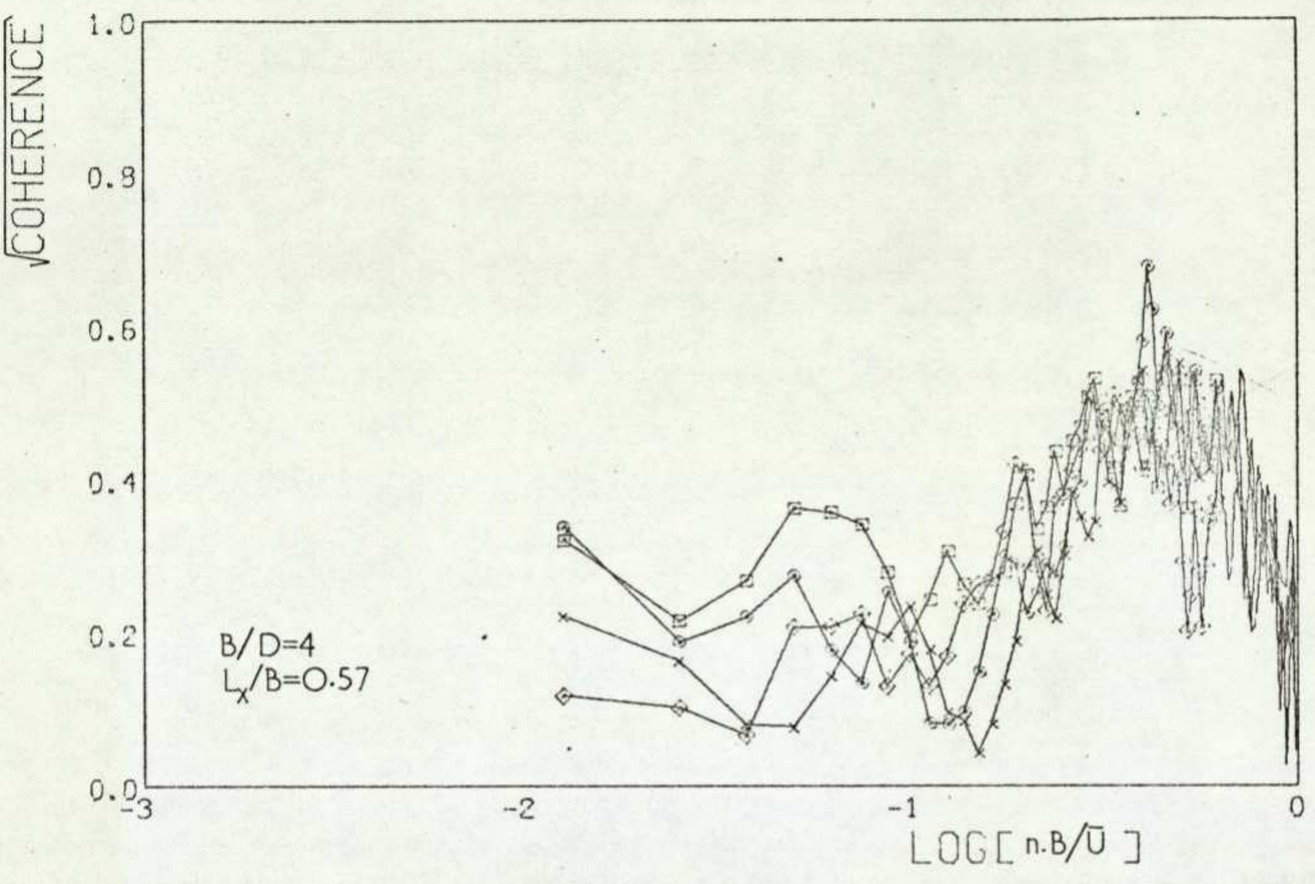

	pressure taps	$\frac{y}{B}$
◊	01−19	0.375
⊡	02−18	0.25
⊙	03−17	0.125
x	04−16	0

FIG 46 $\sqrt{\text{Coherence}}$ between windward and leeward face pressures at $z/H=0.96$.

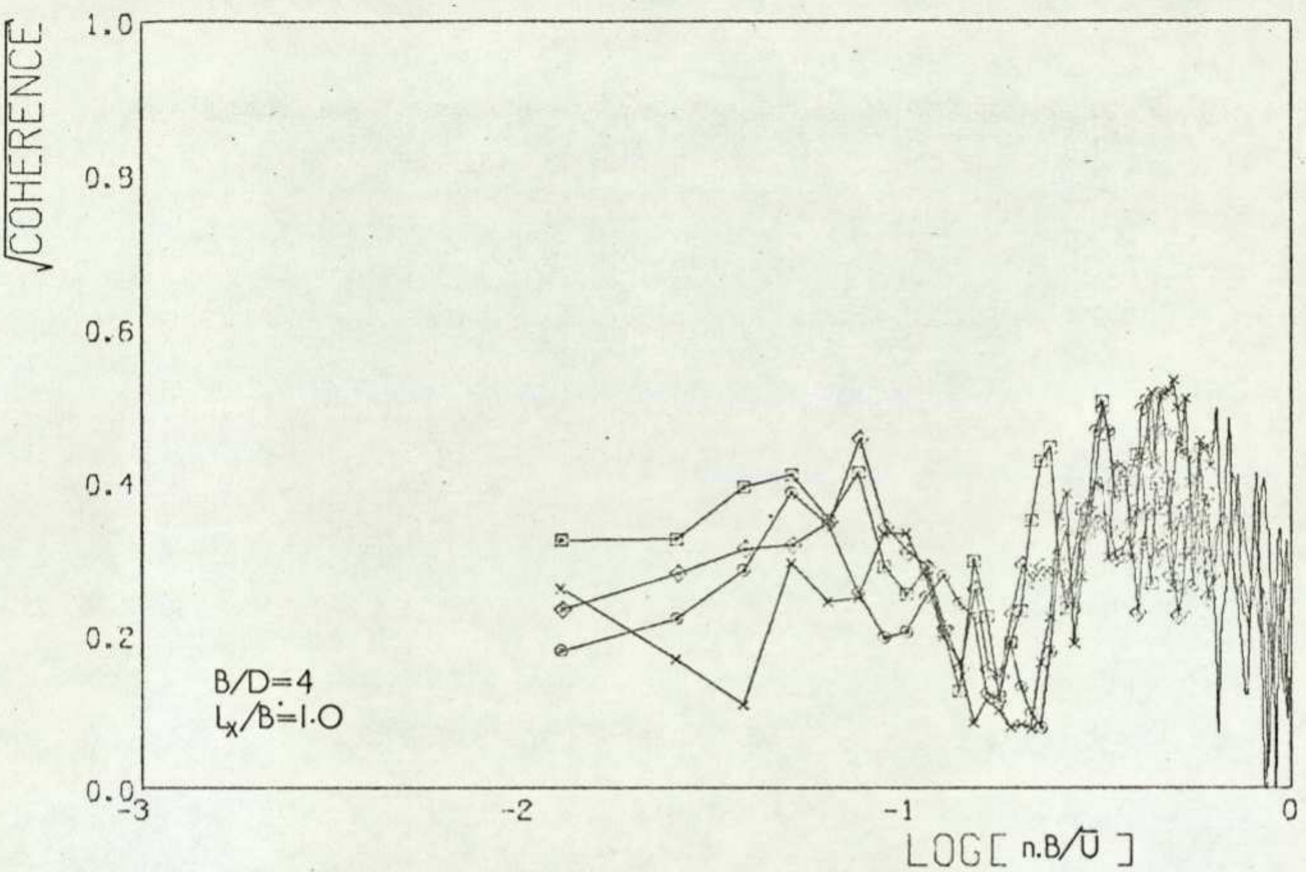
√COHERENCE
1.0
0.8
0.6
0.4
0.2
0.0
-3
-2
-1
0
LOG[n.B/Ū]
B/D=4
L_x/B=1.0

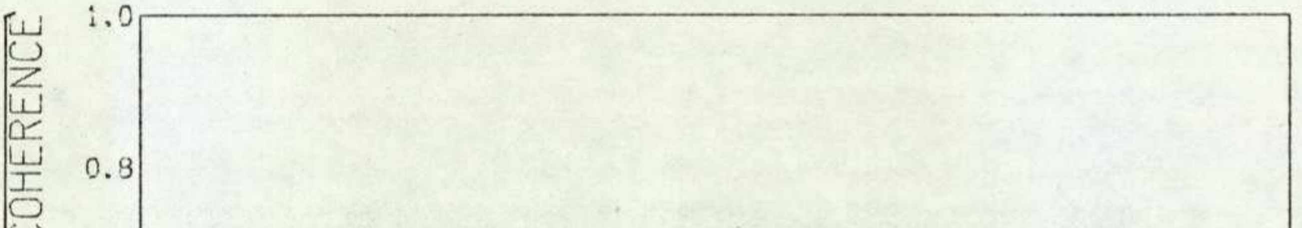
√COHERENCE
1.0
0.8
0.6
0.4
0.2
0.0
-3
-2
-1
0
LOG[n.B/Ū]
B/D=4
L_x/B=1.98

FIG 46 (cont.)

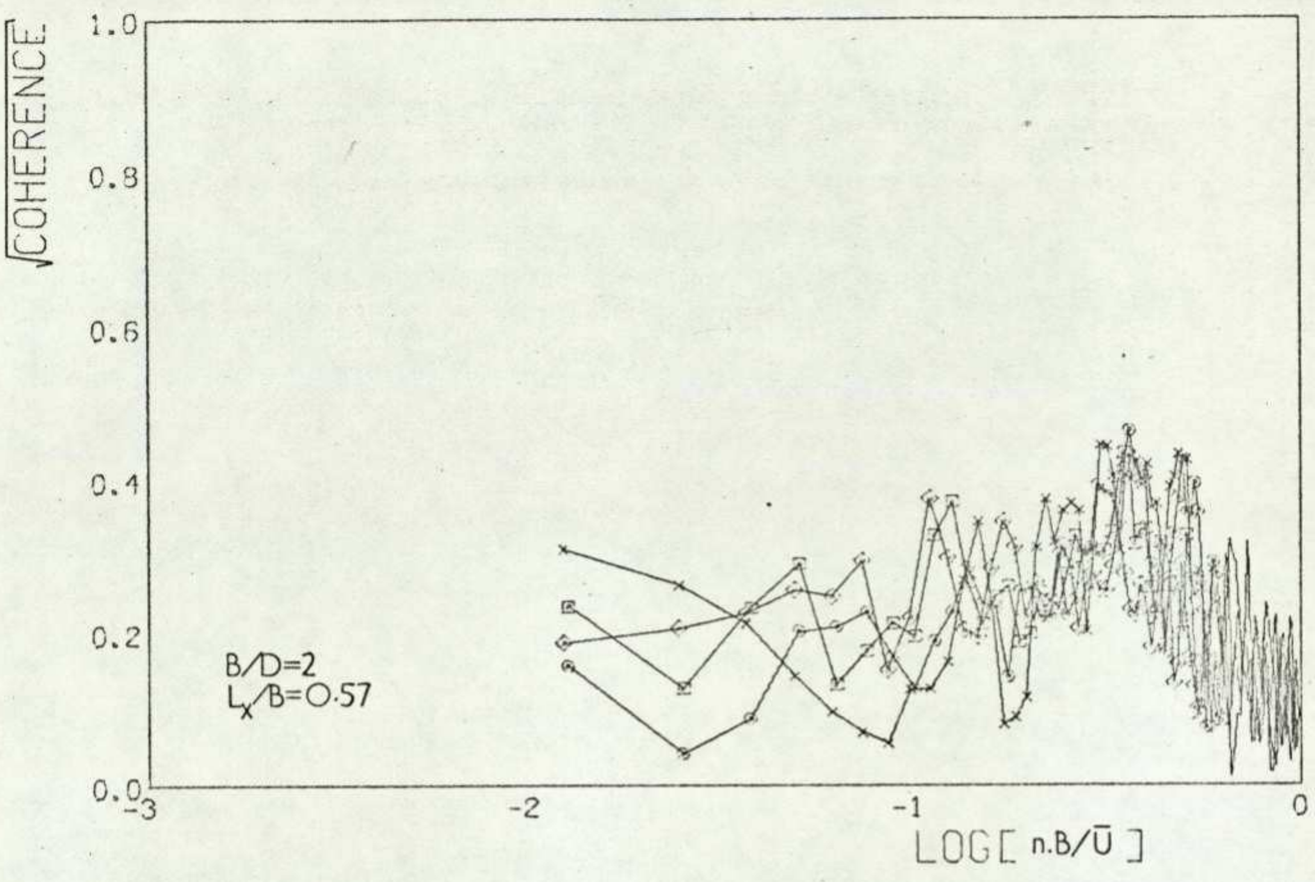
√COHERENCE
1.0
0.8
0.6
0.4
0.2
0.0
-3
-2
-1
0
LOG[n.B/Ū]
B/D=2
L_x/B=0·57

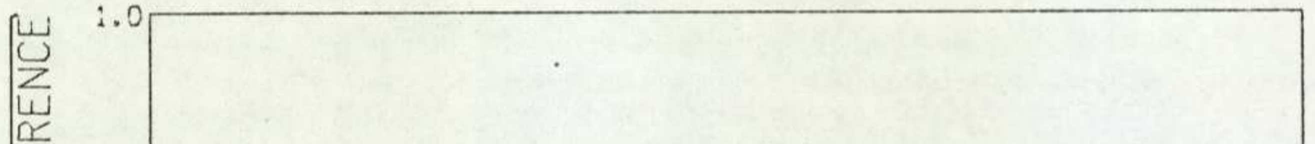
√COHERENCE
1.0
0.8
0.6
0.4
0.2
0.0
-3
-2
-1
0
LOG[n.B/Ū]
B/D=2
L_x/B=1·0

FIG 46 (cont.)

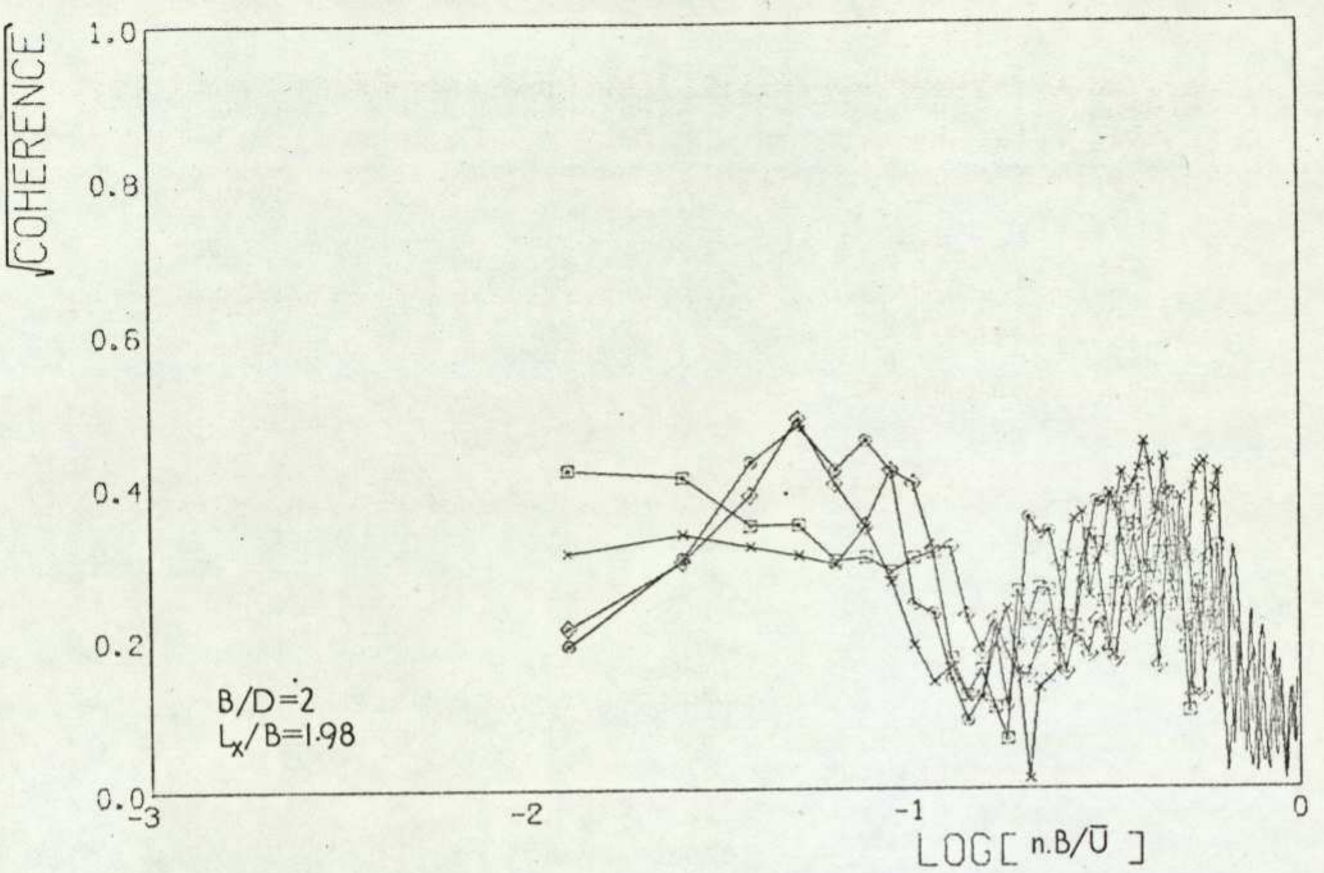

√COHERENCE
1.0
0.8
0.6
0.4
0.2
0.0
-3
-2
-1
0
LOG[n.B/Ū]
B/D=2
L_x/B=1.98

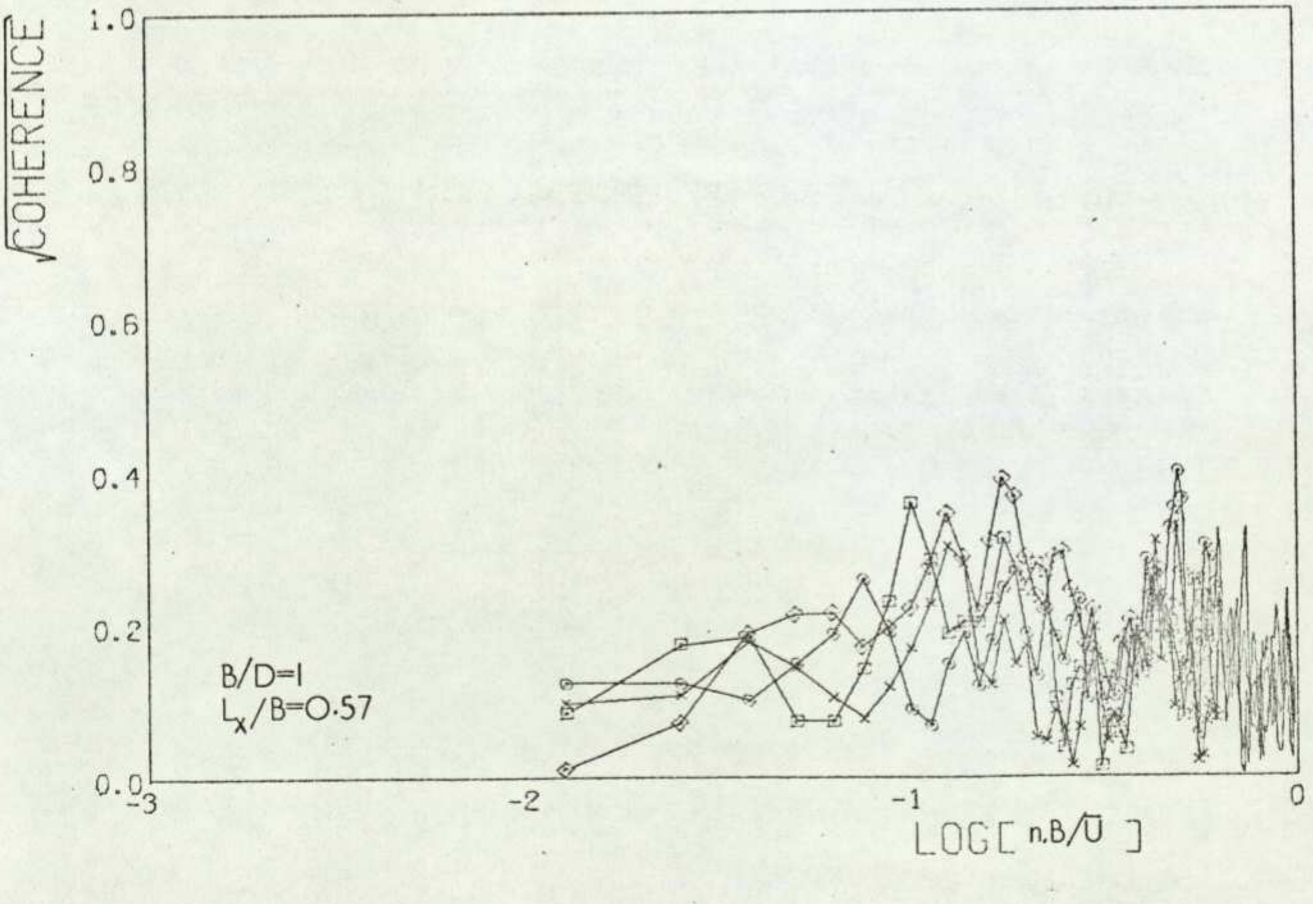

√COHERENCE
1.0
0.8
0.6
0.4
0.2
0.0
-3
-2
-1
0
LOG[n.B/Ū]
B/D=1
L_x/B=0.57

FIG 46 (cont.)

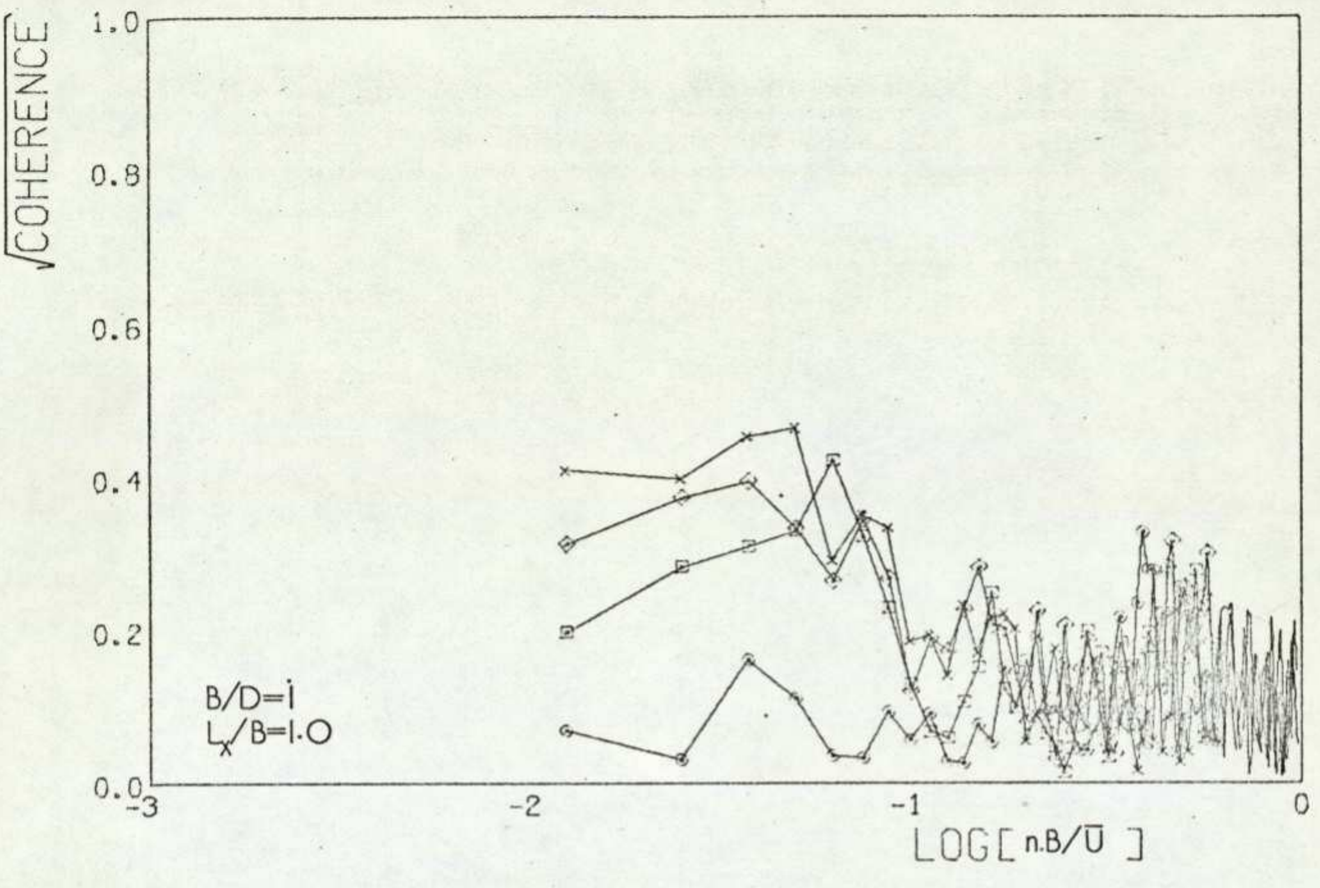

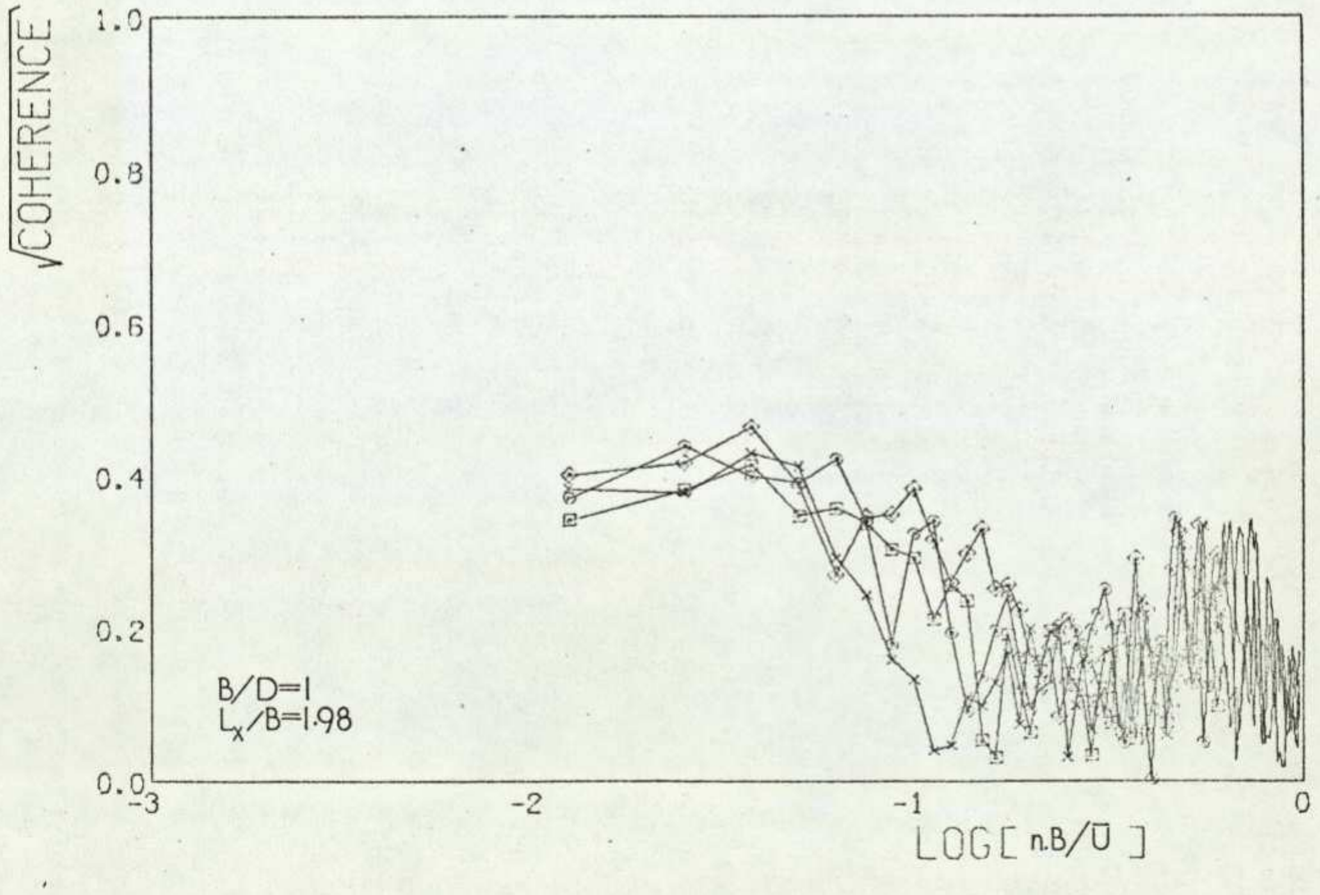

FIG 46(concluded)

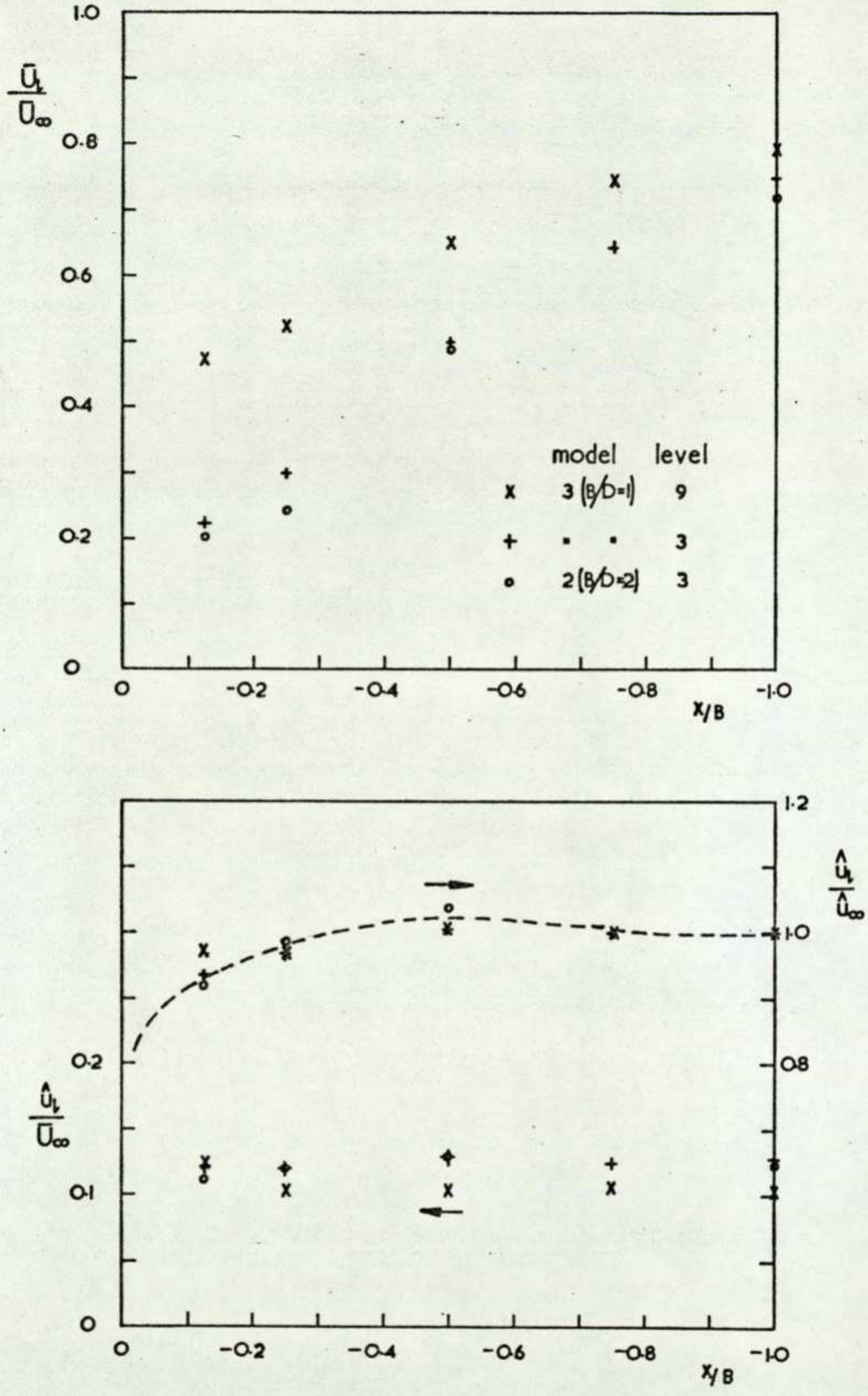

FIG 47 Mean velocity & longitudinal component of turbulence approaching c/L of model [$L_X = B$]

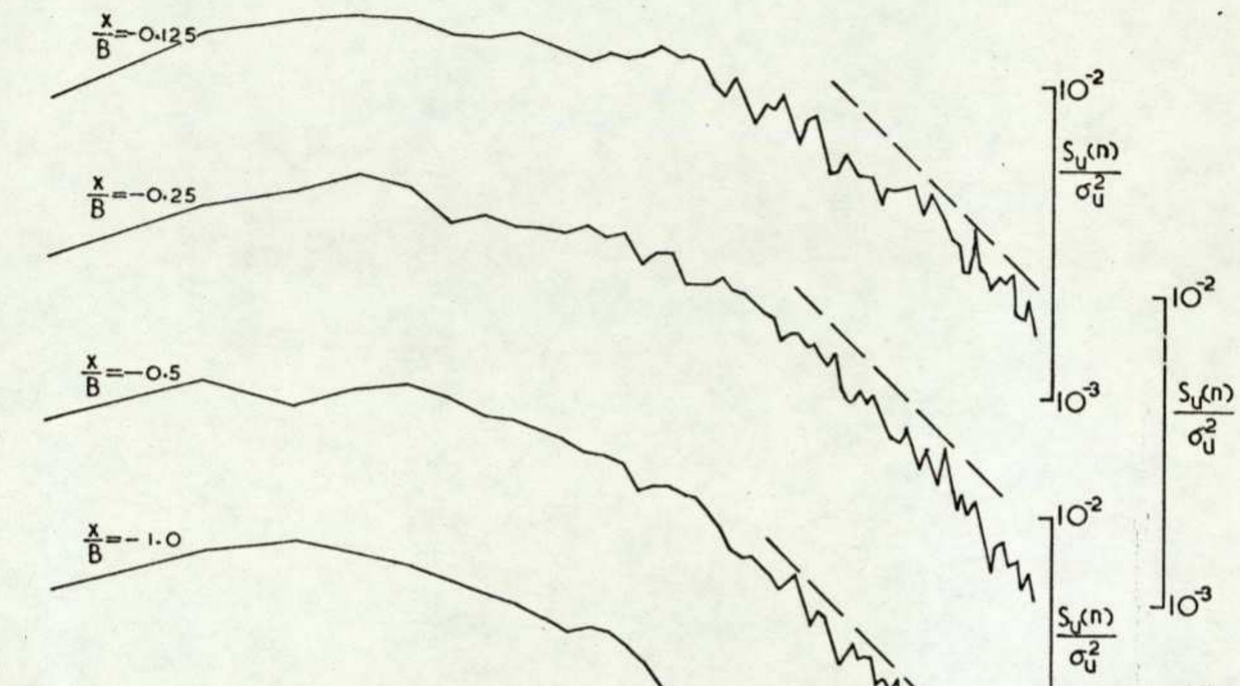

FIG 48 Spectra of longitudinal component of turbulence upstream of model.

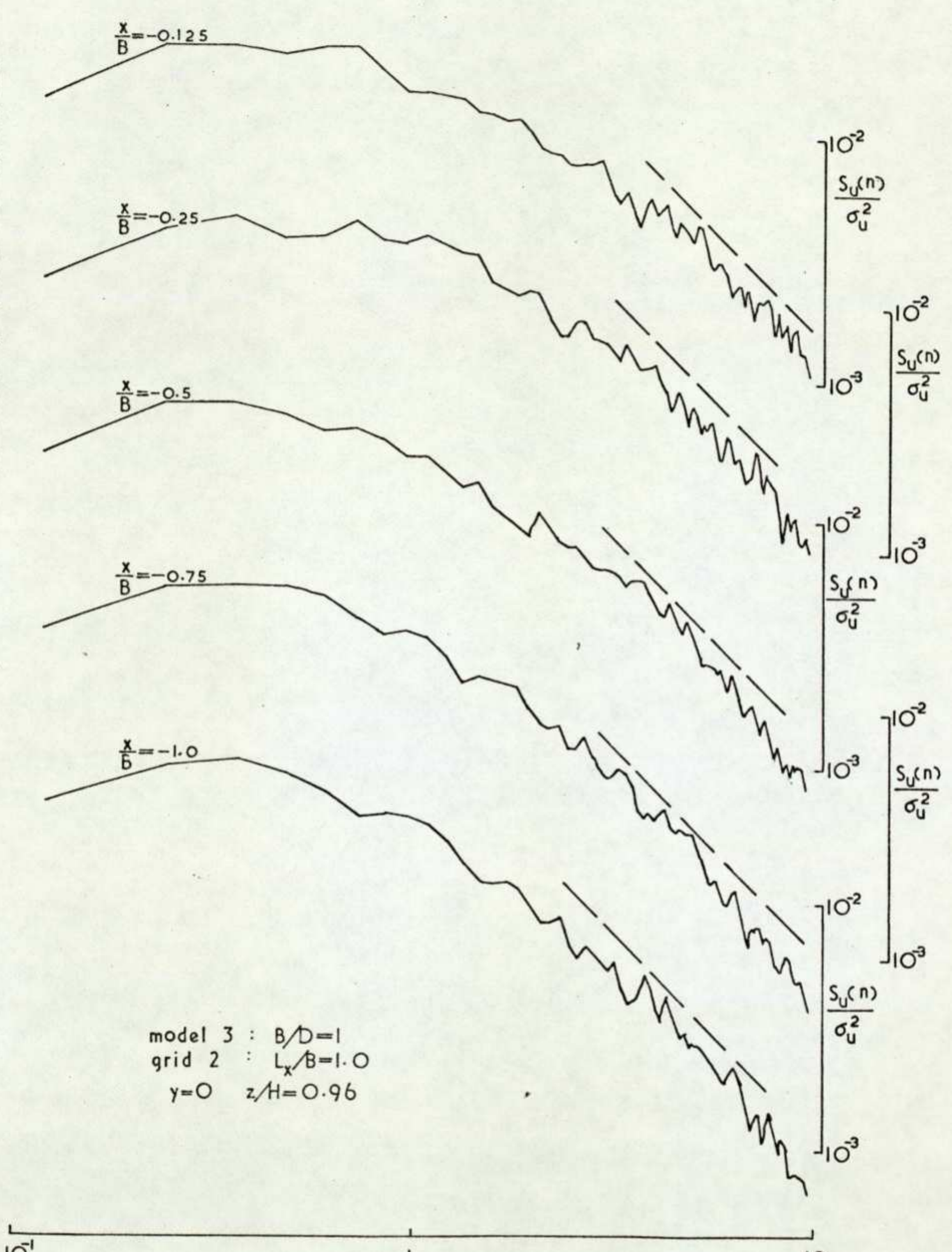

FIG 48 (concluded)

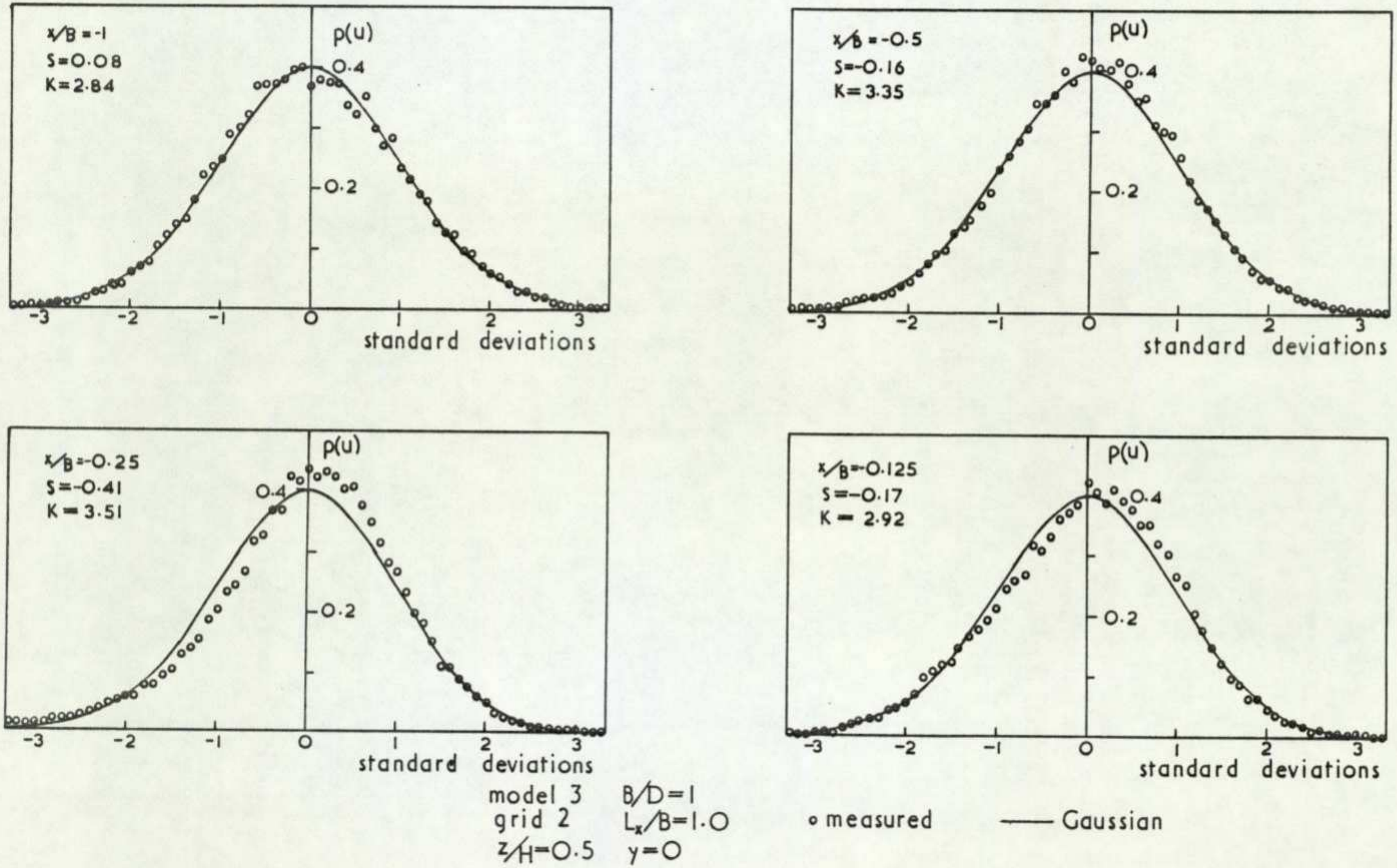

FIG 49 Probability density distribution for longitudinal component of turbulence upstream of model.

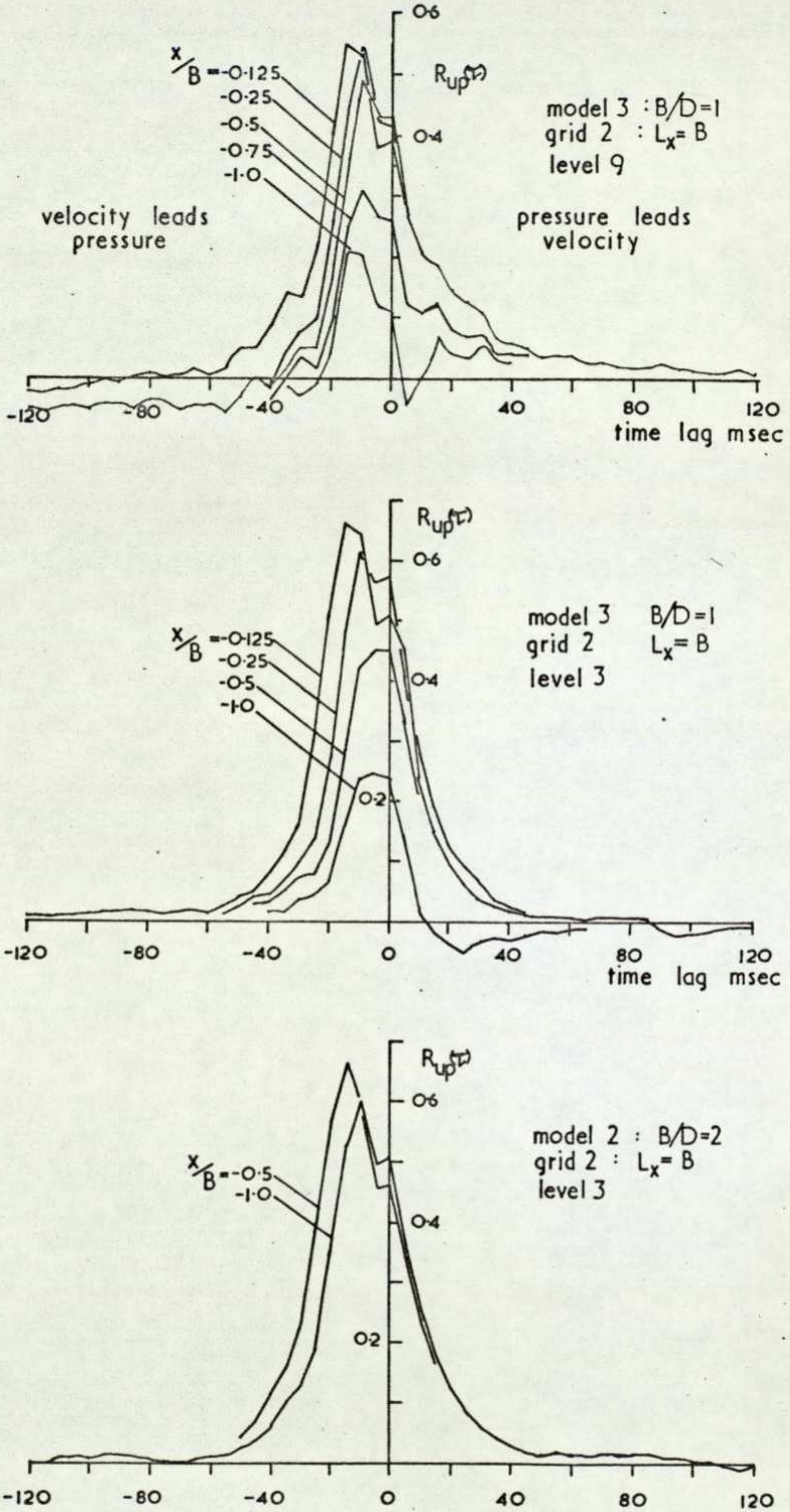

FIG 50 Cross-correlation between longitudinal component of turbulence and pressure fluctuations on ℄ of windward face.

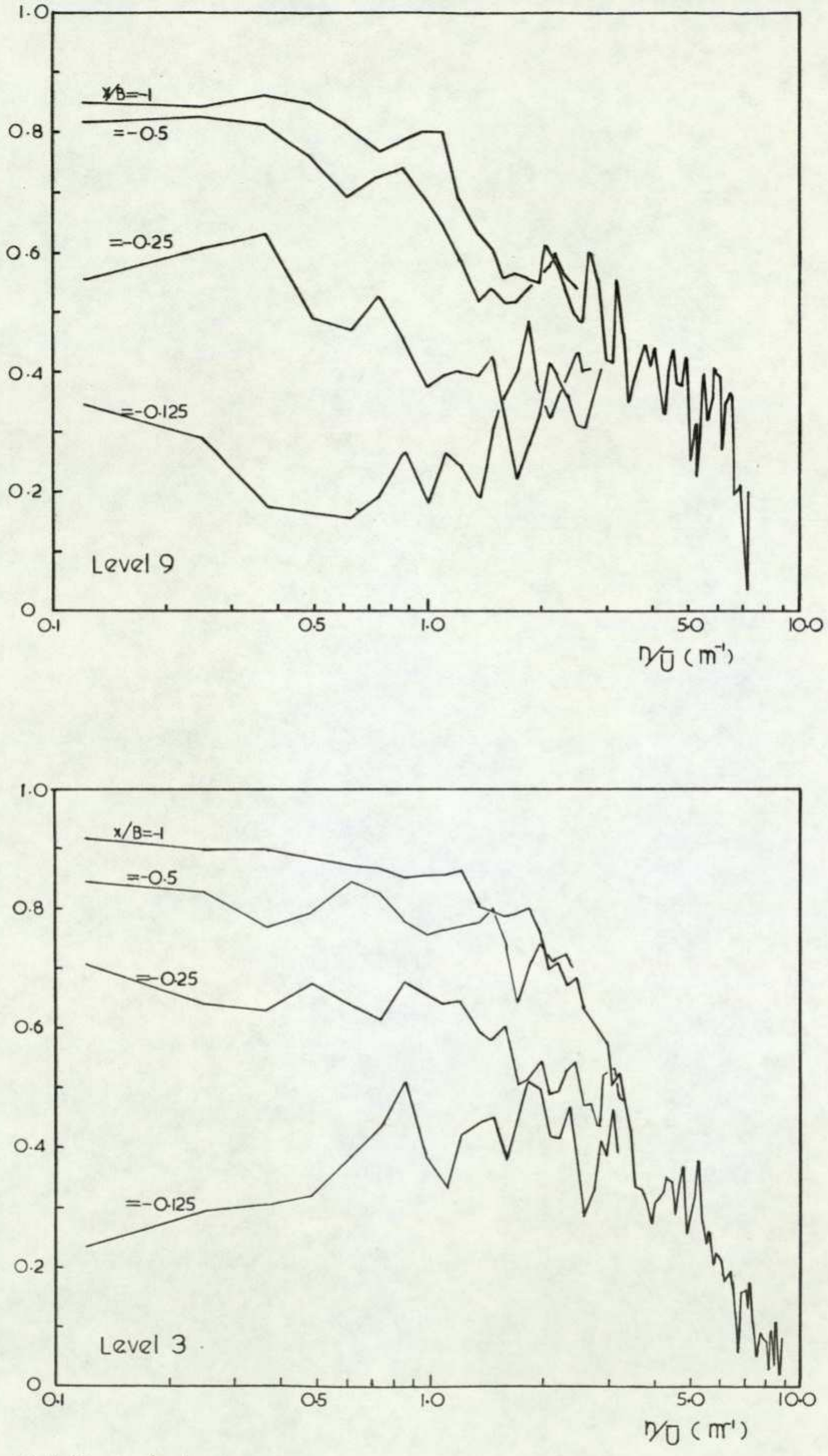

Grid 2 : $L_x/B=1$
Model 3 : $B/D=1$

FIG 51 $\sqrt{\text{Coherence}}$ between longitudinal component of turbulence and pressure fluctuations on ℄ of windward face.

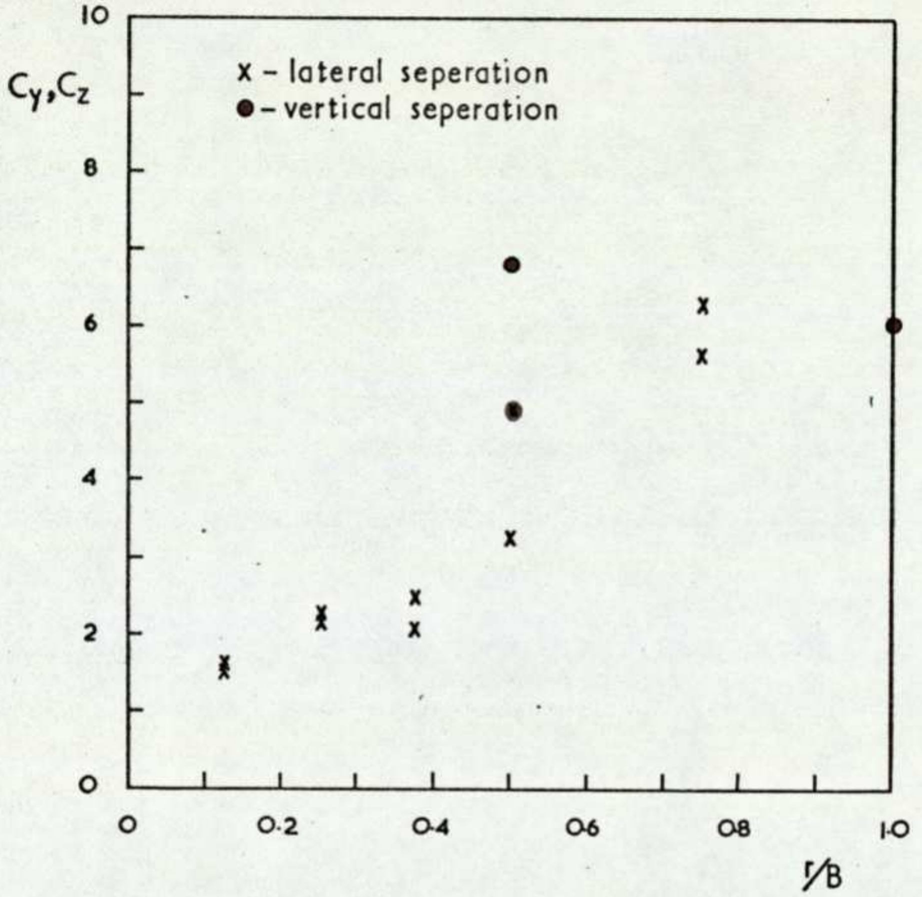

FIG 52 Variation of decay constant in coherence relationship with spatial seperation.

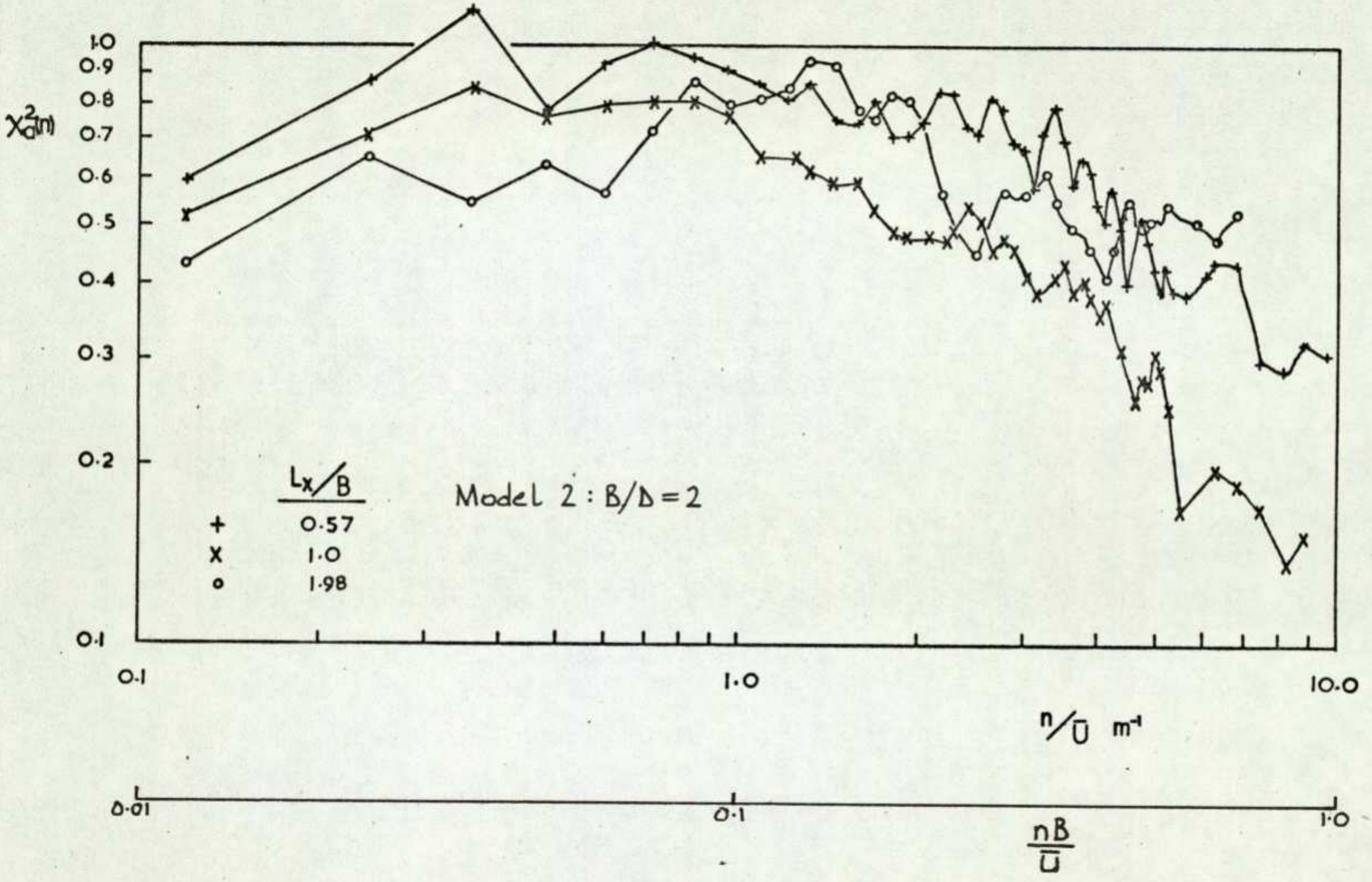

FIG 53 Aerodynamic admittance

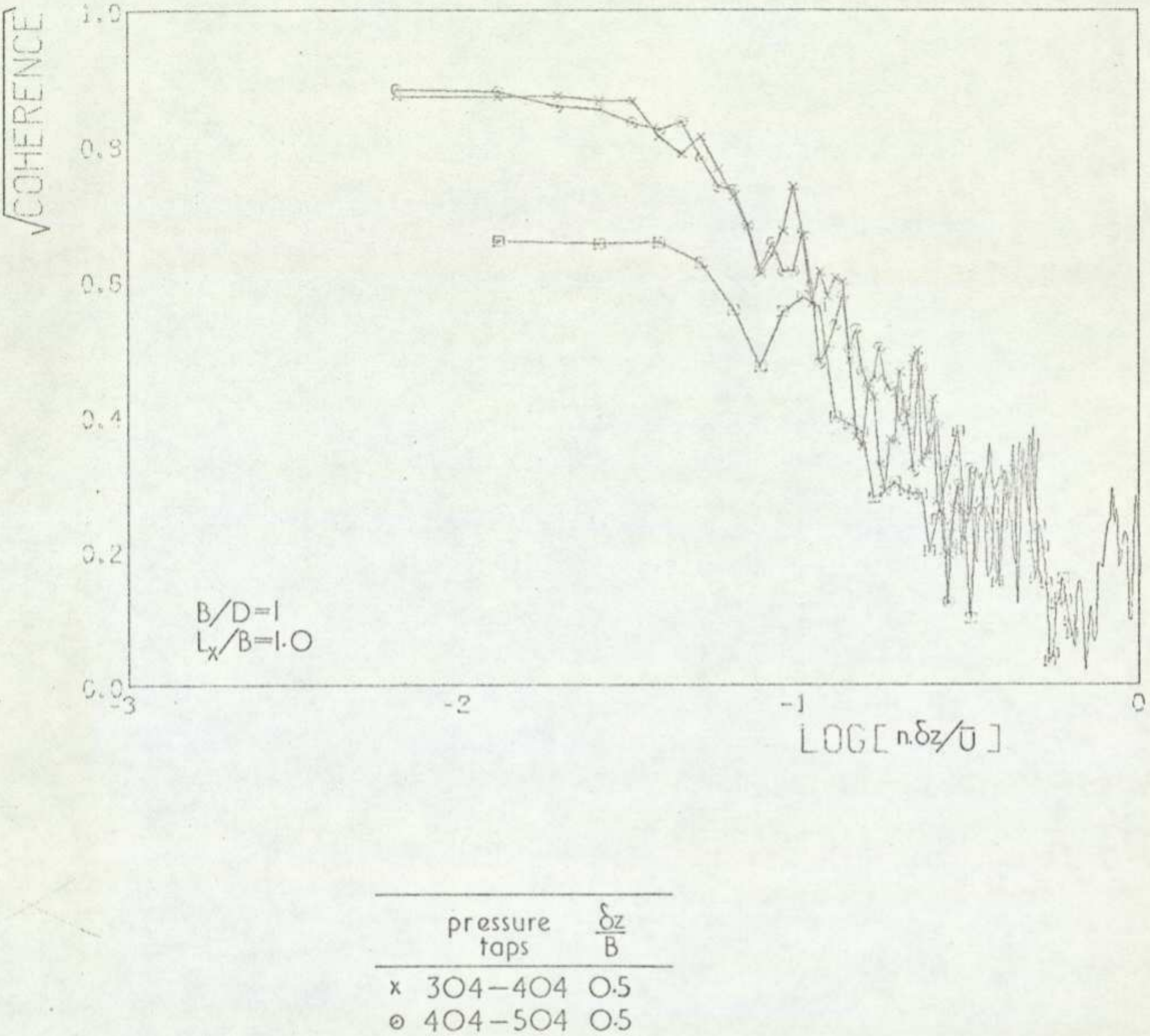

pressure taps	$\frac{\delta z}{B}$
x 304−404	0.5
⊙ 404−504	0.5
⊡ 304−504	1.0

FIG 54 $\sqrt{\text{Coherence}}$ for pressure fluctuations on windward face with vertical seperation.

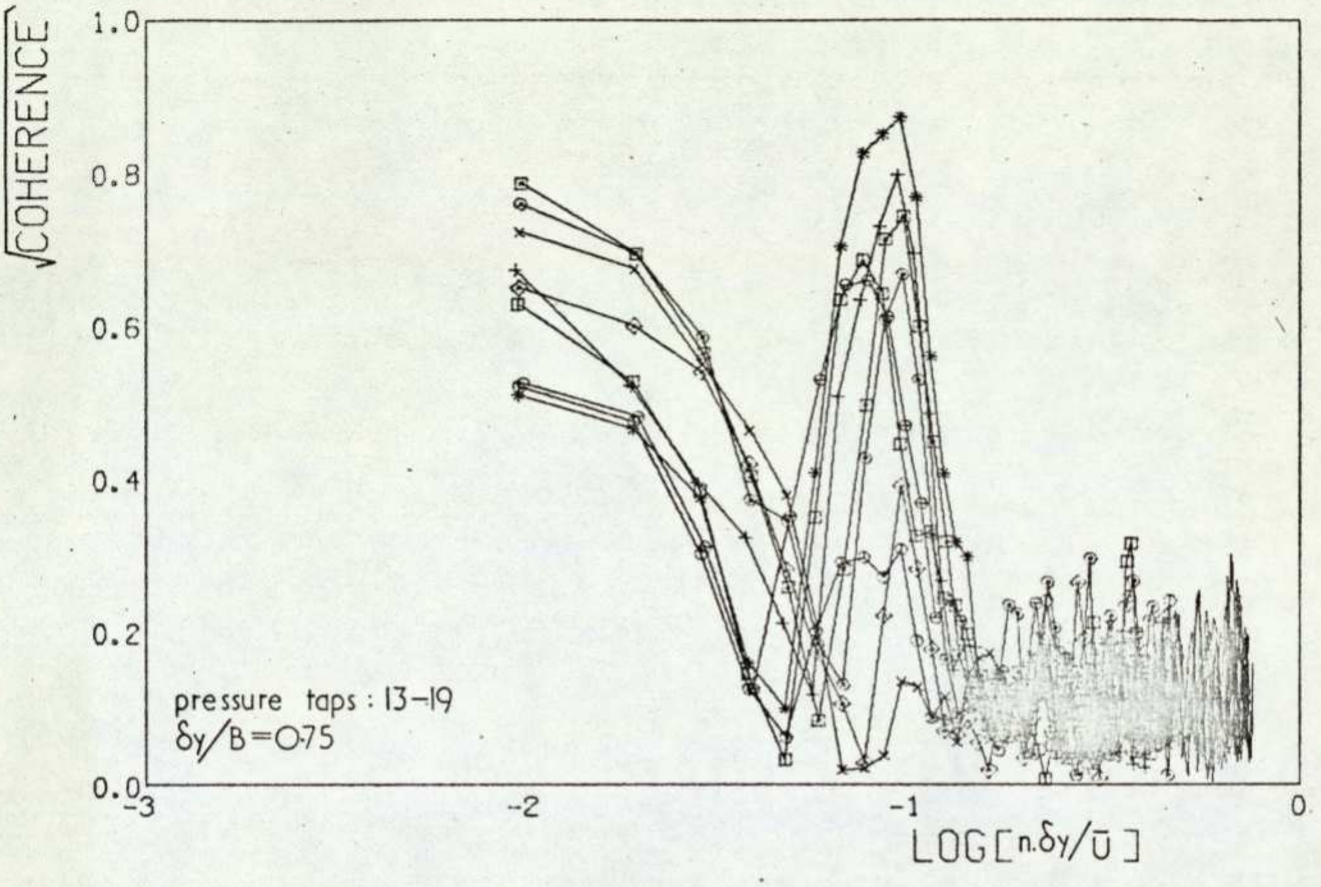

	B/D	L_x/B
x	4	0.57
⊙	4	1.0
⊡	4	1.98
◈	2	0.57
+	2	1.0
✳	2	1.98
Φ	1	0.57
θ	1	1.0
⊞	1	1.98

FIG 55 √Coherence for pressures at z/H=0.5 on leeward face.

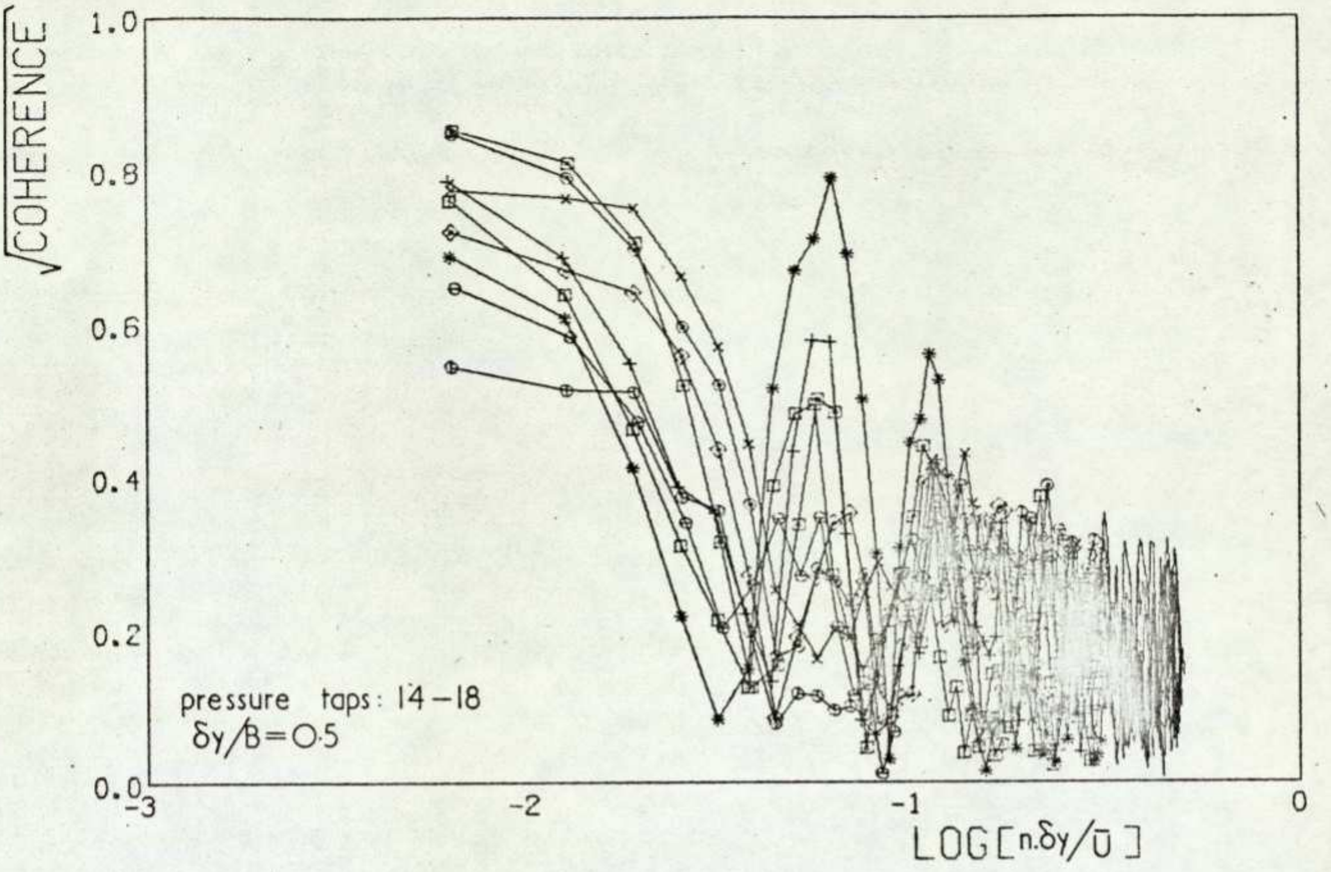

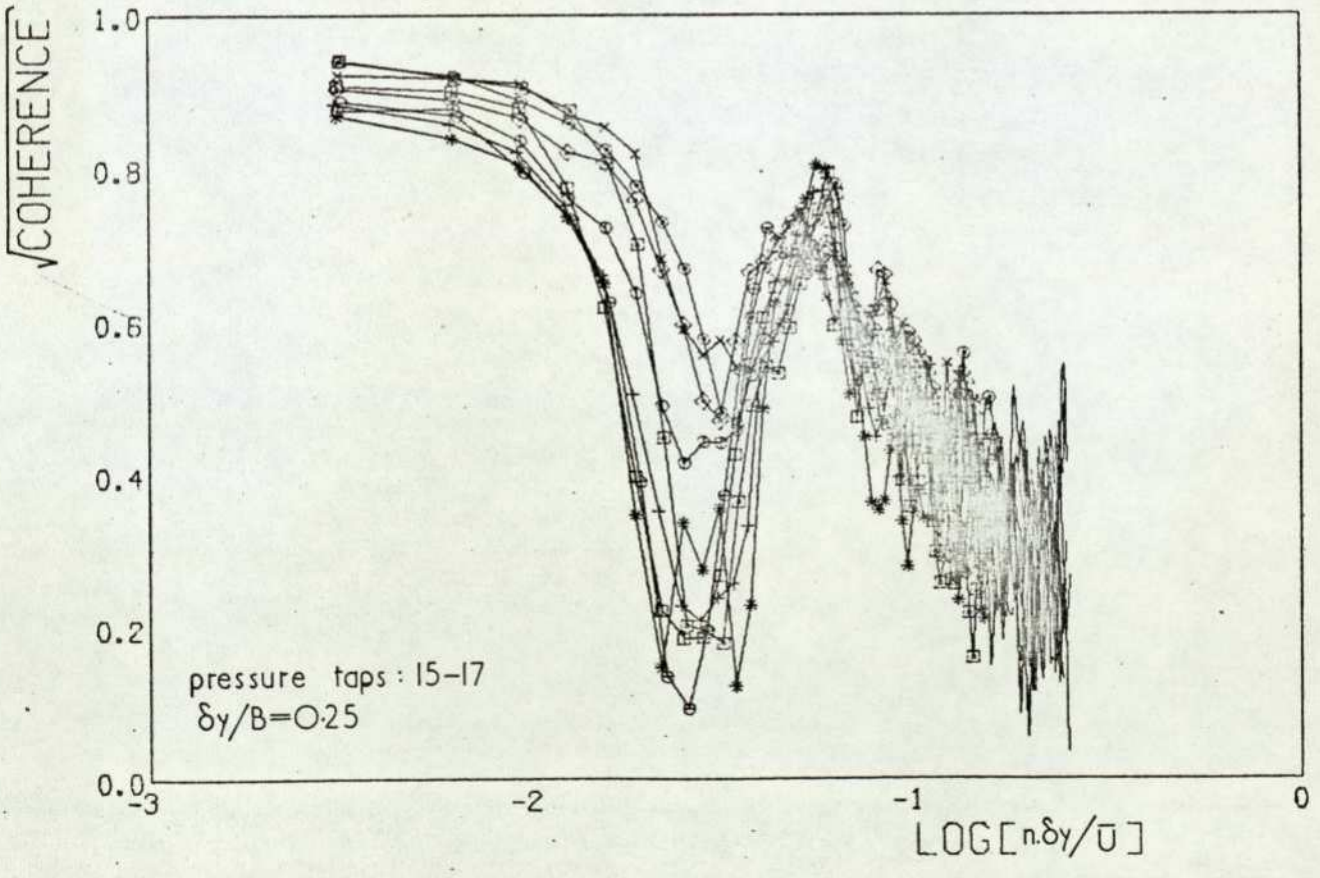

FIG. 55 (concluded)

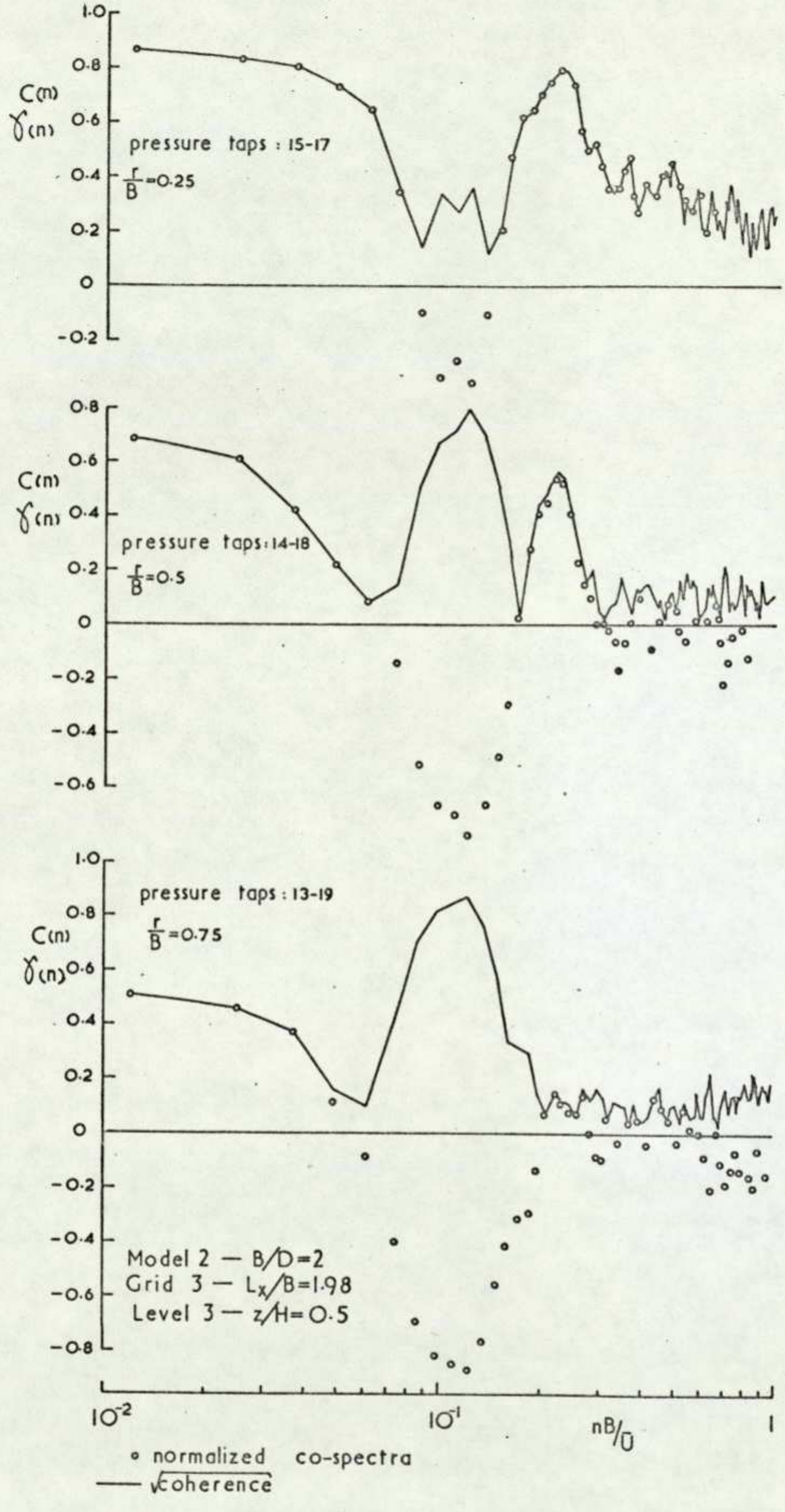

FIG 56 Comparison between normalized co-spectra and $\sqrt{\text{coherence}}$ for leeward face pressures.

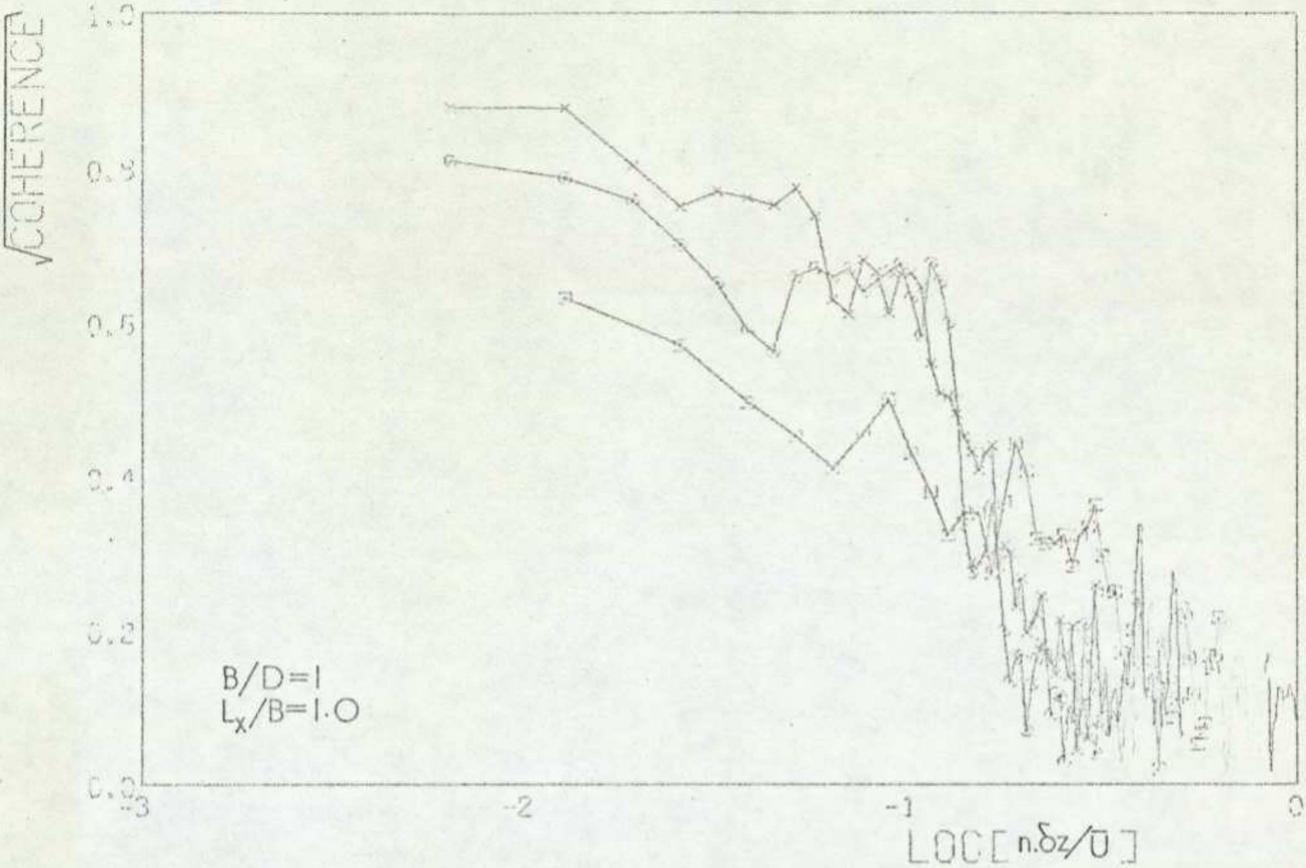

	pressure taps	$\frac{\delta z}{B}$
x	316-416	0.5
⊙	416-516	0.5
⊡	316-516	1.0

FIG 57 √Coherence for pressure fluctuations on leeward face with vertical seperation.

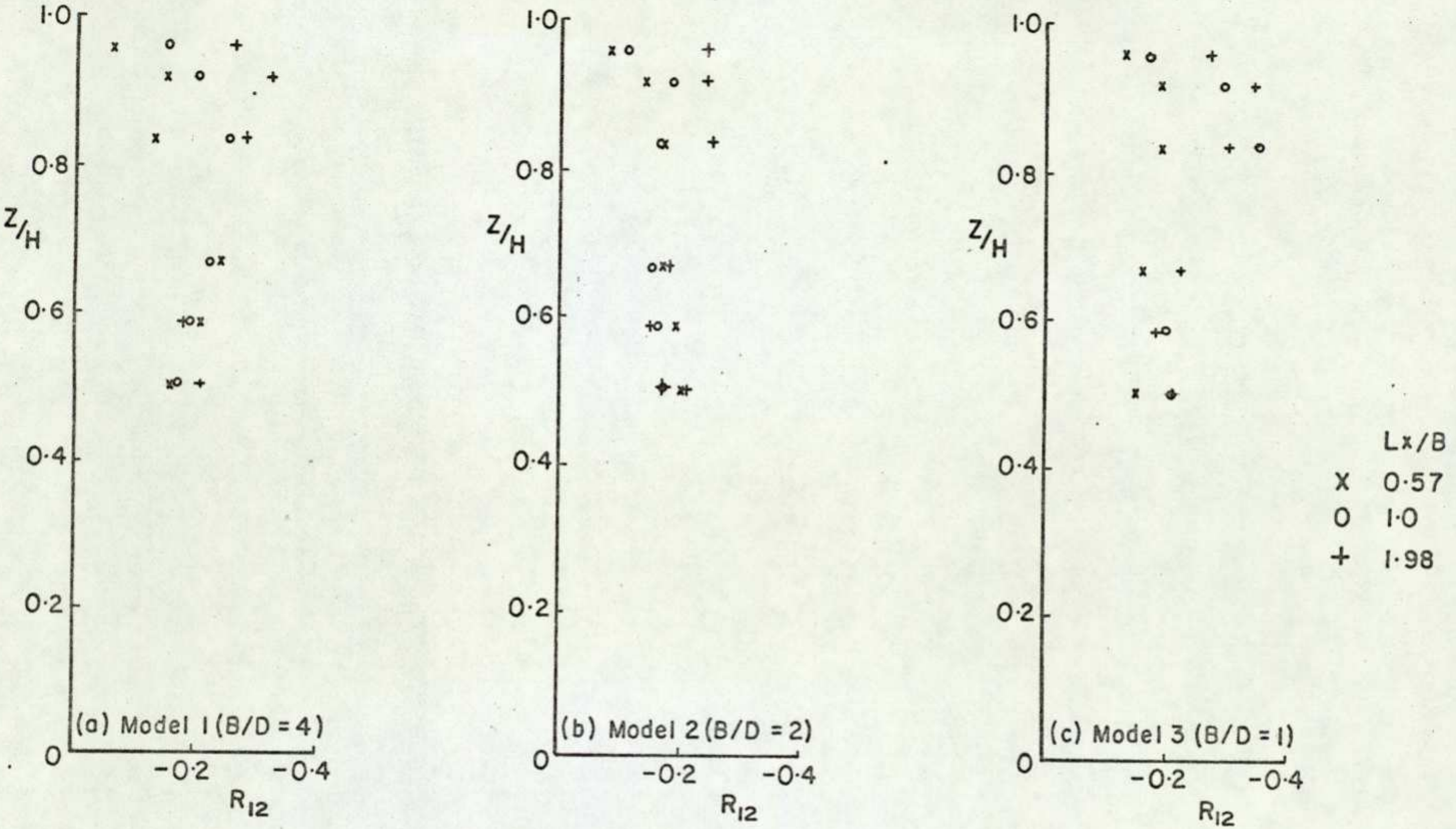

FIG. 58. PEAK CROSS-CORRELATION COEFFICIENTS OF WINDWARD-LEEWARD FACE PRESSURE FLUCTUATIONS.

APPENDIX A

CALIBRATION OF DYNAMIC PRESSURE SYSTEM AND DATA CORRECTION

A.1 Introduction

Many wind tunnel tests of wind loads on buildings involve the measurement of fluctuating surface pressures over a wide frequency range, at a number of positions distributed around the model. This is usually achieved using either flush mounted diaphragm pressure transducers or short lengths of tubing connecting the pressure taps to pressure transducers, so that the upper frequency limit is kept within the flat gain region of the system dynamic response. In many instances, particularly when the number of pressure points to be investigated is very high or when the model is physically small, it can be impracticable or at times impossible to use either of the above methods. A compromise is usually made by accepting a lower value for the frequency range. However, since the natural frequency of pressure tube systems should, as a first approximation, be directly proportional to the internal tube diameter, D, and inversely proportional to the square root of the tubing length, L, the compromise usually involves accepting a very much lower frequency limit. On the other hand, if the dynamic response of the system is known then measurements can be made beyond the flat gain region and appropriate corrections applied to the results.

The following section outlines what is required for such corrections and how they are to be applied, followed by a description of the calibration equipment used to determine the gain and phase angle of the frequency response function of the fluctuating pressure measuring system employed in Chapters 5 and 6.

A.2 Data Correction

In the definition sketch, Fig.A.1, the input signals u(t) and p(t) are the turbulence and surface pressure fluctuations respectively and the output signal P(t) is the pressure signal from the pressure transducer.

The concept of the transfer function has been found to be very useful in the analysis of linear systems that in general operate on a set of input functions to produce a set of output functions, and will therefore be used here. For the following analysis it is assumed that the system is linear; as will be shown in the following section, measurements of the response characteristics for a number of pressure amplitudes indicate that such an assumption is essentially valid.

The frequency response function of a system describes the system response to a sinusoidal input. It is, however, also used in analyses of situations where the input and output are random in nature. This is justified on the basis that the random signals can be analysed into Fourier components and for a linear system the principle of super-position is applicable.

For the pressure system in Fig.A.1 the input $p(t)$ and output $\mathbf{P}(t)$ signals are related by the equation:

$$\mathbf{P}(t) = \int_0^\infty h(\tau) \cdot p(t-\tau)\, d\tau \qquad \ldots \text{(A1)}$$

where $h(\tau)$ is the unit impulse response function[58]. If the input is sinusoidal then Equation A1 reduces to:

$$\mathbf{P}(t) = p(t) \cdot H(n) \qquad \ldots \text{(A2)}$$

where $H(n)$ is the frequency response function and is the Fourier transform of the unit impulse response function, i.e.

$$H(n) = \int_0^\infty h(\tau) \cdot e^{-i2\pi n\tau} d\tau \qquad \ldots \text{(A3)}$$

For two different pressure systems and sources the cross-correlations, $R(\tau)$, between the input signals and the output signals are:

$$R_{\mathbf{P}_1 \mathbf{P}_2}(\tau) = \overline{\mathbf{P}_1(t) \cdot \mathbf{P}_2(t+\tau)}$$

$$= \lim_{T\to\infty} \frac{1}{T} \int_0^T \int_0^\infty \int_0^\infty h_1(\tau_1)\, h_2(\tau_2)\, p_1(t-\tau)\, p_2(t+\tau-\tau_2)\, d\tau_1\, d\tau_2\, dt$$

which reduces to:

$$R_{\mathbf{p}_1\mathbf{p}_2}(\tau) = \int_0^\infty \int_0^\infty h_1(\tau_1)\, h_2(\tau_2)\, R_{p_1p_2}(\tau+\tau_1-\tau_2)\, d\tau_1\, d\tau_2 \qquad \ldots \text{(A4)}$$

Re-organising the expression in the above integral it is possible to Fourier transform to obtain the cross-spectral density functions of the input and output signals, viz.

$$S_{\mathbf{p}_1\mathbf{p}_2}(n) = H_1^*(n) \cdot H_2(n) \cdot S_{p_1p_2}(n) \qquad \ldots \text{(A5)}$$

where $H_1(n)$ and $H_2(n)$ are the frequency response functions of Systems 1 and 2 respectively and the asterisk* denotes complex conjugate of H(n). If instead of pressure, one of the input signals in Equation A5 had been the turbulence signal, u(t), then Equation A5 would have been:

$$S_{u\mathbf{p}}(n) = H(n) \cdot S_{up}(n) \qquad \ldots \text{(A6)}$$

Equation A6 was used to correct the tubing effect on the cross-spectra between turbulence and pressure.

Again, if the auto-correlation of pressures had been made in Equation A4, then Equation A5 would have been:

$$S_{\mathbf{pp}}(n) = |H(n)|^2\, S_{pp}(n) \qquad \ldots \text{(A7)}$$

Equation A7 was used to correct the tubing effect on the pressure spectra.

Finally, if the two pressure systems in the above analysis had been identical then Equation A5 would have reduced to:

$$S_{\mathbf{p}_1\mathbf{p}_2}(n) = |H(n)|^2\, S_{p_1p_2}(n) \qquad \ldots \text{(A8)}$$

Compared with Equation A5, this expression is seen to be easier to implement into a correction procedure, it does not include phase angles. The most important advantage however is the fact that the information required to use the correction procedure is reduced to a single transfer function, which is particularly important when a number of systems in the data collection is involved or when large numbers of signal pairs are to be processed since it considerably simplifies the complexity of data management and processing. Every effort was made to ensure that the two pressure systems employed during the experimental investigations in Chapters 5 and 6 were identical, and Equation A8 was used to correct the tubing effect on the cross-spectra between pressures.

A.3 Dynamic Calibration of Pressure System

The frequency response of the pressure system used for the experimental investigations was measured for various lengths of pressure tubing using the calibration equipment shown in Figs.A.2 & A.3.

Sinusoidal pressures could be generated over a range of frequencies, and rms values of up to about 6.5 mm h_2O. The output of the transducer was referenced to the signal from a flush mounted SEL 25 mm differential pressure transducer. The dynamic performance of the reference transducer had been determined and found to have a natural frequency in excess of 500 Hz and a flat gain up to a frequency of about 300 Hz.

The amplitude response of the system for a range of tube lengths is presented in Fig.A.4. This data, with the requirements discussed in §3.3, was the basis on which the tube length of 0,9 m was selected for the model investigations.

The dynamic performance of the pressure system with a 0.9 m tube length was further investigated to confirm the suitability of the choice, to determine the maximum frequency to which a correction procedure could sensibly be applied and most important to ensure that the two pressure systems responded identically within the frequency range of interest.

To confirm the assumption that the system is linear, and therefore the correction procedure outlined earlier was valid, the dynamic analysis of the system was repeated for low and high pressure inputs. Typical results in Fig.A.4 exhibit very little variation in gain for the pressure range examined and it is concluded that the system is linear.

The phase response, $\phi(n)$, of both pressure systems is shown in Fig.A.5 and had been determined by feeding the output and reference signals into a DISA correlator. The cross-correlation coefficient at zero time lag is:

$$R_{12}(\tau=o) = \cos(-\phi(n)) \qquad \ldots \text{(A9)}$$

from which $\phi(n)$ can easily be obtained.

The amplitude response of both the pressure systems is shown in Fig.A.4. From this and Fig.A.5 it is seen that there is very little difference between the response of the two systems and they were therefore considered to be identical.

Also shown in Figs.A.4 & A.5 is the response of single degree of freedom system with a natural frequency of 61 Hz and a damping ratio 0.39.

The empirical curve, determined by least square curve fitting to minimise the discrepancy between measured and predicted values, is seen to be generally accurate in describing the dynamic performance of the pressure systems over the frequency range 5-120 Hz. At the higher frequencies the measured values are being progressively under-estimated and the correction procedure will therefore over-compensate the spectra at the high frequencies. However, the errors involved are small, about 10%, and because the energy at the high wave-numbers is very low, the errors involved are considered to be within experimental scatter. The empirical curve was therefore used to correct for the effects of the pressure tube and Scanivalve on the pressure spectra in Chapters 5 & 6.

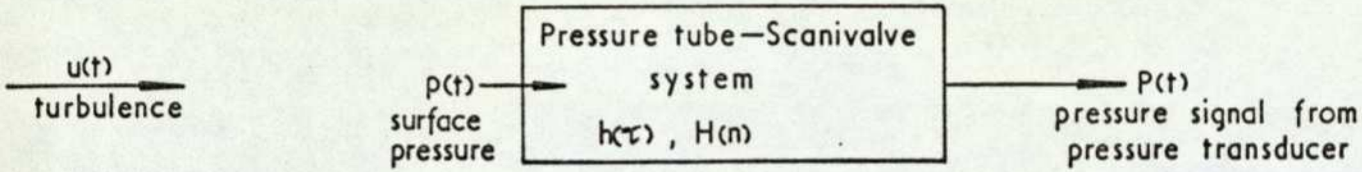

FIG A1 Definition sketch

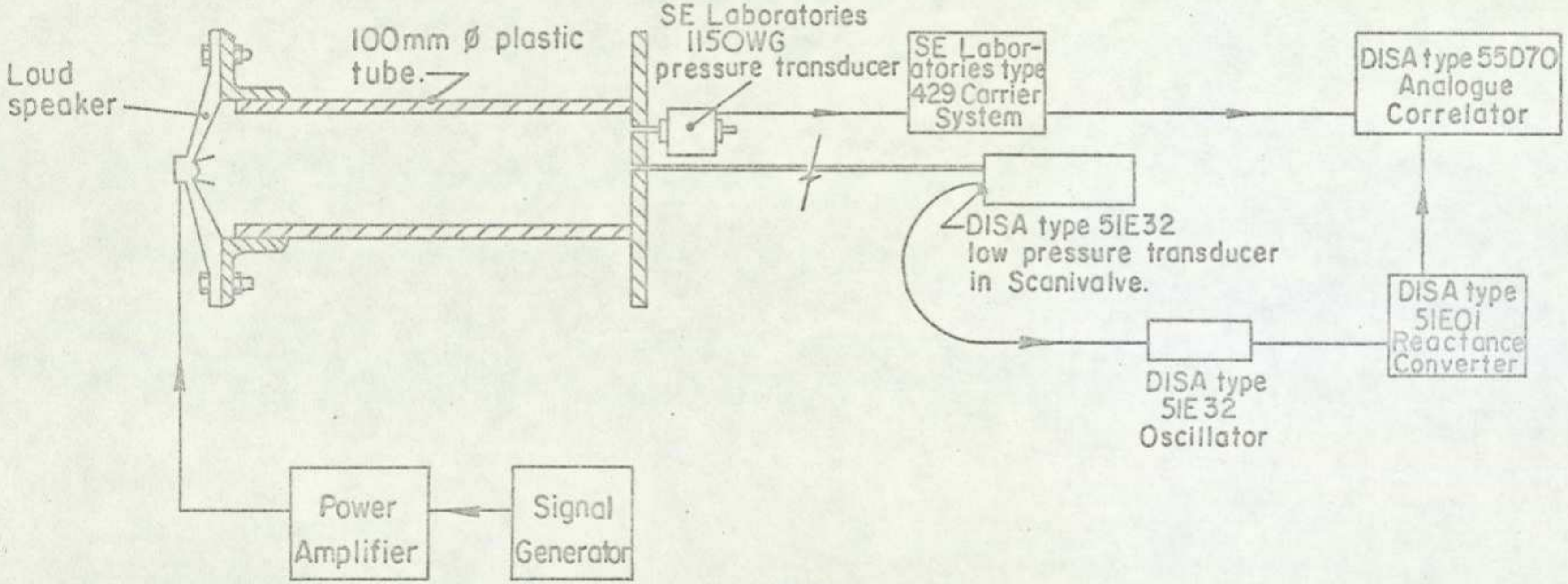

FIG. A2. SCHEMATIC OF SYSTEM FOR CALIBRATION OF PRESSURE TUBE-SCANIVALVE TRANSDUCER.

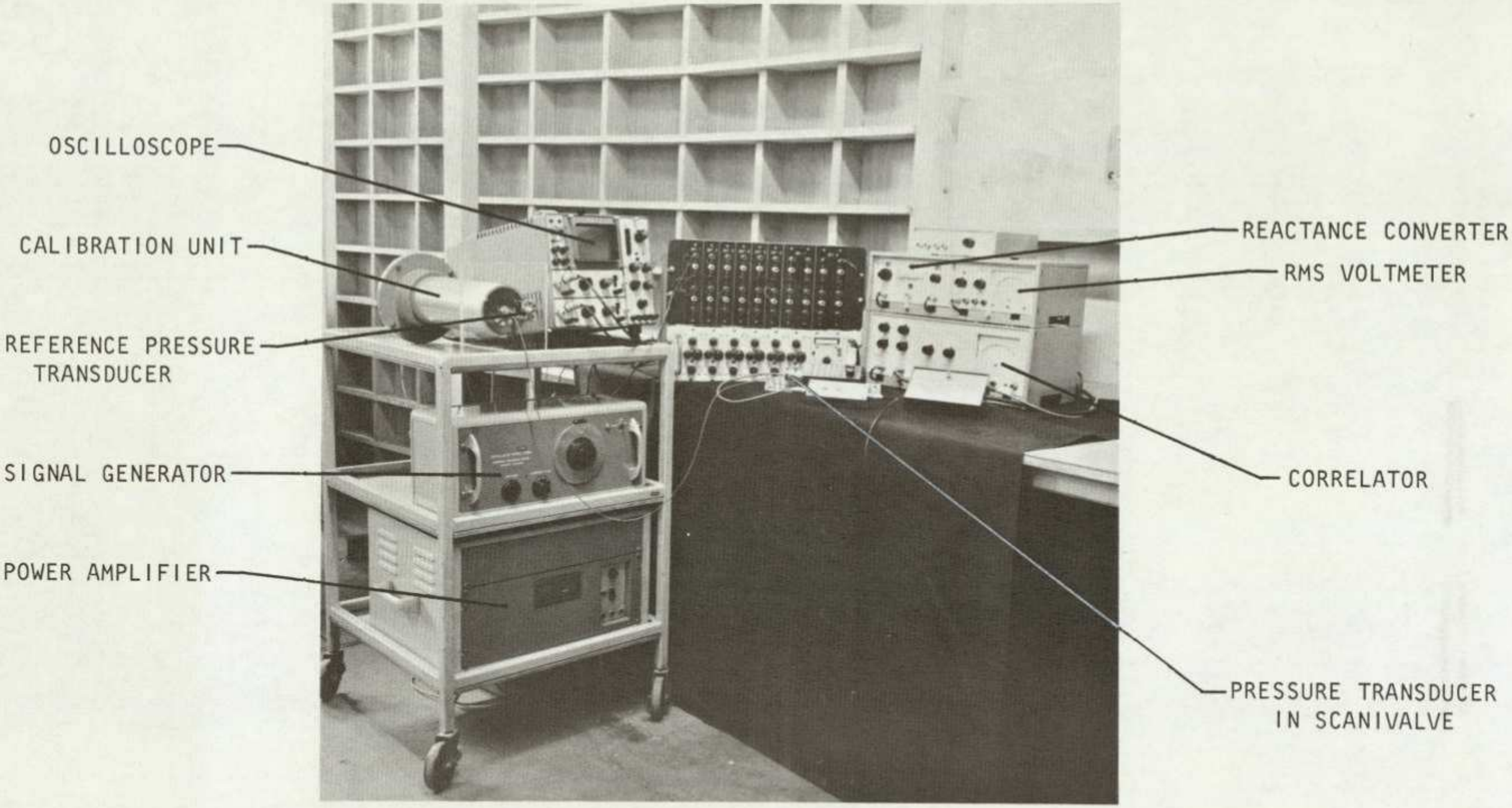

FIG. A3 EQUIPMENT FOR CALIBRATION OF PRESSURE TUBE-SCANIVALVE TRANSDUCER SYSTEM

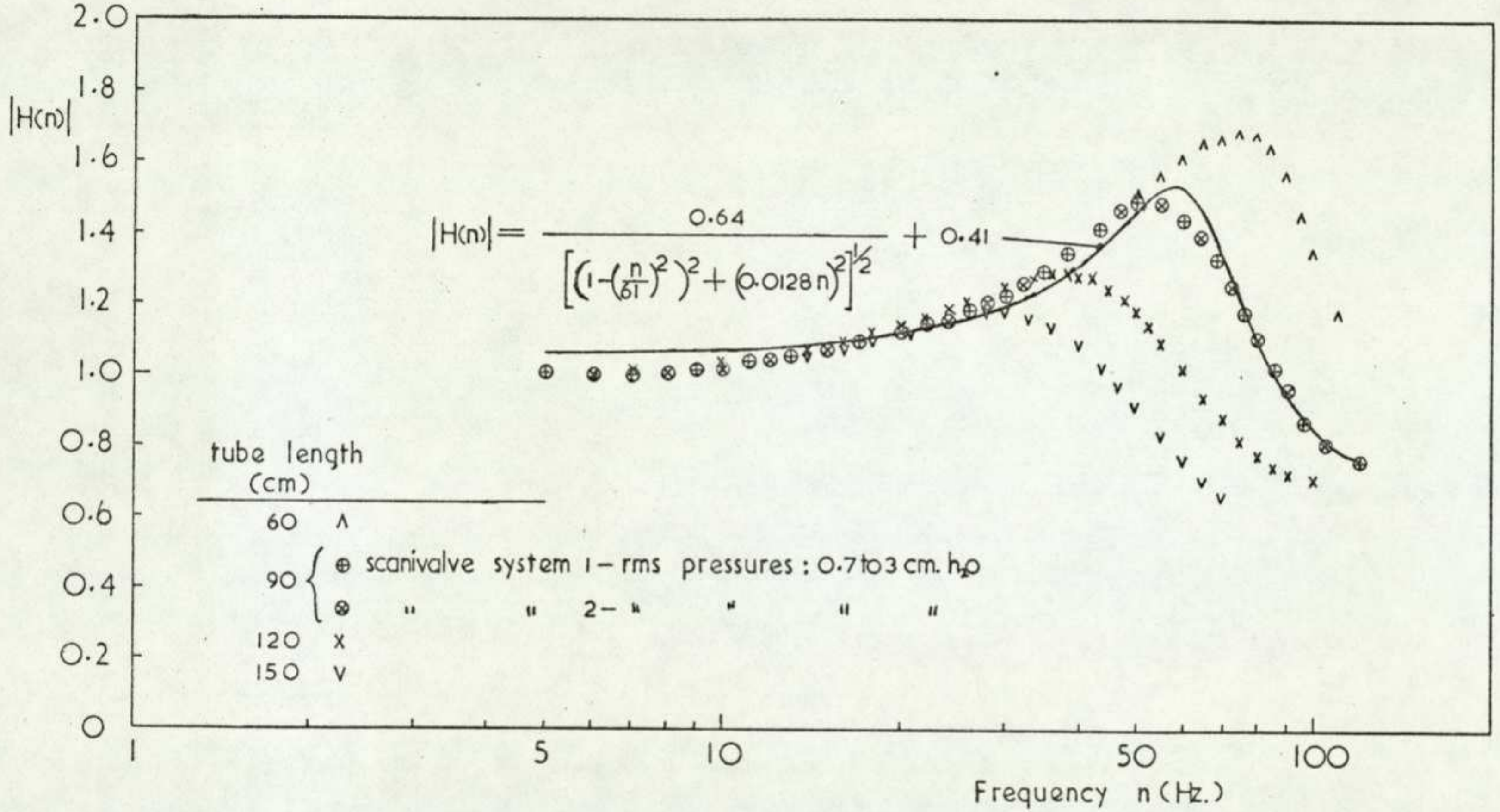

FIG A4. Amplitude response calibration of pressure tube–Scanivalve system.

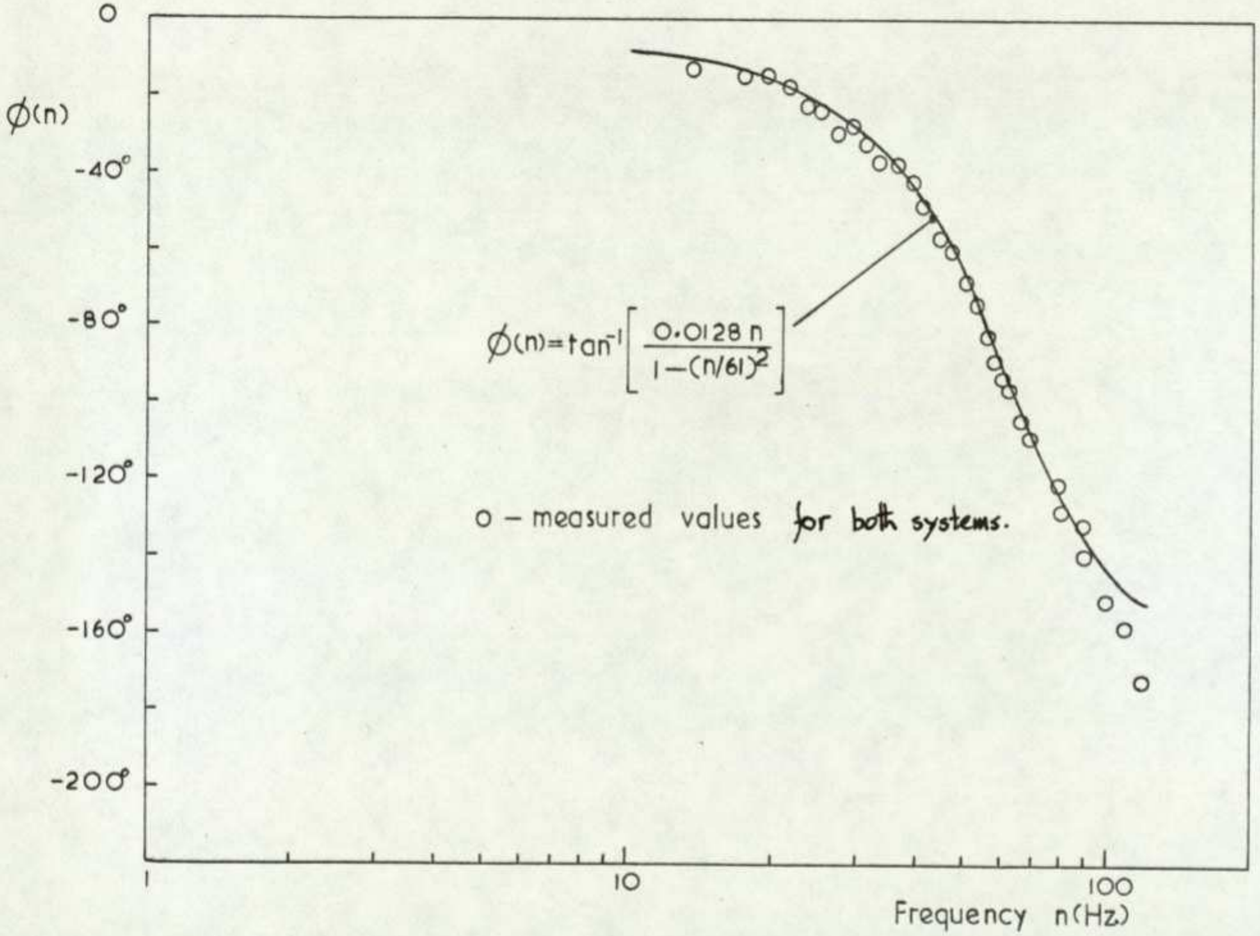

FIG A5 Phase response calibration of 90cm pressure tube-Scanivalve system.

APPENDIX B

RELATION OF DYNAMIC DRAG LOADING ON BUILDINGS TO TURBULENT WINDS

It is currently assumed that from Bernoulli's equation the pressure $P(t)$ on the surface of a building can be related to the upstream flow $U(t)$ by the relationship:

$$P(t) = \tfrac{1}{2}\rho\, U^2(t)\, C_p \qquad \ldots \text{(B1)}$$

in which C_p is a pressure coefficient.

The turbulent flow can be considered as consisting of turbulent fluctuations superimposed on a mean, i.e.

$$U(t) = \bar{U} + u(t) \qquad \ldots \text{(B2)}$$

where $\bar{U}$ and $u(t)$ are the mean and turbulent components of the flow, respectively.

Similarly, for the surface pressure:

$$P(t) = \bar{P} + p(t) \qquad \ldots \text{(B3)}$$

where $\bar{P}$ and $p(t)$ are the mean and fluctuating components of the pressure, respectively.

Substituting Equations B2 and B3 into B1, and separating into mean and fluctuating components, $\bar{P}$ and $p(t)$ have the following values:

$$\left.\begin{aligned} \bar{P} &= \tfrac{1}{2}\rho\, \bar{U}^2\, C_p \left(1 + \frac{\overline{u^2}}{\bar{U}^2}\right) \\ \text{and} \quad p(t) &= \tfrac{1}{2}\rho\, \bar{U}^2\, C_p \left(2\,\frac{u(t)}{\bar{U}} + \frac{u^2(t) - \overline{u^2}}{\bar{U}^2}\right) \end{aligned}\right\} \qquad \ldots \text{(B4)}$$

Neglecting second-order terms:

$$\left.\begin{aligned} \bar{P} &= \tfrac{1}{2}\rho\ \bar{U}^2\ C_p \\ \text{and}\qquad p(t) &= \rho\ \bar{U}\ u(t)\ C_p \end{aligned}\right\}\quad \ldots\ (B5)$$

These equations are assumed to be applicable to both the windward and leeward face of the building. The subscripts ω and ℓ will be used to signify windward and leeward, respectively.

The total instantaneous drag force acting on the building, neglecting skin friction, is:

$$D(t) = \int_{A_\omega} P_\omega(t)\ dA + \int_{A_\ell} P_\ell(t)\ dA \qquad \ldots\ (B6)$$

where A_ω and A_ℓ are the areas of the windward and leeward faces, respectively.

This equation can be rewritten in terms of the spectral density function of the drag $S_D(n)$ and the real part of the cross-spectral density function of the fluctuating pressures on the building:

$$S_D(n) = \int_{A_\omega}\int_{A_\omega} Co_{P_{\omega_1}P_{\omega_2}}(n)\ dA_1 dA_2 + \int_{A_\ell A_\ell} Co_{P_{\ell_1}P_{\ell_2}}(n)\, dA_1 dA_2$$

$$+\ 2\int_{A_\omega}\int_{A_\ell} Co_{P_{\omega_1}P_{\ell_2}}(n)\ dA_1 dA_2 \qquad \ldots\ (B7)$$

Only the real part of the cross-spectral density function of surface pressures is used since $S_D(n)$ is a real valued function.

It is more convenient to express the co-spectra in a normalised form, i.e.

$$R_{P_{\omega_1}P_{\ell_2}}(n) = \frac{Co_{P_{\omega_1}P_{\ell_2}}}{\sqrt{S_{P_{\omega_1}}(n)\cdot S_{P_{\ell_2}}(n)}} \qquad \ldots\ (B8)$$

This is for the case in which points 1 and 2 are on the windward and leeward faces, respectively. Similar expressions can be written for the cases where both points are either on the windward or leeward faces.

From Equation B5 the spectrum of pressure fluctuations $S_p(n)$ can be written in terms of the spectrum of velocity fluctuations:

$$Sp_\alpha(n) = \rho^2\ \bar{U}^2\ C^2_{p_\alpha}\ S_u(n) \qquad \ldots \text{(B9)}$$

where $\alpha = \omega$ or ℓ.

Substituting Equations B8 and B9 into B7 gives the relationship between the drag and turbulence spectrum:

$$\begin{aligned} S_D(n) = &\int_{A_\omega}\int_{A_\omega} \rho^2\ \bar{U}_1\bar{U}_2\ C_{p_{\omega 1}} C_{p_{\omega 2}}\ S_u(n)\ R_{p_{\omega 1}p_{\omega 2}}(n)\ dA_1 dA_2 \\ &+ \int_{A_\ell}\int_{A_\ell} \rho^2\ \bar{U}_1\bar{U}_2\ C_{p_{\ell 1}} C_{p_{\ell 2}}\ S_u(n)\ R_{p_{\ell 1}p_{\ell 2}}(n)\ dA_1 dA_2 \\ &+ 2\int_{A_\omega}\int_{A_\ell} \rho^2\ \bar{U}_1\bar{U}_2\ C_{p_{\omega 1}} C_{p_{\ell 2}}\ S_u(n)\ R_{p_{\omega 1}p_{\ell 2}}(n)\ dA_1 dA_2 \qquad \ldots \text{(B10)} \end{aligned}$$

Frequently, the normalised co-spectra of pressure are assumed to be identical to the normalised co-spectra of turbulence, and further it is the $\sqrt{\text{coherence}}$ not the normalised co-spectrum which is used.

Simiu proposed that the normalised co-spectrum in the last integral of Equation B10 could be expressed in the form:

$$R_u(r, n) \cdot N(n)$$

where $R_u(r, n)$ is the across wind cross-correlation of turbulence for separation r; and N(n) is the along-wind correlation coefficient.

APPENDIX C

MATHEMATICAL MODEL OF SPATIAL CORRELATIONS

C.1 Introduction

The following theoretical analysis assumes that the turbulence is homogeneous and isotropic and momentarily frozen. Further, it is assumed that the cross-correlation of fluctuating pressures on the windward face of a bluff body in turbulent flow is identical to that of the turbulence. The last assumption violates the basic assumption that for homogeneous isotropic turbulence (HIT) there should be no boundaries. In spite of present deficiencies this approach does provide useful results as demonstrated by Harris[35] for atmospheric turbulence and by this study in Chapter 6.

C.2 Theory

It has been shown[35] that the von Karman spectrum is a good model for characterising atmospheric turbulence. It was demonstrated in Chapter 4 that this spectral model was also an accurate representation of wind tunnel grid generated turbulence and will therefore be used in the derivation of the coherence functions. The von Karman spectrum for the u-component of turbulence is given by:

$$\frac{nS_u(n)}{\sigma_u^2} = \frac{4\tilde{n}}{(1 + 1.8\ (2\pi\tilde{n})^2)^{5/6}} \qquad \text{... (C1)}$$

where $\tilde{n} = nL_x/\overline{U}$.

Taking the Fourier transform of $S_u(n)$ (§2.5.1.2 Equation 41 and from tabulated Fourier transforms[87]) the auto-correlation function is found to be:

$$R_u(\tilde{\tau}) = \frac{2^{2/3}}{\Gamma(1/3)} \cdot \tilde{\tau}^{1/3}\ k_{1/3}(\tilde{\tau}) \qquad \text{... (C2)}$$

where $\tilde{\tau} = \frac{\bar{U}\tau}{aL_x}$; $a = \frac{\Gamma(1/3)}{\Gamma(\frac{1}{2})\Gamma(5/6)} = 1.339$; and $k_{1/3}(\tilde{\tau})$ is the modified Bessel function of the second kind.

For HIT the general correlation between velocity components at two points is given by:

$$\rho_{ij}(r) = \frac{f(r)-g(r)}{r^2}\, r_i r_j + g(r)\delta_{ij} \qquad \ldots \text{(C3)}$$

where $\delta_{ij} = 1$ for $i = j$
$= 0$ for $i \neq j$

$f(r)$ is the longitudinal correlation function and $g(r)$ is the transverse correlation functions. Figure C.1 defines $f(r)$ and $g(r)$.

$f(r)$ and $g(r)$ are not independent, but are related by:

$$g(r) = f(r) + \frac{r}{2}\,\frac{df(r)}{dr} \qquad \ldots \text{(C4)}$$

The auto-correlation function of Equation C2, by means of Taylor's frozen turbulence hypothesis can now be expressed as:

$$f(\tilde{r}) = \frac{2^{2/3}}{\Gamma(1/3)}\,\tilde{r}^{1/3} \cdot k_{1/3}(\tilde{r}) \qquad \ldots \text{(C5)}$$

where $\tilde{r} = \frac{r}{aL_x}$

Using Reference 87 $\frac{df(\tilde{r})}{d\tilde{r}}$ is determined to be

$$\frac{df(\tilde{r})}{d\tilde{r}} = \frac{2^{2/3}}{\Gamma(1/3)}\left[1/3\ \tilde{r}^{-2/3}k_{1/3}(\tilde{r}) + \tilde{r}^{1/3}\left(-\frac{1}{3\tilde{r}}\,k_{1/3}(\tilde{r}) - k_{-2/3}(\tilde{r})\right)\right] \qquad \ldots \text{(C6)}$$

$$= -\frac{2^{2/3}}{\Gamma(1/3)}\,\tilde{r}^{1/3}\,k_{2/3}(\tilde{r}) \qquad \ldots \text{(C7)}$$

(note that $k_{-2/3}(\tilde{r}) = k_{2/3}(\tilde{r})$)

Using Equations C5 and C7 in C4 to determine $g(\tilde{r})$ it is now possible to derive $\rho_{ij}(\tilde{r})$. The cross-correlation function of the longitudinal components of turbulence with lateral separations is:

$$g(\tilde{r}) = \frac{2^{2/3}}{\Gamma(1/3)} \tilde{r}^{1/3} \left[k_{1/3}(\tilde{r}) - \tilde{r}\, k_{2/3}(\tilde{r}) \right] \qquad \ldots \text{(C8)}$$

and by Fourier transformation using Reference 87 the cross-spectral function, after some manipulation is found to be:

$$S_{12}(n) = \frac{2^{13/6}}{\Gamma(1/3)} \sqrt{\pi}\ \frac{aL_x}{\bar{U}} \cdot \left(\frac{r}{aL_x} \right)^{5/3} \left[\frac{k_{5/6}(\eta)}{\eta^{5/6}} - \frac{\eta^{-11/6}}{2} k_{11/6}(\eta) \right] \ldots \text{(C9)}$$

where

$$\eta = \frac{r}{aL_x} \sqrt{1 + 1.8(2\pi\tilde{n})^2}$$

Because the cross-correlation function was symmetrical the cross-spectral function is real and equal to the co-spectrum. The coherence function $\gamma_{12}^2(n)$ is therefore equal to the square of the normalised cross-spectrum in Equation C9, i.e.

$$\gamma_{12}(n) = \frac{2^{1/6} a \sqrt{\pi}}{\Gamma(1/3)} \left[\eta^{5/6} k_{5/6}(\eta) - \frac{\eta^{-1/6}}{2} k_{11/6}(\eta) \right] \qquad \ldots \text{(C10)}$$

Comparison between experimentally determined coherences for windward face pressures and theoretical predictions derived from Equation C10 are shown in Fig.41.

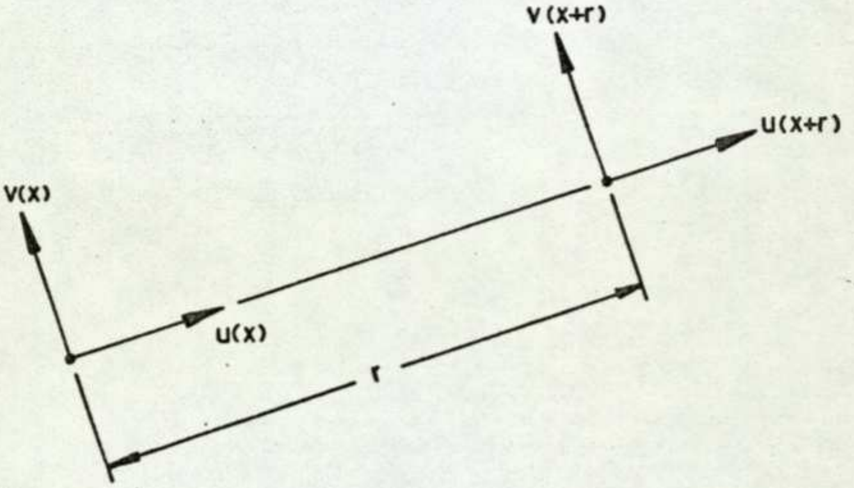

$$f(r) = \frac{\overline{u(x)\cdot u(x+r)}}{\hat{u}^2}$$

$$g(r) = \frac{\overline{v(x)\cdot v(x+r)}}{\hat{v}^2}$$

FIG C1 Fundamental correlation functions.

APPENDIX D

DIGITAL COMPUTER PROGRAMME

D.1 Introduction

The FORTRAN programme PPT1 computes statistical properties of digitised data using the mathematical expressions detailed in Chapter 2. The fast Fourier transform algorithm is from Villasenor[60] and Anderson & Nettleton[61]. A full listing of the main programme and subroutines are given on microfiche at the back.

D.2 General Structure

The programme is designed for analysing both the individual and joint properties of two signals. The data to be analysed is on magnetic tape or disc store.

The programme was developed on The City University ICL 1905E digital computer and to optimise the core capacity required for the large volume of data being processed, the data after each operation was written to disc storage. For operation on the University of London Computer Centres CDC 7600 digital computer, the programme was modified so that all the data was stored in core to minimise the transfer of data to and from disc storage. Where possible data was overwritten when not required any further, thereby optimising core space.

The following presents a short synopsis of the more important operations involved in each segment.

D.2.1 SEGMENT 1

The programme searches the input digital tape or disc store for the data to be analysed. The data for each signal is stored in a two-dimensional array of size 100 × 256.

D.2.2 SEGMENT 2

The probability density function for each signal is calculated and the data is standardised by removing the mean and dividing by its standard deviation. The data in blocks of 256 are then Fourier transformed using the FFT and the ensemble average spectra found.

D.2.3 SEGMENT 3

The Fourier coefficients of each signal from the Fourier transforms are then used to compute the cross-spectra and hence the ensemble average cross-spectrum. From the average spectra the cross-spectrum is also expressed as normalised Co- and Quad-spectra. The transfer function, phase and coherence functions are also determined.

D.2.4 SEGMENT 4

The inverse Fourier transform is performed on the spectra for each signal of the cross-spectrum to obtain the auto- and cross-correlation functions.

REFERENCES

1. Page, J K: Field investigations of wind failures in the Sheffield gales of 1962.
Proceedings of Symposium on Wind Effects on Buildings and Structures, Loughborough University of Technology, UK, April 1968.

2. Report of the committee of inquiry into collapse of cooling towers at Ferrybridge, Monday, November 1965.
Central Electricity Generating Board, London, 1966.

3. Menzies, J B: Wind damage to buildings in the United Kingdom 1962-1969.
B.R.S. Current Paper 35/71, November 1971.

4. Buller, P S J: Gale damage to buildings and structures in the United Kingdom, 2 January 1976.
B.R.S. Current Paper 42/77, August 1977.

5. Buller, P S J: Wind damage to buildings in the United Kingdom 1970-1976.
B.R.S. Current Paper 42/78, April 1978.

6. Eaton, K J: Damage due to tornadoes in SE England, 25 January 1971.
B.R.S. Current Paper 27/71, September 1971.

7. Eaton, K J and Judge, C J: Tornado damage to buildings, 26 June 1973.
B.R.S. Current Paper 16/75, February 1975.

8. British Standards Institution: Code of Practice CP3 : Chapter V : Part 2 : 1972, Wind Loads.

9. American National Standards Institution: American National Standard Building Code Requirements for Minimum Design Loads in Buildings and Other Structures, A58.1, 1972.

10. Standards Association of Australia: SAA Loading Code Part II - Wind Forces. Australian Standard CA34, Part II, 1971.

11. National Building Code of Canada 1975: Supplement No.4 Wind Loads. Associate Committee on the National Building Code and National Research Council of Canada, 1975.

12. Davenport, A G: The application of statistical concepts to the wind loading of structures.
Proc. Inst. Civ. Eng., Vol.19 (August 1961) pp.449-472.

13. Vickery, B J: On the assessment of wind effects on elastic structures.
Civ. Eng. Trans., Inst. of Eng., Australia (Oct.1966) pp.183-192.

14. Simiu, E: Gust factors and along-wind pressure correlations.
J. Struct. Div., ASCE, 99, No.ST4 (April 1973) pp.773-783.

REFERENCES (Contd.)

15. Newberry, C W; Eaton, K J and Mayne, J R: Wind loading on tall buildings - further results from Royex House.
B.R.S. Current Paper 29/73, November 1973.

16. Newberry, C W; Eaton, K J and Mayne, J R: Wind pressure and strain measurements at the Post Office Tower.
B.R.S. Current Paper 30/73, November 1973.

17. Mackey, S and Ko, P K L: Spatial configuration of gusts.
Proceedings of the Fourth Int. Conf. of Wind Effects on Buildings and Structures, Heathrow, England 1975.

18. Vellozi, J and Cohen, E: Gust response factors.
J. Struct. Div., ASCE, 94, No.ST6 (June 1968) pp.1295-1313.

19. Vickery, B J: Discussion of paper 18.
J. Struct. Div., ASCE, 95, No.ST3 (March 1969) pp.494-501.

20. Simiu, E; Marshall, R D and Haber, S: Estimation of along-wind building response.
J. Struct. Div., ASCE, 103, No.ST7 (July 1977) pp.1325-1338.

21. Vickery, B J: On the reliability of gust loading factors.
Civ. Eng. Trans., Inst. of Eng., Australia (Apl.1971) pp.1-9.

22. Lumley, J L and Panofsky, H A: The structure of atmospheric turbulence.
Interscience, New York, 1964.

23. Van der Hoven, I: Power spectrum of horizontal wind speed in the frequency range from 0.0007 to 900 cycles per hour.
J. Met. 14 (1957) pp.160-164.

24. Davenport, A G: The dependence of wind load upon meteorological parameters.
Proceedings of the Int. Research Seminar on Wind Effects on Buildings and Structures, Toronto, Canada, 1968.

25. Panofsky, H A: The atmospheric boundary layer below 150 metres.
Ann. Rev. Fluid Mech., 6 (1974) pp.147-177.

26. Pasquill, F: Effects of buildings on the local wind.
Phil. Trans. Roy. Soc. Lond. A.269, 1971.

27. Sutton, O G: Micrometeorology.
McGraw-Hill, London, 1953.

28. Counihan, J: Adiabatic atmospheric boundary layers : a review and analysis of data from the period 1880-1972.
Atmos. Envir. Vol.9 (1975) pp.871-905.

29. Batchelor, G K: The theory of homogeneous turbulence, Cambridge University Press, 1953.

30. Davenport, A G: The spectrum of horizontal gustiness near the ground in high winds.
Quart. J. Royal Meteorol. Soc., 87 (April 1961) pp.194-211.

31. Harris, R I: On the spectrum and autocorrelation function of gustiness in high winds.
ERA Confidential Report SP1/T4, 1960.

32. Schlichting, H: Boundary layer theory.
McGraw-Hill, New York, 1960.

33. Engineering Science Data Unit: Characteristics of atmospheric turbulence near the ground. Part II : single point data for strong winds (neutral atmosphere).
ESDU Item 74031, 1974.

34. Panofsky, H A; Cramer, H E and Rao, V R K: The relation between Eulerian time and space spectra.
Quart. J. Royal Meteorol. Soc., 84 (July 1958) pp.270-273.

35. Harris, R I: The nature of the wind.
C.I.R.I.A. Seminar on Modern Design of Wind Sensitive Structures, London, 1970.

36. Shiontani, M and Iwatani, Y: Correlation of wind velocities in relation to gust loading.
Proceedings of the Third Conf. on Wind Effects on Buildings and Structures, Tokyo, Japan, 1971.

37. Ropelewski, C F; Tennekes, H and Panofsky, H A: Horizontal coherence of wind fluctuations.
Boundary-Layer Meteorol., 5 (1973) pp.353-363.

38. Parkinson, G V; Feng, G and Ferguson, N: Mechanisms of vortex-excited oscillations of bluff cylinders.
Proceedings of the Symposium of Wind Effects on Buildings and Structures, Loughborough University of Technology, UK, April 1968.

39. Wootton, L R and Scruton, C: Aerodynamic stability.
C.I.R.I.A. Seminar on Modern Design of Wind Sensitive Structures, London, 1970.

40. Parkinson, G V: Aeroelastic galloping in one degree of freedom.
Proceedings of the First Int. Conf. on Wind Effects on Buildings and Structures, London, 1963.

41. Parkinson, G V: Mathematical models of flow-induced vibrations of bluff bodies.
Proceedings of IUTAM-IAHR Symposium on Flow-Induced Structural Vibrations, Karlsruhe, West Germany, 1974.

42. Novak, M and Davenport, A G: Aeroelastic instability of prisms in turbulent flow.
J. Eng. Mech. Div., ASCE, 96, No.EM1 (Feb.1970).

43. Laneville, A; Gartshore, I S and Parkinson, G V: An explanation of some effects of turbulence on bluff bodies.
Proceedings of the Fourth Int. Conf. on Wind Effects on Buildings and Structures, Heathrow, England, 1975.

44. Parkinson, G V and Santosham, T V: Cylinders of rectangular section as aeroelastic nonlinear oscillators.
ASME Vibrations Conf., Boston, Mass., March 1967.

45. Liepmann, H W: On the application of statistical concepts to the buffeting problem.
J. Aeronaut. Sci., 19, (Dec.1952) pp.793-800,822.

46. Hunt, J C R: A theory of turbulent flow around two-dimensional bluff bodies.
J. Fluid Mech., 61 (1973) pp.625-706.

47. Walukiewicz, H: An algebraic solution of wind effects on structures problem and reciprocal theorem for random wind load.
Proc. Second US National Conf. on Wind Engineering Research, Colorado State University 1975.

48. Roberts, J B: Drag spectra of simple structures in turbulence.
J. Eng. Mech. Div., ASCE, No.EM5 (October 1972) pp.1053-1074.

49. Stansby, P K and Wootton, L R: The value of wind research to civil engineering.
Proceedings of the Fourth Int. Conf. on Wind Effects on Buildings and Structures, Heathrow, England, 1975.

50. Davenport, A G: Gust loading factors.
J. Struct. Div., ASCE, 93, No.ST3 (June 1967) pp.11-34.

51. McLaren, F G; Sherratt, A F C and Morton, A S: Effect of free stream turbulence on the drag coefficient of bluff sharp-edged cylinders. Nature, Vol.224 (Nov.1969) pp.908-909.

52. Lee B E: An investigation of the effects of turbulence scale on the mean forces on two-dimensional square prisms.
Dept. of Building Sciences, University of Sheffield, BS24, June 1975.

53. Cook, N J: The effect of scale of turbulence on high rise buildings.
Ph.D. Thesis, Bristol University, 1972.

54. Sykes, D M: A new wind tunnel for industrial aerodynamics.
J. Ind. Aero., 2 (1977) pp.65-78.

55. Bearman, P N: Corrections for the effect of ambient temperature drift on hot wire measurements in incompressible flow.
NPL Aero. Report 1302, 1969.

56. Perera, M D A E S: Wind-tunnel modelling of wind-excited lateral and in-line vibrations of tall structures.
Ph.D. Thesis, Dept. of Aero. Engng., The City University, 1976.

REFERENCES (Contd.)

57. Hassan, U and Perera, M D A E S: Digital analysis of analogue data from wind tunnel experiments.
The City University, Research Memo, Aero 74/4, 1974.

58. Bendat, J S and Piersol, A G: Random data: Analysis and measurement Procedures.
Wiley-Interscience, London, 1971.

59. Blake, C C and Leighton, C C: Linking two alien digital computers via a British Standard Interface.
The Computers Bulletin, 14 (Apl.1970) pp.106-111.

60. Villasenor, A J: Digital spectral analysis.
NASA TN D-4510, Washington, 1968.

61. Anderson, J S and Nettleton, T: Digital spectral and correlation analysis.
The City University, Research Memo. ML31, 1971.

62. Blackman, R B and Tukey, J W: The measurement of power spectra.
Dover Publications, New York, 1958.

63. Cooley, J W; Lewis, P A W and Welch, P D: The fast Fourier transform and its applications.
IBM Research Report RC-1743, IBM Watson Research Centre, New York, February 1967.

64. Cooley, J W and Tukey, J W: An algorithm for the machine calculation of complex Fourier series.
Maths. Compat., 19 (1965) pp.297-301.

65. Glover, D D and Sykes, D M: Design and construction of the 1.5 x 3.0 m low speed wind tunnel.
The City University, Research Memo. Aero 74/2, 1974.

66. Baines, W D and Peterson, E G: An investigation of flow through screens.
Trans. ASME, Vol.73 (1951) pp.467-480.

67. Whitbread, R E: On the introduction of turbulence into wind-tunnel investigations for the determination of wind-induced amplitudes of oscillation.
NPL Aero. Rep.1265, April 1968.

68. Nandascher, E: Unified analysis of grid turbulence.
J. Eng. Mech. Div., ASCE, No.EM2 (April 1970) pp.121-141.

69. Khader, M H A and Elango, K: Grid turbulence in initially turbulent water flow.
J. Eng. Mech. Div., ASCE, No.EM6 (Dec.1974) pp.1149-1165.

70. Armitt, J: 49th Industrial fluid mechanics research meeting held at NPL, 9 June 1976.

71. Hinze, J O: Turbulence.
McGraw-Hill, New York, 1959.

72. Delaney, N K and Sorensen, N E: Low speed drag of cylinders of various shapes.
NACA Tech. Note 3038, 1953.

73. Maskell, E C: A theory of blockage effects on bluff bodies and stalled wings in a closed wind tunnel.
A.R.C. R & M 3400, 1965.

74. Vickery, B J: Fluctuating lift and drag on a long cylinder of square cross-section in a smooth and in a turbulent stream.
J. Fluid Mech., 25 (1966) pp.481-494.

75. Baines, W D: Effects of velocity distribution on wind loads and flow patterns on buildings.
Proceedings of Symposium on Wind Effects on Buildings and Structures, NPL, England, 1963.

76. Bearman, P W and Trueman, D M: An investigation of the flow around rectangular cylinders.
Aero. Quart. J (Aug.1972) pp.229-237.

77. Bearman, P W: Some measurements of the distortion of turbulence approaching a two-dimensional bluff body.
J. Fluid Mech., 53 (1972) pp.451-467.

78. Hunt, J C R: Turbulent velocities near and fluctuating surface pressures on structures in turbulent wind.
Proceedings of Fourth Int. Conf. on Wind Effects on Buildings and Structures, Heathrow, England, 1975.

79. Verley, R L P: Wave forces on structures - an introduction.
BHRA TN1319, England, November 1975.

80. Vickery, B J: On the flow behind a coarse grid and its use as a model of atmospheric turbulence in studies related to wind loads on buildings.
NPL Aero. Report 1143, 1965.

81. Dalgleish, W A; Wright, W and Schriver, W R: Wind pressure measurements on a full-scale high-rise office building.
Int. Seminar on Wind Effects on Buildings and Structures, Ottawa, 1967.

82. Kao, K H: Measurements of pressure/velocity correlation on a rectangular prism in turbulent flow.
University of Western Ontario, BLWT-2-70, Canada, January 1970.

83. Vickery, B J and Kao, K H: Drag or along-wind response of slender structures.
J. Struct. Div., ASCE, 98, No.ST1 (1972) pp.21-36

REFERENCES (Concluded)

84. Petty, D G: The distortion of turbulence by a circular cylinder. Symposium of External Flow, Univ. of Bristol, 1972.

85. Gartshore, I S: The effects of free stream turbulence on the drag of rectangular two-dimensional prisms.
University of Western Ontario, BLWT-4-73, Canada, October 1973.

86. Bearman, P W: An investigation of the forces on flat plates normal to a turbulent flow.
J. Fluid Mech., 46 (1971) pp.177-198.

87. Campbell, G A and Foster, R M: Fourier integrals for practical applications.
D Van Nostrand Co. Inc., New York, 1954.

THE COMPUTER PROGRAMME

A Fortran programme written for the London University Computer Centres CDC 7600 computer to calculate joint statistical functions for two data sets. The structure for the programme is outlined in Appendix D.
A complete list of the statements is provided, following a description of the input data card.

Input of Data

The order and format of the data cards are:

(1) ITIMES in format I4
(2) IFILT in format I4
(3) TYPE in format F10.4 if IFILT = 0
(4) Array NOPUT in format 13I4
(5) Array NCARDS in format 13I4
(6) DATE1 in format A8
(7) DATE2 in format A8
(8) RMODEL in format A8
(9) ISCREEN and IXBAR in format 2I4
(10) DIA and UBAR in format 2F10.4
(11) AMP1, FREQ1, DAMP1 and DC1 in format 4F10.4
(12) AMP2, FREQ2, DAMP2 and DC2 in format 4F10.4
(13) NGP, M, N, NP, and NC in format 5I4
(14) RS, PS and T in format 3F10.4
(15) IBATCH and JBATCH in format 2I4
(16) Array ICNL in format 2I4
(17) RUN
(18) HOLE1
(19) HOLE2
(20) ITMS and array IRUN in format 13I4

The following is a brief explanation of the input symbols, for those which have been omitted their meaning is clear after inspection of the programme.

Symbol	Significance
ITIMES	Number of cases to be analysed
IFILT	Spectral filter: 0 = no filter, 1 = Hanning filter
TYPE	Data window: 0 = box-car, 1 = triangular, 2 = $1-t^2$ 3 = Hann, 4 = Hamm.
NOPUT(I) NCARDS(I)	0 = no output, 1 = output on line printer and punched cards respectively; I denoting the statistical functions: $P_1(x)$ $P_2(x)$ $S_1(n)$ $S_2(n)$ $C(n)$ $Q(n)$ $F_{12}(n)$ $\gamma_{12}(n)$ $H(n)$ $\theta(n)$ $R_1(\tau)$ $R_2(\tau)$ and $R_{12}(\tau)$
DATE1, DATE2	Dates when the data was recorded and analysed, respectively.
RMODEL,DIA,UBAR	Model reference and representative dimension , and mean wind speed
ISCREEN, IXBAR	Screen reference and distance of model from screen
AMP,FREQ,DAMP,DC	Equation for correcting the effects of the pressure tubes
NGP	Number of periodograms used in the spectrum
N, M	Number of data values used per periodogram, $N=2^M$
NP, NC	Number of output values for spectrum and correlation function, respectively.
RS, PS, T	Tape recorder speed during recording and digitising, and ADC sampling rate (samples/sec)
RUN	Experiment reference number
HOLE	Pressure tap reference or hot wire position

```
PROGRAM PPT1(INPUT,OUTPUT,TAPE1=INPUT,TAPE2=OUTPUT,TAPE4,TAP
DIMENSION S1(258),F1(258),A(258),C(258)
DIMENSION STRN(258),S(64),IRUN(20)
DIMENSION PR(105),XX(105),TPROB(105)
DIMENSION NOPUT(13),NCARDS(13),ICNL(2)
LEVEL 2, DAT1
COMMON DAT1(100,258),DAT2(100,258),PSIGMA(2,258)
TYPE=0.0
REWIND 5
READ(1,100) ITIMES
READ(1,100) IFILT
IF(IFILT.EQ.0) READ(1,104) TYPE
READ(1,100) (NOPUT(I),I=1,13)
READ(1,100) (NCARDS(I),I=1,13)
READ(1,102) DATE1
READ(1,102) DATE2
READ(1,102) RMODEL
READ(1,100) ISCREEN,IXBAR
READ(1,104) DIA,UBAR
READ(1,104) AMP1,FREQ1,DAMP1,DC1
READ(1,104) AMP2,FREQ2,DAMP2,DC2
READ(1,100) NGP,M,N,NP,NC
READ(1,104) RS,PS,T
READ(1,100) IBATCH,JBATCH
READ(1,100)(ICNL(LK),LK=1,2)
NN1=N/2
NA=NC
DO 900 JJ=1,ITIMES
CA1=0.0
NC=NA
READ(1,102) RUN
READ(1,102) HOLE1
READ(1,102) HOLE2
READ(1,100)  ITMS,(IRUN(LL),LL=1,IBATCH)
ICOUNT=0
WRITE(2,234)
WRITE(2,221)
WRITE(2,235)
WRITE(2,222)
WRITE(2,235)
WRITE(2,235)
WRITE(2,236) RUN
WRITE(2,223) DATE1
WRITE(2,224) DATE2
WRITE(2,225) RMODEL
WRITE(2,226) ISCREEN
WRITE(2,227)IXBAR
WRITE(2,228) UBAR
WRITE(2,237) HOLE1
WRITE(2,238) HOLE2
WRITE(2,229) N
WRITE(2,230) NGP
WRITE(2,231) RS
WRITE(2,232) PS
WRITE(2,233) T
IF(IFILT.EQ.1) WRITE(2,600)
IF(IFILT.EQ.1) GO TO 701
```

```
      IF(TYPE.EQ.0.0) WRITE(2,601)
      IF(TYPE.EQ.1.0) WRITE(2,602)
      IF(TYPE.EQ.2.0) WRITE(2,603)
      IF(TYPE.EQ.3.0) WRITE(2,604)
      IF(TYPE.EQ.4.0) WRITE(2,605)
  701 WRITE(2,235)
      WRITE(2,221)
      WRITE(2,234)
      WRITE(2,106)
  500 CONTINUE
      CALL POSS(ICH,IRN)
      IF(IRN.EQ.IRUN(1)) ICOUNT=ICOUNT+1
      IF(ICOUNT.EQ.ITMS) GO TO 501
      GO TO 500
  501 BACKSPACE 5
      DO 506 I=1,IBATCH
  720 CALL POSS(II,NN)
      IF(II.NE.ICNL(1).OR.NN.NE.IRUN(I)) GO TO 720
      WRITE(2,107) II,NN
      IB=I*JBATCH
      IA=(IB-JBATCH)+1
      DO 502 J=IA,IB
  502 READ(5,104)(DAT1(J,K),K=1,N)
  721 CALL POSS(II,NN)
      IF(II.NE.ICNL(2).OR.NN.NE.IRUN(I)) GO TO 721
      WRITE(2,107) II,NN
      DO 504 J=IA,IB
  504 READ(5,104)(DAT2(J,K),K=1,N)
  506 CONTINUE
      GP=NGP
      AN=N
      RATIO=RS/PS
      DELTAN=T*RATIO/AN
COMMENT - FREQ IN HZ AT K TH POINT IS (K-1)*T/N
C           WHERE T IS SAMPLING FREQ IN HZ.
      DO 1 K=1,N
      AK=K
    1 STRN(K)=(AK-1.0)*DELTAN
      IZ1=N+2
      IZS=N/8
      DO 2 K=1,N
    2 A(K)=0.
      DO 7 J=1,2
      DO 3 K=1,105
    3 PR(K)=0.
      IF(NOPUT(J).EQ.0) GO TO 522
      WRITE(2,219) J
  522 CONTINUE
      DO 5 I=1,NGP
      DO 702 K=1,N
      IF(J.EQ.1) S1(K)=DAT1(I,K)
  702 IF(J.EQ.2) S1(K)=DAT2(I,K)
      IF(TYPE.EQ.0.0) GO TO 700
      CALL WINDOW(S1,C,N,TYPE,CA1)
  700 CONTINUE
      CALL PROB(S1,N,XBAR,SIGMA,TPROB,XX)
      PSIGMA(1,I)=XBAR
```

```
      PSIGMA(2,I)=SIGMA**2
      DO 4 K=1,105
    4 PR(K)=PR(K)+TPROB(K)
      CALL FOURIER(S1,S,M,IFERR,IZ1,IZS)
      DO 703 K=1,N
      IF(J.EQ.1) DAT1(I,K)=S1(K)
  703 IF(J.EQ.2) DAT2(I,K)=S1(K)
    5 CONTINUE
      DO 6 K=1,105
    6 PR(K)=PR(K)/GP
      XBAR=0.
      SIGMA=0.
      DO 53 K=1,NGP
      XBAR=PSIGMA(1,K)+XBAR
   53 SIGMA=(PSIGMA(2,K))+SIGMA
      XBAR=XBAR/FLOAT(NGP)
      SIGMA=SQRT(SIGMA/FLOAT(NGP))
      IF(NOPUT(J).EQ.0) GO TO 800
      WRITE(2,244) XBAR,SIGMA
      CALL MOMENTS(PR,XX)
      WRITE(2,220)
      CALL PLOT(PR,XX,105)
  800 IF(NCARDS(J).EQ.0) GO TO 801
      WRITE(4,300) J,RUN
      WRITE(4,242) (PR(I),I=1,105)
  801 CONTINUE
    7 CONTINUE
COMMENT - COMPUTE THE POWER SPECTRA OF EACH
C         SUBRECORD OF THE 1ST AND 2ND ENSEMBLE.
      DO 11 IL=1,2
      DO 37 J=1,N
   37 A(J)=0.
      DO 9  I=1,NGP
      DO 704 K=1,N
      IF(IL.EQ.1) S1(K)=DAT1(I,K)
  704 IF(IL.EQ.2) S1(K)=DAT2(I,K)
      CALL NEWHANN(S1,N,IZ1,3,IFILT)
      CALL NPR(S1,N,IZ1)
      CALL NEWHANN(S1,N,IZ1,1,0)
COMMENT - SUM THE ABOVE AND STORE THE AVERAGE
C         POWER SPECTRA ON DISC IN BLOCKS 1 AND 2.
      DO 9 K=1,NN1
    9 A(K)=A(K)+S1(K)
      FID=1.0
      IF(IFILT.EQ.1) FID=8.0/3.0
      IF(TYPE.EQ.1) FID=3.0
      IF(TYPE.EQ.2) FID=1.875
      IF(TYPE.EQ.3) FID=8.0/3.0
      IF(TYPE.EQ.4) FID=2.52
      DO 10 K=1,NN1
   10 A(K)=A(K)*FID*2.0/(DELTAN*GP)
      IF(IL.EQ.2) GO TO 32
      CALL MODTRN(A,STRN,N,AMP1,FREQ1,DAMP1,DC1)
      GO TO 23
   32 CALL MODTRN(A,STRN,N,AMP2,FREQ2,DAMP2,DC2)
   23 DO 706 I=1,N
      IF(IL.EQ.1) PSIGMA(1,I)=A(I)
```

```
  706 IF(IL.EQ.2) PSIGMA(2,I)=A(I)
   11 CONTINUE
      DO 12 K=1,N
      C(K)=0.
   12 A(K)=0.
COMMENT - COMPUTE CROSS POWER SPECTRA FROM APPROPIATE
C         PAIRS OF SUBRECORDS READ FROM DISC AND SUMMED.
      DO 19 I=1,NGP
      DO 705 K=1,N
      S1(K)=DAT1(I,K)
  705 F1(K)=DAT2(I,K)
      CALL NEWHANN(S1,N,IZ1,3,IFILT)
      CALL NEWHANN(F1,N,IZ1,3,IFILT)
      CALL CRPR(S1,F1,N,IZ1)
      DO 17 K=1,N
      C(K)=C(K)+F1(K)
   17 A(K)=A(K)+S1(K)
   19 CONTINUE
      CALL TFN(A,STRN,N,AMP1,FREQ1,DAMP1,DC1,AMP2,FREQ2,DAMP2,DC2)
      CALL TFN(C,STRN,N,AMP1,FREQ1,DAMP1,DC1,AMP2,FREQ2,DAMP2,DC2)
      DO 60 K=1,N
   60 C(K)=C(K)*FID*2.0/(DELTAN*GP)
      DO 707 K=1,N
      DAT1(1,K)=PSIGMA(1,K)
      DAT1(2,K)=PSIGMA(2,K)
  707 PSIGMA(1,K)=C(K)
      DO 20 K=1,N
      A(K)=A(K)*FID*2.0/(DELTAN*GP)
   20 C(K)=A(K)
      DO 722 K=1,N
      S1(K)=DAT1(1,K)
  722 F1(K)=DAT1(2,K)
      CALL MAX(S1,N,AMAX)
      AMAX1=AMAX/1000.0
      CALL MAX(F1,N,AMAX)
      AMAX2=AMAX/1000.0
      DO 29 I=1,NN1
      J=2*I
      K=J-1
      IF(S1(I).LT.AMAX1) GO TO 28
      IF(F1(I).LT.AMAX2) GO TO 28
      A(K)=A(K)/SQRT(S1(I)*F1(I))
      A(J)=A(J)/SQRT(S1(I)*F1(I))
      GO TO 29
   28 A(J)=0.
      A(K)=0.
   29 CONTINUE
      DO 709 I=1,N
      DAT1(3,I)=A(I)
  709 DAT1(4,I)=C(I)
COMMENT - STORE AVERAGE CROSS POWER IN
C         COMPLEX FORM IN BLOCK 3.
COMMENT - COMPUTE THE MODULUS OF CROSS SPECTRA
C         AND STORE ON DISC IN BLOCK 4
      CALL MCPR(A,N,IZ1)
      DO 22 I=1,N
   22 A(I)=A(I)**2
```

```
      DO 710 I=1,N
  710 DAT1(5,I)=A(I)
COMMENT - COMPUTE COHERENCE FUNCTION AND STORE IN BLOCK 5
      CALL MCPR(C,N,IZ1)
COMMENT - COMPUTE TRANSFER FUNCTION
C           AND STORE IN BLOCK 6.
      DO 43 I=1,NN1
      IF(S1(I).LT.AMAX1) GO TO 42
      C(I)=C(I)/S1(I)
      GO TO 43
   42 C(I)=0.
   43 CONTINUE
      DO 711 I=1,N
  711 DAT1(6,I)=C(I)
COMMENT / COMPUTE PHASE ANGLE THETA(N)
C           AND STORE IN BLOCK 7.
      DO 24 I=1,N
   24 A(I)=DAT1(3,I)
      CALL PHASE(A,S1,N,IZ1)
      DO 25 I=1,N
   25 DAT1(7,I)=A(I)
COMMENT - COMPUTE AUTO-CORRELATION FUNCTIONS
C           OF 1ST AND 2ND ENSEMBLES AND CROSS
C           CORRELATION AND STORE IN BLOCKS 8,9,10
      DO 712 I=1,N
      A(I)=DAT1(1,I)
      S1(I)=DAT1(2,I)
      F1(I)=DAT1(4,I)
  712 C(I)=PSIGMA(1,I)
      CALL NEWHANN(A,N,IZ1,2,0)
      CALL NEWHANN(S1,N,IZ1,2,0)
      CALL HARMON(A,S,M-1,1,IFERR,IZ1,IZS)
      CALL HARMON(S1,S,M-1,1,IFERR,IZ1,IZS)
      CALL HARMON(F1,S,M-1,1,IFERR,IZ1,IZS)
      CALL HARMON(C,S,M-1,1,IFERR,IZ1,IZS)
      CALL NEWHANN(A,N,IZ1,1,0)
      CALL NEWHANN(S1,N,IZ1,1,0)
      CALL NEWHANN(F1,N,IZ1,1,0)
      CALL NEWHANN(C,N,IZ1,1,0)
      DO 26 I=1,N
      A(I)=A(I)*DELTAN
      S1(I)=S1(I)*DELTAN
      C(I)=C(I)*DELTAN
   26 F1(I)=F1(I)*DELTAN
      SIG1=A(1)
      SIG2=S1(1)
   91 CONTINUE
      DO 27 I=1,N
      DAT1(8,I)=A(I)
      DAT1(9,I)=S1(I)
   27 DAT1(10,I)=F1(I)
COMMENT - OUTPUT THE RESULTS OF THE PROGRAM
      DO 33 I=1,N
      F1(I)=STRN(I)
   33 STRN(I)=STRN(I)*DIA/UBAR
      DO 21 I=1,N
      A(I)=DAT1(1,I)
```

```
 21 S1(I)=A(I)/SIG1
    IF(NCARDS(3).EQ.0) GO TO 524
    WRITE(4,301) RUN
    WRITE(4,243) (S1(I),I=2,NP)
524 IF(NOPUT(3).EQ.0) GO TO 802
    CALL SIMPS(A,NP,DELTAN,AREA)
    AREA1=AREA
    DO 34 I=1,N
 34 A(I)=A(I)*STRN(I)/SIG1
    WRITE(2,201)
    WRITE(2,202) AREA1
    CALL PLOT(A,STRN,NP)
802 CONTINUE
    DO 38 I=1,N
    A(I)=DAT1(2,I)
 38 S1(I)=A(I)/SIG2
    IF(NCARDS(4).EQ.0) GO TO 523
    WRITE(4,302) RUN
    WRITE(4,243) (S1(I),I=2,NP)
523 IF(NOPUT(4).EQ.0) GO TO 503
    CALL SIMPS(A,NP,DELTAN,AREA)
    AREA2=AREA
    DO 35 I=1,N
 35 A(I)=A(I)*STRN(I)/SIG2
    WRITE(2,203)
    WRITE(2,204) AREA2
    CALL PLOT(A,STRN,NP)
503 CONTINUE
    DO 30 I=1,NN1
    K=2*I
    J=K-1
    S1(I)=DAT1(3,J)
 30 A(I)=DAT1(3,K)
    IF(NOPUT(5).EQ.0) GO TO 804
    WRITE(2,205)
    WRITE(2,206)
    CALL PLOT(S1,STRN,NP)
804 IF(NCARDS(5).EQ.0) GO TO 505
    WRITE(4,303) RUN
    WRITE(4,243) (A(I),I=2,NP)
505 IF(NOPUT(6).EQ.0) GO TO 806
    WRITE(2,207)
    WRITE(2,208)
    CALL PLOT(A,STRN,NP)
806 IF(NCARDS(6).EQ.0) GO TO 807
    WRITE(4,304) RUN
    WRITE(4,243) (A(I),I=2,NP)
807 CONTINUE
    DO 713 I=1,N
713 A(I)=DAT1(4,I)
    CALL MCPR(A,N,IZ1)
    DO 36 I=1,N
 36 A(I)=A(I)*STRN(I)/SQRT(SIG1*SIG2)
    IF(NOPUT(7).EQ.0) GO TO 508
    WRITE(2,209)
    WRITE(2,210)
    CALL PLOT(A,STRN,NP)
```

```
508 IF(NCARDS(7).EQ.0) GO TO 509
    WRITE(4,305) RUN
    WRITE(4,243) (A(I),I=2,NP)
509 CONTINUE
    DO 714 I=1,N
714 A(I)=DAT1(5,I)
    IF(NOPUT(8).EQ.0) GO TO 510
    WRITE(2,211)
    WRITE(2,212)
    CALL PLOT(A,STRN,NP)
510 IF(NCARDS(8).EQ.0) GO TO 511
    WPITE(4,306) RUN
    WRITE(4,243) (A(I),I=2,NP)
511 CONTINUE
    DO 715 I=1,N
715 A(I)=DAT1(6,I)
    IF(NOPUT(9).EQ.0) GO TO 512
    WRITE(2,240)
    WRITE(2,241)
    CALL PLOT(A,STRN,NP)
512 IF(NCARDS(9).EQ.0) GO TO 513
    WRITE(4,307) RUN
    WRITE(4,243) (A(I),I=2,NP)
513 CONTINUE
    DO 716 I=1,N
716 A(I)=DAT1(7,I)
    IF(NOPUT(10).EQ.0) GO TO 514
    WRITE(2,213)
    WRITE(2,214)
    CALL PLOT(A,STRN,NP)
514 IF(NCARDS(10).EQ.0) GO TO 515
    WRITE(4,308) RUN
    WRITE(4,243) (A(I),I=2,NP)
515 CONTINUE
    DO 31 I=1,NC
 31 STRN(I)=2.0*(I-1.0)/(T*RATIO)
    DO 717 I=1,N
717 A(I)=DAT1(8,I)
    IF(NOPUT(11).EQ.0) GO TO 516
    WRITE(2,215)
    WRITE(2,216) SIG1
    DO 40 I=1,N
 40 A(I)=A(I)/SIG1
    CALL PLOT(A,STRN,NC)
516 IF(NCARDS(11).EQ.0) GO TO 517
    WRITE(4,309) RUN
    WRITE(4,243) (A(I),I=1,NC)
517 CONTINUE
    DO 718 I=1,N
718 A(I)=DAT1(9,I)
    IF(NOPUT(12).EQ.0) GO TO 518
    WRITE(2,217)
    WRITE(2,216) SIG2
    DO 41 I=1,N
 41 A(I)=A(I)/SIG2
    CALL PLOT(A,STRN,NC)
518 IF(NCARDS(12).EQ.0) GO TO 519
```

```
      WRITE(4,310) RUN
      WRITE(4,243) (A(I),I=1,NC)
  519 CONTINUE
      DO 719 I=1,N
  719 A(I)=DAT1(10,I)
      DO 61 I=1,NC
      K=(NC-I)+1
   61 S1(I)=C(K)/SQRT(SIG1*SIG2)
      DO 62 I=1,NC
      K=(NC+I)-1
   62 S1(K)=A(I)/SQRT(SIG1*SIG2)
      DO 63 I=1,NC
   63 STRN(I)=-2.0*(NC-I)/(T*RATIO)
      DO 64 I=1,NC
      K=(NC+I)-1
   64 STRN(K)=2.0*(I-1)/(T*RATIO)
      IF(NOPUT(13).EQ.0) GO TO 520
      WRITE(2,218)
      WRITE(2,216)
      NC=2*NC-1
      CALL PLOT(S1,STRN,NC)
  520 IF(NCARDS(13).EQ.0) GO TO 521
      WRITE(4,311) RUN
      WRITE(4,243) (S1(I),I=1,NC)
  521 CONTINUE
  900 CONTINUE
  100 FORMAT(13I4)
  102 FORMAT(A8)
  103 FORMAT(A4)
  104 FORMAT(8F10.4)
  106 FORMAT(10X,26HDATA FROM CHANNEL, AND RUN/)
  107 FORMAT(20X,I4,6X,I4)
  201 FORMAT(1H1,20X,51HREDUCED SPECTRUM OF FLUCTUATING VELOCITY AT POIN
     1T 1)
  202 FORMAT(1H0,6X,4HND/U,4X,6HS.F[N],20X,7HS.F1[N],5X,5HAREA=,E10.4)
  203 FORMAT(1H1,6X,4HSTRN,4X,5HPOWER,5X,51HREDUCED SPECTRUM OF FLUCTUAT
     1ING PRESSURE AT POINT 2)
  204 FORMAT(1H0,6X,4HND/U,4X,6HS.S[N],20X,7HS.F2[N],5X,5HAREA=,E10.4)
  205 FORMAT(1H1,6X,4HSTRN,4X,5HPOWER,5X,22HNORMALIZED CO-SPECTRUM)
  206 FORMAT(1H0,6X,4HND/U,4X,4HC[N],20X,12HHC[N] V ND/U)
  207 FORMAT(1H1,6X,4HSTRN,4X,5HPOWER,5X,23HNORMALIZED QUAD-SPECTRA)
  208 FORMAT(1H0,6X,4HND/U,4X,4HQ[N],20X,11HQ[N] V ND/U)
  209 FORMAT(1H1,6X,4HSTRN,4X,5HPOWER,5X,24HMODULUS OF CROSS SPECTRA)
  210 FORMAT(1H0,6X,4HND/U,8H  S F[N],20X,17HS.MOD F12[N] V S )
  211 FORMAT(1H1,6X,4HSTRN,4X,8HGAMMA**2,10X,18HCOHERENCE FUNCTION)
  212 FORMAT(1H0,6X,4HND/U,20X,31HCOHERENCE=F12[N]**2/F1[N]*F2[N()
  213 FORMAT(1H1,6X,4HSTRN,4X,8HTHETA[N],10X,11HPHASE ANGLE)
  214 FORMAT(1H0,6X,4HND/U,4X,7HDEGREES)
  215 FORMAT(1H1,6X,4HTIME,4X,10HCORR COEFF,10X,50HCORRELATION COEFFICIE
     1NT OF PRESS FLUCT. AT POINT 1)
  216 FORMAT(1H0,6X,6HT[SEC],4X,4HR[T],10X,5HR(0)=,E10.4)
  217 FORMAT(1H1,6X,4HTIME,4X,10HCORR COEFF,10X,50HCORRELATION COEFFICIE
     1NT OF PRESS FLUCT. AT POINT 2)
  218 FORMAT(1H1,6X,4HTIME,4X,10HCORR COEFF,10X,29HCROSS CORRELATION COE
     1FFICIENT)
  219 FORMAT(1H1,10X,10HCHANNEL=  ,I2,10H**********,
     11X,24HPROBABILITY DISTRIBUTION,10H**********)
```

```
220 FORMAT(1H0,7H SIGMA ,3X,4HPROB,//)
221 FORMAT(30X,60H***************************************************
   1*********)
222 FORMAT(30X,1H*,20X,18HCONDITIONS OF TEST,20X,1H*)
223 FORMAT(30X,1H*,10X,20HDATE DATA RECORDED  ,A8,20X,1H*)
224 FORMAT(30X,1H*,10X,20HDATE DATA ANALYSED  ,A8,20X,1H*)
225 FORMAT(30X,1H*,10X,20HMODEL USED IN TEST  ,A8,20X,1H*)
226 FORMAT(30X,1H*,10X,20HSCREEN USED IN RUN  ,I1,27X,1H*)
227 FORMAT(30X,1H*,10X,27HDISTANCE MODEL FROM SCREEN  ,I3,18X,1H*)
228 FORMAT(30X,1H*,10X,14HMEAN VELOCITY ,F5.2,5H FT/S,24X,1H*)
229 FORMAT(30X,1H*,10X,35HNUMBER OF POINTS IN EACH SUBRECORD ,I3,1
   1H*)
230 FORMAT(30X,1H*,10X,35HNUMBER OF SUBRECORDS AVERAGED OVER ,I3,1
   1H*)
231 FORMAT(30X,1H*,10X,17HDATA RECORDED AT ,F7.3,6H INS/S,18X,1H*)
232 FORMAT(30X,1H*,10X,17HDATA REPLAYED AT ,F7.3,6H INS/S,18X,1H*)
233 FORMAT(30X,1H*,10X,16HDATA SAMPLED AT ,F7.2,6H PTS/S,19X,1H*)
234 FORMAT(1H1)
235 FORMAT(30X,1H*,58X,1H*)
236 FORMAT(30X,1H*,10X,10HRUN NO    ,A8,30X,1H*)
237 FORMAT(30X,1H*,10X,9HHOLE 1 N0,3X,A8,28X,1H*)
238 FORMAT(30X,1H*,10X,9HHOLE 2 N0,3X,A8,28X,1H*)
240 FORMAT(1H1,20X,17HTRANSFER FUNCTION)
241 FORMAT(1H0,6X,4HND/U,4X,4HH[N])
242 FORMAT(8F10.4)
243 FORMAT(8E10.3)
244 FORMAT(20X,6HXBAR= ,E10.3,3X,7HSIGMA= ,E10.3)
300 FORMAT(5HPROB ,I1,10X,5HRUN  ,A8)
301 FORMAT(6HSPEC 1,10X,5HRUN  ,A8)
302 FORMAT(6HSPEC 2,10X,5HRUN  ,A8)
303 FORMAT(7HCO-SPEC,10X,5HRUN  ,A8)
304 FORMAT(9HQUAD-SPEC,10X,5HRUN  ,A8)
305 FORMAT(10HCROSS-SPEC,10X,5HRUN  ,A8)
306 FORMAT(9HCOHERENCE,10X,5HRUN  ,A8)
307 FORMAT(17HTRANSFER FUNCTION,10X,5HRUN  ,A8)
308 FORMAT(11HPHASE ANGLE,10X,5HRUN  ,A8)
309 FORMAT(6HCORR 1,10X,5HRUN  ,A8)
310 FORMAT(6HCORR 2,10X,5HRUN  ,A8)
311 FORMAT(10HCROSS-CORR,10X,5HRUN  ,A8)
600 FORMAT(30X,1H*,10X,19HHANNING FILTER USED,29X,1H*)
601 FORMAT(30X,1H*,10X,19HBOX-CAR FILTER USED,29X,1H*)
602 FORMAT(30X,1H*,10X,27HTRIANGULAR DATA WINDOW USED,21X,1H*)
603 FORMAT(30X,1H*,10X,22H1-T*T DATA WINDOW USED,26X,1H*)
604 FORMAT(30X,1H*,10X,21HHANN DATA WINDOW USED,27X, 1H*)
605 FORMAT(30X,1H*,10X,21HHAMM DATA WINDOW USED,27X, 1H*)
    STOP
    END
```

```
      SUBROUTINE PROB(X,N,XBAR,SIGMA,Y,XX)
      DIMENSION X(N),IPROB(52),JPROB(52),II(1)
      DIMENSION Y(105),XX(105)
      AN=FLOAT(N)
      XBAR=0.
      DO 1 I=1,N
      XBAR=XBAR+X(I)
    1 CONTINUE
      XBAR=XBAR/AN
      DO 2 I=1,N
      X(I)=X(I)-XBAR
    2 CONTINUE
      VAR=0.
      DO 3 I=1,N
      VAR=VAR+(X(I)*X(I))
    3 CONTINUE
      VAR=VAR/AN
      SIGMA=SQRT(VAR)
      RSIGMA=5.0*SIGMA
      DO 4 I=1,52
      IPROB(I)=0
      JPROB(I)=0
    4 CONTINUE
      II(1)=0
      DO 6 I=1,N
      X1=X(I)
      X2=(X1/RSIGMA)*50.0
      X3=X2+0.5
      IF(X2.LT.0.0) X3=X2-0.5
      IF(INT(X3)) 10,20,30
   30 IX2=INT(X3)
      IF(IX2.GT.51) IX2=52
      IPROB(IX2)=IPROB(IX2)+1
      GO TO 5
   20 II(1)=II(1)+1
      GO TO 5
   10 X2=ABS(X3)
      JX2=INT(X2)
      IF(JX2.GT.51)  JX2=52
      JPROB(JX2)=JPROB(JX2)+1
      GO TO 5
    5 CONTINUE
    6 CONTINUE
      DO 7 I=1,52
      Y(I)=FLOAT(JPROB(53-I))*10.0/AN
      XX(I)=-(FLOAT(53-I))/10.0
    7 CONTINUE
      Y(53)=FLOAT(II(1))*10.0/AN
      XX(53)=0.0
      DO 8 I=54,105
      Y(I)=FLOAT(IPROB(I-53))*10.0/AN
      XX(I)=(FLOAT(I-53))/10.0
    8 CONTINUE
      RETURN
      END
```

```
      SUBROUTINE MOMENTS(X,XX)
      DIMENSION X(105),XX(105)
      A1=0.
      A2=0.
      A3=0.
      A4=0.
      DO 1 I=1,105
      B1=X(I)*XX(I)*0.1
      B2=B1*XX(I)
      B3=B2*XX(I)
      B4=B3*XX(I)
      A1=A1+B1
      A2=A2+B2
      A3=A3+B3
      A4=A4+B4
    1 CONTINUE
      A3=A3/(A2*SQRT(A2))
      A4=A4/(A2*A2)
      WRITE(2,100) A1,A2,A3,A4
  100 FORMAT(10X,3HM1=,E11.3,5X,3HM2=,E11.3,5X,9HSKEWNESS=,E11.3,5
     1RTOSIS=,E11.3)
      RETURN
      END
```

```
      SUBROUTINE TFN(X,Y,N,A1,F1,D1,DC1,A2,F2,D2,DC2)
      DIMENSION X(N),Y(N)
      NN1=N/2
      DO 1 I=1,NN1
      FR1=Y(I)/F1
      FR2=Y(I)/F2
      DR1=2.0*FR1*D1
      DR2=2.0*FR2*D2
      DR1S=DR1**2
      DR2S=DR2**2
      FR1=1.0-(FR1**2)
      FR1S=FR1**2
      FR2=1.0-(FR2**2)
      FR2S=FR2**2
      AMP1=SQRT(1.0/((A1/(FR1S+DR1S))+DC1))
      AMP2=SQRT(1.0/((A2/(FR2S+DR2S))+DC2))
      THETA1=ATAN(DR1/FR1)
      THETA2=ATAN(DR2/FR2)
      DELTA=THETA2-THETA1
      J=2*I
      K=J-1
      REAL=X(K)*COS(DELTA)+X(J)*SIN(DELTA)
      COMP=X(J)*COS(DELTA)-X(K)*SIN(DELTA)
      X(K)=REAL*AMP1*AMP2
    1 X(J)=COMP*AMP1*AMP2
      RETURN
      END
```

```
  SUBROUTINE MODTRN(X,Y,N,AMP,FREQ,DAMP,DC)
  DIMENSION X(N),Y(N)
  DO 1 I=1,N
  FR=Y(I)/FREQ
  DR=(2.0*DAMP*FR)**2
  FR=(1.0-(FR**2))**2
1 X(I)=X(I)/((AMP/(FR+DR))+DC)
  RETURN
  END


  SUBROUTINE PHASE(X,Y,N,IX)
  DIMENSION X(IX),Y(IX)
  PI=4.0*ATAN(1.0)
  NN1=N/2
  DO 1 I=1,NN1
  J=(2*I)-1
1 Y(I)=X(J)
  DO 2 I=1,NN1
  J=2*I
2 X(I)=X(J)
  CALL MAX(X,N/2,AMAX)
  AMAX=AMAX/500.0
  DO 4 I=1,NN1
  A=-1.0
  B=-1.0
  IF(X(I).GT.0.0) A=1.0
  IF(Y(I).GT.0.0) B=1.0
  IF(ABS(X(I)).LT.AMAX) GO TO 3
  IF(ABS(Y(I)).LT.0.1E-40) GO TO 7
  X(I)=ATAN(X(I)/Y(I))*180.0/PI
  GO TO 5
7 X(I)=90.0
  GO TO 5
3 X(I)=0.0
5 IF(A.EQ.1.0.AND.B.EQ.1.0) GO TO 4
  IF(A.EQ.1.0.AND.B.EQ.-1.0) X(I)=180.0+X(I)
  IF(A.EQ.-1.0.AND.B.EQ.-1.0) X(I)=X(I)+180.0
  IF(A.EQ.-1.0.AND.B.EQ.1.0) X(I)=360.0+X(I)
4 CONTINUE
  RETURN
  END
```

```
      SUBROUTINE HARMON(A,S,M,IFS,IFERR,IA,IS)
      DIMENSION A(IA),S(IS)
      DIMENSION K(12)
      EQUIVALENCE (K(11),K11),(K(10),K10),(K(9),K9),(K(8),K8),(K(
     1(K(6),K6),(K(5),K5),(K(4),K4),(K(3),K3),(K(2),K2),(K(1),K1)
      IF(M)2,2,3
    3 IF(M-11)5,5,2
    2 IFERR=1
    1 RETURN
    5 IFERR=0
      N=2**M
      IF(IABS(IFS)-1) 200,200,10
   10 IF(N-NP)20,20,12
   12 IFERR=1
      GO TO 200
   20 K(1)=2*N
      DO 22 L=2,M
   22 K(L)=K(L-1)/2
      DO 24 L=M,10
   24 K(L+1)=2
      IJ=2
      J1=2
   25 DO 30 J2=J1,K10,K11
      DO 30 J3=J2,K9,K10
      DO 30 J4=J3,K8,K9
      DO 30 J5=J4,K7,K8
      DO 30 J6=J5,K6,K7
      DO 30 J7=J6,K5,K6
      DO 30 J8=J7,K4,K5
      DO 30 J9=J8,K3,K4
      DO 30 J10=J9,K2,K3
      DO 30 JI=J10,K1,K2
      IF(IJ-JI)28,30,30
   28 T=A(IJ-1)
      A(IJ-1)=A(JI-1)
      A(JI-1)=T
      T=A(IJ)
      A(IJ)=A(JI)
      A(JI)=T
   30 IJ=IJ+2
      J1=J1+2
      IF(K(11)-J1) 31,25,25
   31 IF(IFS)32,2,36
   32 FN=FLOAT(N)
      DO 34 I=1,N
      A(2*I-1)=A(2*I-1)/FN
   34 A(2*I)=-A(2*I)/FN
   36 DO 40 I=1,N,2
      T=A(2*I-1)
      A(2*I-1)=T+A(2*I+1)
      A(2*I+1)=T-A(2*I+1)
      T=A(2*I)
      A(2*I)=T+A(2*I+2)
   40 A(2*I+2)=T-A(2*I+2)
      IF(M-1)2,1,50
   50 LEXP1=2
      LEXP=8
```

```
      NPL=2**MT
      DO 130 L=2,M
      DO 80 I=2,K1,LEXP
      I1=I+LEXP1
      I2=I1+LEXP1
      I3=I2+LEXP1
      T=A(I-1)
      A(I-1)=T+A(I2-1)
      A(I2-1)=T-A(I2-1)
      T=A(I)
      A(I)=T+A(I2)
      A(I2)=T-A(I2)
      T=-A(I3)
      TI=A(I3-1)
      A(I3-1)=A(I1-1)-T
      A(I3)=A(I1)-TI
      A(I1-1)=A(I1-1)+T
   80 A(I1)=A(I1)+TI
      IF(L-2)120,120,90
   90 KLAST=K(1)-LEXP
      JJ=NPL
      DO 110 J=4,LEXP1,2
      NPJJ=NT-JJ
      UR=S(NPJJ)
      UI=S(JJ)
      ILAST=J+KLAST
      DO 100 I=J,ILAST,LEXP
      I1=I+LEXP1
      I2=I1+LEXP1
      I3=I2+LEXP1
      T=A(I2-1)*UR-A(I2)*UI
      TI=A(I2-1)*UI+A(I2)*UR
      A(I2-1)=A(I-1)-T
      A(I2)=A(I)-TI
      A(I-1)=A(I-1)+T
      A(I)=A(I)+TI
      T=-A(I3-1)*UI-A(I3)*UR
      TI=A(I3-1)*UR-A(I3)*UI
      A(I3-1)=A(I1-1)-T
      A(I3)=A(I1)-TI
      A(I1-1)=A(I1-1)+T
  100 A(I1)=A(I1)+TI
  110 JJ=JJ+NPL
  120 LEXP1=2*LEXP1
      LEXP=2*LEXP
  130 NPL=NPL/2
      IF(IFS)145,2,1
  145 DO 150 I=1,N
  150 A(2*I)=-A(2*I)
      GO TO 1
  200 NP=N
      NT=N/4
      MP=M
      MT=M-2
      IF(MT)260,260,205
  205 THETA=0.7853981634
      JSTEP=NT
```

```
      JDIF=NT/2
      S(JDIF)=SIN(THETA)
      IF(MT-2) 260,220,220
  220 DO 250 L=2,MT
      THETA=THETA/2.0
      JSTEP2=JSTEP
      JSTEP=JDIF
      JDIF=JDIF/2
      S(JDIF)=SIN(THETA)
      JC1=NT-JDIF
      S(JC1)=COS(THETA)
      JLAST=NT-JSTEP2
      IF(JLAST-JSTEP) 250,230,230
  230 DO 240 J=JSTEP,JLAST,JSTEP
      JC=NT-J
      JD=J+JDIF
  240 S(JD)=S(J)*S(JC1)+S(JDIF)*S(JC)
  250 CONTINUE
  260 IF(IFS) 20,1,20
      END
```

```
      SUBROUTINE FOURIER(A,S,M,IFERR,IA,IS)
      DIMENSION A(IA),S(IS)
      N=2**(M-1)
      CALL HARMON(A,S,M-1,-1,IFERR,IA,IS)
      NHALF=N/2
      NTWO=2*N+2
      RN=N
      X=COS(3.1415926536/RN)
      X0=X
      Y=SIN(3.1415926536/RN)
      Y0=Y
      DO 1 K2=4,N,2
      K1=K2-1
      N2=NTWO-K2
      N1=N2-1
      BK1=A(K1)+A(N1)
      BK2=A(K2)-A(N2)
      BN1=A(K2)+A(N2)
      BN2=A(K1)-A(N1)
      XBN1=X*BN1
      XBN2=X*BN2
      YBN1=Y*BN1
      YBN2=Y*BN2
      A(K1)=0.5*(BK1+XBN1-YBN2)*0.5
      A(K2)=0.5*(-BK2+XBN2+YBN1)*0.5
      A(N1)=0.5*(BK1-XBN1+YBN2)*0.5
      A(N2)=0.5*(BK2+XBN2+YBN1)*0.5
      Q=X*X0-Y*Y0
      Y=Y*X0+X*Y0
    1 X=Q
      A(2*N-1)=0.25*(A(1)-A(2))
      A(2*N)=0.0
      A(1)=0.25*(A(1)+A(2))
      A(2)=0.
      RETURN
      END
```

```
  SUBROUTINE NEWHANN(X,N,IX,J,IFILT)
  DIMENSION X(IX),Y(256)
  N2=N/2
  IF(J-2) 1,4,7
1 DO 2 I=1,N2
2 X(I)=X(2*I-1)
  IF(IFILT) 3,6,3
3 CALL HANNING(X,N2,IX)
  IF(J-1) 4,6,4
4 DO 5 I=2,N,2
  J=N+2-I
  X(J)=0.
5 X(J-1)=X(J/2)
  GO TO 6
7 IF(IFILT.EQ.0) GO TO 6
  DO 8 I=1,N2
  X(I)=X(2*I-1)
8 Y(I)=X(2*I)
  CALL HANNING(X,N2,IX)
  CALL HANNING(Y,N2,IX)
  DO 9 I=1,N2
  K=N2+1-I
  X(2*K-1)=X(K)
9 X(2*K)=Y(K)
6 RETURN
  END
```

```
  SUBROUTINE HANNING(A,N,IA)
  DIMENSION A(IA)
  NN=N-1
  X1=A(1)
  A(1)=(X1+A(2))*0.5
  DO 1 I=2,NN
  X2=A(I)
  A(I)=0.5*X2+0.25*(X1+A(I+1))
1 X1=X2
  A(N)=0.5*(A(N)+X1)
  RETURN
  END
```

```
      SUBROUTINE CRPR(X,Y,N,IX)
      DIMENSION X(IX),Y(IX)
      DO 1 I=1,N,2
      I1=I+1
      TEMP=X(I)*Y(I)+X(I1)*Y(I1)
      X(I1)=X(I)*Y(I1)-X(I1)*Y(I)
      Y(I1)=-X(I1)
      Y(I)=TEMP
    1 X(I)=TEMP
      RETURN
      END
```

```
      SUBROUTINE MCPR(X,N,IX)
      DIMENSION X(IX)
      DO 1 I=1,N,2
      I1=I+1
    1 X(I)=SQRT(X(I)**2+X(I1)**2)
      NN1=N/2
      DO 2 I=1,NN1
    2 X(I)=X(2*I-1)
      RETURN
      END
```

```
      SUBROUTINE NPR(X,N,IX)
      DIMENSION X(IX)
      DO 1 I=1,N,2
      I1=I+1
      X(I)=X(I)**2+X(I1)**2
    1 X(I1)=0.
      RETURN
      END
```

```
      SUBROUTINE PLOT(Y,F,NPTS)
      DIMENSION IGRAPH(91),F(NPTS),Y(NPTS)
      REAL MAXE,MINE
      DATA IP/4H+   /,IS/4H    /,IDOT/4H.   /
      DO 1 K=1,91
    1 IGRAPH(K)=IS
      MAXE=0.
      MINE=0.
      DO 2 K=1,NPTS
      IF(MAXE.LT.Y(K)) MAXE=Y(K)
    2 IF(MINE.GT.Y(K)) MINE=Y(K)
      IF(ABS(MAXE).LE.0.1E-10.AND.ABS(MINE).LE.0.1E-10) GO TO 10
      IF(MAXE.GT.0.AND.MINE.EQ.0) GO TO 3
      IF(MAXE.EQ.0.AND.MINE.LT.0) GO TO 5
      IF(MAXE.GT.0.AND.MINE.LT.0) GO TO 7
    3 SCALE=90./MAXE
      IGRAPH(1)=IDOT
      DO 4 K=1,NPTS
      ISCALE=INT(SCALE*Y(K))+1
      IGRAPH(ISCALE)=IP
      WRITE(2,9) F(K),Y(K),IGRAPH
      IGRAPH(ISCALE)=IS
    4 IGRAPH(1)=IDOT
      IGRAPH(1)=IS
      GO TO 10
    5 SCALE=90./MINE
      IGRAPH(91)=IDOT
      DO 6 K=1,NPTS
      ISCALE=INT(SCALE*Y(K))+1
      IGRAPH(ISCALE)=IP
      WRITE(2,9) F(K),Y(K),IGRAPH
      IGRAPH(ISCALE)=IS
    6 IGRAPH(91)=IDOT
      IGRAPH(91)=IS
      GO TO 10
    7 SCALE=90./(MAXE-MINE)
      NZERO=INT(-SCALE*MINE)+1
      IGRAPH(NZERO)=IDOT
      DO 8 K=1,NPTS
      ISCALE=INT(SCALE*(Y(K)-MINE))+1
      IGRAPH(ISCALE)=IP
      WRITE(2,9) F(K),Y(K),IGRAPH
      IGRAPH(ISCALE)=IS
    8 IGRAPH(NZERO)=IDOT
      IGRAPH(NZERO)=IS
   10 CONTINUE
    9 FORMAT(2X,F8.3,E13.4,6X,91A1)
      RETURN
      END
```

```
      SUBROUTINE WINDOW(A,C,N,TYPE,CA1)
      DIMENSION A(N),C(N)
      PI=4.0*ATAN(1.0)
      AN=FLOAT(N)
      IF(CA1.EQ.1.0) GO TO 9
      CA1=1.0
      IF(TYPE.EQ.1.0) GO TO 1
      IF(TYPE.EQ.2.0)GO TO 3
      IF(TYPE.EQ.3.0) GO TO 5
      IF(TYPE.EQ.4.0) GO TO 7
    1 DO 2 I=1,N
      B=(2.0*FLOAT(I)/AN)-1.0
    2 C(I)=1.0-ABS(B)
      GO TO 9
    3 DO 4 I=1,N
      B=(2.0*FLOAT(I)/AN)-1.0
    4 C(I)=1.0-B*B
      GO TO 9
    5 DO 6 I=1,N
      B=COS(2.0*PI*FLOAT(I)/AN)
    6 C(I)=0.5*(1.0-B)
      GO TO 9
    7 DO 8 I=1,N
      B=COS(2.0*PI*FLOAT(I)/AN)
    8 C(I)=0.54-0.46*B
    9 DO 10 I=1,N
   10 A(I)=A(I)*C(I)
      RETURN
      END
```

```
      SUBROUTINE POSS(II,JJ)
      INTEGER CHAN
      DATA CHAN/10HCHAN      /
    2 READ(5,1) ITEST
      IF(ITEST.NE.CHAN) GO TO 2
    3 BACKSPACE 5
      READ(5,4) II,JJ
    1 FORMAT(A4)
    4 FORMAT(8X,I4,6X,I4)
      RETURN
      END
```

```
      SUBROUTINE SIMPS(X,NP,DELTAN,AREA)
      DIMENSION X(NP)
      AREA=0.
      DO 1 I=1,NP
    1 AREA=AREA+X(I)
      AREA=AREA*DELTAN
      RETURN
      END
```

```
      SUBROUTINE MAX(X,N,AMAX)
      DIMENSION X(N)
      AMAX=0.
      DO 1 I=1,N
    1 IF(ABS(X(I)).GT.AMAX) AMAX=ABS(X(I))
      RETURN
      END
```